NNT : 2019SACLS249

Thèse de doctorat

On the multiphase structure of the turbulent neutral interstellar medium

Thèse de doctorat de l'Université Paris-Saclay
préparée à l'Université Paris-Sud et au Commissariat à l'énergie atomique

Ecole doctorale n°127 Astronomie et Astrophysique d'Ile de France (AAIF)
Spécialité de doctorat : voir spécialités par l'ED

Thèse présentée et soutenue à Gif-sur-Yvette, le 25 septembre 2019, par

ANTOINE PAUL HENRI MARCHAL

Composition du Jury :

Mathieu Langer Professeur, Université Paris-Sud	Président
Robert Benjamin Professor, University of Wisconsin	Rapporteur
John Dickey Professor, University of Tasmania	Rapporteur
Naomi McClure-Griffiths Professor, Australian National University	Examinateur
François Orieux Maitre de conférence, Universté Paris-Sud	Examinateur
Benjamin Godard Astronome-Adjoint, Ecole normale supérieure de Paris	Examinateur
Marc-Antoine Miville Deschênes DR CNRS, Commissariat à l'énergie atomique (AIM)	Directeur de thèse
Patrick Hennebelle CEA Scientist, Commissariat à l'énergie atomique (AIM)	Invité

Acknowledgement

First of all, I would like to thank my PhD supervisor, Marc-Antoine Miville-Deschênes, for guiding me during these three years. Our field of research, the interstellar medium, is simply fascinating. Many thanks for guiding me through this extremely rich literature. It would have been very easy for me to get lost otherwise. Finally, thank you for the many discussions we shared during this adventure. I try every day to be inspired by your enthusiasm and your overflowing scientific curiosity.

Je voudrais remercier très chaleuresement François Orieux pour m'avoir enseigné les outils dont j'avais besoin pour accomplir ce travail. Merci également à Charles Soussen pour ces excellents cours auxquels j'ai eu la chance d'assister. Merci à Marie-Jeanne Lesot, Adrien Revault d'Allonnes et Nicolas Gac pour toutes les riches discussions que nous avons eu lors de nos réunions hyperstars.

Many thanks to the members of my jury, Mathieu Langer, Robert Benjamin, John Dickey, Naomi McClure-Griffiths, François Orieux, Benjamin Godard and Patrick Hennebelle for evaluating this manuscript and for providing me with very constructive comments for its improvement. It was an honour for me to share this work with you, who have already advanced science so much.

Merci à l'Institut d'Astrophysique Spatial (IAS), au Commisariat à l'énergie atomique et aux énergies renouvelables (CEA) et aux équipes AMIS, COSM!X et LMPA de m'avoir acceuilli si chaleuresement. Un grand merci à Alain Abergel. Tu as été d'un grand soutien pour cette aventure.

Merci à tous les gens que j'ai rencontré et avec qui j'ai partagé ces trois belles années à l'IAS et au CEA. Merci Thomas, Victor, Thiébaut, Nadèje, Daniela, Raphaël, Adélie, Céline, Louis, Edouard, Lisa, Elena, Maximilien, Chiara, Baptiste, Solène, Anna, Rose, Ivan, Goeffrey, Geoffroy, Andrea, Adèle, Michelle ...

Merci à ma merveilleuse et grande famille, mon frère Louis, mes soeurs Jeanne et Léa, mes grands mères Elisabeth et Andrée, et mes parents Alexandre et Isabelle. Merci également à Julien, Pierre, Mélodie, Anne et Michel.

Merci à mes amis proches, Julien-Pierre qui m'a guidé vers la recherche, Bertrand, Arthur, Camille, Youri, Alexis, Tom, Steven, Melissa, Maximilien, Misha, Thiébaut, Thomas, Marie et Nilaï pour votre soutien.

Merci Wenjia. Merci d'être là et mille mercis pour ton grand soutien lors de l'écriture de ce manuscript.

À mon grand-père, Michel Marchal.

Contents

1 Introduction

General context According to human conception, the Universe is *almost* empty. In the heart of galaxies, the average density of gas is about one particle per cubic centimetre. Brought back to sizes that the human mind can conceive, it would be necessary to fill the volume occupied by the earth with only a few liters of water to obtain the same value (Christopher McKee interview, 2014). It is because of its immensity, just as inconceivable to the human mind as its density, that the Galaxy draws all its baryonic mass. Like for the Universe as a whole, the hydrogen atom is the most abundant element in galaxies, being in neutral (HI), ionized (HII) or molecular (H_2) form. It is from these states that the modern theory of the interstellar medium emerged, grouping together a total of five distinct phases. From the hottest to the coldest phase, the first of these is the *hot ionized medium* (HIM), an ionized gas with temperatures $\gtrsim 10^6$ K and densities $\lesssim 0.003$ cm^{-3}. This phase, also called the *hot corona*, is mainly heated by supernovae explosions. The second is the *warm ionized medium* (WIM). Having temperatures of $\sim$6000-12000 K, this diffuse gas is primarily ionized by UV photons emitted by O and B stars in the Galaxy. The third and fourth are the *warm neutral medium* (WNM) and *cold neutral medium* (CNM). Temperatures and densities of these two phases can vary considerably, from $\sim$50 to 8000 K and $\sim$0.5 to 50 cm^{-3}. The fifth and last is made of molecular clouds whose temperatures are typically $\sim$10-20 K and densities $\gtrsim 10^3$ cm^{-3}. Interestingly, these phase are roughly in pressure equilibrium and the vertical thickness of each phase increases with temperature. Despite this pressure equilibrium on large scale, the Milky Way is a system that is highly out-of-equilibrium from a dynamical point of view. All the phases appear to be in constant interaction.

Among these interactions, the accretion of neutral gas from the Galactic halo is of primary interest. A major component of the neutral ISM (WNM+CNM) is a population of clouds, named High-Velocity Clouds (HVCs), which are located in the Galactic corona. These structures are falling into the gravitational potential of the Milky Way, providing gas supply to the star formation. In the Galactic plane, the neutral and molecular phases are particularly interesting for understanding the star formation cycle in galaxies. Stars form by gravitational collapse of dense and cold structures located in molecular clouds. However, the process that leads to the formation of these over-densities is still unclear. It is believed that the radiative condensation of the diffuse WNM to produce a thermally unstable lukewarm medium and a dense cold medium is closely related to the initial step leading the atomic-to-molecular (HI-to-H2) transition and the formation of molecular clouds. Huge efforts have been made to understand this transition, but the step that led to the formation of the cold HI still remains unclear. In particular, one key element to understand the star formation cycle seems to be related to the efficiency of formation of this cold HI (Ostriker et al., 2010), whether it is form in the Galactic disk or accreted from the Galactic halo (HVCs).

The current vision of this condensation process from the warm to the cold phase has a long history. Early observations of the 21 cm line showed a significant difference between emission and absorption spectra. On lines of sight to radio-sources, the HI appears in absorption with very narrow features

(a few km s^{-1}). In emission the 21 cm line contains these narrow features on top of much boarder spectral structures (10-20 km s^{-1}). Clark (1965) was the first to suggest that this might be the signature of a cloud-intercloud medium in pressure equilibrium. Very rapidly Field (1965) and Field et al. (1969) introduced the concept of thermal instability and laid out the theoretical ground of a "two phase" HI model showing that, at the pressure of the ISM, the heating and cooling processes naturally lead to two thermally stable states: a dense cold neutral medium (CNM - $T \sim 50$ K, $n \sim 50$ cm^{-3}) immersed in a diffuse warm neutral medium (WNM - $T \sim 8000$ K, $n \sim 0.3$ cm^{-3}). This view was later complemented by Wolfire et al. (1995) and Wolfire et al. (2003) who considered updated heating (dominated by the photo-electric effect on small dust grains) and cooling (dominated by CII - 158 μm, OI - 63 μm, Lα and electron recombinations onto positive charged grains) processes of the ISM.

This description of the diffuse neutral gas complemented a parallel hypothesis that emerged in the 1950s (e.g., Weizsäcker, 1951; Hoerner, 1951; Chandrasekhar and Münch, 1952) and considered the ISM as a multi-scale turbulent medium. In this case, the density and velocity structures are the result of a highly dynamical and out-of-equilibrium medium. In order to reconcile the 'static/two-phase' and the 'turbulent' hypotheses, several studies have aimed at understanding the production of the CNM in a turbulent and thermally unstable flow using numerical simulations (e.g., Hennebelle and Pérault, 1999; Koyama and Inutsuka, 2002; Audit and Hennebelle, 2005; Hennebelle et al., 2008; Saury et al., 2014). In general, these numerical studies show that the WNM has the properties of a trans-sonic turbulent flow, while the CNM shows a much more contrasted density structure, in accordance with the cloud-intercloud picture. In addition, such studies indicate the presence of a significant fraction of the mass being in the thermally unstable regime (i.e., with a temperature mid-way between the CNM and WNM stable states). For instance, Saury et al. (2014) showed that 30% of the HI is in the thermally unstable regime. Interestingly, these latter authors also show that this lukewarm neutral medium (LNM) is spatially located around the cold structures, pointing at the transitional nature of this thermal state.

From an observational standpoint, studies combining 21 cm absorption and emission data have clearly revealed the presence of HI at intermediate/unstable temperatures, typically between 500 and 5000 K (e.g., Heiles and Troland, 2003b; Kanekar et al., 2003; Roy et al., 2013a; Roy et al., 2013b; Murray et al., 2015; Murray et al., 2018b). Based on a coherent modeling of emission and absorption spectra, Heiles and Troland (2003), Murray et al. (2015) and Murray et al. (2018) estimated that about 30% of the HI is in the cold CNM phase, 20% in the thermally unstable regime, and 50% in the WNM. Nevertheless the fraction of the HI in each phase remains uncertain and large variations are observed: the fraction of the mass in the CNM ranges from $\sim$1% to more than 50% (Murray et al., 2018b).

Motivation The nature of these variations and how they relate to the dynamical conditions of the gas remains largely unexplored from the observational point of view. One main hurdle in getting access to this information is the fact that our knowledge of the multiphase nature of the HI relies on 21 cm absorption measurements that are limited to lines of sight to radio sources. By construction, this way of observing prevents us from mapping the HI phases. To go further, and really compare with numerical simulations that are currently under-constrained by observation, it is necessary to map the column density structure of each phase and study the spatial variations of their centroid velocity and velocity dispersion. This calls for methods that can extract the information of each HI phase from fully sampled 21 cm emission data only. Huge efforts have been made to map the 21 cm emission of the Galactic HI (recent examples are Taylor et al., 2003; Kalberla et al., 2005; Stil et al., 2006;

McClure-Griffiths et al., 2009; Winkel et al., 2016; Peek et al., 2018) and a large amount of data is now available. The information about the multiphase and multi-scale nature of the HI contained in these large hyper-spectral data cubes has remained elusive due to the difficulty in separating the emission from the different phases on each line of sight. The work presented in this thesis aims to develop a new tool capable of extracting this information from the 21 cm emission data only. The second objective of this work is to use this new algorithm to study the thermal and turbulent properties of the neutral interstellar medium, especially in the WNM where very little information have been obtained to date.

Thesis structure Chapter 2 is dedicated to giving the reader a brief introduction to fluid mechanics and turbulence. The Navier-Stokes equations are used to present and discuss the concept of turbulence. Some historical experiments and concepts related to turbulence are presented in parallel in order to understand the emergence and evolution of this discipline of primary interest for astrophysics. Tools to analyze statistical properties of turbulence are then presented. Finally, the specific case of interstellar turbulence and the mechanisms that generate it at all scales of the interstellar medium are discussed, as well as the application of the statistical tools presented for the study of interstellar turbulence.

Chapter 3 provides a brief historical overview of the detection and early works related to interstellar neutral hydrogen. The main steps in the calculation of thermal instability are presented as well as the heating and cooling processes necessary to understand the growth of perturbations that cause the thermal condensation of the fluid. Then, an observational overview of the thermal and morphological structure of the neutral ISM is presented in order to establish the environments in which this phase transition occurs in the interstellar medium. This variety of object and medium will allow us in particular to highlight the major stakes that the separation of the phases of the interstellar medium represents.

The goal of Chapter 4 is to present a new algorithm developed to perform the separation of diffuse sources in hyper-spectral data. Specifically, the algorithm is designed in order to address the velocity blending problem by taking advantage of the spatial coherence of the individual sources. The main scientific driver of this effort was to extract the multiphase structure of the HI from 21 cm line emission only, providing a means to map each phase separately, but the algorithm developed here should be generic enough to extract diffuse structures in any hyper-spectral cube. This new Gaussian decomposition algorithm named *ROHSA* (Regularized Optimization for Hyper-Spectral Analysis) is based on a multi-resolution process from coarse to fine grid. *ROHSA* uses a regularized nonlinear least-square criterion to take into account the spatial coherence of the emission and the multiphase nature of the gas simultaneously. In order to obtain a solution with spatially smooth parameters, the optimization is performed on the whole data cube at once. The performances of *ROHSA* are tested on a synthetic observation computed from numerical simulations of thermally bi-stable turbulence. We then apply *ROHSA* to a 21 cm observation of a region of high Galactic latitude from the GHIGLS survey and present our findings.

Chapter 5 is dedicated to the study of the different inter-connected properties of the diffuse neutral ISM, namely the thermal properties, the statistical properties of the turbulent cascade acting in the fluid, and the properties of the condensation mode of the thermal instability allowing the formation of the dense neutral phase. For this analysis we use the same region of high Galactic latitude from the GHIGLS survey as presented in Chapt. 4. In particular, the goal of this chapter is to analyze these properties in

the vicinity of the Sun, at the border of the Local Bubble. The studied field is therefore chosen in order to focus only on the local velocity component (LVC) of the emission.

Conclusion and perspective related to this thesis are addressed in Chapter 6.

2 Interstellar turbulence

> ***Eddie**:*
> *You know, it's funny... you come to someplace new, an'... and everything looks just the same.*
> ***Willie**:*
> *No kiddin' Eddie.*
>
> — **Stranger than Paradise (1984)**
> Jim Jarmusch

Contents

2.1 Fluid mechanics

This section is dedicated to giving the reader a brief introduction to the concept of turbulence emerging from fluid mechanics, by limiting ourselves to incompressible flows[1]. The equations presented here are largely taken from the following book: "turbulence, an introduction for scientist and engineers" of P. A. Davidson (Davidson, 2015). In this short overview, we derive the Navier-Stokes equation and the kinetic energy equation to establish the expression of the internal energy transfer rate which is of primary interest for describing the turbulence cascade acting in the ISM. We finally introduce the concept of turbulence by making a brief description of vorticity dynamics. For complementary discussions of these equations, we refer the reader to the Chapter 2 of Davidson (2015).

2.1.1 The Navier-Stokes equation

The continuity equation First, let us consider a fluid element of volume δV with a density ρ, moving at a local velocity $\mathbf{u}$. Its mass is

$$\delta m = \rho \delta V. \tag{2.1}$$

Assuming that this mass is conserved, its time-rate-of-change is zero and we have

$$\frac{D(\delta m)}{Dt} = 0. \tag{2.2}$$

Combining Eqs. 2.1 and 2.2, we have

$$\frac{D\rho}{Dt} + \rho \left[\frac{1}{\delta V} \frac{D(\delta V)}{Dt} \right] = 0 \tag{2.3}$$

where the term in bracket is the time rate of change of the volume of the fluid element, per unit volume. It can be easily shown (see Sect. 2.4 of Anderson (1995)) that it is the physical meaning of the divergence of the velocity $\boldsymbol{\nabla} \cdot \mathbf{u}$. Equation 2.3 becomes

$$\frac{D\rho}{Dt} + \rho \boldsymbol{\nabla} \cdot \mathbf{u} = 0. \tag{2.4}$$

This is the continuity equation. In the case of an incompressible fluid, Eq. 2.4 reduces to

$$\boldsymbol{\nabla} \cdot \mathbf{u} = 0. \tag{2.5}$$

The momentum equation The Newton's second law applied to the same fluid element can be written in the form

$$(\rho \delta V) \frac{D\mathbf{u}}{Dt} = - (\boldsymbol{\nabla} p) \, \delta V + \text{viscous forces} \tag{2.6}$$

where the first term on the right hand is the net pressure force acting on the fluid element and the second term represents the forces arising from the viscous stresses[2]. The viscous stresses are

[1] It is now well known that turbulence in the interstellar medium is far from being considered incompressible. Nevertheless, this framework allows us to first understand the fundamental principles related to turbulence.

[2] Note that we will give a physical meaning of the viscous stresses in the following when introducing Newton's law of viscosity.

composed of shear stresses and normal stresses that, if we consider a cubic fluid element, are noted τ_{xy}, τ_{xz}, ..., τ_{xx}, τ_{yy} and τ_{zz}. Any imbalance in stress arising between faces of a fluid element implies a net viscous force. As a result, the fluid element experiences a deformation that leads to a change in its trajectory. The viscous force in each direction i of the cube is then proportional to the sum of the variation of stresses (dependent of i) between the top and the bottom of each faces. Following the summation over repeated index i and j (convention), the viscous forces are

$$f_i = \frac{\partial \tau_{ji}}{\partial x_j}\,\delta V. \tag{2.7}$$

Combining Eqs. 2.6 and 2.7, we obtain

$$\rho\,\frac{D\mathbf{u}}{Dt} = -\,\boldsymbol{\nabla} p \,+\, \frac{\partial \tau_{ji}}{\partial x_j}. \tag{2.8}$$

We shall now use Newton's law of viscosity (shear stress is directly proportional to velocity gradient) to link τ_{ij} to the rate of deformation of the fluid element:

$$\tau_{ij} = \rho\,\nu\,\left\{\frac{\partial u_i}{\partial x_j} \,+\, \frac{\partial u_j}{\partial x_i}\right\}. \tag{2.9}$$

Note that the coefficient of proportionality is simply the absolute viscosity μ=$\rho\nu$, where ν is the kinematic viscosity of the fluid. Physically, we can get an idea of what a viscous stress represents by considering a shear flow $\mathbf{u}$=($u_x(y)$,0,0). Each layer of fluid slides over each other, causing a deformation of fluid elements. In this case, the viscous stress τ_{yx} is proportional to a rate of sliding (or distortion rate) which is simply the velocity gradient $\frac{\partial u_x}{\partial y}$ and the coefficient of proportionality is the absolute viscosity μ of the fluid. Introducing the *strain-rate tensor* S_{ij}

$$S_{ij} = \frac{1}{2}\left[\frac{\partial u_i}{\partial x_j} \,+\, \frac{\partial u_j}{\partial x_i}\right] \tag{2.10}$$

we rewrite τ_{ij} in its well-know compact form

$$\tau_{ij} = 2\rho\nu S_{ij} \tag{2.11}$$

Substituting Eq. 2.11 in Eq. 2.8 with ρ constant, we obtain the so-called Navier-Stokes equation

$$\frac{D\mathbf{u}}{Dt} = -\,\boldsymbol{\nabla}\left(\frac{p}{\rho}\right) \,+\, \nu\,\boldsymbol{\nabla}^2\mathbf{u} \tag{2.12}$$

Note that Eq. 2.12 is expressed using the convective derivative D( )/Dt used in Eq. 2.3, that takes into account both temporal and spatial variations of each component of the vector field $\mathbf{u}$. The convective derivative can be developed using the chain rule (see Sect. 2.1.2 of Davidson (2015)) to obtain an explicit formula of the acceleration of the fluid element

$$\frac{D\mathbf{u}}{Dt} = \frac{\partial \mathbf{u}}{\partial t} \,+\, (\mathbf{u}\,.\,\boldsymbol{\nabla})\,\mathbf{u} \tag{2.13}$$

The Navier-Stokes equation presented in Eq. 2.12 then becomes

$$\frac{\partial \mathbf{u}}{\partial t} \,+\, (\mathbf{u}\,.\,\boldsymbol{\nabla})\,\mathbf{u} = -\,\boldsymbol{\nabla}\left(\frac{p}{\rho}\right) \,+\, \nu\,\boldsymbol{\nabla}^2\mathbf{u} \tag{2.14}$$

We can already note that terms $(\mathbf{u}\,.\,\boldsymbol{\nabla})\,\mathbf{u}$ and $\nu\,\boldsymbol{\nabla}^2\mathbf{u}$ of Eq. 2.14 can be, respectively, seen as an advection term and a diffusion term. We will see in the following Sect. 2.2 that the development from a laminar to a turbulent regime depends on the ratio of these two terms, defined as the Reynolds number Re. It is important to note here that the advection term is quadratically non-linear in $\mathbf{u}$. It is via this non-linearity that instabilities can grow and eventually, if Re is sufficiently high, cause turbulence.

The energy equation The third and last fundamental equation of fluid mechanics results from the first law of thermodynamics: the total energy of the moving fluid element is conserved. However, its derivation is not of primary interest for the present chapter and we shall come back to it in the following Chapt.3 to understand the concept of thermal instability in astrophysical plasma. Instead, we focus here on the kinetic energy equation which allows us to introduce the concept of dissipation of mechanical energy per unit of mass.

2.1.2 Kinetic energy equation

Let us now derive the kinetic energy equation by multiplying Eq. 2.12 by $\mathbf{u}$

$$\mathbf{u}\,.\,\frac{D\mathbf{u}}{Dt} = \frac{D}{Dt}\left(\frac{u^2}{2}\right) = -\,\boldsymbol{\nabla}\,.\,\left[\frac{p}{\rho}\,\mathbf{u}\right] + \nu\,\mathbf{u}\,.\,\left(\boldsymbol{\nabla}^2\mathbf{u}\right) \tag{2.15}$$

The second term of the right hand side of Eq. 2.15 can be decomposed as

$$\nu\,\mathbf{u}\,.\,\left(\boldsymbol{\nabla}^2\mathbf{u}\right) = u_i\,\frac{\partial}{\partial x_j}\,\left[\tau_{ij}\,/\,\rho\right] = \frac{\partial}{\partial x_j}\,\left[u_i\,\tau_{ij}\,/\,\rho\right] - 2\nu S_{ij}S_{ij}. \tag{2.16}$$

Equation 2.15 then becomes

$$\frac{\partial\left(u^2\,/\,2\right)}{\partial t} = -\,\boldsymbol{\nabla}\,.\,\left[\left(u^2\,/\,2 + p/\rho\right)\mathbf{u}\right] - \frac{\partial}{\partial x_j}\,\left[u_i\,\tau_{ij}\,/\,\rho\right] - 2\nu S_{ij}S_{ij}. \tag{2.17}$$

Integrating Eq. 2.17 over an arbitrary volume V gives

$$\frac{\mathrm{d}}{\mathrm{d}t}\int_V \left(u^2\,/\,2\right)\,\mathrm{d}V = \underbrace{-\int_V \boldsymbol{\nabla}\,.\,\left[\left(u^2\,/\,2\right)\mathbf{u}\right]\,\mathrm{d}V}_{\text{- (rate at which kinetic energy is transported across the boundary)}} \tag{2.18}$$

$$\underbrace{-\int_V \boldsymbol{\nabla}\,.\,\left[(p/\rho)\,\mathbf{u}\right]\,\mathrm{d}V}_{\text{+ (rate at which the pressure forces do work on the boundary)}} \tag{2.19}$$

$$\underbrace{-\int_V \frac{\partial}{\partial x_j}\,\left[u_i\,\tau_{ij}\,/\,\rho\right]\,\mathrm{d}V}_{\text{+ (rate at which the viscous forces do work on the boundary)}} \tag{2.20}$$

$$\underbrace{-\int_V 2\nu S_{ij}S_{ij}\mathrm{d}V}_{\text{+ (rate of loss of mechanical energy to heat)}} \tag{2.21}$$

where the meaning of the last term of the right hand side is directly inferred from the conservation of energy. When applied to a small volume δV, this term is the dissipation of mechanical energy per unit of mass and is noted

$$\epsilon = 2\nu S_{ij} S_{ij}. \tag{2.22}$$

This quantity is of primary interest since, as we will see in the following Sect. 2.3, it allows one to characterize the turbulence cascade acting in the fluid. It is also possible, after some algebra, to write the total rate of dissipation of mechanical energy as function of the curl of the velocity field $\mathbf{u}$

$$\int \epsilon \mathrm{d}V = \nu \int (\boldsymbol{\nabla} \times \mathbf{u})^2 \, \mathrm{d}V = \nu \int \boldsymbol{\omega}^2 \mathrm{d}V \tag{2.23}$$

where $\boldsymbol{\omega}$=$\boldsymbol{\nabla} \times \mathbf{u}$ is the vorticity field. We can anticipate via this result that the vorticity field $\boldsymbol{\omega}$ plays an important role in describing the properties of a turbulent flow since it is directly related to the rate of dissipation of mechanical energy. Note that $\boldsymbol{\omega}$ can be seen as a measure of the local rotation of a fluid element. Therefore, a fluid element can be distorted/strained at a rate S_{ij} **and** rotated at a rate $\boldsymbol{\omega}$. These two quantities are naturally linked by the gradient of the velocity field at any point in the fluid

$$\frac{\partial u_i}{\partial x_j} = \frac{1}{2}\left(\frac{\partial u_i}{\partial x_j} + \frac{\partial u_j}{\partial x_i}\right) + \frac{1}{2}\left(\frac{\partial u_i}{\partial x_j} - \frac{\partial u_j}{\partial x_i}\right) = S_{ij} - \frac{1}{2}\epsilon_{ijk}\boldsymbol{\omega} \tag{2.24}$$

where ϵ_{ijk} is the Levi-Civita symbol.

2.1.3 Vorticity dynamics

The idea that the vorticity field plays an important role in describing turbulence can be exploited by looking at its dynamics. In particular, we shall compare in this section the behaviour of governing equations of velocity and vorticity fields. This comparison will allow us to develop a first definition of turbulence.

Let us write its governing equation[3]

$$\frac{\partial \boldsymbol{\omega}}{\partial t} = \boldsymbol{\nabla} \times [\mathbf{u} \times \boldsymbol{\omega}] + \nu \boldsymbol{\nabla}^2 \boldsymbol{\omega} \tag{2.25}$$

that can also, using the identity

$$\boldsymbol{\nabla} \times (\mathbf{u} \times \boldsymbol{\omega}) = (\boldsymbol{\omega} \,.\, \boldsymbol{\nabla})\, \mathbf{u} - (\mathbf{u} \,.\, \boldsymbol{\nabla})\, \boldsymbol{\omega} \tag{2.26}$$

be rewritten as

$$\frac{D\boldsymbol{\omega}}{Dt} = (\boldsymbol{\omega} \,.\, \boldsymbol{\nabla})\, \mathbf{u} + \nu \boldsymbol{\nabla}^2 \boldsymbol{\omega}. \tag{2.27}$$

It is important to note that unlike the governing equation of the velocity field $\mathbf{u}$ expressed in Eq. 2.14, Eq. 2.27 is only composed of a diffusion term and a term of creation of vorticity fuelled by variations of the velocity field along the vorticity tubes, and that these two mechanisms are *local*. Therefore, unlike the velocity field, the vorticity can only be locally spread.

[3] The vorticity equation can be easily obtained by rewriting Eq. 2.14 using the identity $\boldsymbol{\nabla}\left(\mathbf{u}^2 / 2\right) = (\mathbf{u} \,.\, \boldsymbol{\nabla})\, \mathbf{u} + \mathbf{u} \times \boldsymbol{\omega}$ and by taking its curl.

To understand why the evolution of velocity field is non-local, it is useful to compare Eqs. 2.14 and 2.27 which respectively are the governing equations of the velocity field $\mathbf{u}$ and the vorticity field $\boldsymbol{\omega}$. The main difference between Eqs. 2.14 and 2.27 is that the governing equation of the velocity field contains the term $-\boldsymbol{\nabla}\left(p/\rho\right)$. To better understand its nature and impact on the fluid, we can take the divergence of Eq. 2.12. In this way, we can relate directly the pressure field to the velocity field. It follows

$$\boldsymbol{\nabla}^2\left(p\,/\,\rho\right) = -\,\boldsymbol{\nabla}\,.\,\left(\mathbf{u}\,.\,\boldsymbol{\nabla}\mathbf{u}\right) \tag{2.28}$$

that can be reversed using the Biot-Savart law, giving

$$p(\mathbf{x}) = \frac{\rho}{4\pi}\int \frac{\left[\boldsymbol{\nabla}\,.\,\left(\mathbf{u}\,.\,\boldsymbol{\nabla}\mathbf{u}\right)\right]'}{|\mathbf{x}\,-\,\mathbf{x}'|}\,\mathrm{d}x'. \tag{2.29}$$

The pressure field can be calculated at every point of space using the velocity field $\mathbf{u}$. An important property of incompressible fluid is that pressure waves travel at infinite speed. The information contained in $p(\mathbf{x})$ is therefore instantaneously transferred to the entire fluid. It makes the pressure field a non-local one, unlike the vorticity field $\boldsymbol{\omega}$. In other words, any modification of $\mathbf{u}$ in space is instantaneously felt by the fluid whose response is controlled, again at any point in space, by the term $-\boldsymbol{\nabla}\left(p/\rho\right)$ in Eq. 2.14. This instantaneous propagation of the information makes a representation of $\mathbf{u}$ impossible in terms of sub-regions of the fluid. On the other hand, it is natural to think about the vorticity field as a group of local regions called vortices evolving together in space. In general, these vortices are called "eddies". Following Davidson (2015), we shall now be able to define turbulence, as suggested by Stanley Corrsin in 1961, by the following

> *Incompressible hydrodynamic turbulence is a spatially complex distribution of vorticity which advects itself in a chaotic manner in accordance with Eq. 2.27. The vorticity field is random in both space and time, and exhibits a wide and continuous distribution of length and time scales.*

2.1.4 The closure problem of turbulence

We have seen previously that the pressure p can be determined instantaneously using the velocity field u using Eq. 2.29. It therefore appears that for incompressible flows, the Navier-Stokes equation presented in Eq. 2.14 is not anymore a function of p and $\mathbf{u}$ but can be formally written as

$$\frac{\partial \mathbf{u}}{\partial t} = F(\mathbf{u}) \tag{2.30}$$

where $F(\mathbf{u})$ contains the inertial, pressure and viscous forces. It turns out that Eq. 2.30 is deterministic and can be solved over time to obtain $\mathbf{u}(\mathbf{x},t)$. So why is it well known that "turbulence is the most unsolved problem of classical physics" (Richard Feynman) ? The answer to that question is called *the closure problem*. Because of the chaotic behaviour of $\mathbf{u}(\mathbf{x},t)$ in the turbulent regime, most of the turbulence theories developed so far are based on statistical modelling, involving the *Reynolds decomposition*

$$\mathbf{u}(\mathbf{x},t) = \overline{\mathbf{u}}(\mathbf{x}) + \mathbf{u}'(\mathbf{x},t) \tag{2.31}$$

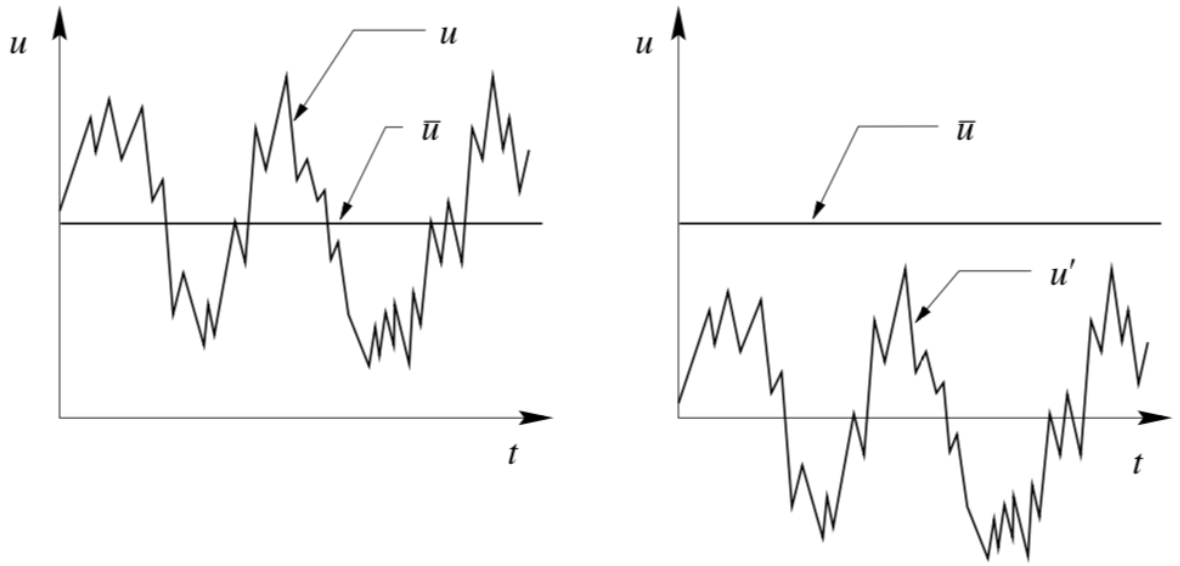

Fig. 2.1.: Plots of parts of Reynolds decomposition. *From Introductory Lectures on Turbulence: Physics, Mathematics and Modeling (James M. McDonough)*

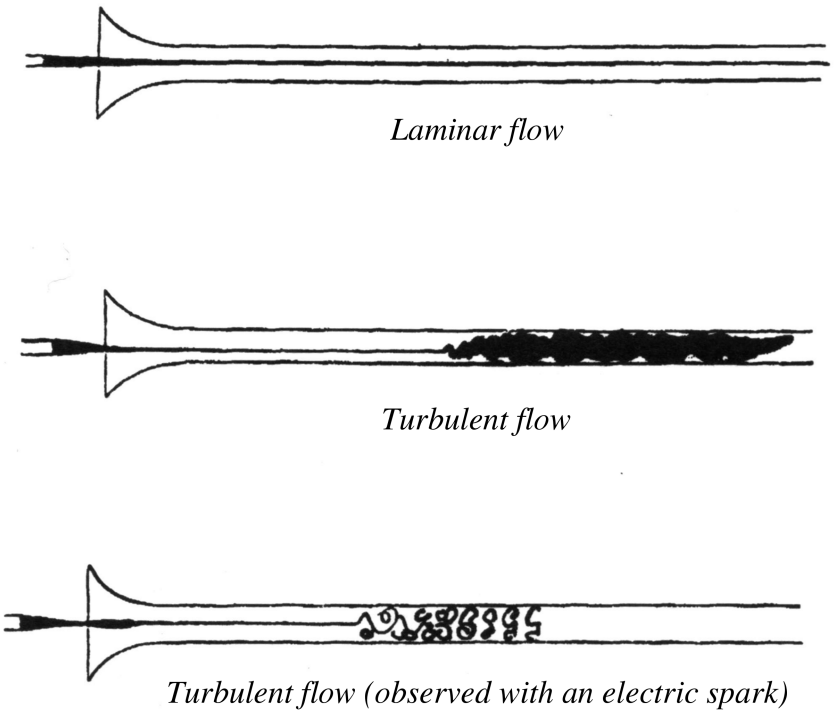

Fig. 2.2.: Sketch of the transition from laminar (top) to turbulent flow (middle) from Reynolds (1883). The bottom panel shows the same turbulent flow when observed with the light of an electric spark to reveal the "eddies" (now viewed as vorticies) of the flow.

where $\overline{\mathbf{u}}$ is the mean flow and $\mathbf{u}'$ is a random fluctuation also called the "*fluctuating part*". Figure 2.1 shows a sketch of the temporal evolution of $\overline{\mathbf{u}}(\mathbf{x})$ and $\mathbf{u}'(\mathbf{x}, t)$. The traditional way of solving Eqs. 2.14

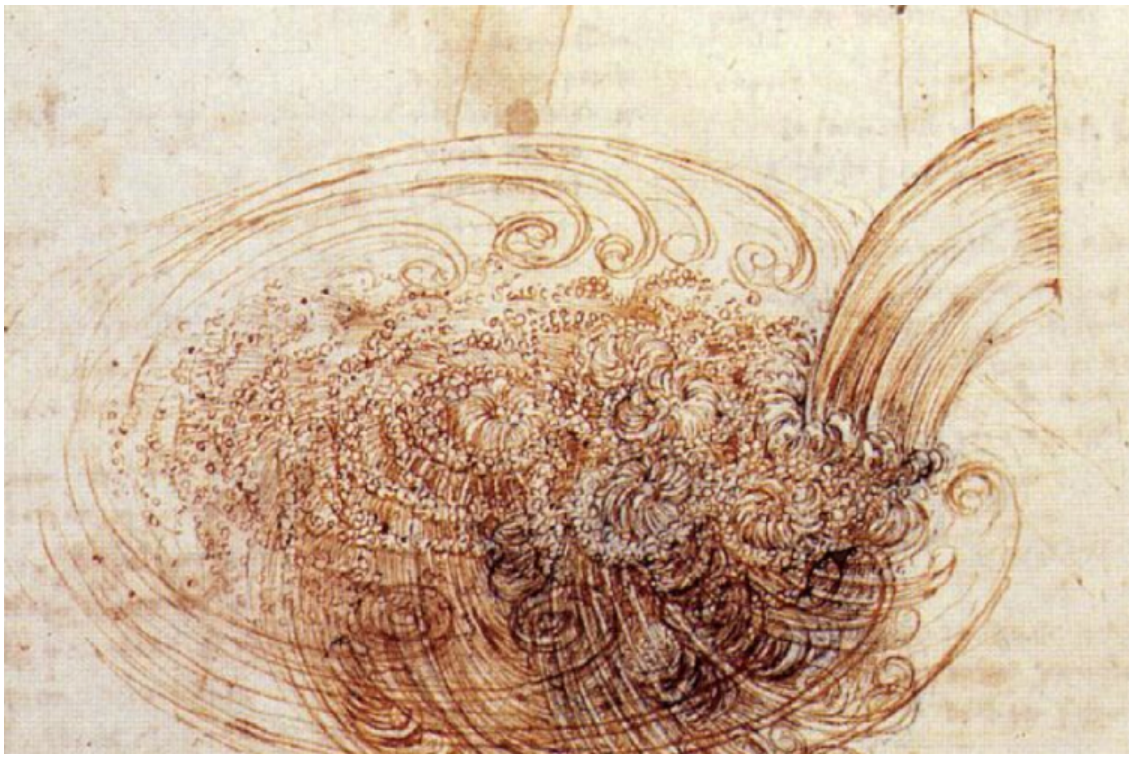

Fig. 2.3.: Drawing made by Leonardo da Vinci (*circa* 1510) about the movement of water.

statistically is by using a decomposition of the form of 2.31 involving in particular the two-point and three-point correlation function[4]. The formulation of an equation of the three-point correlation function involves the four-point correlation function, and so on. The set of equations inferred from this method is therefore not a closed system. It turns out that it is a direct consequence of the non-linearity of the term $(\mathbf{u}\,.\,\boldsymbol{\nabla})\,\mathbf{u}$, which is also mostly responsible for the development of turbulence. Therefore, no exact solution can be found for the velocity field $\mathbf{u}(\mathbf{x},\mathbf{t})$ in space and time, even when considering its statistical properties. We will limit ourselves here to mentioning that a wide variety of approximations have been developed to close this system since the first try by Joseph Valentin Boussinesq at the end of the nineteenth century.

2.2 Reynolds's experiment

Now that we have an idea of the equations that govern incompressible fluids, we can ask ourselves under what precise conditions turbulence develops to form this collection of "eddies" called vortices ? Or in other words, under what conditions do we switch from a laminar regime to a turbulent regime ? Osborne Reynolds, in 1883, was the first to address the question by studying a simple flow passing through a pipe. The sketch of his experiment is shown in Fig. 2.2 where the top and middle panels represent the laminar and turbulence cases. He argued that the transition of turbulence represented here depends on the viscosity ν of the fluid, the velocity u of the flow and the diameter d of the pipe

[4]The notion of correlation function will be introduced in following Sect. 2.4.1

which corresponds to the characteristic length l of the flow. The dimensionless combination of these quantities is now called the Reynolds number Re

$$Re = \frac{ul}{\nu}. \tag{2.32}$$

Reynolds found that turbulence appears at $Re \sim$2000 if initial perturbations applied to the flow are not too small. On the other hand, when minimizing these perturbations, the flow can remains in a laminar regime up to $Re \sim$ 13 000. This wide range over which turbulence may eventually appear highlights the crucial role played by the amplitude of initial disturbances.

A modern interpretation of the Reynolds number can be obtained with a simple dimensional analysis of the ratio of the advection term and the diffusion term of Eq. 2.14. Using the characteristic length l of the system, the ratio is approximately

$$\frac{(\mathbf{u} \,.\, \boldsymbol{\nabla})\, \mathbf{u}}{\nu\, \boldsymbol{\nabla}^2 \mathbf{u}} \sim \frac{u^2/l}{\nu u/l^2} = \frac{ul}{\nu} = Re \tag{2.33}$$

As shown in Fig. 2.2 (bottom), when observed with the light of an electric spark, the turbulent regime described by Reynolds results in a collection of "eddies" (vorticies). It is interesting to note, however, that the first visual representation of a turbulent flow should be attributed to Leonardo da Vinci (∼1510) whose infinite detail drawing shown in Fig. 2.3 exhibits a complex collection of "eddies" emerging from a laminar flow of water. It is also astonishing to read the annotation associated to the drawing,

> *Observe the motion of the surface of the water which resembles that of hair, and has two motions, of which one goes on with the flow of the surface, the other forms the lines of the eddies; thus the water forms eddying whirlpools one part of which are due to the impetus of the principal current and the other to the incidental motion and return flow.*

which is reminiscent of Eq. 2.31.

2.3 The phenomenology of Richardson and Kolmogorov

One striking thing that appears when you look at da Vinci's drawing is the variety of size of the eddies. It is now well known, as we will see in the following, that the size of the largest eddies is comparable to the characteristic length l of the flow and the size of the smallest eddies depends on the Reynolds number Re. It was by attempting to describe the properties of this variety of "eddies" that Richardson introduced the concept of energy cascade at high Re. His commentary on the behaviour of clouds in the atmosphere (1922) is probably the most quoted since the emergence of turbulence theories.

> *One gets a similar impression when making a drawing of a rising cumulus from a fixed point; the details change before the sketch can be completed. We realize that big whirls have little whirls that feed on their velocity, and little whirls have lesser whirls and so on to viscosity.*

The idea has evolved since 1922, thanks in particular to Geoffrey Ingram Taylor and Andrey Nikolaevich Kolmogorov, whose contributions allow us to express the modern vision of this energy cascade.

When instabilities are generated on a large scale in the flow, this creates eddies (a collection of vortices). These coherent structures in space can then themselves be subject to new instabilities, which cause the transfer of their respective energies (ideally without creation or destruction because the viscous stresses acting on large scales are negligible) to smaller scales. In other words, the eddies break into smaller ones. The same process of energy accumulation subjected to new instabilities generates a new transfer on a lower scale and so on until the viscous forces become dominant (i.e. $Re \sim$1) and dissipate the energy.

This vision of the energy cascade led Kolmogorov to introduce in 1941 the two following hypothesis:

1. At sufficiently high Reynolds numbers, there is a region of high wave numbers, where the turbulence is statistically in equilibrium and uniquely determined by the dissipation of mechanical energy per unit of mass ϵ and the viscosity of the fluid ν. This state of equilibrium is universal and at this state, the turbulence is statistically homogeneous and locally isotropic.
2. At sufficiently high Reynolds numbers, the statistics of the motions of scale l in the range $l_0 \ll l \ll \eta$ have a universal form that is uniquely determined by the dissipation of mechanical energy per unit of mass ϵ, independent of the viscosity of the fluid ν.

These are now called *Kolmogorov's hypothesis*. The range $l_0 \ll l \ll \eta$ is called the *inertial range* where l_0 is the *integral length scale* and η is the *Kolmogorov length scale*. In other words, it corresponds to the range of scales where the statistical properties of the flow are self-similar. Having this in mind, it is now possible with a simple dimensional analysis to determine the dissipation scale η of the flow. Let us consider the turn-over time τ_{l_0}=l_0/u_0 of the largest eddies which correspond approximately to their timescale or lifespan. The rate of energy per unit mass transferred to the next lower scale is then

$$\Pi \sim u_0^2/(l_0/u_0) = u_0^3/l_0. \tag{2.34}$$

This was introduced by Taylor in 1935, whose idea was that a large eddy loses a significant fraction of its kinetic energy within one eddy turn-over time. Considering now the velocity of the smallest eddies v, the rate of dissipation associated is given by Eq. 2.22 and can be approximated using $S_{ij} \sim v/\eta$ as

$$\epsilon \sim \nu S_{ij} S_{ij} \sim \nu(v^2/\eta^2). \tag{2.35}$$

The energy cascade as expressed above (no accumulation of energy at any intermediate scale, i.e. statistically steady turbulence) implies that the energy transfer rate is constant over scales and so Π=ϵ,

$$u^3/l \sim \nu(v^2/\eta^2). \tag{2.36}$$

Knowing that the Reynolds number on the dissipation scale is

$$Re_\eta = v\eta/\nu \sim 1, \tag{2.37}$$

We obtain the following relations

$$\eta \sim l_0 Re^{-3/4} \sim (\nu^3/\epsilon)^{1/4} \tag{2.38}$$

and

$$v \sim u_0 Re^{-1/4} \sim (\nu\epsilon)^{1/4} \tag{2.39}$$

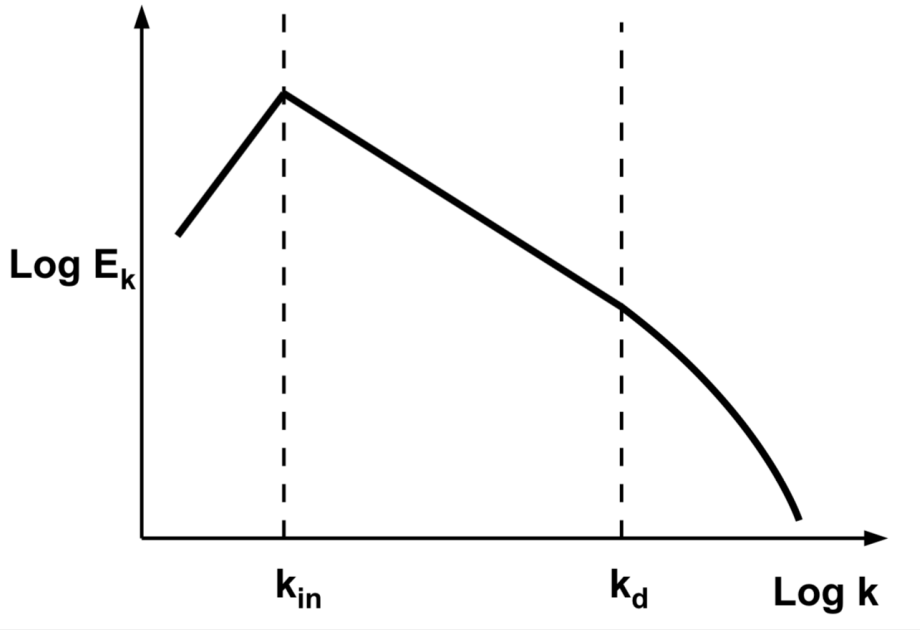

Fig. 2.4.: From Saury (2012): Sketch of the energy spectrum of a fully developed turbulence where $k_{in} \sim 1/l_0$ and $k_d \sim 1/\eta$ are the limit of the inertial range.

where Re=$u_0 l_0/\nu$ is taken at large scales. It is useful to note that, since $\epsilon \sim u_0^3/l_0$ and ϵ is considered constant over the cascade, we have the proportionality relationship

$$u_l \propto l^{1/3} \tag{2.40}$$

where u_l is the characteristic velocity at scale l. Using Eq. 2.40 it follows that the scaling law for the dispersion velocity of u_l with a zero-mean distribution is

$$\sigma_{u_l} = \left\langle u_l^2 \right\rangle^{1/2} \propto l^{\beta}. \tag{2.41}$$

where β=1/3. This relation is well-know in astrophysics as the "σ_{u_l}-l relation". In particular, this was observed for the first time in HI and molecular clouds by Richard Larson (Larson, 1979; Larson, 1981). Therefore, it is often referred to as Larson's law in molecular clouds. It is interesting to note that the exponent β can vary for different type of turbulence such as compressible turbulence (see Boldyrev (2002) and references within).

With Eq. 2.40 in hand, it becomes straightforward to infer the scaling law of the kinetic energy $E(k)$, where $k \sim 1/l$ is the wavenumber associated to the length l. Since $E(k)k \sim u_l^2$, we have

$$\epsilon \sim u_l^3/l \sim k\left(E(k)k\right)^{3/2} \sim E(k)^{3/2}k^{5/2} \tag{2.42}$$

The kinetic energy spectrum in the spectral range is then

$$E(k) \sim \epsilon^{2/3}k^{-5/3}. \tag{2.43}$$

Equation 2.43 is called the Kolmogorov's "5/3" law. A sketch of this energy spectrum in the inertial range is presented in Fig. 2.4.

2.4 Statistical properties of turbulence

We present in this section a brief overview of the Fourier analysis of homogeneous turbulence based on the Chapter 5 of Lesieur (1987). The formalism presented here allows us to introduce two fundamental tools used for studying the statistical properties of turbulence, the *spectral* tensor and the *second-order structure function*. We refer the reader to Lesieur (1987) for complementary discussions.

2.4.1 Spectral tensor

In this section, we introduce the spectral tensor $U_{ii}(\mathbf{k})$ of homogeneous turbulence which is an observable quantity in interstellar turbulence. In particular, we shall derive here the relation between $U_{ii}(\mathbf{k})$ and the kinetic energy spectrum $E(k)$ derived in Eq. 2.43. Note that $\hat{U}_{ii}(\mathbf{k})$ is usually called *power spectrum* in interstellar turbulence and we shall refer to it using the notation $P(k)$ in the following chapters. It is a quantity of primary interest since it is measurable using astronomical observation.

We assume here a purely solenoidal velocity field $u(\mathbf{r})$, meaning that we are still working under the incompressibility condition. Furthermore, we assume that the field is isotropic and therefore homogeneous (because a translation can be decomposed as the product of two rotations, see after the definition of homogeneity and isotropy). Considering these assumptions, the spectral analysis of this particular case of turbulence can be easily described in the Fourier space by the following development. Let us consider $\langle u_i(\mathbf{x_1})\, u_j(\mathbf{x_2})\rangle$, the velocity correlation tensor at point $\mathbf{x_1}$ and $\mathbf{x_2}$. The assumption of homogeneity implies that all quantities built with $(\mathbf{x_1}, \mathbf{x_2})$ are invariant by translation of the set $(\mathbf{x_1}, \mathbf{x_2})$. Therefore, the velocity correlation tensor is

$$\langle u_i(\mathbf{x_1})\, u_j(\mathbf{x_2})\rangle = \langle u_i(\mathbf{x_1}+\mathbf{r})\, u_j(\mathbf{x_2}+\mathbf{r})\rangle\,, \tag{2.44}$$

and the second order velocity correlation tensor is

$$U_{ij}(\mathbf{r}) = \langle u_i(\mathbf{x_1})\, u_j(\mathbf{x_1}+\mathbf{r})\rangle\,. \tag{2.45}$$

The spectral tensor of homogeneous turbulence is given by the Fourier transform of the second order velocity correlation tensor

$$\hat{U}_{ij}(\mathbf{k}) = \left(\frac{1}{2\pi}\right)^3 \int e^{-i\,\mathbf{k}\,.\,\mathbf{r}}\, U_{ij}(\mathbf{r})\, d^3\mathbf{r}. \tag{2.46}$$

Equation 2.46 can be simplified considering isotropy (all quantities build with $(\mathbf{x_1}, \mathbf{x_2})$ are invariant by rotation of the set $(\mathbf{x_1}, \mathbf{x_2})$) and incompressibility. Incompressibility condition implies $k_i\, \hat{U}_{ij}(\mathbf{k}) = k_j\, \hat{U}_{ij}(\mathbf{k}) = 0$. For isotropic turbulence, $\hat{U}_{ij}(\mathbf{k})$ must be an isotropic tensor and after some algebra

described in Lesieur (1987), the spectral tensor, neglecting the helicity[5] term, can be written as a function of $E(k)$ the kinetic energy spectrum which is the density of kinetic energy at wavenumber k

$$\hat{U}_{ij}(\mathbf{k}) = \frac{1}{2}\hat{U}(k)\, Q_{ij}(\mathbf{k}) = \frac{E(k)}{4\,\pi\,k^2}\, Q_{ij}(\mathbf{k}) \tag{2.47}$$

where $\hat{U}(k)$ is the trace of the spectral tensor $\hat{U}_{ij}(\mathbf{k})$ and $Q_{ij}(\mathbf{k})$ is a projected tensor introduced thanks to the fact that for incompressible turbulence, the Fourier transform $\underline{\hat{u}}$ of the velocity is in the plane $\mathbf{\Pi}$ perpendicular to the vector $\mathbf{k}$, i.e $\mathbf{k}\,.\,\underline{\hat{u}}(\mathbf{k}) = 0$, and can be written as

$$Q_{ij}(\mathbf{k}) = \delta_{ij} \; - \; \frac{k_i\, k_j}{k^2} \tag{2.48}$$

with $\delta_{ij} = \delta_i^j = [i \; = \; j]$, using the Iverson bracket, is the Kronecker tensor. We note that for the case δ_i^i, it implies a summation over indice i and therefore $\delta_i^i = 3$. It follows

$$Q_{ii}(\mathbf{k}) = 3 \; - \; \frac{k_x^2 \; + \; k_y^2 \; + \; k_z^2}{k^2} = 2. \tag{2.49}$$

Therefore, according to this condition, the spectral tensor is equal to its trace and equation 2.47 becomes

$$\hat{U}_{ii}(\mathbf{k}) = \hat{U}(k) = \frac{E(k)}{2\,\pi\,k^2}. \tag{2.50}$$

We can now rewrite the Kolmogorov "5/3" law in term of $\hat{U}(k)$. Equation 2.43 becomes

$$\hat{U}(k) \sim \frac{\epsilon^{2/3} k^{-5/3}}{2\pi k^2} \sim \frac{1}{2\pi}\epsilon^{2/3} k^{-11/3}. \tag{2.51}$$

2.4.2 Second order velocity structure function

In this section, we derive the second order velocity structure function $S_2(r)$ which is, as the spectral tensor, measurable using astronomical observation. We shall derive here the link between $S_2(r)$ and the kinetic energy spectrum $E(k)$.

The *second-order structure function* is defined as

$$S_2(r) = \left\langle [u(\mathbf{x}+\mathbf{r}) - u(\mathbf{x})]^2 \right\rangle \tag{2.52}$$

where $\mathbf{r}$ is a vector pointing between two nearby locations of "measurement" of u and $\langle . \rangle$ denotes a spatial ensemble average. For the velocity field $\mathbf{u}$ and the vorticity field $\boldsymbol{\omega}$, the *transverse* and *longitudinal* structure functions can be defined as

$$S_{2\perp}(r) = \left\langle [u_\perp(\mathbf{x}+\mathbf{r}\hat{\mathbf{e}}_\perp) - u_\perp(\mathbf{x})]^2 \right\rangle \tag{2.53}$$

[5] Note that we deliberately omit to introduce here the concept of helicity since it is not of primary interest for the understanding of this section.

and

$$S_{2\parallel}(r) = \left\langle \left[u_\parallel(\mathbf{x} + \mathbf{r}\hat{\mathbf{e}}_\parallel) - u_\parallel(\mathbf{x}) \right]^2 \right\rangle \tag{2.54}$$

where $\hat{\mathbf{e}}_\parallel$ and $\hat{\mathbf{e}}_\perp$ are unit vectors in the transverse and perpendicular direction with respect to $u_\perp$ and $u_\parallel$. It is interesting to note that in astronomy, only the projection of the velocity field along the line of sight (i.e. perpendicular to the plane of the sky) is generally available. This is particularly the case when hyper-spectral imaging is used to observe atomic and molecular lines in the interstellar medium. Any structure function calculated from hyper-spectral data is therefore a transverse structure function.

Generally, $S_2(r)$ can be approximately seen as the energy per unit of mass contained in eddies of size r or less. A simple way of getting a hint of the link between $S_2(r)$ and an energy is by considering the Taylor expansion of the velocity field u at small r,

$$u(\mathbf{x} + \mathbf{r}) - u(\mathbf{x}) \simeq \frac{\partial u}{\partial x} r. \tag{2.55}$$

The right hand side can be seen as a small-scale fluctuation corresponding to a change in u over a small distance r. The square of Eq. 2.55 therefore represents the energy of this small fluctuation. The formal relationship between the spectral tensor and the second-order structure function can be derived using the spectral tensor $\hat{U}_{ij}(\mathbf{k})|_{i=j}$. Equation 2.52 becomes

$$S_2(r) = 2 \int \hat{U}_{ii}(\mathbf{k}) \left(1 - e^{i\,\mathbf{k}\cdot\mathbf{r}}\right) d^3\mathbf{k}. \tag{2.56}$$

To simplify this equation, let us now express it using spherical coordinates, $d^3k = k^2\, dk\, d(cos\theta)\, d\phi$. Combining Eq. 2.50 and 2.56, it follows

$$S_2(r) = 2 \int_{-1}^{+1} d(cos\theta) \int dk\, E(k) \left(1 - e^{i\,\mathbf{k}\cdot\mathbf{r}}\right). \tag{2.57}$$

If $\mathbf{k}$ is aligned with (O_z), then we can decompose the exponential $e^{i\,\mathbf{k}\cdot\mathbf{r}}$ as

$$e^{i\,\mathbf{k}\cdot\mathbf{r}} = \sum_l (2\,l + 1)\, i^l\, j_l(kr)\, P_l(cos\theta) \tag{2.58}$$

where P_l is the Legendre Polynomial. Furthermore, since

$$\int_{-1}^{+1} d(cos\theta)\, P_l(cos\theta) = \begin{cases} 2, & \text{for } l = 0 \\ 0, & \text{for } l \geq 1 \end{cases} \tag{2.59}$$

the second order structure function can be written as

$$S_2(r) = 4 \int_0^{+\infty} dk\, E(k) \left(1 - \frac{sin\, kr}{kr}\right). \tag{2.60}$$

2.5 Turbulence in the ISM

2.5.1 Beyond the incompressible turbulence

It is important to keep in mind that all the formalism used previously results from the Navier-Stokes equation with very specific conditions, namely incompressibility and isotropy. Things get considerably more complicated when it comes to interstellar turbulence because assumptions used previously break down. In particular, the interstellar medium is compressible, magnetized and self-gravitating. Gravity, in general, will be introduced in Eq. 2.14 by adding a force $\mathbf{F}$ on the right hand side. The magnetic field, on the other hand, requires a rewriting of the Navier-stokes equations using magnetohydrodynamics (MHD). The fields associated with these components are distorted by the velocity field, which then provides feedback on it (Elmegreen and Scalo, 2004). We will limit ourselves here to saying that generally, all these considerations have the effect of changing the scaling laws that we have previously deduced in the incompressible case. Moreover, it is even possible to question the fluid approximation used in all cases mentioned so far when the *Kolmogorov scale* is very close to the mean free path of atoms and molecules constituting the fluid (Lequeux, 2012).

2.5.2 Energy injections

The complexity of turbulence that we have just mentioned remains, however, a field of research that has been studied extensively for decades from both a theoretical and experimental point of view by fluid dynamicists. The most important difficulty when it comes to interstellar turbulence is undoubtedly the wide variety of physical processes by which kinetic energy can be converted into turbulence. To illustrate this, we use here the list of the main sources compiled by Elmegreen and Scalo (2004):

1. Protostellar winds, expanding HII regions, O star and Wolf-Rayet winds, supernovae, and combinations of these producing superbubbles.
2. Shocks of spiral arms or bars due to Galactic rotation, the Balbus-Hawley (1991) instability, and the gravitational scattering of cloud complexes at different epicyclic phases.
3. Gaseous self-gravity through swing-amplified instabilities and cloud collapse.
4. Kelvin-Helmholtz and other fluid instabilities.
5. Galactic gravity during disk-halo circulation, the Parker instability, and galaxy interactions.
6. Sonic reflections of shock waves hitting clouds.
7. Cosmic ray streaming.
8. Field star motions.

It is striking to note that the energy injections via all these processes are carried out at very variable scales ranging from kiloparsec to tenths of a parsec. It is even more surprising to note that all the scaling laws observed so far in various environments of the interstellar medium are generally[6] single power laws. Note that most of these studies used density fields instead of velocity fields. Whatever the

[6]Note that Elmegreen et al. (2001) observed a broken power law in the Large Magellanic Cloud (LMC) but this behavior is more considered as a signature of the transition from 2D to 3D turbulence rather then a real energy injection or dissipation.

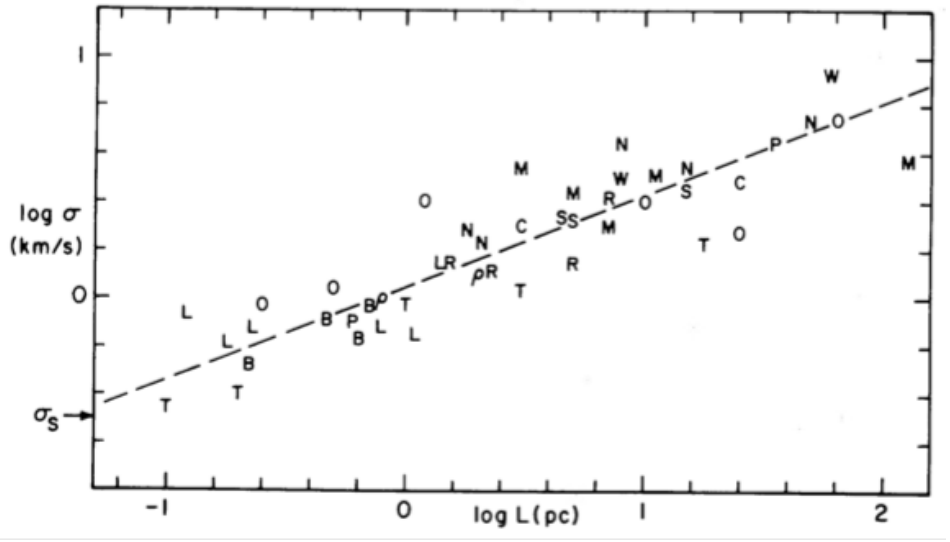

Fig. 2.5.: From Larson (1981): The three-dimensional internal velocity dispersion σ plotted versus the maximum linear dimension L of molecular clouds and condensations, based on data from Table 1; the symbols are identified in Table 1. The dashed line represents equation (1), and σ_s is the thermal velocity dispersion.

nature of the field studied, the signature of these processes in the power spectrum statistics remains non-trivial and not well understood. We will discuss this further in the following Sect. 2.5.3.

2.5.3 Observations of interstellar turbulence

Early works The first optical observations suggesting that the interstellar medium is turbulent date back to the middle of the 20th century. Ten years after Kolmogorov described the scaling laws of incompressible turbulence, astronomical observations of emission-line velocities in the Orion Nebula revealed their self-similar nature (Hoerner, 1951), suggesting that interstellar fluid follows the same statistics. Note that the second order velocity structure function introduced in Eq. 2.52 was used to perform the statistical analysis by measuring the scaling law[7] $S_{2\perp} \propto r^{\beta}$. In line with this idea, Hoerner (1951) introduced the idea of a hierarchical cloud structure in the interstellar medium. Several years after, still using the second order velocity structure function, Wilson et al. (1959) inferred from a sample of $\sim$ 10 000 lines-of-sight a higher exponent $\beta \sim 0.66$, suggesting that it results from a compressible turbulence. Then, Miville-Deschenes et al. (1995) found $\beta \sim 0.8$ in an HII region, suggesting again a compressible turbulence with a possible energy input from a stellar wind. In parallel with these observations, the theory of interstellar turbulence began. Based on Hoerner (1951) suggestions, Weizsäcker (1951) suggested that this hierarchy of structures is formed in interacting shock waves by large-scale supersonic turbulent flows and then dissipated at small-scales by atomic viscosity (Elmegreen and Scalo, 2004). As noted by Elmegreen and Scalo (2004), the vision proposed by Weizsäcker (1951) is similar to what is believed today. In this model, the density ρ_ν and the cloud size l_ν are connected by the following relation

$$\frac{\rho_\nu}{\rho_{\nu+1}} = \left(\frac{l_\nu}{l_{\nu+1}}\right)^{-3k_\nu} \tag{2.61}$$

[7] Note that following the same reasoning as for velocity dispersion, we find that β=1/3 for incompressible turbulence.

where k_ν is the degree of compression at the step ν, ρ_ν is the average density at the step ν being an integer increasing with the cloud size l_ν. This model was the first attempt to describe a turbulent astrophysical fluid by its density fluctuations instead of velocity fluctuations. Since this work, several models have aimed at understanding the scaling laws of the density field in a turbulent fluid. Notably, Von Weizsacker's model was the basis of the Flech model whose goal was to incorporate density fluctuations into predictions for power spectra of incompressible turbulence (Vogel, 2011).

Larson's law The study of interstellar turbulence underwent a considerable change when the first observations in the millimetre range appeared. In particular, the CO line revealed considerably large widths that were incompatible with the temperature of the gas ($T_k \sim 10$ K) measured using ^{12}CO, ^{13}CO and OH (Lequeux, 2012). It turned out that this incompatibility was due to a turbulent broadening of the line which is quadratically added to its thermal broadening. It was in 1979 and 1981 (Larson, 1979; Larson, 1981) that Richard Larson published the first relationship between the line widths of atomic and molecular lines and the respective maximum linear dimension of the clouds, thus revealing the scaling laws of the turbulent cascade presented in Eq. 2.41 in different environments of the interstellar medium. Notably, he measured a scaling exponent $\beta \sim 0.38$ close to an incompressible turbulence. Figure 2.5 from Larson (1981) shows this relationship for a set of molecular clouds in the Milky-Way. In contrast, Solomon et al. (1987) found $\beta \sim 0.5$, suggesting a compressible turbulence. More recently, Miville-Deschênes et al. (2017) found $\beta \sim 0.63$ for 8107 molecular clouds in the Milky-Way disk, closer to the result of Solomon et al. (1987). It is important to note here that this relationship is likely to be influenced also by the gravity of clouds, which can modify the value of the exponent. This is still a matter of debate.

Power spectrum of the integrated density The notion of a power spectrum of the density introduced here must be absolutely dissociated from the power spectrum introduced previously in Eq. 2.50 which was directly related to the energy cascade acting in the fluid. The fundamental reason for this is that the scaling law described above are derived for incompressible fluids. Nevertheless, as discussed in Sect. 2.5.1, interstellar fluids are often compressible and since density fields are observable quantities in astronomy, their statistical properties have generated some interest in characterizing interstellar turbulence. Using numerical simulation of isothermal, compressible and subsonic turbulence, Kim and Ryu (2005) showed that the power spectral index of the density field follows that of the velocity field, i.e. $\propto k^{-11/3}$. This work also showed that when simulating a supersonic regime, it causes the creation of small scale density fluctuations (due to shocks), which has the effect of flattening the power spectrum of the density field. It is interesting to note that the same behaviour was observed in numerical simulations of subsonic bi-stable turbulence of atomic gas (Saury et al., 2014; Gazol and Kim, 2010) which are highly non-isothermal cases. High density contrasts in these simulations result from the condensation of diffuse warm gas into cold dense clouds caused by the thermal instability. Even if it occupies a very small fraction of the volume, these dense structures are likely to have exactly the same impact, flattening the power spectrum of the density field.

Power spectrum of the centroid velocity The statistical properties of the 3D velocity field can be inferred from its 2D projection, also called the centroid velocity. However, the statistical properties of these fields can differ drastically since the centroid velocity results from a weighting by the density field (Ossenkopf et al., 2006). Several studies have shown that the statistics of the centroid velocity field reflects those of the velocity field only when the fluctuations of the density field are small, i.e. $\sigma(\rho)/\rho \lesssim$

1 (Miville-Deschênes et al., 2003b; Esquivel and Lazarian, 2005; Ossenkopf et al., 2006). It must be noted, for the same reason as discussed above for the density power spectrum, that this condition is very rarely satisfied for interstellar turbulence. For that reason, the statistical properties of the velocity field of interstellar turbulence is still not well characterized.

The neutral interstellar medium

3

> *"What makes the desert beautiful",*
> *said the little prince,*
> *"is that somewhere it hides a well..."*
>
> — **Le Petit Prince (April 1943)**
> Antoine de Saint-Exupéry

Contents

3.1 Introduction

3.1.1 Prediction and detection

Neutral hydrogen is the most abundant element in galaxies. Its observation is carried out through its hyper-fine transition emitting at the frequency 1420.406 MHz. It results from the spin-flip of the atom from the triplet state to the singlet state. Predicted by Hendrik C. van de Hulst in 1944, the transition was first detected by Harold Ewen and Edward Purcell on March 25, 1951 at the Lyman Laboratory of Harvard University. The horn antenna they used is now in the NRAO Green Bank campus. After this detection, Ewen learned that Prof. Van de Hulst was spending a sabbatical year at Harvard (NRAO archive). He wrote:

> *At the suggestion of Purcell, I went to the Harvard Observatory, in mid April, to meet and talk to Van de Hulst for the first time, and to tell him about the discovery. Ed told me that Van de Hulst was teaching a course at Harvard during the spring term. It was the same course that he taught at Leiden, during the prior fall term. When I met with Van de Hulst at the Observatory he called Oort, and I talked with Oort for nearly an hour describing the switch frequency technique. This was the first time that we learned the Dutch had been searching for the line for several years. Had we known, we would not have tried.*

The Dutch group adopted Ewen's frequency switching technique and succeeded in detecting the line on May 11, 1951 (NRAO archive). The study of the neutral interstellar medium could then begin.

3.1.2 Early work

The observations of the 21 cm line that followed revealed a significant difference between emission and absorption spectra. On lines-of-sight crossing radio-sources the HI appears in absorption with very narrow features (a few km.s^{-1}). In emission the 21 cm line contains these narrow features on top of much boarder spectral structures (10-20 km.s^{-1}). Clark (1965) was the first to suggest that this might be the signature of a cloud-intercloud medium in pressure equilibrium. However, it appeared that the existence of these clouds could not be explained by self-gravitation. The same year, George B. Field wrote the following:

> *Most astronomical objects owe their existence to self-gravitation. However, there is a class of objects, including solar prominences, interstellar clouds, and condensations in planetary nebulae, whose existence cannot be explained in this way, as their calculated gravitational energies are far smaller than those due to internal pressure. In each case it appears reasonable to assume that internal pressure is being balanced by pressure in an external diffuse medium. It then appears likely that the objects in question are formed from the diffuse medium by some kind of condensation process not involving gravitation.*

It was in search of this process that he introduced his work on thermal instability (Field, 1965). It turned out that this condensation process in question could be the condensation mode of this instability. We

will introduce it more formally in following Sect. 3.2. Very rapidly, Field et al. (1969) published a study combining thermal instability, heating and cooling processes of the interstellar medium and laid out the theoretical ground of a "two-phase" model showing that, at the pressure of the ISM, the heating and cooling processes naturally lead to two thermally stable states. Field et al. (1969) used cosmic-rays as main source of heating but it was shown later that the dominant heating process comes from UV starlight with a heating due to photoelectric emission from the dust grains in the gas (Watson, 1972). This vision of a "two-phase" medium in equilibrium was later complemented by Wolfire et al. (1995); Wolfire et al. (2003) considering this updated heating and cooling (dominated by CII - 158 μm, OI - 63 μm, Lα and electron recombinations onto positive charged grains) processes of the ISM. Since this work, the neutral ISM has been seen as a dense cold neutral medium (CNM - $T \sim 50$ K, $n \sim 50$ cm^{-3}) immersed in a diffuse warm neutral medium (WNM - $T \sim 8000$ K, $n \sim 0.3$ cm^{-3}).

3.2 Thermal instability

This section is dedicated to giving the reader the keys to understand the basic concepts of thermal instability. We refer the reader to Field (1965) for a more detailed analysis about the stability of the dispersion relation.

3.2.1 The energy equation

As stated in Sect. 2.1.1, we derive in this section the energy equation of fluid mechanics based on *Fluid Dynamics: Theory and computation" by Dan S. Henningson and Martin Berggren* and Anderson (1995). Note that, contrary to Chapt. 2, we do not use an incompressible gas.

The conservation of energy implies that the rate of change of total energy inside a fluid element = rate of working done on the element due to surface forces + net flux of heat into the element[1]

$$\rho \frac{D}{Dt}\left(e + \frac{u^2}{2}\right) = -\frac{\partial}{\partial x_i}(pu_i) + \frac{\partial}{\partial x_i}(\tau_{ij}u_j) - \frac{\partial q_i}{\partial x_i} - \rho\mathscr{L} \tag{3.1}$$

where e is the internal energy of the fluid element, q_i the heat flux vector due to thermal conduction and $\mathscr{L}$ is the net loss function. The loss function $\rho\mathscr{L}$ can be written as

$$\rho\mathscr{L} = n^2\Lambda(T) - n\Gamma \tag{3.2}$$

where $\Lambda(T)$ and Γ are respectively called the cooling function and heating function and $n \equiv \rho/(\mu' m_H)$ with μ'=1.4 is the molecular weight for fully atomic hydrogen in astrophysical plasma and has to be carefully dissociated from the molecular viscosity μ introduced in Chapt. 2. Note that these two functions are very general and must be replaced at some point by the physical processes acting in the studied plasma. In our case, these are heating and cooling processes acting in the neutral ISM that we will introduce in following Sect. 3.3.

[1] Note that this term can be decomposed into two parts due to: (1) heat transfer across the surface due to thermal conduction, and (2) volumetric heating or cooling due to the physical processes acting in the fluid.

Equation 3.1 is a combination of the thermal energy and the mechanical energy of the fluid element. Subtracting Eq. 2.15 from Eq. 3.1, we obtain the thermal energy equation

$$\rho\frac{De}{Dt} = -p\frac{\partial u_i}{\partial x_i} + \tau_{ij}\frac{\partial u_i}{\partial x_j} - \frac{\partial q_i}{\partial x_i} - \rho\mathscr{L}. \tag{3.3}$$

The two first terms of the right hand side of Eq. 3.3 are thermal terms (force$\times$deformation) respectively corresponding to the heat generated by compression and viscous dissipation. The third and forth terms are associated to the heat loss due to temperature gradients, i.e thermal conduction and the volumetric heating or cooling due to the physical processes acting in the fluid. The heat flux vector due to thermal conduction is related to the temperature gradients by the relation

$$q_i = -\kappa\frac{\partial T}{\partial x_i} \tag{3.4}$$

where κ=$\kappa(T)$ is the thermal conductivity. Equation 3.3 becomes

$$\rho\frac{De}{Dt} = -p\frac{\partial u_i}{\partial x_i} + \tau_{ij}\frac{\partial u_i}{\partial x_j} + \frac{\partial}{\partial x_i}\left(\kappa\frac{\partial T}{\partial x_i}\right) - \rho\mathscr{L}. \tag{3.5}$$

Note that Eq. 2.16 allows to identify that

$$\tau_{ij}\frac{\partial u_i}{\partial x_j} = \rho\epsilon. \tag{3.6}$$

As anticipated in Eq. 2.21, the true physical meaning of ϵ can be seen here: the heat generated by viscous dissipation in a fluid element is nothing else than its loss of mechanical energy. Combining Eqs. 3.6 and 3.5, the thermal energy equation can be written as

$$\rho\frac{De}{Dt} = -p\frac{\partial u_i}{\partial x_i} + \rho\epsilon + \frac{\partial}{\partial x_i}\left(\kappa\frac{\partial T}{\partial x_i}\right) - \rho\mathscr{L}, \tag{3.7}$$

or

$$\rho\frac{De}{Dt} = -p\boldsymbol{\nabla}\cdot\mathbf{u} + \rho\epsilon + \boldsymbol{\nabla}\cdot(\kappa\boldsymbol{\nabla}T) - \rho\mathscr{L}. \tag{3.8}$$

3.2.2 Perfect gas

In the following, we use a perfect gas to simplify Eq. 3.8. For a calorifically perfect gas (constant specific heats),

$$e = C_v T \tag{3.9}$$

where C_v is the specific heat at constant volume and the pressure is

$$p = \frac{k_B}{\mu' m_H}\rho T. \tag{3.10}$$

Finally, C_v can be written

$$C_v = \frac{k_B}{(\gamma-1)\mu' m_H} \tag{3.11}$$

where γ is the ratio of specific heats. Combining Eqs.3.9, 3.10 and 3.8 allows to write the thermal energy equation for a perfect gas in the form

$$C_v\rho\left(\frac{DT}{Dt}+(\gamma-1)T\frac{\partial u_i}{\partial x_i}\right)=-\rho\mathscr{L}+\rho\epsilon+\frac{\partial}{\partial x_i}\left(\kappa\frac{\partial T}{\partial x_i}\right). \tag{3.12}$$

3.2.3 Equilibrium state and perturbation

This section is dedicated to study the thermal instability in 1D using a perfect gas and in a uniform medium. To simplify our approach, we neglect here the viscosity of the fluid. Eqs. 2.4, 2.12, 3.12 and 3.10 become

$$\frac{\partial\rho}{\partial t}+u\frac{\partial\rho}{\partial x}+\rho\frac{\partial u}{\partial x}=0 \tag{3.13}$$

$$\rho\left(\frac{\partial u}{\partial t}+u\frac{\partial u}{\partial x}\right)+\frac{\partial p}{\partial x}=0 \tag{3.14}$$

$$C_v\rho\left(\frac{\partial T}{\partial t}+u\frac{\partial T}{\partial x}+(\gamma-1)T\frac{\partial u}{\partial x}\right)+\rho\mathscr{L}-\frac{\partial}{\partial x}\left(\kappa\frac{\partial T}{\partial x}\right)=0 \tag{3.15}$$

$$p-\frac{k_B}{\mu' m_H}\rho T=0. \tag{3.16}$$

Following Field (1965), we consider an equilibrium state characterized by ρ=ρ_0, T=T_0, u=0, and $\mathscr{L}$(ρ_0,T_0)=0. We assume perturbations of the form

$$a(x,t)=a_1 exp\left(\omega t+ik.x\right). \tag{3.17}$$

The linearized system of equations for the perturbations is then

$$\omega\rho_1-ik\rho_0u_1=0 \tag{3.18}$$

$$\rho_0\omega u_1-ikp_1=0 \tag{3.19}$$

$$C_v\left(\omega T_1-ikT_0(\gamma-1)u_1\right)+\mathscr{L}_\rho\rho_1+\mathscr{L}_T T_1-\kappa_0k^2T_1=0 \tag{3.20}$$

$$\frac{p_1}{p_0}-\frac{T_1}{T_0}-\frac{\rho_1}{\rho_0}=0 \tag{3.21}$$

where $\mathscr{L}_\rho\equiv\left(\partial\mathscr{L}/\partial\rho\right)_T$, $\mathscr{L}_T\equiv\left(\partial\mathscr{L}/\partial\rho\right)_\rho$ and κ_0 are taken at the equilibrium. After some algebra, the dispersion relation can be written as

$$\omega^3+\omega^2\left(\frac{\mathscr{L}_T}{C_v}+\frac{\kappa_0k^2}{C_v}\right)+\omega c^2k^2+\frac{p_0k^2}{C_vT_0}\left[\frac{T_0}{\rho_0}\mathscr{L}_T-\mathscr{L}_\rho+\frac{\kappa_0k^2T_0}{\rho_0}\right]=0 \tag{3.22}$$

where $c\equiv\sqrt{\gamma p_0/\rho_0}$ is the sound speed at the equilibrium. In 1965, George B. Field published a detailed study of the stability of Eq. 3.22 (Field, 1965), including also the effect of magnetic field, rotation, external gravitational field, and expansion of the medium. We will restrict ourselves to comment the condensation mode of the thermal instability. If Eq. 3.22 has a negative coefficient, it admits at least one real positive solution and an instability can grow. The last term of the left hand sign of Eq. 3.22 gives us the stability criterion

$$\frac{T_0}{\rho_0}\mathscr{L}_T-\mathscr{L}_\rho<-\frac{\kappa_0k^2T_0}{\rho_0}. \tag{3.23}$$

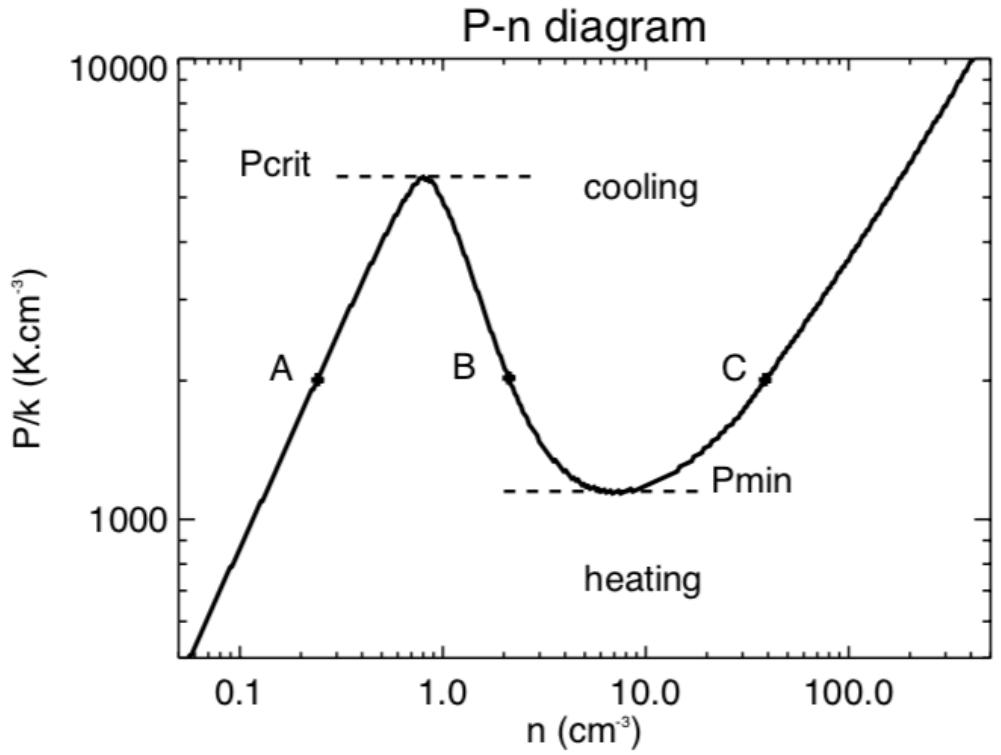

Fig. 3.1.: From Saury (2012): Representation of thermal equilibrium in a pressure-density diagram. The area above the curve is a cooling area and the area below the curve is a heating area. Points A and C are in state of stable equilibrium while point B denotes a state where Eq. 3.26 is satisfied.

If thermal conduction is neglected, Eq. 3.23 becomes

$$\frac{T_0}{\rho_0}\mathscr{L}_T - \mathscr{L}_\rho < 0 \tag{3.24}$$

which after some algebra turns out to be an isobaric instability criterion

$$\left(\frac{\partial \mathscr{L}}{\partial T}\right)_P < 0. \tag{3.25}$$

The real positive root associated to Eq. 3.25 corresponds to the formation of condensations under constant pressure conditions. Field (1965) referred to it as the condensation mode of the thermal instability. After some algebra, Eq. 3.25 can be rewritten as

$$\left(\frac{\partial p}{\partial \rho}\right)_{\mathscr{L}} < 0 \tag{3.26}$$

which is more often used to describe the condensation mode of the thermal instability at thermal equilibrium. A sketch of a pressure-density diagram at thermal equilibrium is shown in Fig. 3.1 where point B denotes a state where Eq. 3.26 is satisfied.

3.2.4 Static scale

When thermal conduction is considered, because the term $\kappa_0 k^2 T_0/\rho_0$ on the right hand side of Eq. 3.23 is always positive, Field (1965) noted that its effect is always to reduce instability. The condensation mode of the thermal instability is then suppressed by thermal conduction on a characteristic scale λ_F (named the Field length after Field (1965)) where the cooling or heating is comparable to conductive energy exchange. Since under this scale the thermal instability is suppressed, it also represents the smallest scale of structures formed by condensation. Following Begelman and McKee (1990), the rate of energy exchange due to conduction per unit volume is

$$\frac{\partial}{\partial x_i}\left(\kappa\frac{\partial T}{\partial x_i}\right) \sim \kappa T/l^2 \tag{3.27}$$

where l is the length over which temperature varies. The energy exchange due to cooling is taken as the maximum between the two terms of Eq. 3.2

$$\rho\mathscr{L}_M \equiv \max\left(n^2\Lambda, n\Gamma\right). \tag{3.28}$$

Therefore, when cooling or heating is comparable to conductive energy exchange it follows,

$$\kappa T/\lambda_F^2 \sim \rho\mathscr{L}_M. \tag{3.29}$$

The field length is then define as

$$\lambda_F \equiv \sqrt{\frac{\kappa(T)T}{\rho\mathscr{L}_M}}. \tag{3.30}$$

Note that λ_F is a static spatial scale since it does not involve a characteristic time.

3.2.5 Dynamical scales

In the previous section, we demonstrated that if inequality of Eq. 3.26 is satisfied, a perturbation of the form of Eq. 3.17 in a uniform medium could grow. In this section, following Hennebelle and Pérault (1999), we present a qualitative description of the dynamic condition under which this perturbation may or may not be inhibited.

When the gas experiences a perturbation, i.e. it undergoes a compression, the condensation is possible if the cooling time of the fluid element is shorter than its dynamical time. Otherwise, the energy lost by radiation is small compared to the increase of internal energy and the process can be considered as an adiabatic process (no transfer of heat between the system, i.e. the fluid element, and the surrounding medium). The system can therefore return to its initial state. Let us consider an homogeneous compression of a fluid element of size λ_{dyn}, its variation of internal energy per unit volume is

$$\rho\Delta e = C_v\Delta(\rho T). \tag{3.31}$$

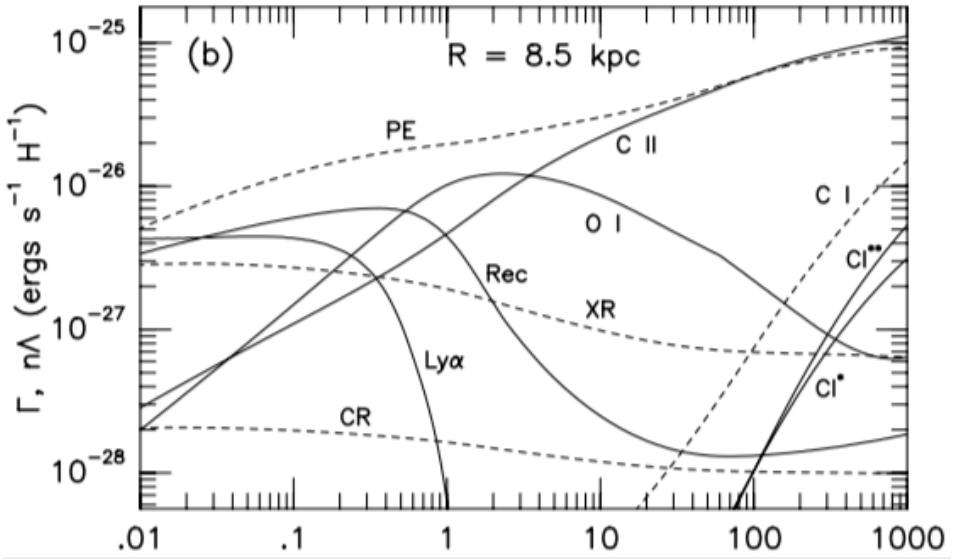

Fig. 3.2.: From Wolfire et al. (2003), Fig. 10: Heating and cooling curves vs. hydrogen nucleus density n at various Galactic distances, R=8.5 kpc. Heating rates (dashed curve): photoelectric heating from small grains and PAHs ("PE"); EUV and X-ray ("XR"); cosmic ray ("CR"); photoionization of C ("CI"). Cooling rates (solid curve): CII 158 µm fine-structure ("CII"); OI 63 µm fine-structure ("OI"); recombination onto small grains and PAHs ("Rec"); Lyα plus metastable transitions ("Ly"); CI fine-structure 609 ("CI*"); CI fine-structure 370 µm ("CI**").

The time needed to radiate away this increase of internal energy is called the cooling time and can be written as

$$\tau_{cool} = \frac{\rho \Delta e}{\langle \rho \mathscr{L} \rangle} \tag{3.32}$$

where $\langle \rho \mathscr{L} \rangle$ is the average net cooling rate during the compression. The duration of the compression, called the dynamical time, is

$$\tau_{dyn} = \frac{\lambda_{dyn}}{C_s}. \tag{3.33}$$

As stated before, the condensation condition is

$$\tau_{cool} < \tau_{dyn}. \tag{3.34}$$

It follows

$$\lambda_{dyn} > \lambda_{cool} = \frac{C_v \Delta(\rho T)}{\langle \rho \mathscr{L} \rangle}. \tag{3.35}$$

Therefore, λ_{cool} represents a critical scale at which the gas is non-linearly unstable and can undergo a condensation. Under this scale, the perturbation is inhibited.

3.3 Heating and cooling processes

We present in this section the main heating and cooling processes acting in the diffuse interstellar medium. Most of these equations are derived from Wolfire et al. (1995) and Wolfire et al. (2003). This work, introduced in the mid 90's build for the first time a complete picture of the heating and cooling

processes, and thermal instability in the diffuse ISM based on a realistic distribution of dust grains and metals abundances. Each heating and cooling process presented here is shown in Fig. 3.2. Solid lines represent the cooling functions of each process as function of the density between 0.01 < n (cm^{-3}) < 1000. Note that we only present in the section the dominant processes acting in the neutral ISM: photo-electric heating from small grains and PAHs and heating by recombination into dust grains, cooling and recombination by CII, OI, and Lyα.

3.3.1 Photoelectric heating from small grains and PAHs

The main process responsible for heating gas in the diffuse interstellar medium is the photoelectric ejection of electrons from dust grains by UV photons of the interstellar radiation field (Watson, 1972).These photons, once absorbed by the grains, affect the structure of the internal electrons, which leads some of them to reach the surface and then be ejected. The released energy (from which the energy required for ejection has been subtracted) is then available to heat the gas via thermalisation. We call these ejected electrons, suprathermic electrons. There are three stages in this thermalisation process. First of all, the suprathermic electrons quickly put themselves in thermal equilibrium via elastic collisions with the electron gas into which they enter. Secondly, once the electron gas is heated, it reaches thermal equilibrium with the ion gas. Finally, elastic collisions between ions and neutrals lead to a new thermal equilibrium. Note that due to the low momentum of gas electrons, collisions between electrons and neutrals are much less effective. Detail calculations of this process are presented in Spitzer (1978) and Lequeux (2012).

The heating rate coming from this process has been theoretically studied in detail by Bakes and Tielens (1994) based on the atomic physics. They adopted the MRN (Mathis et al., 1977) grain size distribution for spherical grains ($n(a)\mathrm{d}a \propto a^{-3.5}\mathrm{d}a$) for particles with a radius a > 15 Å. For PAH (*Polycyclic Aromatic Hydrocarbons*) molecules (a < 15 Å and assumed to be small disks) they adopted a distribution given by $n(N_C)\mathrm{d}N_C = 1.15 \times 10^{-5} N_C^{-2.25}\mathrm{d}N_C$. Wolfire et al. (2003) used a single PAH size containing N_C = 35 carbon atoms and corresponding to the mean size of the distribution between 3 and 15 Å. In addition to this single PAH size, Wolfire et al. (2003) took into account two modifications: 1) an higher PAH abundances based on ISO (*Infrared Space observatory*) observations of PAH emission in the galaxy (Tielens et al., 1999), and 2) a parameter ϕ_{PAH} scaling the electron-PAH collision rate. This leads to a modified heating rate per unit volume

$$n\Gamma_{pe} = 1.3 \times 10^{24} n \epsilon G_0 \qquad (\mathrm{erg\,cm^{-3}\,s^{-1}}). \tag{3.36}$$

The heating efficiency ϵ is given by

$$\epsilon = \frac{4.9 \times 10^{-2}}{1 + 4.0 \times 10^{-3} \left(G_0 T^{1/2} / n_e \phi_{PAH}\right)^{0.73}} + \frac{3.7 \times 10^{-2} \left(T/10^4\right)^{0.7}}{1 + 2.0 \times 10^{-4} \left(G_0 T^{1/2} / n_e \phi_{PAH}\right)} \tag{3.37}$$

where n_e is the electron density and $G_0 \sim 1.7$ is the Draine field in units of Habing field. An analytic expression of the electron density is calculated by Wolfire et al. (2003) (Appendix C2) and is given by

$$n_e = 2.4 \times 10^{-3} {\zeta'_t}^{1/2} (T/100)^{1/4} {G'_0}^{1/2} {Z'_d}^{-1/2} \phi_{PAH}^{-1} \qquad (\mathrm{cm^{-3}}). \tag{3.38}$$

where $\zeta'_t = \zeta_t/10^{-16}$ is the ionization rate with ζ_t the total ionization of H by photons and cosmic rays, G'_0=G_0/1.7 is the scale intensity of FUV ISRF (interstellar radiation field), and Z'_d is the dust-PAH abundance.

In Eq. 3.37, the term $G_0 T^{1/2}/n_e$ is proportional to the rate of ionization divided by the rate of recombination (Wolfire et al., 1995a). When this term is low ($\ll 5 \times 10^3$ K$^{1/2}$ cm^3), grains are mainly neutral or negatively charged. On the other hand, when this term is high, the efficiency drops due to positive charging of the grains. The important parameter here is the grains charge, that determines the ability to remove electrons from the grains. As stated previously, the electron density presented in Eq. 3.38 is detailed in appendix C2 of Wolfire et al. (2003). This shows that the electron density is approximately by the density of H^+ which is the dominant ion species in the solar circle. H^+ is mainly produced by UV and soft X-ray radiation and secondarily by cosmic rays. This translates into the parameter ζ'_z. Its destruction is dominated by reactions with PAH in different ionization states. The reactions are

$$\mathrm{H}^+ + \mathrm{PAH}^- \rightarrow \mathrm{H} + \mathrm{PAH}^0, \tag{3.39}$$

$$\mathrm{H}^+ + \mathrm{PAH}^0 \rightarrow \mathrm{PAH}^+ + \mathrm{H}, \tag{3.40}$$

$$\mathrm{H}^+ + e \rightarrow \mathrm{H} + h\nu, \tag{3.41}$$

where PAH^-, PAH^0 and PAH^+ denote the PAH ionization state. Note that PAH^+ is formed by FUV photoreaction and destroyed primarily by recombination with electrons. PAH^+ is destroyed by photodetachement. In general, the reaction coefficient associated to these reactions involves the temperature of the gas, the parameter ϕ_{PAH} introduced previously that scales the electron-PAH collision rate, and G'_0 when the FUV radiation field is involved.

3.3.2 Cooling and recombination

CII [158 μm] and OI [63 μm] lines From ∼1 to 1000 K, the main cooling processes in the diffuse interstellar medium are the CII [158 μm] and OI [63 μm] lines. These ions are excited by collision with electrons and hydrogen atoms in the gas and can be de-excited spontaneously or by collision. They then emit radiation, generally considered optically thin, which then escapes from the medium and cools it. The probability of spontaneous de-excitation is so low that we call it a "forbidden" transition. However, due to the relatively low density of the diffuse ISM, especially the neutral ISM, collisional de-excitation is even less likely to occur. Combining previous studies by Launay and Roueff (1977) and Hayes and Nussbaumer (1984), Wolfire et al. (1995) gives the CII cooling function

$$\Lambda_{CII} = 2.54 \times 10^{-14} \mathscr{A}_C f_{CII} \left[\gamma x_e + \gamma_e\right] \exp\left(-92\mathrm{K}/T\right) \qquad (\mathrm{erg\,cm^3\,s^{-1}}), \tag{3.42}$$

where $x_e \equiv n_e/n$, γ and γ_e are the collisional excitation rate coefficients for collisions with neutral and electrons, and f_{CII} is the fraction of C in C^+ and $\mathscr{A}_C$ is the gas phase carbon abundance per H nucleus. Note that we use here $\mathscr{A}_C$=1.4×10^{-4} based on Wolfire et al. (2003) and references within. Wolfire et al. (1995) used

$$\gamma = 8.86 \times 10^{-10} \qquad (\mathrm{cm^3\,s^{-1}}), \tag{3.43}$$

and

$$\gamma_e = 2.1 \times 10^{-7} T_2^{-1/2} \Omega(T) \qquad (\mathrm{cm^3\,s^{-1}}), \tag{3.44}$$

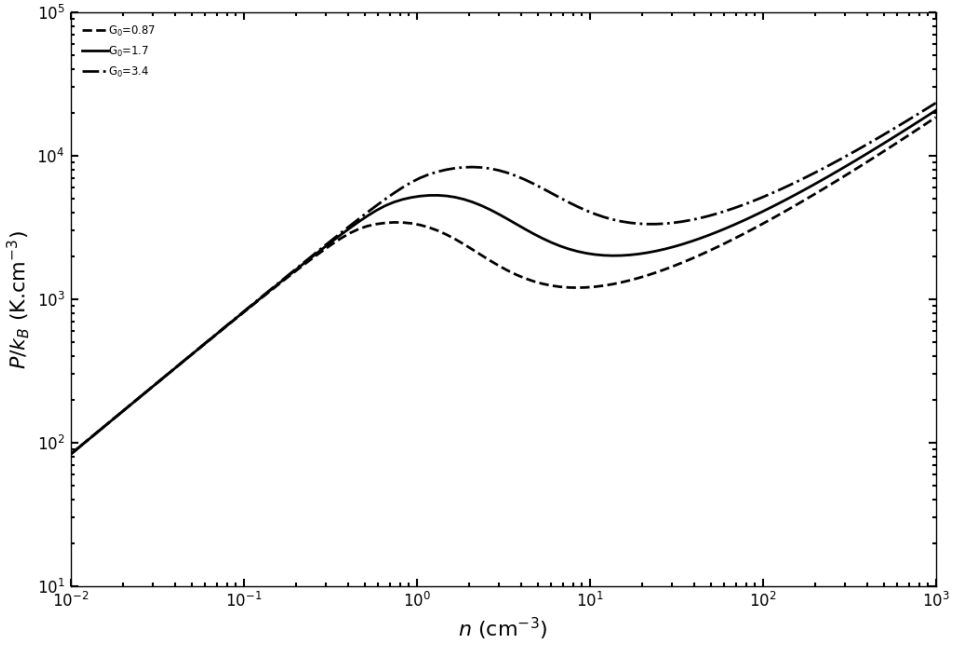

Fig. 3.3.: Phase diagrams showing thermal pressure for $\mathscr{A}_C$, $\mathscr{A}_O$, ζ_t taken in the solar neighborhood and ϕ_{PAH}=0.5. Variations of the FUV ISRF is shown with G_0=1.7 (solid) corresponding to a Draine field, G_0/2 (dash), and $G_0\times$ 2 (dash-dot).

where $T_n \equiv T/10^n$ K and the collision strength Ω(T) is

$$\Omega(T) = 1.80 + 0.484T_4 + 4.01T_4^2 - 3.39T_4^3. \tag{3.45}$$

Similarly, we use the OI cooling function used by Saury (2012)

$$\Lambda_{\rm OI} = 10^{-26}\mathscr{A}_O T^{1/2}\left(24\exp\left(\frac{-228{\rm K}}{T}\right) + 7\exp\left(\frac{-326{\rm K}}{T}\right)\right) \qquad ({\rm erg\,cm^3\,s^{-1}}), \tag{3.46}$$

where $\mathscr{A}_O$=3.2×10^{-4} is the gas phase carbon abundance per H nucleus and is taken from Wolfire et al. (2003) and reference within.

Lyman-alpha line At high temperature $T \gtrsim$ 8000 K, the cooling is dominated by the collisional excitation of the n=2 level of hydrogen which is de-excited by the emission of the Lyα line at 1215 Å. Spitzer (1978) gives the Lyα cooling function

$$\Lambda_{{\rm Ly}\alpha} = 7.3\times10^{-19}x_e\times\exp\left(\frac{-118400{\rm K}}{T}\right) \qquad ({\rm erg\,cm^3\,s^{-1}}), \tag{3.47}$$

valid for temperature between 400 < T(K) < 12000.

Recombination onto dust grains Finally, at very low temperature $T \lesssim$ 90 K, recombination onto positively charged grains is dominant. Electrons at thermal equilibrium can recombine and as for the

heating, Wolfire et al. (2003) calculated the modified cooling function taking into account higher PAH abundances and a parameter ϕ scaling the electron-PAH collision rate

$$\Lambda_{rec} = 4.65 \times 10^{-30} T^{0.94} \left(\frac{G_0 T^{1/2}}{n_e \phi_{\rm PAH}} \right)^{\beta} \times x_e \phi_{\rm PAH} \qquad (\rm erg\,cm^3\,s^{-1}). \tag{3.48}$$

Similarly to Eq. 3.37, Eq. 3.48 is a function of the term $G_0 T^{1/2}/n_e$ which is proportional to the rate of ionization divided by the rate of recombination (Wolfire et al., 1995a).

The total cooling function is the sum of cooling functions of these four mechanisms

$$\Lambda = \Lambda_{CII} + \Lambda_{OI} + \Lambda_{Ly\alpha} + \Lambda_{rec}. \tag{3.49}$$

3.3.3 Thermal equilibrium

We have seen in Sect. 3.2.3 that the isobaric criterion presented in Eq. 3.26 must be satisfied for a perturbation to grow. The schematic view of the phase diagram shown in Fig. 3.1 can be now calculated using the heating and cooling function presented above. Equation 3.2 is solved for a density range from 0.01 < n (cm^{-3}) < 1000 to find the thermal equilibrium. The resulting phase diagram is shown in Fig. 3.3, where we have only varied the parameters G_0. Other variations of the parameters can be found in Wolfire et al. (1995) and Wolfire et al. (2003). In general, as in Fig. 3.3, these phase diagrams show that, at thermal equilibrium, a pressure where Eq. 3.26 is satisfied exists. This shows that at the typical pressure of the interstellar medium, $P/k_B \sim$ 3000 K.cm^{-3} (Jenkins and Tripp, 2011), the "two-phase" equilibrium initially introduced by Field et al. (1969) is still valid using updated heating and cooling processes.

3.4 Thermal structure of the neutral ISM

From the observational standpoint, the understanding of the thermal structure of the multiphase neutral medium comes from surveys of the 21 cm line against continuum radio sources (e.g., Heiles and Troland, 2003b; Murray et al., 2015). Since opacity is inversely proportional to the spin (equivalent to kinetic) temperature : $\tau(\nu) = N_{HI}(\nu)/C\,T_{spin}$, only the CNM is observed in absorption. On the other hand, all the neutral ISM, including the warm and lukewarm gas is seen in emission. To illustrate this difference, Figs. 3.4 shows the emission-absorption pairs towards the radio source G331.35+1.07 from Dickey et al. (2003). The emission spectrum is at the top and the absorption spectrum is below. This fundamental difference between the two allows to infer the amount of cold, lukewarm and warm gas along the line-of-sight (via column densities). It also allows the determination of the temperature associated to each phase. Using radiative transfer modeling, the combined analysis of 21 cm absorption and emission data have revealed some of the thermodynamical properties of the neutral ISM. Among them, temperatures probed by these surveys reveal the presence of HI at unstable states, typically between 500 and 5000 K (e.g., Heiles and Troland, 2003b; Kanekar et al., 2003; Roy et al., 2013a; Murray et al., 2015; Murray et al., 2018b). More precisely, Heiles and Troland (2003), Murray et al. (2015) and Murray et al. (2018) estimated that about 30% of the HI is in the cold CNM phase, 20% in

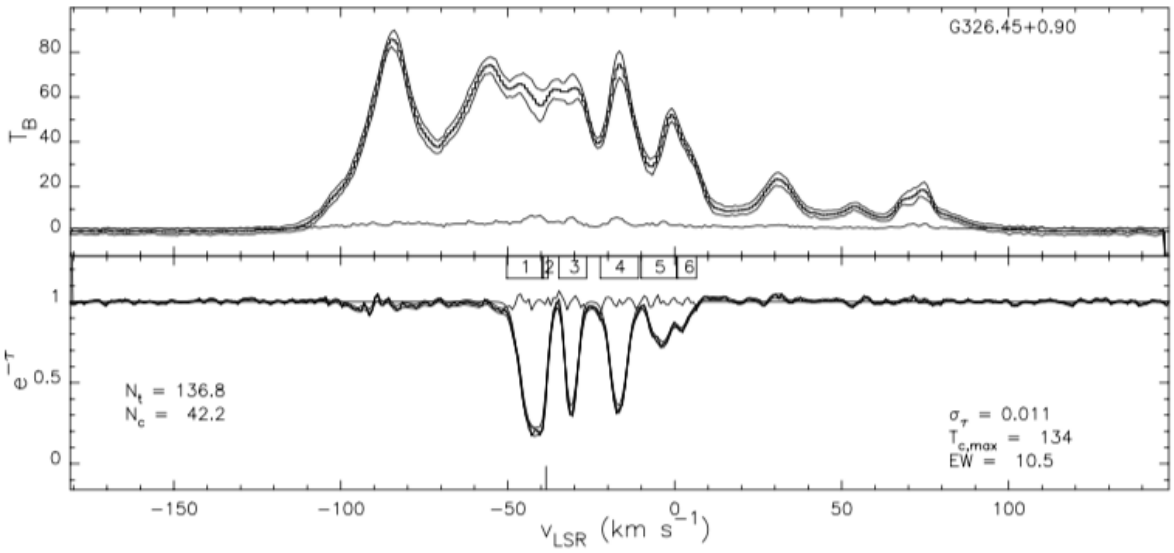

Fig. 3.4.: From Dickey et al. (2003): Fig. 2: Emission-absorption spectrum pairs toward G331.35+1.07. the emission spectrum is at the top and the absorption spectrum is below. Both spectra have error envelopes, which are computed from the errors of the interpolation of the emission in the direction of the continuum source. The numbered boxes in between show the velocity ranges of the different blended lines. The rms noise in the absorption, coming primarily from the emission fluctuations, is indicated as σ_τ, the peak continuum brightness temperature is indicated as $T_{c,max}$ (in kelvins), and the equivalent width, EW, is indicated (in km s^{-1}).

the thermally unstable regime, and 50% in the WNM. Nevertheless the fraction of the HI in each phase remains uncertain and large variations are observed: the fraction of the mass in the CNM ranges from ∼1% to more than 50% (Murray et al., 2018b). Two other parameters can be derived from absorption lines surveys: turbulent Mach numbers and magnetic fields[2]. As summarized by Heiles et al. (2019), CNM structures are characterized by column density below 10^{20} cm^{-2} with a median value around $N_{\rm HI,CNM} \sim 0.5{\times}10^{20}$ cm^{-2}, a turbulent Mach number $\mathcal{M}_s$ ∼3.7, and a magnetic field around ∼6 µG (Heiles and Troland, 2005). For the WNM, median column density of high Galactic latitude gas ($|b|$>10°) is around $N_{\rm HI,WNM} \sim 1.3{\times}10^{20}$ cm^{-2}. A rough estimation of the volume filling factor of ∼0.5 for the WNM was derived. As noted by Heiles et al. (2019), these result are "statistical results and individual detections are too sparse to make a meaningful histogram".

3.5 Morphological structure of the neutral ISM

3.5.1 Mapping the neutral ISM

From a point of view of the structure of matter in space, it was from the 1970s that the beauty of the neutral interstellar medium started to be completely revealed, with in particular a new sky survey published by Heiles and Jenkins (1976). For the first time, the "two-phase" structure of the neutral ISM made of cold clouds and warm diffuse gas appeared clearly from a spatial perspective. Since that first large survey, huge efforts have been made to map the 21 cm emission of the Galactic HI (recent

[2]Note that these values have been obtained using Zeeman-splitting measurements of the 21 cm line.

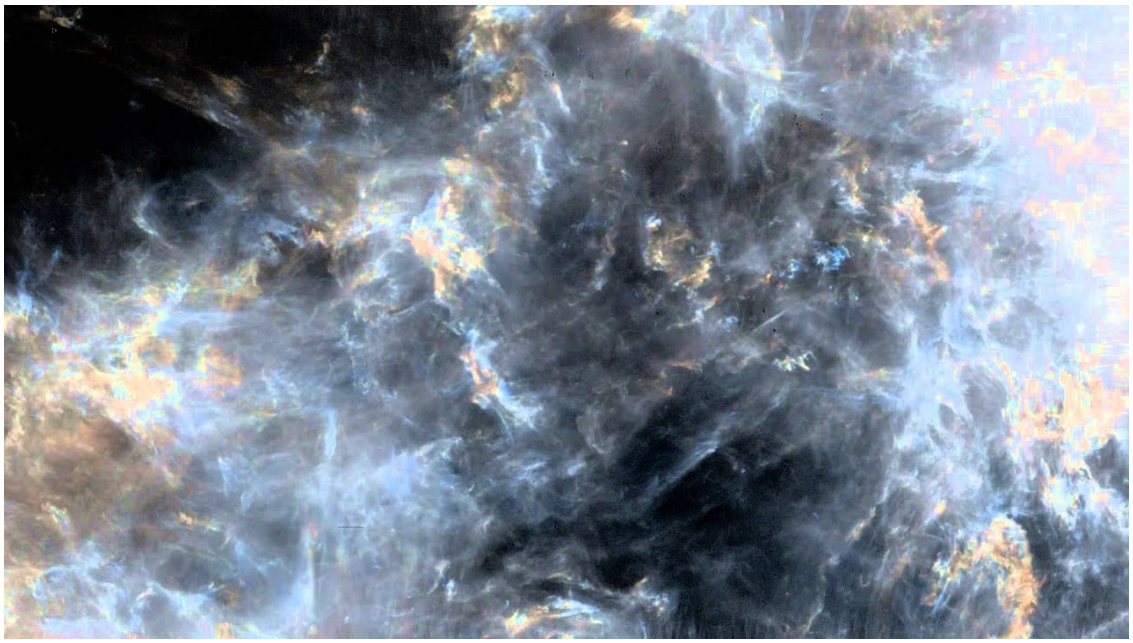

Fig. 3.5.: A View of Galactic Arecibo L-band Feed Array HI (GALFA-HI) DR2W survey: image of the HI sky, 40 degrees in declination, whose colors represent few velocity channels of the local emission.

examples are Taylor et al., 2003; Kalberla et al., 2005; Stil et al., 2006; McClure-Griffiths et al., 2009; Peek et al., 2011a; Martin et al., 2015; Winkel et al., 2016; Blagrave et al., 2017; Peek et al., 2018) and a large amount of data is now available. Among them, the GALFA-HI survey (Peek et al., 2011a; Peek et al., 2018) have recently revealed astonishing features, corresponding to narrow HI channel map structures, and now called "HI fibers". Figure 3.5 shows an image of the HI sky, whose colors represent few velocity channels of the local emission. It turned out that these fibers are remarkably aligned with the magnetic field orientation (Clark et al., 2014; Clark et al., 2015).

3.5.2 Vertical structure

On a global scale, the distribution of HI gas in the Milky Way can be approximated by a layer whose thickness increases exponentially as it moves outwards from the Galaxy (Kalberla and Kerp, 2009). This flaring of the HI disk is illustrated in Fig. 3.6. In particular, this behaviour emerges from the balance between gravitational forces and the pressure constituents (Kalberla and Kerp, 2009). However, it is important to note that this description of the distribution of HI gas is considered on large scales and as a steady state, but as noted by Kalberla and Kerp (2009), the pressure and density on hundreds of parsecs can vary due to dynamical aspects such as turbulence or phase transition. In this global picture, the scale height $b_z(R)$ (corresponding to a half width at half maximum of a Gaussian layer) can be written as

$$b_z(R) = b_0\, exp\left(\frac{R - R_\odot}{R_0}\right) \text{ kpc} \tag{3.50}$$

where b_0 = 0.15 kpc and R_0 = 9.8 kpc for $5 \lesssim R \lesssim 35$ kpc. At the location of the Sun, this corresponds to a full width at half max (FWHM), $\text{FWHM}_{tot}(R_\odot)$ = 300 pc. Figure 3.6 shows the fit performed by Kalberla and Dedes (2008) on the average flaring of the HI gas layer as function of R. Using again

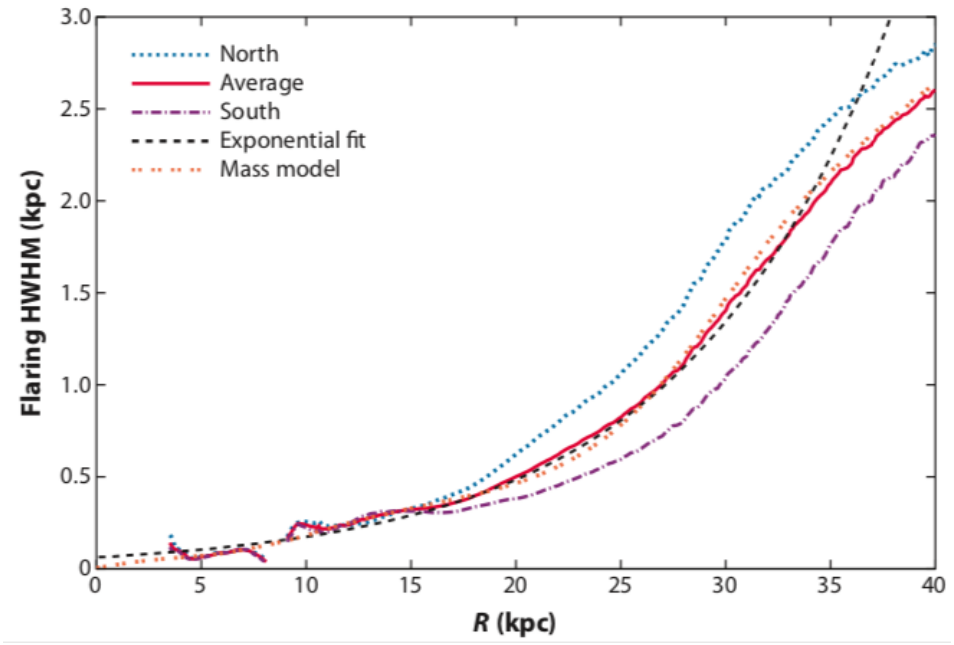

Fig. 3.6.: From Kalberla and Kerp (2009): Fig. 6: Average flaring of the HI gas layer as a function of R (from Kalberla and Dedes (2008)). The observations can be approximated very well by an exponential relation (black dashed line) or by fitting a mass model to an isothermal Hi gas distribution (Kalberla et al., 2007).

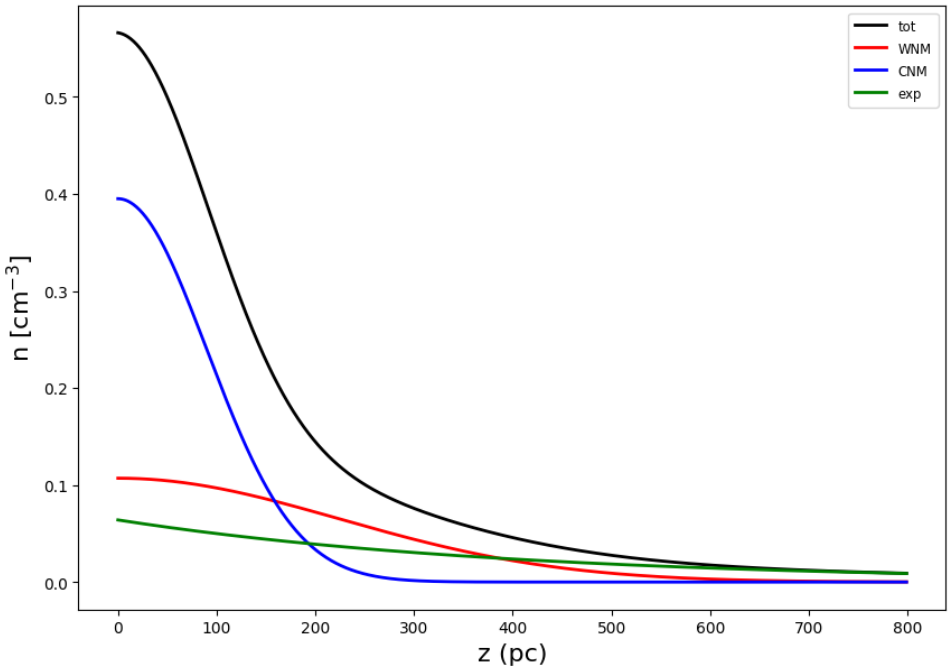

Fig. 3.7.: Density profile as function of the distance above the galactic plane scaled at R_0 = 8.5 kpc from Dickey and Lockman (1990). The corresponding formula is presented in Eq. 3.51.

an hydro-static equilibrium approach, Kalberla et al. (2007) estimated FWHMs of the warm and cold phases, $\mathrm{FWHM_{CNM}}$ = 250 pc and $\mathrm{FWHM_{WNM}}$ = 666 pc. It is very interesting to relate this estimation to the fit (unrelated to hydrostatic equilibrium assumptions) of HI data published by Dickey and Lockman

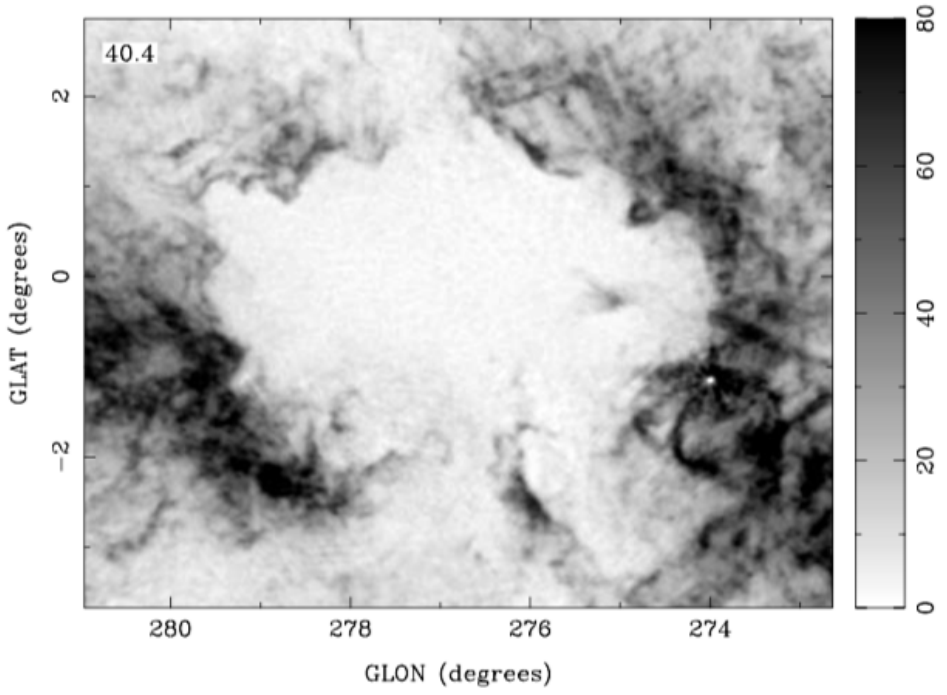

Fig. 3.8.: From McClure-Griffiths et al. (2003): Fig. 7: Gray-scale image of GSH 277+00+36 at v = 40.4 km s^{-1}. The gray scale is linear from 0 to 80 K, as shown at the wedge on the right. Note the scalloping of the shell wall all around the shell.

(1990) at $R = R_0$. These authors obtained that the total density distribution of HI is well fitted by a sum of three function:

$$n(z) = \frac{0.57}{\mathrm{cm}^{-3}} \left\{ 0.70 \exp\left[-\left(\frac{|z|}{127\mathrm{pc}} \right)^2 \right] + 0.19 \exp\left[-\left(\frac{|z|}{318\mathrm{pc}} \right)^2 \right] + 0.11 \exp\left(-\frac{|z|}{403\mathrm{pc}} \right) \right\}. \quad (3.51)$$

The two first terms of Eq 3.51 are Gaussian and the last term is an exponential. For the two Gaussian, the corresponding FWHMs are FWHM$_{(1)}$ = 212 pc and FWHM$_{(2)}$ = 530 pc. Although these Gaussian have not been explicitly defined or discussed as the WNM and CNM phases of the neutral ISM, it is striking to see how they match with estimations obtained by Kalberla et al. (2007). For example, Wolfire et al. (2003) used FWHMs from Dickey and Lockman (1990) to characterize the scale height of the WNM and the CNM in their analysis. Figure 3.7 graphically shows the function fitted by Dickey and Lockman (1990) with the two Gaussian and the exponential.

3.5.3 HI shells

In the galactic plane, a considerable amount of HI is found in the form of HI shells, super-shells and chimneys. These objects are defined and detected as HI voids with walls in the neutral ISM. It is believed that shells form from stellar wind and supernovae. An example combining shell and chimney is the Galactic shell GSH 277+00+36 located at a distance of about 6.5 kpc from the Sun (McClure-Griffiths et al., 2003a). This remarkable shell shown in Fig. 3.8, shows a chimney extensions reaching more than 1 kpc above the midplane. In general, walls are the location of compressed gas and

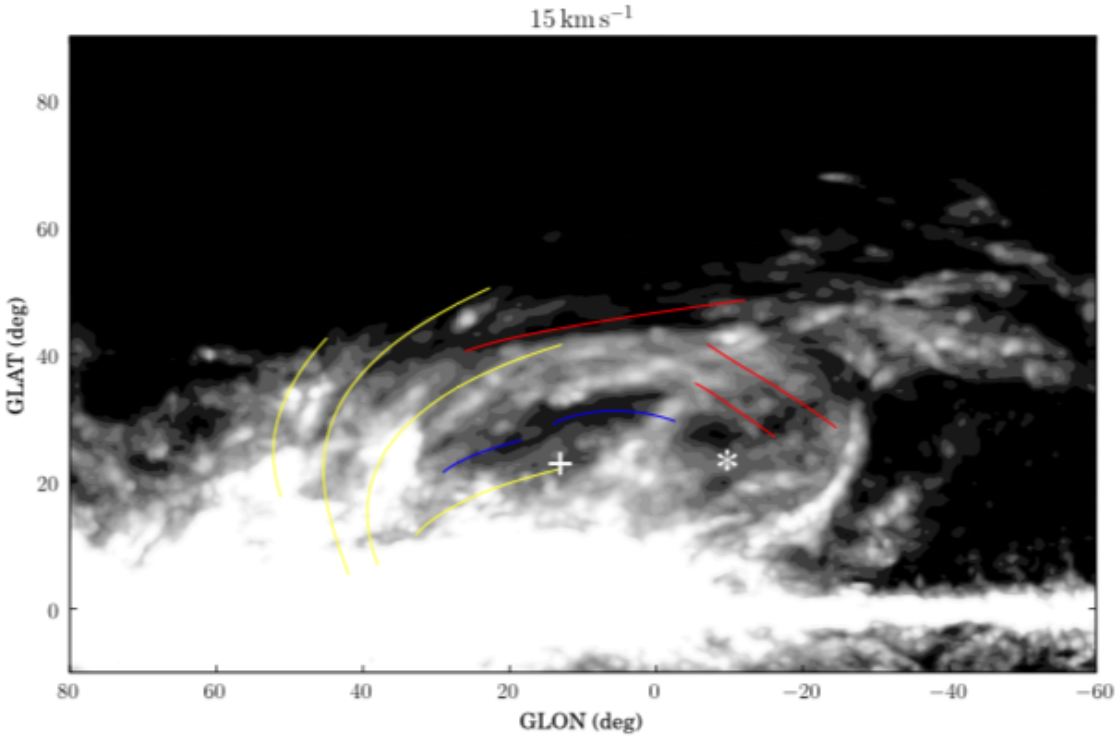

Fig. 3.9.: From Wolleben et al. (2010): Fig. 3: Map of the Hi brightness temperature at v_{lsr} = 15 km s^{-1} in a logarithmic gray scale. The position of the polarized filaments, as well as the position of the Upper Sco subgroup (Sco OB2_2) today ("*") and 5 Myr ago ("+") are shown. The brightness temperatures of the HI shells are about 3 K stronger than the background.

are characterized by a significant jump in density (about a factor of ∼10 over ∼18 pc) (McClure-Griffiths et al., 2003a). Interestingly, these regions also show narrow lines of the 21 cm emission, revealing that the gas is colder at the interface. This suggests that the gas is experiencing a phase transition. It is also believed that, at some point, this compression phenomenon could be at the origin of molecular cloud formation. Indeed, CO observations obtained with the Mopra telescope have revealed the presence of molecular clouds at the edges of HI shells (Dawson et al., 2011). The presence of a giant molecular cloud has also been reported at the interface between two colliding super-shells (Dawson et al., 2015). These observations suggest the importance of the dynamic processes taking place within these structures.

Magnetic fields have been observed in HI shells. An interesting example has been published by Wolleben et al. (2010) using Faraday rotation measurements of the diffuse Galactic polarized radio emission over the northern Galactic hemisphere. The latter quantity can be related to a combination of the electron density along the line-of-sight and the strength of the parallel component of the magnetic field. Using the rotational measure (RM) synthesis technique, these authors have characterized the position of polarized filaments and have found that they coincide with an HI emission at v=15 km s^{-1}. They concluded that the Faraday rotation observed is dominated by the magnetic field around the shell located at a distance of about 100 pc. Interestingly, they derived magnetic field properties with ∼20-34 µG which is significantly higher than the mean value of ∼6 µG (parallel and perpendicular) observed in the WIM/WNM of the solar neighborhood (Beck, 2001). Given this result, one can wonder which phase

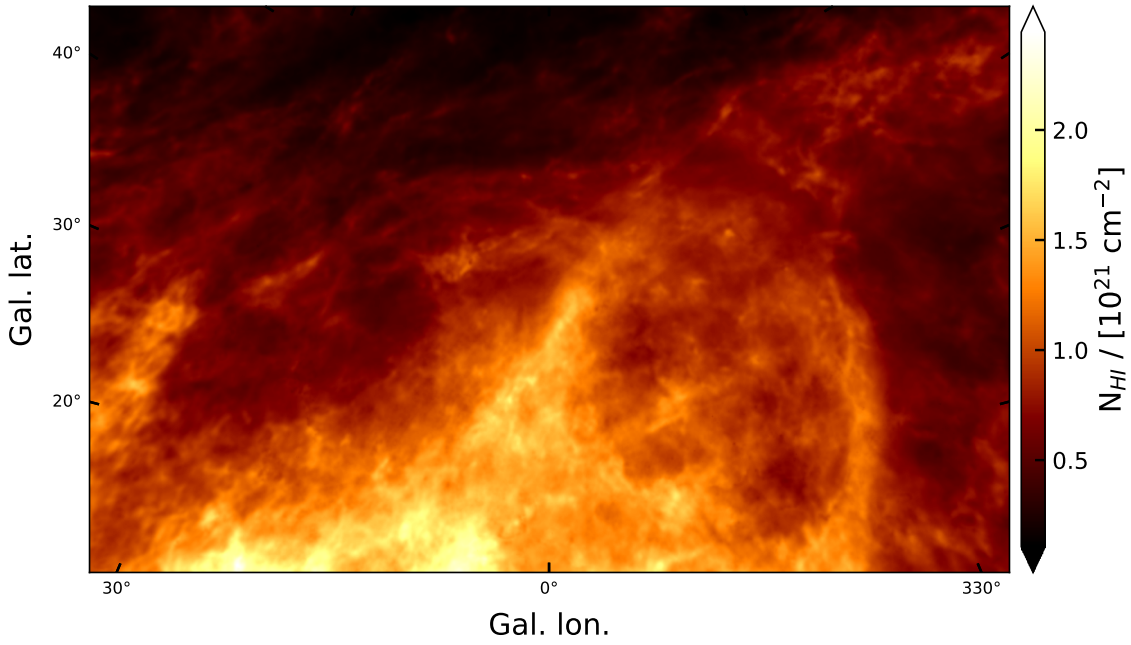

Fig. 3.10.: Integrated column density of the warm and unstable local gas (WNM+LNM) centered on the HI shell described in Wolleben et al. (2010). This decomposition is based on a phase separation obtained with *ROHSA*.

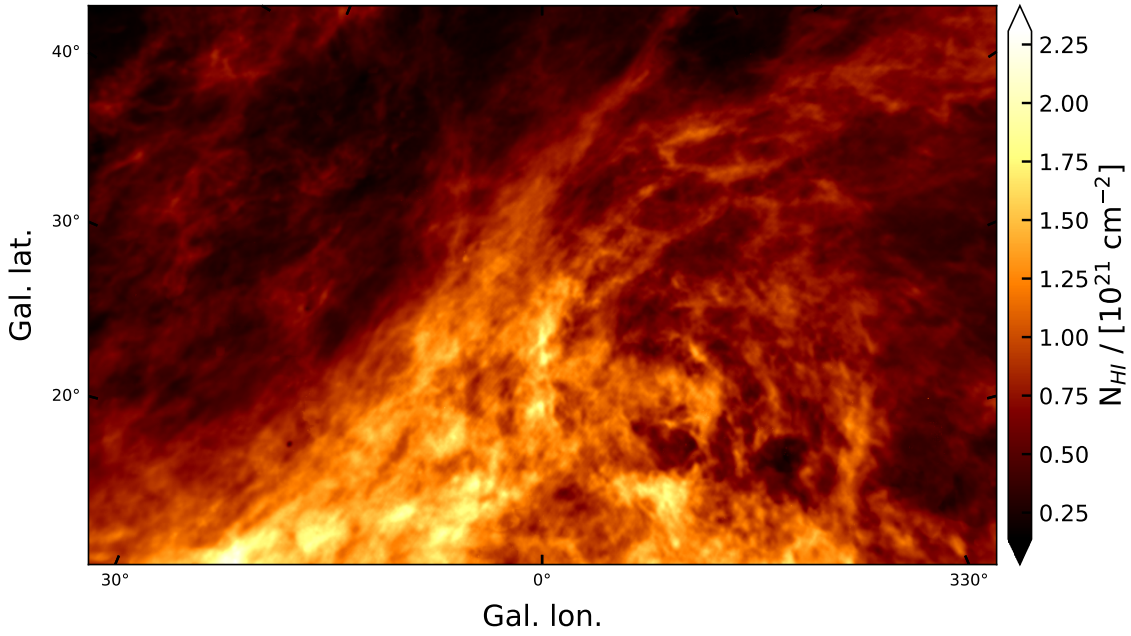

Fig. 3.11.: Integrated column density of the cold local gas (CNM) centered on the HI shell described in Wolleben et al. (2010). This decomposition is based on a phase separation obtained with *ROHSA*.

dominates the emission of the HI shell. Figures 3.10 and 3.11 show a multiphase view[3] of the neutral gas from the emission of the 21 cm line (HI4PI survey), centred on the HI shell described in Wolleben et al. (2010). This first qualitative description of the thermal state of the gas seems to reveal that the

[3]Note that this multiphase separation has been obtained using *ROHSA*, a Gaussian decomposition algorithm described in following Chapt. 4

HI shell in question is mainly traced by warm HI. This highlights the link between the WNM and the magneto-ionic medium traced by diffuse polarized radio emission.

3.5.4 Intermediate and high velocity clouds

A major component of the neutral ISM corresponds to the gas whose dynamics cannot be explained by the rotation of the Galactic disk. These objects have been discovered in the late 40's. Among 300 stars observed in absorption, Adams (1949) noticed that 8 of them showed neutral gas with absolute velocities $|v_{r,lsr}|$ > 20 km s^{-1}. From there, several authors started systematic surveys of such objects (e.g., Schlüter et al., 1953) and ended up with a new class of object called "high velocity clouds" (HVC). Interestingly, the possibility of a circumstellar origin from O stars and B stars observed was also suspected at that time (Woerden et al., 2004). Based on the possibility of neutral clouds located outside the Galactic plane, Spitzer suggested the existence of a "Galactic corona" of ionized gas that would confine this gas at pressure equilibrium. Spitzer's suggestion led Oort to suggest that some of this neutral gas located in the Galactic corona should reach velocities of about 100 km s^{-1}. Several years after, Muller et al. (1963) reported its discovery. From this moment on, two types of HI cloud populations are studied: IVCs (intermediate velocity clouds) with 20 < $|v_{r,lsr}|$ (km s^{-1}) < 80 and HVCs with $|v_{r,lsr}|$ > 80 km s^{-1}. The definition has evolved since the 60's, thanks in particular to Bart Wakker who defined the "deviation velocity" v_{dev} as the negative or positive difference between the observed velocity and the maximum radial velocity implied by the Galactic rotation curve (Wakker and Woerden, 1991).

The origins of HVCs and IVCs was first considered by Oort, whose suggestions are listed in Woerden et al. (2004) and reported here: (a) nearby supernova remnants (he considered this unlikely); (b) condensations formed in a gaseous corona at high temperature; (c) clouds ejected from the Galactic Nucleus; (d) clouds ejected as cool clouds from the disk; (e) intergalactic gas accreted by the Galaxy; (f) small satellites of the Galaxy or independent galaxies in the Local Group. Woerden et al. (2004) noted that if one added the gas tidally extracted from the Magellanic clouds, this is still a valid summary of their possible origins. Option (d) is now known as the "Galactic fountain". One main source of discrimination between these possible options remains the presence of dust particles in these structures. Their non-detection in HVCs suggests that they have an extra-galactic origin. Metal abundance also support the hypothesis that some of the HVCs are extragalactic.

In addition to the fundamental interest of studying the internal properties of HVCs and IVCs and their origins, an important question is the following: What is the impact of infalling matter on the star formation rate in galaxies ? As gas falls in the potential wells of galaxies it interacts with the interstellar medium. This input of momentum modifies the energy balance of the disk and can favor, or suppress, the formation of stars. The infall of low metallicity gas from the inter-galactic medium helps to sustains the star formation in the Milky Way. Given the challenges in understanding the star formation cycle, it seems essential to understand the impact of this input of matter on the interstellar medium.

One of the main difficulties in understanding these components of the neutral ISM is the identification of structures that compose them. To date, no complete IVC catalogue has been made based on large HI surveys. The fundamental reason is that IVCs and LVCs (local velocity clouds) show a continuum

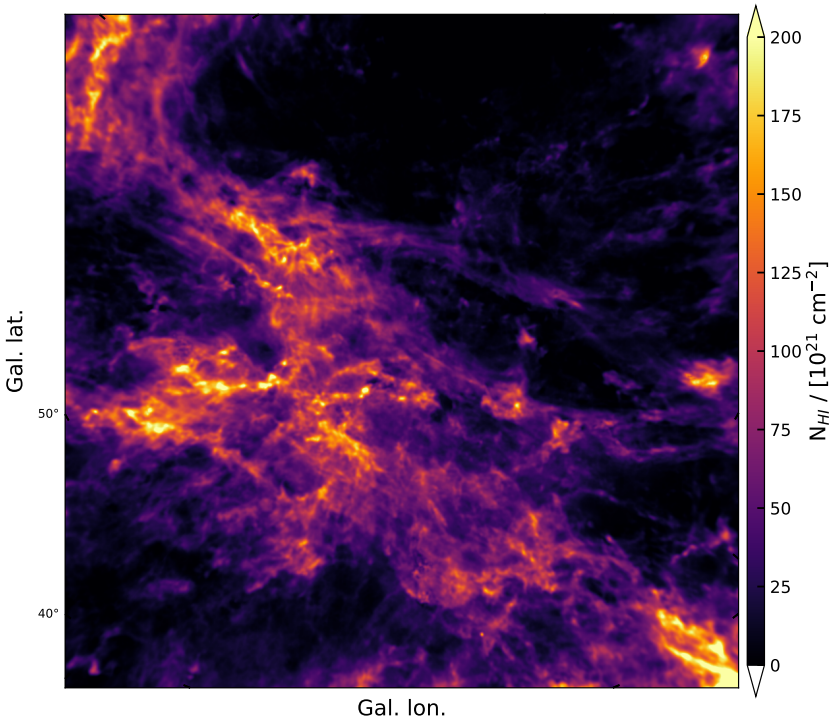

Fig. 3.12.: Integrated column density of warm IVCs from an HI4PI field centered on (l,b)=(140°,80°). This decomposition is based on a phase separation obtained with *ROHSA*, a Gaussian decomposition design for the multiphase separation of the 21 cm line and presented in following Chapt. 4.)

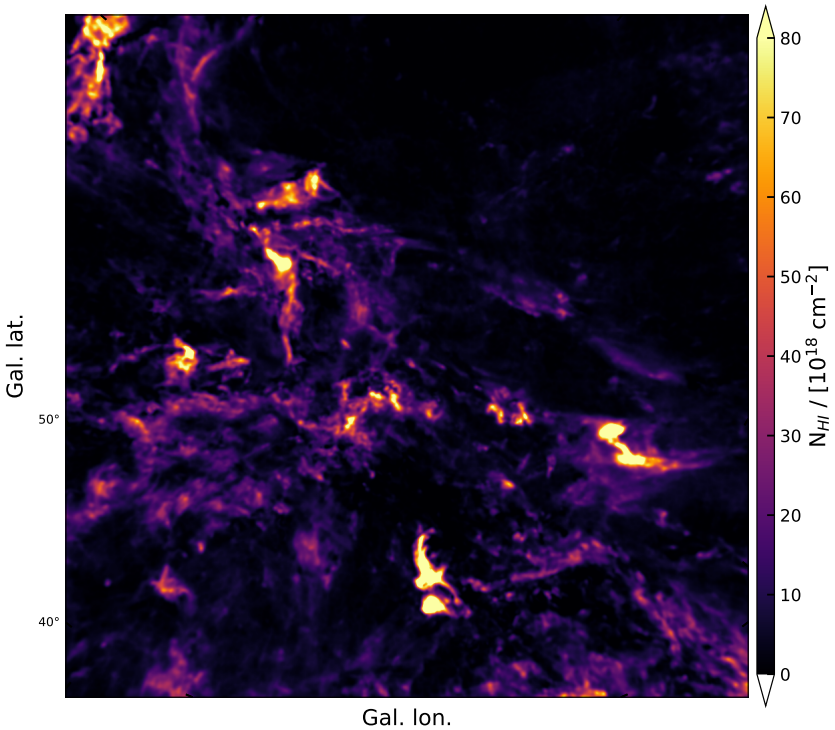

Fig. 3.13.: Integrated column density of cold IVCs from an HI4PI field centered on (l,b)=(140°,80°). This decomposition is based on a phase separation obtained with *ROHSA*.

that makes their separation highly challenging from a computational perspective. On the other hand, the confusion between HVCs and IVCs appears to be lower. This allowed in particular the recent inventory of 1693 objects (Moss et al., 2013). The second hurdle to obtaining more information about the physical properties of these structures is the determination of their distances. The most accurate determinations are based on absorption lines studies (e.g., Wakker, 2001) but the number of available lines are considerably limited regarding the amount of clouds. Several methods have been proposed to overcome this hurdle. First, Wolfire et al. (1995) proposed a method based on the thermal stability of a two-phase cloud located in the Galactic hot corona. Similarly to the thermal equilibrium curve in the solar neighborhood presented in Fig. 3.3, a multiphase cloud can only exist if its pressure is between P_{min} and P_{max}, where the condensation mode of the thermal instability can grow. However, for HVCs, this corresponding range varies notably with the distance of the cloud above the Galactic plane. Consequently, for HVCs with both cold and warm gas, lower and upper limits of their distances can be determined. Unfortunately, this remains unexplored due to the difficulty of separating the different phases in HVCs. Secondly, Benjamin et al. (1996) proposed a determination of HVCs distance by using a dynamic model of their fall in the Galactic interstellar medium. In this model, the acceleration of a cloud falling from the Galactic corona is given by the decelerating force of ram pressure and the accelerating force of gravity. When these two forces are equal, the cloud is at its "terminal velocity". Assuming that drag forces are sufficient to bring HVCs to this velocity, and knowing the column density of the cloud, one can determine the distance of the cloud based on a gravitational potential model of the Milky Way. In particular, this model have correctly predicted the distance of the HVC Complex M. As noted by Heitsch et al. (2016), the latter requires the inclination angle between the cloud trajectory and the line-of-sight. To overcome this constraint, Heitsch et al. (2016) proposed a method calibrated on numerical simulation which allows the determination of this inclination angle from cloud's morphology and kinematics.

Finally, their internal structure remains also uncertain. It has been shown that these clouds may have a multiphase structure, often coupled with a "head-tail" structure (Brüns et al., 2001; Putman et al., 2011). Interestingly, the cold gas seems to be located in the head of the cloud, while most of the warm gas seems to be in the tail. This multiphase cometary shape suggests that HVCs are accreted by the gravitational potential of the Galaxy and subjected to a strong interaction with the gaseous environment (Kalberla and Kerp, 2009). Just like the local component of the neutral ISM, a systemic investigation of the multiphase structure of HVCs and IVCs remains challenging. Indirect observational evidence of cold HI in IVCs have been revealed through several studies which have aimed at understanding the atomic-to-molecular transition in high latitude IVCs using HI, FIR and CO observations (Röhser et al., 2016b; Röhser et al., 2016a). To illustrate the importance of this multiphase aspect, Figs. 3.12 and 3.13 respectively show integrated column density fields of warm and cold IVCs of a high latitude HI field extracted from the HI4PI[4] survey. This phase separation has been obtained with the algorithm developed in following Chapt. 4. This multiphase view of high Galactic latitude IVCs shows a very good spatial correlation between the two phases. Cold structures seem to be well correlated with the warm inter-connected envelope. Contrary to the observation of local gas that we will discuss in Chapt. 5, this strong correspondence between cold and warm gas seems to indicate that the condition of condensation is not the same. This could be due to significant ram pressure. Future investigations on the multiphase structure of these IVCs remain to be explored.

[4]HI4PI is a full sky survey of the 21 cm line mapped at a spatial resolution of $\sim$16' (HI4PI Collaboration et al., 2016)

TABLE 5
SUMMARY OF PREVIOUS SPS STUDIES

Object	Tracer	Optical Depth	Scale	Slope	Reference
Polaris Flare	Dust	Thin	0.01∼8 pc	-2.7 ± 0.1	(1)
High Latitude Cirrus	Dust	Thin	0.01∼50 pc	-2.9 ± 0.1	(2)
CNM	HI Absorption	Thin	0.01∼3 pc	-2.75 ± 0.25	(3)
WNM	HI Emission	Thin	–	-4	(4)
Ursa Major	HI Emission	Thin	0.1∼25 pc	-3.6 ± 0.2	(5)
MBM16	HI Emission	Thin	0.1∼20 pc	-3.7 ± 0.2	(6)
North Ecliptic Pole	HI Emission	Thin	–	from -2.86 ± 0.04 to -2.59 ± 0.07	(7)

Reference:
(1) Miville-Deschênes et al. (2010): *Herschel* observations at 250 μm, 350 μm, and 500 μm were used to study the diffuse interstellar cloud Polaris flare.
(2) Miville-Deschênes et al. (2016): Dust-scattered light in the CFHT g-band was analyzed.
(3) Deshpande et al. (2000): The cold HI seen in absorption against Cassiopeia A and Cygnus A was examined.
(4) Dickey et al. (2001): One patch of the sky observed in the Southern Galactic Plane Survey was probed.
(5) Miville-Deschênes et al. (2003): The non-star-forming, high latitude cirrus cloud Ursa Major was under study.
(6) Pingel et al. (2013)
(7) Martin et al. (2015): GBT HI emission observations of low-, intermediate-, and high-velocity clouds at the north ecliptic pole were analyzed.

Fig. 3.14.: From Pingel et al. (2018): Table 5: Summary of Previous SPS Studies

3.6 Turbulence in the neutral ISM

The way in which all the environments presented in the previous section are related to the turbulent cascade of the interstellar medium is still poorly understood at this time. There is considerable evidence in the literature of the existence of interstellar turbulence, but its statistical properties remain largely to be explored, especially in the diffuse warm phase of the neutral ISM. The emergence of ideas related to interstellar turbulence presented in Chapt. 2 encountered a lot of pitfalls. For example, Oort and Spitzer (1955) did not believe Von Weizsaäcker's model, presented in Chapt. 2. One of the main arguments put forward by them was that the ISM morphology did not look like what we could expect from incompressible turbulence: a collection of vortices. They noticed that "instead of more or less continuous vortices, we find concentrated clouds that are often separated by much larger spaces of negligible density." As noted by Elmegreen and Scalo (2004), the discovery of the broad emission of the 21 cm line reinforced the picture of the static two-phase model introduced by Field (1965); Field et al. (1969), and the turbulence nature of the neutral ISM was eclipsed again. During the 1970's, before Larson (1979); Larson (1981) highlighted the $\sigma_v - l$ relationship in HI and molecular clouds, very few studies had aimed at understanding the HI emission in the context of turbulent fluid (Baker, 1973; Mebold et al., 1974). It is remarkable to see how Baker's vision of the 21 cm line is similar to what is believed today: HI lines are a mixture of thermal and turbulent broadening. Two years after Larson's discovery, Crovisier and Dickey (1983) published a power spectrum analysis of HI velocity channels, revealing the existence of a correlated emission over a wide range of spatial scales. In particular, they suggested that it could be analyzed in the context of turbulence. As noted by Dickey et al. (2001), the link between the spatially correlated emission observed in projection on the sky and the scaling law of incompressible or compressible turbulence was not clear at that time, and it was only in the late 1990's that the link between the two was studied in more details (Goldman, 2000; Lazarian and Pogosyan, 2000). These different contributions definitively marked the return of interstellar turbulence in the modeling of the ISM.

Recent studies using spatial power spectra to analyze the statistical properties of the turbulent cascade in the neutral ISM have been recently compiled by Pingel et al. (2018), and are reported here in

Fig. 3.14. These variations in the slopes of the power spectrum illustrate the complexity of their interpretation. It should be strongly emphasized that in addition to the fact that these values come from different sky regions, they are generally not obtained with the same technique. Power spectra are sometimes deduced directly from velocity channels (Crovisier and Dickey, 1983), from the integrated column density (Miville-Deschênes et al., 2003a; Martin et al., 2015), or from specific techniques such as the velocity channel analysis (Dickey et al., 2001; Lazarian and Pogosyan, 2000). The interpretation of this latter technique is still a matter of debate.

4 ROHSA : Regularized Optimization for Hyper-Spectral Analysis

> *One of These Days I'm Going to Cut You Into Little Pieces.*
>
> — **One of these days (1971)**
> Pink Floyd

Contents

In this chapter, we propose a new method to map out the contribution of each phase to the 21 cm emission. The method is based on a decomposition of the 21 cm emission line with Gaussian profiles and constraints that favor spatially coherent parameters. This chapter is organized as follows. In Sect. 4.1, we describe the methodology used to develop our Gaussian decomposition algorithm. An evaluation of numerical simulation is presented in Sect. 4.2. In Sect. 4.3 we present an application to observations. The discussion and summary are presented Sects. 4.4 and 4.5.

4.1 Methodology

4.1.1 Gaussian decomposition of the 21 cm emission

Very early on after its detection, the 21 cm line was observed to be well described by a sum of a small number of Gaussian components. This was found to be true for the least confused absorption spectra (Muller, 1957; Muller, 1959; Clark, 1965) but also for emission spectra observed away from the Galactic plane (Heeschen, 1955). Very few spectra at high Galactic latitudes do not comply with that rule, whatever the angular resolution of the data. Recently, Kalberla and Haud (2018) showed that more than 60% of the spectra over the whole sky can be described by the sum of seven Gaussian components or less. In the two decades after the detection of the 21 cm line, many studies used the Gaussian decomposition to infer physical parameters from the data (Matthews, 1957; Davis, 1957; Muller, 1957; Muller, 1959; Dieter, 1964; Dieter, 1965; Lindblad, 1966; Takakubo and Woerden, 1966; Mebold, 1972). The fact that a small number of Gaussian components is needed to describe the signal was seen as a convenient way to describe the emission profiles with a small set of parameters (Takakubo and Woerden, 1966). It is also a very strong element in favor of the Gaussian function as a significant descriptor of the underlying physics.

Takakubo (1967) showed that the width of the 21 cm emission line could be grouped in three components ($\sigma \leq 3\,\mathrm{km\,s^{-1}}$; $3 < \sigma < 7\,\mathrm{km\,s^{-1}}$; $\sigma \geq 7\,\mathrm{km\,s^{-1}}$), a result confirmed later on (Mebold, 1972; Haud and Kalberla, 2007; Kalberla and Haud, 2018). Takakubo (1967) also showed that the narrow 21 cm features are well correlated with Ca+ K line absorption measurements. These latter authors concluded that the narrow component, also seen in 21 cm absorption spectra, is likely to be isolated cold clouds (CNM) in the Solar neighborhood. They also showed that the spatial distribution of the centroid velocity, velocity width, and column density of the large feature is compatible with a warm (WNM) and diffuse disk that follows Galactic rotation. The second group of Gaussians, with a width (σ) of between 3 and $7\,\mathrm{km\,s^{-1}}$, is generally attributed to gas in the thermally unstable range, but a fraction of them could be caused by blending of narrow features.

The exact mass fraction of gas in each phase (CNM, LNM, and WNM) is still a matter of debate. In addition, because this knowledge is based on absorption measurements, there is very little information about the structure of these phases on the sky. Being able to separate the different phases on each line of sight would allow us to study the structure and kinematics of the cold phase and its relationship with the more diffuse gas. In theory, one could expect that Gaussian decomposition of the emission spectra could provide such mapping.

4.1.2 Limitation of the Gaussian model

There are many pitfalls in the description of the 21 cm emission spectra as a sum of Gaussian components: velocity blending, ambiguities of the number of components, nonGaussian profiles, noise peaks, plurality of solutions. Another important limitation is the effect of optical depth of the 21 cm line that modifies the shape of the line. More generally, the main opposition to Gaussian decomposition of emission spectra is that any spectrum can be decomposed that way provided that enough Gaussians are used. If that is the case, how can one be sure that the Gaussian representation provides some real physical information about the emitting gas? For instance, two spatially disconnected cold structures present on the same line of sight could appear at the same projected velocity. In this case their respective emission profiles would be confused. This velocity blending affects both the emission and absorption spectra; it is present in the data, and more so at lower Galactic latitudes where the length of the line of sight is larger and the number of HI structures increases.

This line of reasoning led Dickey and Lockman (1990) to advise against using Gaussian decomposition to analyze 21 cm spectra. Later on, it continued to be used (Verschuur and Schmelz, 1989; Verschuur and Magnani, 1994; Poppel et al., 1994; Haud, 2000; Verschuur, 2004; Begum et al., 2010; Martin et al., 2015; Kalberla and Haud, 2018) but overall there was a loss of interest, except for the analysis of absorption spectra. Indeed by comparing nearby absorption and emission spectra one can recover the effect of optical depth on the 21 cm emission. In addition, absorption measurements are only sensitive to cold gas, limiting the velocity blending problem. For these reasons, the Gaussian decomposition continued to be used in this context (Dickey et al., 2003; Kanekar et al., 2003), and especially after the seminal work of Heiles and Troland (2003) who developed a dedicated formalism which has been used in several other studies since (e.g. Stanimirović and Heiles, 2005; Begum et al., 2010; Stanimirović et al., 2014; Lee et al., 2015; Murray et al., 2014; Murray et al., 2015; Murray et al., 2018a). Indeed, key information about the nature of the HI came from the joint Gaussian decomposition of emission and absorption spectra.

4.1.3 Development of a new approach

Following what has been done for the comparison of emission and absorption spectra where the Gaussian decomposition is considered valid, we would like to argue that a similar decomposition could be envisaged for emission data only, at least at high Galactic latitudes where the effect of optical depth of the 21 cm line has been shown to be negligible (Murray et al., 2018a).

The fact that physical information could be obtained using a Gaussian decomposition of absorption data reveals the fact that thermal broadening has a significant effect in shaping the line profile, or in other words, that the dynamics of each HI phase is typical of sub- or trans-sonic turbulence. When the amplitudes of turbulent and thermal motions are commensurate, the line appears smooth and can be represented by a small number of Gaussian components (Miville-Deschênes et al., 2003b). If the HI at high Galactic latitude is indeed represented by a two-phase medium with small, cold, and trans-sonic structures immersed in a relatively low-Mach-number and warm diffuse phase, the Gaussian representation could bear significant physical information.

The perspective of mapping the phases of the HI is so important that we ventured to explore new ways of decomposing the emission spectra that could be applicable to the high Galactic sky. The main difficulty is the effect of velocity blending for cold structures. As mentioned by Takakubo and Woerden (1966), there will always be cases where a given spectrum can be fitted with a smaller number of components than its neighbors, if two or more components have similar central velocity and velocity dispersion. One way to avoid this confusion is to look for solutions that have a spatial continuity, or that have a slow spatial variation. Poppel et al. (1994), Haud (2000), Martin et al. (2015) and Miville-Deschênes et al. (2017) have implemented Gaussian decomposition methods that use some information about their neighbors in order to favor spatially coherent solutions. Formally nevertheless, these algorithms do not force solutions to be spatially coherent; they simply provide initial guesses to the fit of a single spectrum based on the most likely solutions found in some surrounding area. The optimization is not bound to this initial guess and it can always converge to another solution that would break the spatial smoothness of the parameter space.

The novelty of the algorithm we present here is that it is the first one that imposes the spatial coherence in the determination of the parameters. In order to do that, all the spectra of the emission cube are fitted at the same time. To make sure that the recovered parameters are spatially smooth, specific regularization terms are added to the cost function with non-negativity constraints on the amplitude. This algorithm, called ROHSA, is described below.

4.1.4 ROHSA

ROHSA performs a regression analysis using a regularized nonlinear least-square criterion. We formulate in this section the Gaussian model used as well as the energy terms added to the cost function to take into account the spatial coherence of the emission and the multiphase nature of the gas simultaneously. The quasi-Newton algorithm, L-BFGS-B, used to perform the optimization is then briefly described. Finally, we formulate the algorithm performed by ROHSA based on a multi-resolution process from coarse to fine grid.

Model The data are the measured brightness temperature $T_B(v_z, \boldsymbol{r})$ at a given projected velocity v_z across sky coordinates $\boldsymbol{r}$. The proposed model $\tilde{T}_B\big(v_z, \boldsymbol{\theta}(\boldsymbol{r})\big)$ is a sum of N Gaussian $G\big(v_z, \boldsymbol{\theta}_n(\boldsymbol{r})\big)$

$$\tilde{T}_B\big(v_z, \boldsymbol{\theta}(\boldsymbol{r})\big) = \sum_{n=1}^{N} G\big(v_z, \boldsymbol{\theta}_n(\boldsymbol{r})\big), \tag{4.1}$$

with $\boldsymbol{\theta}(\boldsymbol{r}) = \big(\boldsymbol{\theta}_1(\boldsymbol{r}), \dots, \boldsymbol{\theta}_n(\boldsymbol{r})\big)$ and where

$$G\big(v_z, \boldsymbol{\theta}_n(\boldsymbol{r})\big) = \boldsymbol{a}_n(\boldsymbol{r}) \exp\left(-\frac{\big(v_z - \boldsymbol{\mu}_n(\boldsymbol{r})\big)^2}{2\boldsymbol{\sigma}_n(\boldsymbol{r})^2}\right) \tag{4.2}$$

is parametrized by $\boldsymbol{\theta}_n = \big(\boldsymbol{a}_n, \boldsymbol{\mu}_n, \boldsymbol{\sigma}_n\big)$ with $\boldsymbol{a}_n \geq 0$ being the amplitude, $\boldsymbol{\mu}_n$ the position, and $\boldsymbol{\sigma}_n$ the standard deviation 2D maps of the n-th Gaussian profile across the plan of sky. The residual is

$$L\big(v_z, \boldsymbol{\theta}(\boldsymbol{r})\big) = \tilde{T}_B\big(v_z, \boldsymbol{\theta}(\boldsymbol{r})\big) - T_B(v_z, \boldsymbol{r}). \tag{4.3}$$

The estimated parameters $\hat{\boldsymbol{\theta}}$ are defined as the minimizer of a cost function that includes the sum of the squares of the residual,

$$Q(\boldsymbol{\theta}) = \frac{1}{2}\left\|L(v_z, \boldsymbol{\theta})\right\|_{\boldsymbol{\Sigma}}^2 = \frac{1}{2}\sum_{v_z,\boldsymbol{r}}\left(\frac{L(v_z, \boldsymbol{\theta}(\boldsymbol{r}))}{\boldsymbol{\Sigma}(\boldsymbol{r})}\right)^2, \tag{4.4}$$

where Σ is the standard deviation 2D map of the noise assumed without spatial correlation. In practice this term is estimated using a sequence of empty velocity channels of $T_B(v_z, \boldsymbol{r})$.

For each of the N Gaussians, we want to obtain a spatially coherent solution, meaning that for each parameter, the values have to be close for neighboring lines of sight. This can be done by penalizing the small-scale spatial fluctuations of each parameter, measured by the energy at high spatial frequencies. The considered high-pass filter is the second-order differences, that is the Laplacian filtering, defined by the 2D convolution kernel,

$$d = \begin{bmatrix} 0 & -1 & 0 \\ -1 & 4 & -1 \\ 0 & -1 & 0 \end{bmatrix}. \tag{4.5}$$

The following regularization term, itself containing energy terms, is added to the cost function given in Eq. (4.4),

$$R(\boldsymbol{\theta}) = \frac{1}{2}\sum_{n=1}^{N}\lambda_{\boldsymbol{a}}\|\boldsymbol{D}\boldsymbol{a}_n\|_2^2 + \lambda_{\boldsymbol{\mu}}\|\boldsymbol{D}\boldsymbol{\mu}_n\|_2^2 + \lambda_{\boldsymbol{\sigma}}\|\boldsymbol{D}\boldsymbol{\sigma}_n\|_2^2, \tag{4.6}$$

where $\boldsymbol{D}$ is a matrix performing the 2D convolution using the kernel d and $\lambda_{\boldsymbol{a}}$, $\lambda_{\boldsymbol{\mu}}$, and $\lambda_{\boldsymbol{\sigma}}$ are hyper-parameters that tune the balance between the different terms.

These terms ensure a positive spatial correlation of the model parameters for neighboring pixels. However, each term is free to have large variation across the field at larger scale. Since $\boldsymbol{\sigma}_n$ contains information about the gas thermodynamics, we design an additional term in the cost function to group Gaussians with similar σ_n. This is implemented in order to favor any solution that would produce components ascribable to each of the phases (WNM, LNM or CNM). In order to do that we add another term, $\lambda'_{\boldsymbol{\sigma}}\|\boldsymbol{\sigma}_n - m_n\|_2^2$, which constrains $\boldsymbol{\sigma}_n$ to be close to an unknown scalar value m_n. The full regularization term is then

$$\begin{aligned} R(\boldsymbol{\theta}, \boldsymbol{m}) = \frac{1}{2}\sum_{n=1}^{N}&\lambda_{\boldsymbol{a}}\|\boldsymbol{D}\boldsymbol{a}_n\|_2^2 + \lambda_{\boldsymbol{\mu}}\|\boldsymbol{D}\boldsymbol{\mu}_n\|_2^2 + \lambda_{\boldsymbol{\sigma}}\|\boldsymbol{D}\boldsymbol{\sigma}_n\|_2^2 \\ &+ \lambda'_{\boldsymbol{\sigma}}\|\boldsymbol{\sigma}_n - m_n\|_2^2, \end{aligned} \tag{4.7}$$

with $\boldsymbol{m} = (m_1, \ldots, m_N)$ and $\boldsymbol{a}_n \geq 0$, $\forall\, n \in [1, \ldots, N]$. The last two terms in Eq. (4.7), representative of a joined constraint imposed on σ_n, allow us to interpret a posteriori and simultaneously the morphology and the thermodynamical state of each component extracted from the data. The full cost function is then

$$J(\boldsymbol{\theta}, \boldsymbol{m}) = Q(\boldsymbol{\theta}) + R(\boldsymbol{\theta}, \boldsymbol{m}). \tag{4.8}$$

Optimization algorithm Unlike $Q(\boldsymbol{\theta})$, each energy term proposed in Eq (4.6) involves linear dependences on the parameter $\boldsymbol{\theta}$. The cost function in Eq. (4.8) is therefore a regularized nonlinear least-square criterion. The minimizer,

$$[\hat{\boldsymbol{\theta}}, \hat{\boldsymbol{m}}] = \underset{\boldsymbol{\theta}, \boldsymbol{m}}{\operatorname{argmin}}\ J(\boldsymbol{\theta}, \boldsymbol{m}),\ \text{wrt. } \boldsymbol{a}_n \geq 0,\ \forall\, n \in [1, \ldots, N], \tag{4.9}$$

has no closed form expression and is not directly tractable because of the complexity of the model $\tilde{T}_B$ and the size of the unknown and data. The proposed solution relies instead on an iterative optimization algorithm that uses the gradient

$$\nabla J(\boldsymbol{\theta}, \boldsymbol{m}) = \begin{bmatrix} \nabla L(\boldsymbol{\theta}) \times L(\boldsymbol{\theta}) \\ \mathbf{0} \end{bmatrix} + \begin{bmatrix} \nabla_{\boldsymbol{\theta}} R(\boldsymbol{\theta}, \boldsymbol{m}) \\ \nabla_{\boldsymbol{m}} R(\boldsymbol{\theta}, \boldsymbol{m}) \end{bmatrix}, \tag{4.10}$$

which is tractable since it involves the residual, the Jacobian of the residual $\nabla L(\boldsymbol{\theta})$, and 2D convolutions with the kernel d for $\boldsymbol{D}$ and $\boldsymbol{D}^t$. The gradient $\nabla R^t(\boldsymbol{\theta}, \boldsymbol{m}) = [\nabla_{\boldsymbol{\theta}} R^t(\boldsymbol{\theta}, \boldsymbol{m}), \nabla_{\boldsymbol{m}} R^t(\boldsymbol{\theta}, \boldsymbol{m})]$ and $\nabla L(\boldsymbol{\theta})$ can be written

$$\nabla L(v_z, \boldsymbol{\theta}(\boldsymbol{r})) = \begin{bmatrix} \exp\left(-\frac{\left(v_z - \mu_1(\boldsymbol{r})\right)^2}{2\sigma_1(\boldsymbol{r})^2}\right) \\ \frac{a_1(v_z - \mu_1(\boldsymbol{r}))}{\sigma_1^2} \exp\left(-\frac{\left(v_z - \mu_1(\boldsymbol{r})\right)^2}{2\sigma_1(\boldsymbol{r})^2}\right) \\ \frac{a_1(v_z - \mu_1(\boldsymbol{r}))^2}{\sigma_1^3} \exp\left(-\frac{\left(v_z - \mu_1(\boldsymbol{r})\right)^2}{2\sigma_1(\boldsymbol{r})^2}\right) \\ \vdots \\ \frac{a_N(v_z - \mu_N(\boldsymbol{r}))^2}{\sigma_N^3} \exp\left(-\frac{\left(v_z - \mu_N(\boldsymbol{r})\right)^2}{2\sigma_1(\boldsymbol{r})^2}\right), \end{bmatrix} \tag{4.11}$$

$$\nabla_{\boldsymbol{\theta}} R(\boldsymbol{\theta}, \boldsymbol{m}) = \begin{bmatrix} \lambda_{\boldsymbol{a}} \boldsymbol{D}^t \boldsymbol{D} \boldsymbol{a}_1 \\ \lambda_{\mu} \boldsymbol{D}^t \boldsymbol{D} \boldsymbol{\mu}_1 \\ \lambda_{\boldsymbol{\sigma}} \boldsymbol{D}^t \boldsymbol{D} \boldsymbol{\sigma}_1 \\ \lambda'_{\boldsymbol{\sigma}}(\boldsymbol{\sigma}_1 - m_1) \\ \vdots \\ \lambda'_{\boldsymbol{\sigma}}(\boldsymbol{\sigma}_N - m_N) \end{bmatrix}, \tag{4.12}$$

and,

$$\nabla_{\boldsymbol{m}} R(\boldsymbol{\theta}, \boldsymbol{m}) = \begin{bmatrix} -\sum_{\boldsymbol{r}} \lambda'_{\boldsymbol{\sigma}}(\boldsymbol{\sigma}_1 - m_1) \\ \vdots \\ -\sum_{\boldsymbol{r}} \lambda'_{\boldsymbol{\sigma}}(\boldsymbol{\sigma}_N - m_N) \end{bmatrix}. \tag{4.13}$$

For the optimization, `ROHSA` relies on L-BFGS-B (for Limited-memory Broyden-Fletcher-Goldfarb-Shanno with Bounds), a quasi-Newton iterative algorithm described by Zhu et al. (1997) which allows for the positivity constraints of the amplitudes to be taken into account. In this algorithm, after an initialization $\boldsymbol{\theta}_{(0)}$, the solution is approached iteratively by

$$\boldsymbol{\theta}_{(k+1)} = \boldsymbol{\theta}_{(k)} - \alpha_{(k)} \boldsymbol{H}_{(k)}^{-1} \nabla J\left(\boldsymbol{\theta}_{(k)}, \boldsymbol{m}_{(k)}\right), \tag{4.14}$$

Algorithm 1 ROHSA based on a multi-resolution process from coarse to fine grid where $\langle T_B \rangle_i$ is the averaged data at i scale.

Require: $T_B(v_z, \boldsymbol{r})$, $\boldsymbol{\theta}^{(0)}$, $\boldsymbol{m}^{(0)} = \boldsymbol{0}$, N, $\lambda_{\boldsymbol{a}}$, $\lambda_{\boldsymbol{\mu}}$, $\lambda_{\boldsymbol{\sigma}}$, $\lambda'_{\boldsymbol{\sigma}}$

1: **for** $i = 1$ to I **do**

2: $\left[\boldsymbol{\theta}^{(i)}, \boldsymbol{m}^{(i)}\right] \leftarrow \underset{\boldsymbol{\theta}, \boldsymbol{m}}{\text{argmin}}\ J\left(\boldsymbol{\theta}^{(i-1)}; \boldsymbol{m}^{(i-1)}, \langle T_B \rangle_i\right)$.

3: **end for**

return $\boldsymbol{\theta}^{(I)}$, $\boldsymbol{m}^{(I)}$

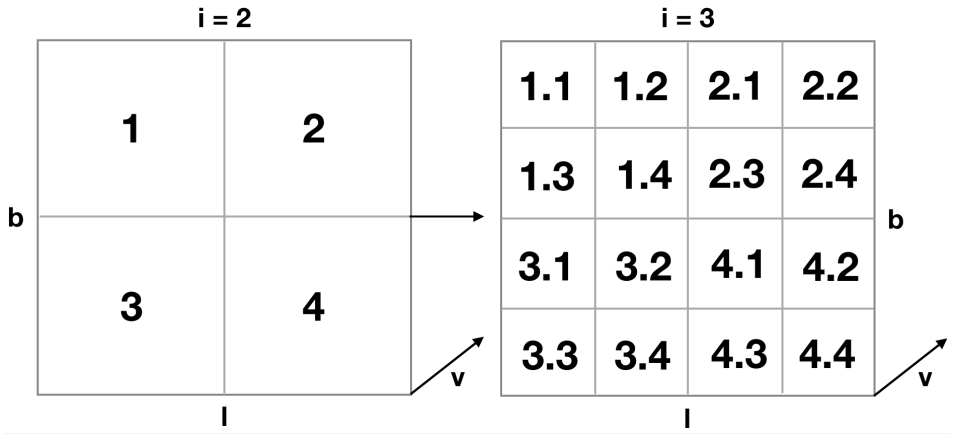

Fig. 4.1.: Graphic visualization of neighborhoods $\mathcal{V}_2$ and $\mathcal{V}_3$ used to obtain the spatially averaged data versions $\langle T_B \rangle_2$ and $\langle T_B \rangle_3$.

where $\boldsymbol{H}^{-1} \nabla J\left(\boldsymbol{\theta}, \boldsymbol{m}\right)$ is approximated with the L-BFGS formula. The iterations are repeated until one of the two following criteria is met : (1) the total number of evaluations of $J(\boldsymbol{\theta}, \boldsymbol{m})$ and $\nabla J(\boldsymbol{\theta}, \boldsymbol{m})$ exceeds a maximum number of iterations defined by the user; (2) the projected gradient is sufficiently small (i.e., |proj $\nabla J(\boldsymbol{\theta}, \boldsymbol{m})$| / (1+|$J(\boldsymbol{\theta}, \boldsymbol{m})$|) < 10^{-10}).

Due to its nonlinearity, the least-square criterion $J(\boldsymbol{\theta}, \boldsymbol{m})$ described in Eq. (4.8) is likely to include local minimizers. Therefore, the L-BFGS-B algorithm used by ROHSA is also likely to converge toward one of these local minima, making the solution highly dependent on the initialization $\boldsymbol{\theta}^{(I)}_{(0)}$. In order to overcome this difficulty, we based the design of ROHSA on an iterative multi-resolution process from coarse to fine grid (described in the following section) to automatically choose $\boldsymbol{\theta}^{(I)}_{(0)}$ and to converge towards a satisfactory local minimum.

ROHSA algorithm ROHSA is based on an iterative algorithm using a multi-resolution process from coarse to fine grid presented in Algorithm 1. The number of iterations I depends on the size of the fine grid S and is defined by the relation $2^I = S$. For example, a grid of size $S^2 = 256^2$ requires $I = 8$ iterations. Each iteration is made of three steps.

1. Data are averaged at scale i as

$$\langle T_B \rangle_i = \frac{1}{K_i} \sum_{k \in \mathcal{V}_i} T_B(v_z, \boldsymbol{r}_k), \tag{4.15}$$

where $\mathcal{V}_i$ defines the neighborhood at scale i, as described in Fig. 4.1, and K_i is the number of positions in that neighborhood. For $i = 1$, all the spatial information is compressed into a single spectrum: $\langle T_B \rangle_1 = \langle T_B(v_z, \boldsymbol{r}) \rangle$.

2. The parameters $\boldsymbol{\theta}^{(i)}$ and $\boldsymbol{m}^{(i)}$ are estimated on that spatially averaged data version $\langle T_B \rangle_i$ by minimizing the cost function given in Eq. (4.8).
   The minimization (line 2 of Algorithm 1) is made using L-BFGS, described in the previous section. We note that for scale $i = 1$, there is no spatial information $\langle T_B \rangle_1$ and the result does not depend on the regularization.
3. Parameters $\boldsymbol{\theta}^{(i)}$ are spatially interpolated at nearest neighborhood to serve as initialization for the next scale $i + 1$.

The free hyper-parameters λ_a, λ_μ, λ_σ, λ'_σ remain constant during the iterations.

4.2 Evaluation on numerical simulation

To evaluate the performance of ROHSA, we applied it to synthetic 21 cm observations computed from a numerical simulation of thermally bi-stable turbulence flow. This allowed us to directly compare the solution given by ROHSA to the properties of the gas present in the simulation. That direct comparison with numerical reality is an essential test to evaluate the performances of a source-separation algorithm like ROHSA.

4.2.1 Numerical simulation

To test ROHSA we used the hydrodynamical simulation of thermally bi-stable turbulence performed by Saury et al. (2014). We used their 1024N01 simulation (1024^3 pixels and a physical size of the box of 40 pc) characterized by (1) an initial density $n_0 = 0.1\,\mathrm{cm}^{-3}$, (2) a large-scale velocity $v_S = 12.5\,\mathrm{km\,s}^{-1}$ and (3) a spectral weight $\zeta = 0.2$. The initial density corresponds to the typical density of the WNM before condensation, the large-scale velocity represents the amplitude given to the field that generates large-scale turbulent motions in the box, and finally the spectral weight controls the modes of the turbulent mixing (here a majority of compressible modes). The Mach number of this simulation has been evaluated to be around $\mathcal{M} = 0.85$ for $T > 200\,\mathrm{K}$.

In order to explore the performances of ROHSA we use only a subset of this simulation. We concentrate our analysis on a region of $256 \times 256 \times 1024$ pixels with a moderate CNM fraction in order to limit the effect of HI self-absorption (see Sect. 4.2.2).

4.2.2 21cm line synthetic observations

The synthetic 21 cm observations were computed using the formalism described by Miville-Deschênes and Martin (2007).

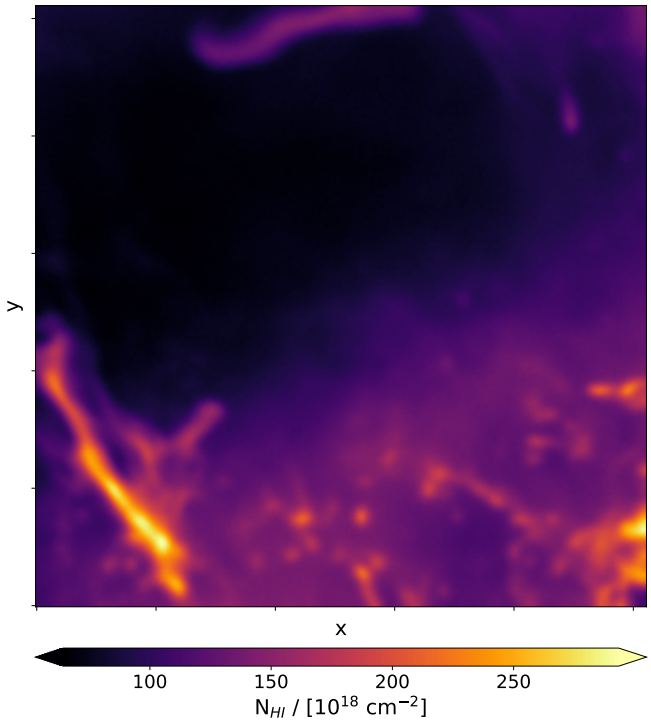

Fig. 4.2.: Integrated column density N_{HI} (optically thin approximation) of the 21 cm synthetic observation computed from the thermally bi-stable numerical simulation of Saury et al. (2014).

Distribution of velocity fluctuations In the 3D spatial space, the neutral hydrogen can be described by three 3D fields: the temperature $T(\mathbf{x})$, the density $\rho(\mathbf{x})$, and the z-component of the turbulent velocity field $v_z(\mathbf{x})$. Here the 3D spatial positions are denoted by the vector $\mathbf{x}$ while the 2D vector expressing the line-of-sight is denoted by $\boldsymbol{r}$. The z-axis is taken along the line of sight.

Information about the velocity field is inevitably lost because of the projection along the z-axis. This makes this description of HI a nonexhaustive one. For each position $\mathbf{x}$, we assume that the velocity dispersion of a given cell is dominated by thermal motions. This is a fair approximation as the turbulent velocity dispersion at the cell size (0.04 pc) is $\sigma_{\rm turb} \sim 0.3\,{\rm km\,s^{-1}}$, which is smaller than the thermal broadening everywhere in the simulation: the smallest thermal broadening for the coldest gas found in the simulation ($T = 20\,{\rm K}$) is $\sigma_{\rm therm} = 0.4\,{\rm km.s^{-1}}$. The distribution function of the z-component of the velocity $v_z(\mathbf{x})$ of a given cell is then given by $\phi_{v_z}(\mathbf{x})$, a Maxwellian shifted by $v_z(\mathbf{x})$,

$$\phi_{\nu_z}(\mathbf{x})dv'_z = \frac{1}{\sqrt{2\pi}\Delta(\mathbf{x})} \times \exp\left(-\frac{(v'_z - v_z(\mathbf{x}))^2}{2\Delta^2(\mathbf{x})}\right) dv'_z, \tag{4.16}$$

where $\Delta(\mathbf{x}) = \sqrt{k_B T(\mathbf{x})/m_H}$, which is the thermal broadening of the 21 cm line, m_H is the hydrogen atom mass, and k_B the Boltzmann constant.

Brightness temperature: general case The general case for the computation of the 21 cm brightness temperature $T_b(v_z, \boldsymbol{r})$ is based on the following radiative transfer equation.

$$T_b(v_z, \boldsymbol{r}) = \sum_z T(\boldsymbol{r}, z) \left[1 - e^{-\tau(v_z, \boldsymbol{r}, z)}\right] e^{-\sum_{z'<z} \tau(v_z, \boldsymbol{r}, z')}, \tag{4.17}$$

where $\tau(v_z, \boldsymbol{r}, z)$ is the optical depth of the 21 cm line defined as

$$\tau(v_z, \boldsymbol{r}, z) = \frac{1}{C} \frac{\rho(\boldsymbol{r}, z)\, \phi_{\nu_z}(\boldsymbol{r}, z)}{T(\boldsymbol{r}, z)}\, dz, \tag{4.18}$$

and C=$1.82243 \times 10^{18}\,\mathrm{cm}^{-2}\,(\mathrm{K\ km\ s}^{-1})^{-1}$. In this representation, a gas cell at position z' absorbs emission from the cell located behind it along the line of sight, i.e., at $z > z'$.

Optically thin limit In the optically thin limit, in cases where the self-absorption is negligible (i.e., $\tau(v_z, r, z) << 1$ everywhere), the 21 cm brightness temperature is proportional to the density ρ :

$$T_B^{\mathrm{thin}}(v_z, \boldsymbol{r})\, dv'_z = B(\boldsymbol{r}) \otimes \frac{1}{C} \int_0^H dz\, \rho(\boldsymbol{r}, z)\, \phi_{v_z}(\boldsymbol{r}, z)\, dv'_z, \tag{4.19}$$

where H is the depth of the cloud and $\otimes$ the spatial convolution. Here we consider the case that includes spatial smoothing by a telescope beam $B(\boldsymbol{r})$.

The integrated column density $N_{\mathrm{HI}}^{\mathrm{thin}}(\boldsymbol{r})$ and the centroid velocity $\langle v_z(\boldsymbol{r})\rangle$ of the 21 cm line can be obtained directly by integrating $T_B^{\mathrm{thin}}(v_z, \boldsymbol{r})$ along the velocity axis:

$$N_{\mathrm{HI}}^{\mathrm{thin}}(\boldsymbol{r}) = C \int_{-\infty}^{+\infty} T_B(v_z, \boldsymbol{r})\, dv_z, \tag{4.20}$$

and

$$\langle v_z(\boldsymbol{r})\rangle = \frac{\int_{-\infty}^{+\infty} v_z\, T_B(v_z, \boldsymbol{r})\, dv_z}{\int_{-\infty}^{+\infty} T_B(v_z, \boldsymbol{r}) dv_z}. \tag{4.21}$$

Synthetic observation We computed the synthetic position-position-velocity (PPV) data cube in the general case using Eq. (4.17). Each spectrum has an effective velocity resolution of 0.8 km s^{-1} and covers $-40 < v_z < 40\,\mathrm{km\,s}^{-1}$. We considered the beam $B(\boldsymbol{r})$ of the instrument by convolving the synthetic PPV cube with a Gaussian kernel characterized by standard deviations of two pixels along the spatial axis. We then added a homogeneous Gaussian noise of 0.05 K to each spectrum.

In order to mimic observation, integrated column density maps shown in the rest of the paper are computed using the optically thin limit presented in Eq. (4.20). The integrated column density map of the synthetic PPV cube is shown in Fig. 4.2.

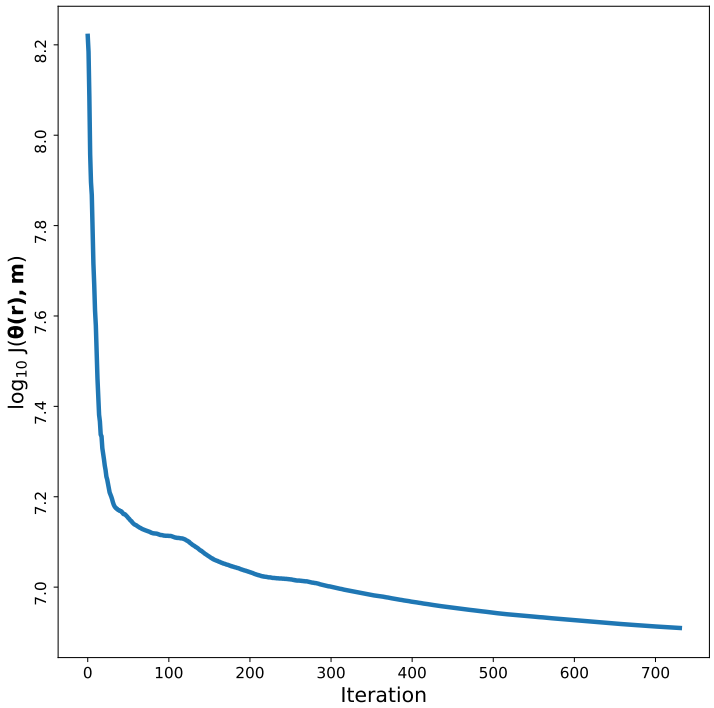

Fig. 4.3.: Evolution of the cost function $J(\boldsymbol{\theta}(\boldsymbol{r}), \boldsymbol{m})$ as a function of the number of iterations performed by ROHSA on the synthetic observation computed in Sect. 4.2.2.

4.2.3 Results

ROHSA was then applied to decompose the synthetic observation computed in Sect. 4.2.2. In this section we discuss the choice of the free parameters of ROHSA, the global properties of the Gaussian sample, and the properties of individual components identified by the decomposition. Subsequently, the mapping of a three-phase coherent model is presented with direct comparisons to the phases extracted directly from the simulation.

Choosing the free parameters of ROHSA ROHSA has six free parameters : the number of Gaussian components N, four hyper-parameters λ_i and, the maximum number of iterations of the LBFGS algorithm.

The most important parameter is N. This has to be sufficiently high to ensure a complete encoding of the signal, that is, to ensure that the residual is dominated by noise. As we discuss in Sect. 4.2.3, a given number of Gaussian components does not imply that all components are used to describe the signal along every line of sight. Components are allowed to have an amplitude of zero at any position. This is especially relevant for components encoding cold features. Since the CNM clouds occupy a small fraction of the total volume (see also Sect. 4.2.3), we expect the associated amplitude fields to have a large fraction close to zero. This is ensured by the energy term $\|\boldsymbol{\sigma}_n - m_n\|_2^2$ which minimizes the variance of the dispersion velocity of each component. Amplitudes are brought to zero if there is no need for a Gaussian to describe the signal at some location, instead of encoding another phase like the WNM for example. Avoiding phase mixing allows for overfitting to be prevented.

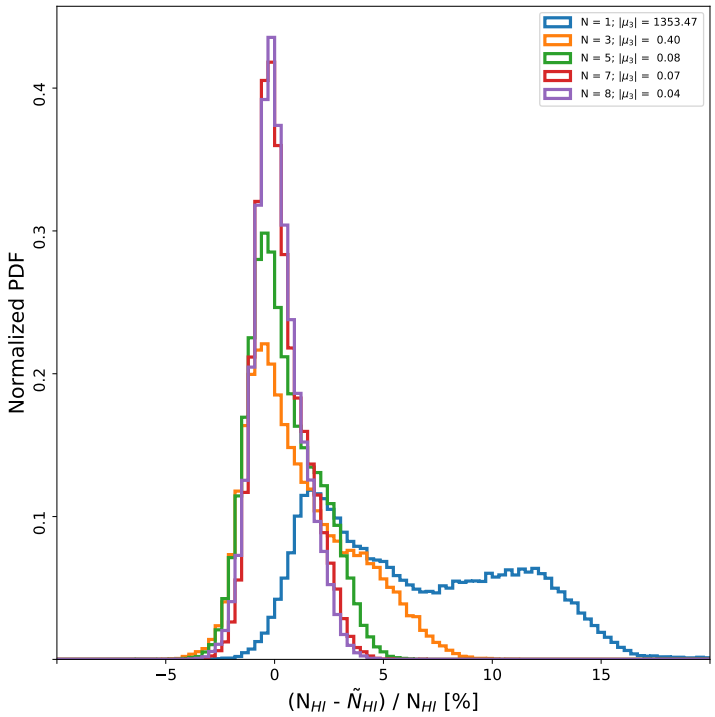

Fig. 4.4.: Normalized probability distribution function of the relative difference (N_{HI} - $\tilde{N}_{HI}$) / N_{HI} between the solution $\tilde{N}_{HI}$ inferred with ROHSA and the data N_{HI} for different numbers of Gaussian components $N = [1, 3, 5, 7, 8]$. The norm of the skewness $|\mu_3|$ is shown in the legend to quantify the quality of the encoding.

As with N, different values of the hyper-parameters $\lambda_{\boldsymbol{a}}$, $\lambda_{\boldsymbol{\mu}}$, $\lambda_{\boldsymbol{\sigma}}$, $\lambda'_{\boldsymbol{\sigma}}$ can be tested to obtain a satisfactory solution. If the hyper-parameters are null (i.e., no regularization) the signal could be fully encoded, but no spatial coherence will appear in the solution $\boldsymbol{\theta}^{(I)}$. On the other hand, if the hyper-parameters are too high, the solution will tend towards a solution that could be too spatially coherent, or even flat, wiping out small-scale fluctuations and providing a bad fit to the data. A spatially coherent solution that describes the data well with the smallest value of N is a good criterion to select the values of the hyper-parameters.

The last criterion set by the user is the maximum number of iterations of the LBFGS algorithm computing Eq. (4.14); see section 4.1.4. That parameter must be large enough to ensure the convergence of the solution. The convergence of ROHSA from a numerical perspective is presented in Fig. 4.3, which shows the evolution of the cost function $J(\boldsymbol{\theta}(\boldsymbol{r}), \boldsymbol{m})$ for 730 iterations.

The decomposition of the synthetic observations presented in this section converges to a satisfactory solution with $N = 8$, $\lambda_{\boldsymbol{a}}$ = 10000, $\lambda_{\boldsymbol{\mu}}$ = 10000, $\lambda_{\boldsymbol{\sigma}}$ = 10000, and $\lambda'_{\boldsymbol{\sigma}}$ = 1000. As previously recommended, these values are empirically found to converge towards a noise-dominated residual and a signal that is encoded with a minimum number of Gaussian components. To illustrate this, Fig. 4.4 shows the normalized probability distribution function of the relative difference (NHI - $\tilde{N}HI$) / NHI between the solution $\tilde{N}HI$ inferred with ROHSA and the data N_{HI} for different values of N.

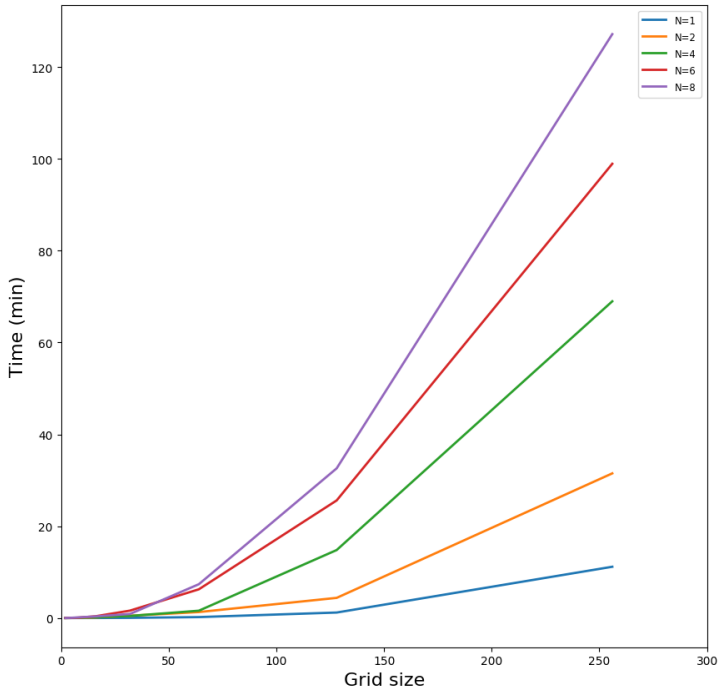

Fig. 4.5.: Computation time used by one CPU to perform the Gaussian decomposition of the simulated PPV cube used in Sect. 4.2, for N=1,2,4,6, and 8, as function of the size grid. The maximum number of iterations in each case has been set to 800.

As an a posterior assessment, the skewness μ_3 of the residual is shown to quantify the quality of the encoding. As the emission is only positive and noise has a symmetric distribution centered on zero, the skewness of the residual can be used as a way to evaluate if the emission is well estimated or if the algorithm has over-fitted the data and included some noise in the solution. A positive skewness is usually an indication that some emission is left in the residual. If the model has not enough freedom to encode the emission fully; more components are needed or the regularization terms should be lowered. On the other hand, a negative skewness indicates that the decomposition is over-fitting the data; positive noise fluctuations are included in the model leaving more negative noise fluctuations than positive ones in the residual. This is usually an indication that the regularization coefficients (λ_i) should be larger to increase the spatial smoothness of the solution. A skewness of the residual close to zero is an indication of a valid solution, one that is not distorted by the regularization and that does not overfit the signal. For the case of the synthetic observations presented here, $N = 8$ fully encodes the signal with a relatively low skewness $|\mu_3|$ = 0.04.

The computation time depends on the number of Gaussian components N, the size of the cube (number of spectra and number of velocity channels), and the maximum number of iterations used in the optimization. For each step of the multi-resolution process from coarse to fine grid, the computation time used by `ROHSA` for this particular case (purple line) is presented in Fig. 4.5 with a lower number of Gaussian components for the sake of comparison. For a given N, the computation time scales linearly with the number of spectra and the number of velocity channels. Therefore, as for each step of the multi-resolution process, from coarse to fine grid, the size of the grid is multiplied by a factor of four; the computation time also increases by a factor four at each step. We note that each step has the same maximum number of iterations (here 800) that also linearly impact the computation time.

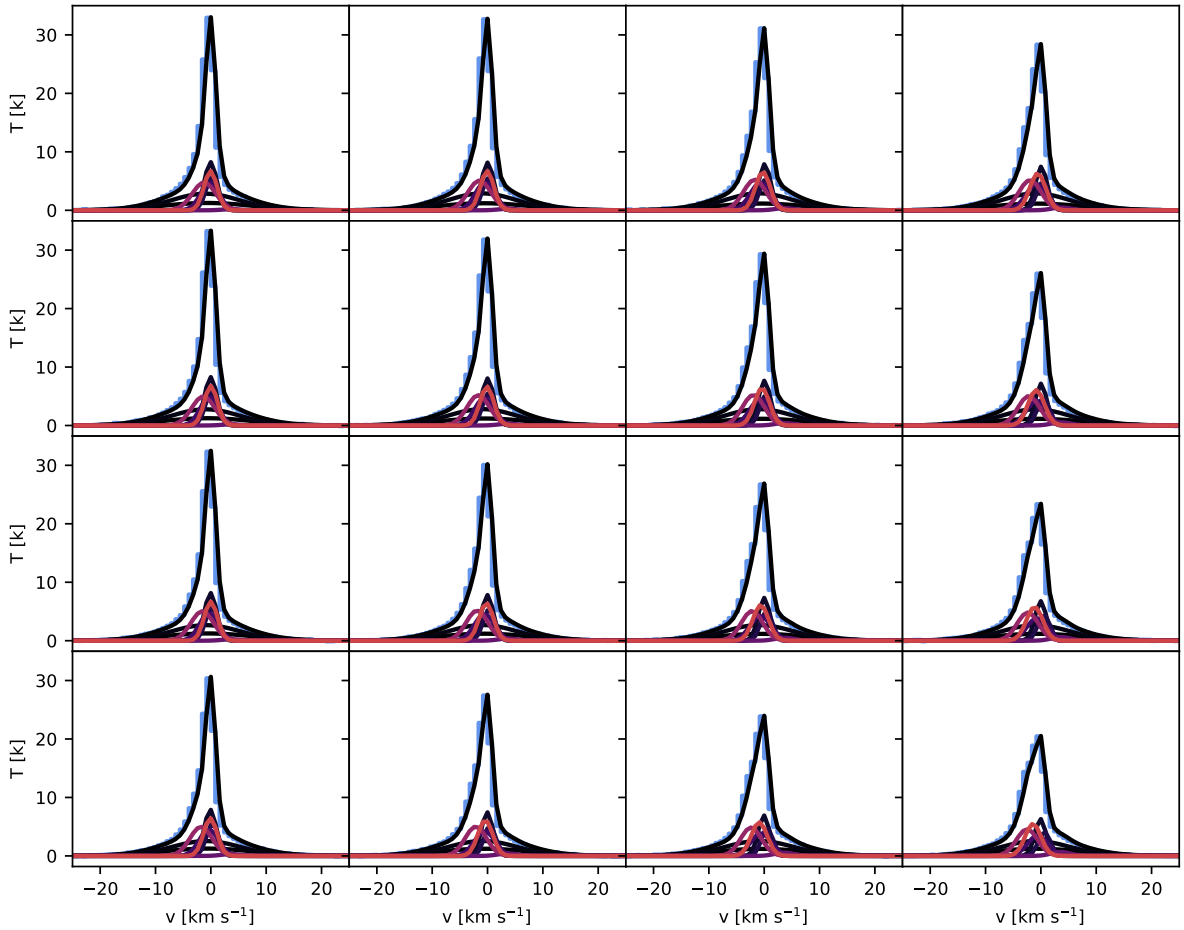

Fig. 4.6.: Example of the Gaussian decomposition obtained by ROHSA for a random 4x4 mosaic of the synthetic observation. The original signal is shown in blue and the total brightness temperature encoded by ROHSA is shown in black. The other lines show the individual Gaussian components. The spatial coherence of the solution can be seen over the mosaic with a smooth variation of the amplitude, the central velocity and the dispersion velocity of each component.

The evaluation performed here requires nearly two hours of computation time on a single CPU, which makes it difficult to explore a large range of hyper-parameters and number of Gaussian components. To overcome this difficulty, a GPU implementation of ROHSA is under development. Finally, we observed that the computation time depends nonlinearly on N, as seen in Fig. 4.5.

Global properties of the Gaussian sample ROHSA recovered the total emission of the synthetic observation with a relative variation of 0.3 %. An example of the Gaussian decomposition for a representative 4x4 mosaic of the simulation is shown Fig. 4.6. The spatial coherence of the solution can be seen over the mosaic with a smooth variation of the amplitude, the central velocity, and the velocity dispersion of each Gaussian. It is already possible to distinguish in those spectra the convergence of the decomposition toward different velocity dispersions, that is, different temperatures/phases of the gas due to the energy term $\lambda'_{\boldsymbol{\sigma}} \|\boldsymbol{\sigma}_n - m_n\|_2^2$. To have a clear view of these different components, let us take a look at the probability distribution function $\boldsymbol{\sigma}$ weighted by the fraction of total emission of each Gaussian $\sqrt{2\pi}\boldsymbol{a}_n\boldsymbol{\sigma}_n / \sum_{\boldsymbol{r}} N_{HI}(\boldsymbol{r})$ presented in Fig. 4.7. This diagram shows the amount of gas in a given range of velocity dispersion (i.e., indirectly a certain range of temperature). It is clear that ROHSA, in this case,

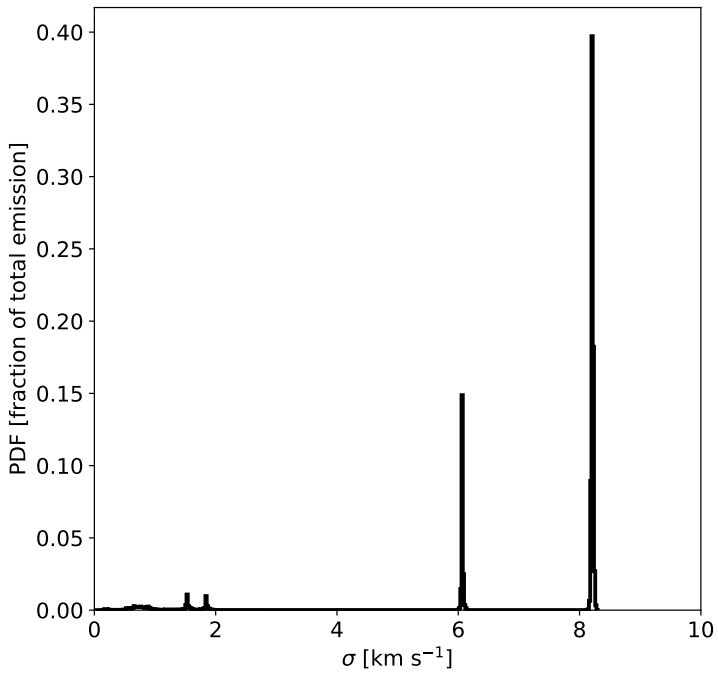

Fig. 4.7.: Probability distribution function $\boldsymbol{\sigma}$ weighted by the fraction of total emission of each Gaussian $\sqrt{2\pi}\boldsymbol{a}_n\boldsymbol{\sigma}_n / \sum_{\boldsymbol{r}} N_{HI}(\boldsymbol{r})$ of the simulated field. ROHSA converges toward three distinguishable phases associated to the WNM, LNM, and CNM.

	G_1	G_2	G_3	G_4	G_5	G_6	G_7	G_8
$\langle\boldsymbol{\mu}_n\rangle$ [km s^{-1}]	0.2	-1.7	0.5	2.3	-0.1	5.0	-3.7	-2.5
$\langle\boldsymbol{\sigma}_n\rangle$ [km s^{-1}]	8.2	6.1	0.5	0.6	1.5	1.5	1.8	0.9

Tab. 4.1.: Mean velocity $\langle\boldsymbol{\mu}_n\rangle$ and mean velocity dispersion $\langle\boldsymbol{\sigma}_n\rangle$ of the eight Gaussian components G_n inferred by ROHSA on the 21 cm synthetic observation of the numerical simulation described in Sect. 4.2.2.

converges toward a three-phase model with typical velocity dispersion close to the expected values in the CNM ($\sigma < 2\,\mathrm{km\,s^{-1}}$), LNM ($\sigma \sim 6\,\mathrm{km\,s^{-1}}$), and WNM ($\sigma \sim 8\,\mathrm{km\,s^{-1}}$). We see that a similar behavior is also present in the application to an observation of high Galactic latitude presented in Sect. 4.3. We note also that since eight Gaussian components have been used by ROHSA, some phases are encoded by several components. Association of the different components to characterize a three-phase model is presented in Sect. 4.2.3.

Properties of individual components Integrated column density maps of each component obtained with ROHSA for $N = 8$ Gaussian are presented in Fig. 4.8. For each component G_n, the mean velocity $\langle\boldsymbol{\mu}_n\rangle$ and mean velocity dispersion $\langle\boldsymbol{\sigma}_n\rangle$ averaged over the field are presented in Table 4.1. The surface filling factor appears to vary considerably between the eight components. The components with low values of $\langle\boldsymbol{\sigma}_n\rangle$ are sparsely present, while the component with the largest velocity dispersion is present everywhere on the field.

We recall that the numerical simulations used here were designed to reproduce the WNM-CNM condensation process of the HI through the thermal instability. The factor 100 difference in density between the two phases, and the fact that the mass fraction in each one is about 50%, implies that the

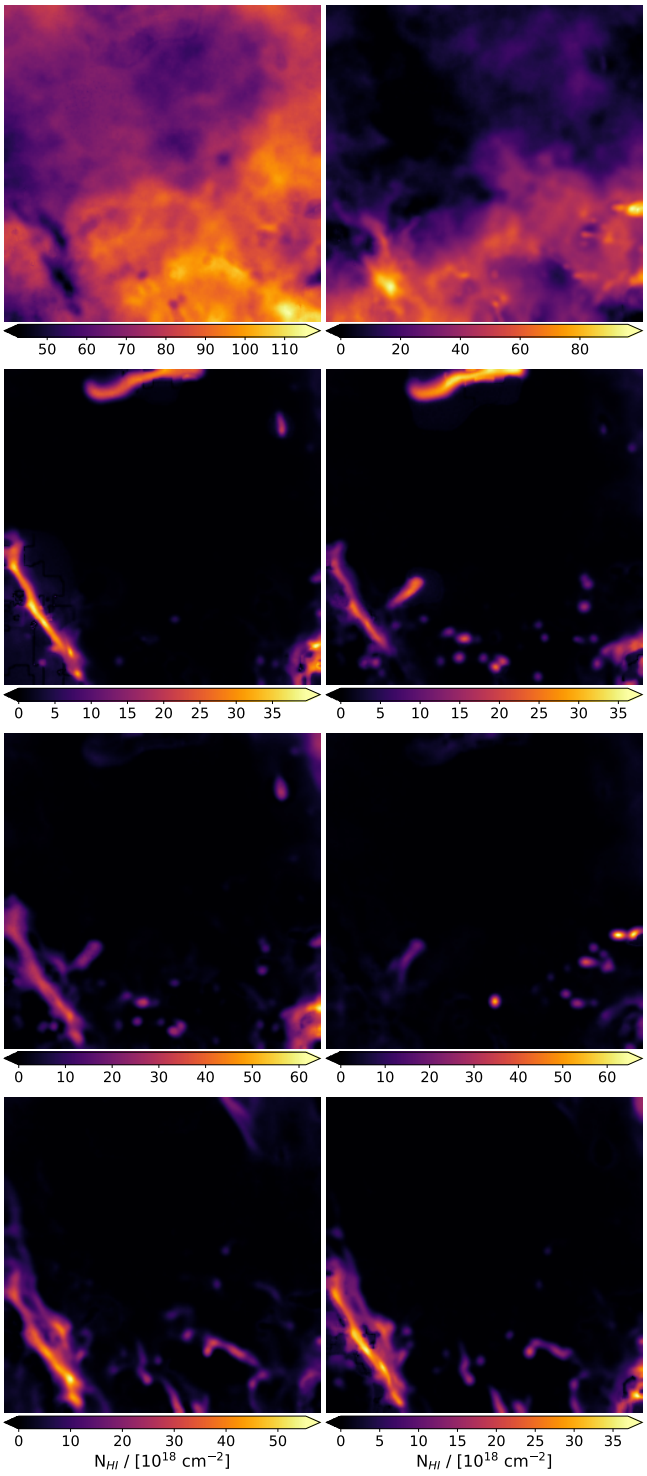

Fig. 4.8.: Integrated column density maps (left : G_1, G_3, G_5, G_7); right : G_2, G_4, G_6, G_8) obtained by ROHSA on the synthetic observation computed in Sect. 4.2.2. Mean velocity $\langle \boldsymbol{\mu}_n \rangle$ and mean velocity dispersion $\langle \boldsymbol{\sigma}_n \rangle$ are presented in Table 4.1. The surface filling factor varies considerably between components, depending on their $\langle \boldsymbol{\sigma}_n \rangle$ value.

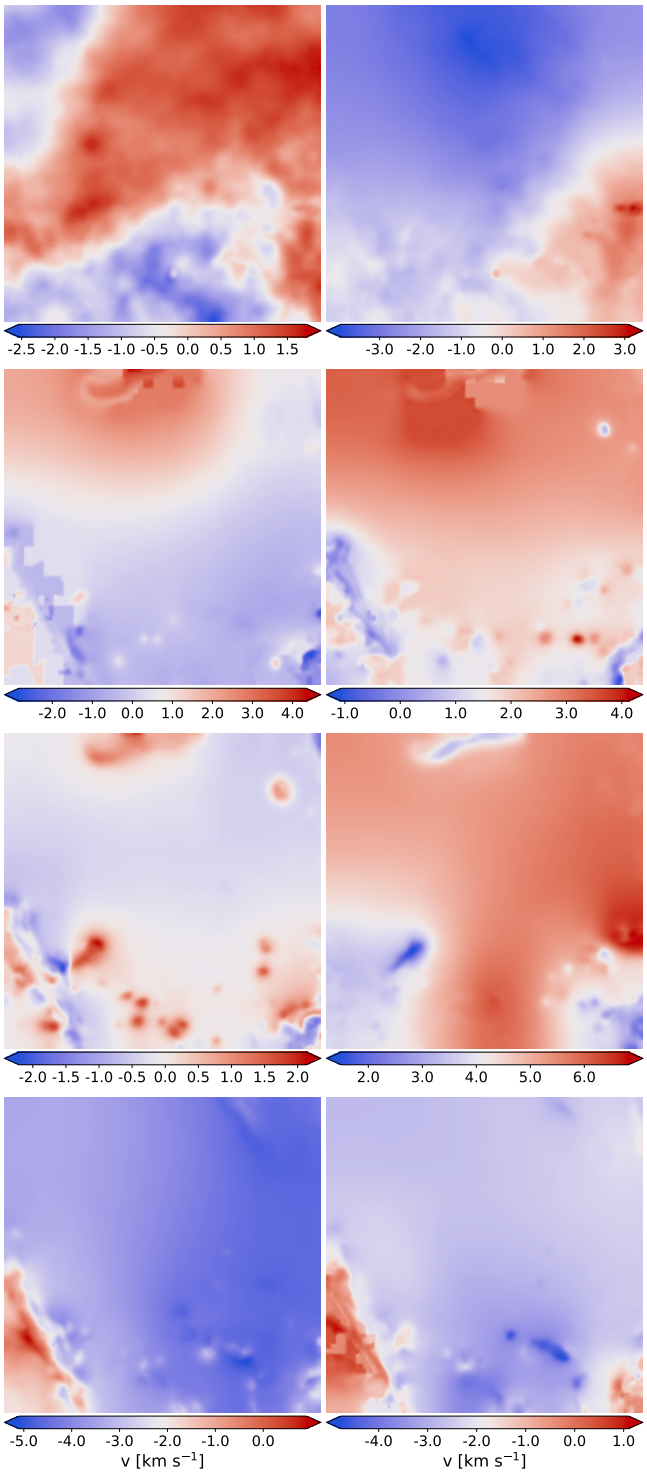

Fig. 4.9.: Centroid velocity fields $\boldsymbol{\mu}$ (left : μ_1, μ_3, μ_5, μ_7); right : μ_2, μ_4, μ_6, μ_8) obtained by ROHSA using the synthetic observation computed in Sect. 4.2.2.

cold phase fills only a few percent of the volume (Saury et al., 2014). This translates directly in the

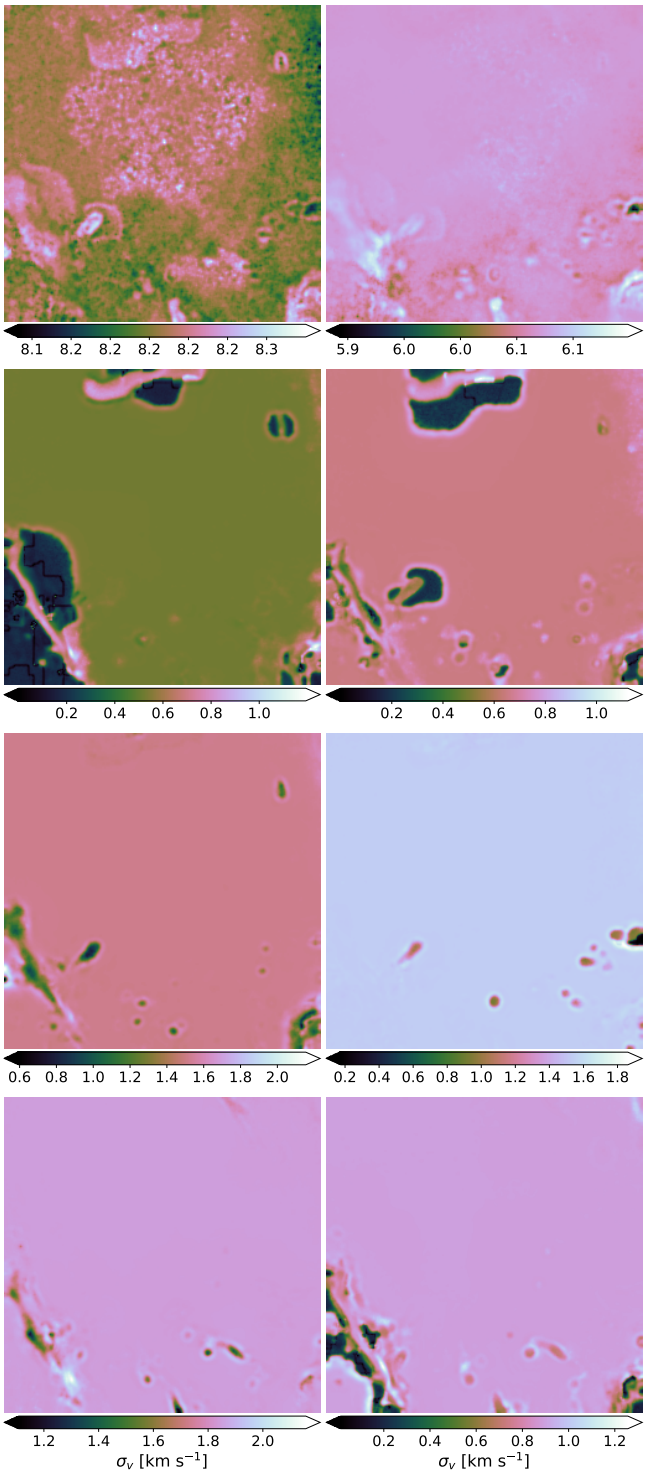

Fig. 4.10.: Dispersion velocity fields $\boldsymbol{\sigma}$ (left : σ_1, σ_3, σ_5, σ_7); right : σ_2, σ_4, σ_6, σ_8) obtained by ROHSA using the synthetic observation computed in Sect. 4.2.2.

column density maps recovered by ROHSA; the narrow components, corresponding to colder structures, fill only a fraction of the projected field of view, while the larger component is present everywhere.

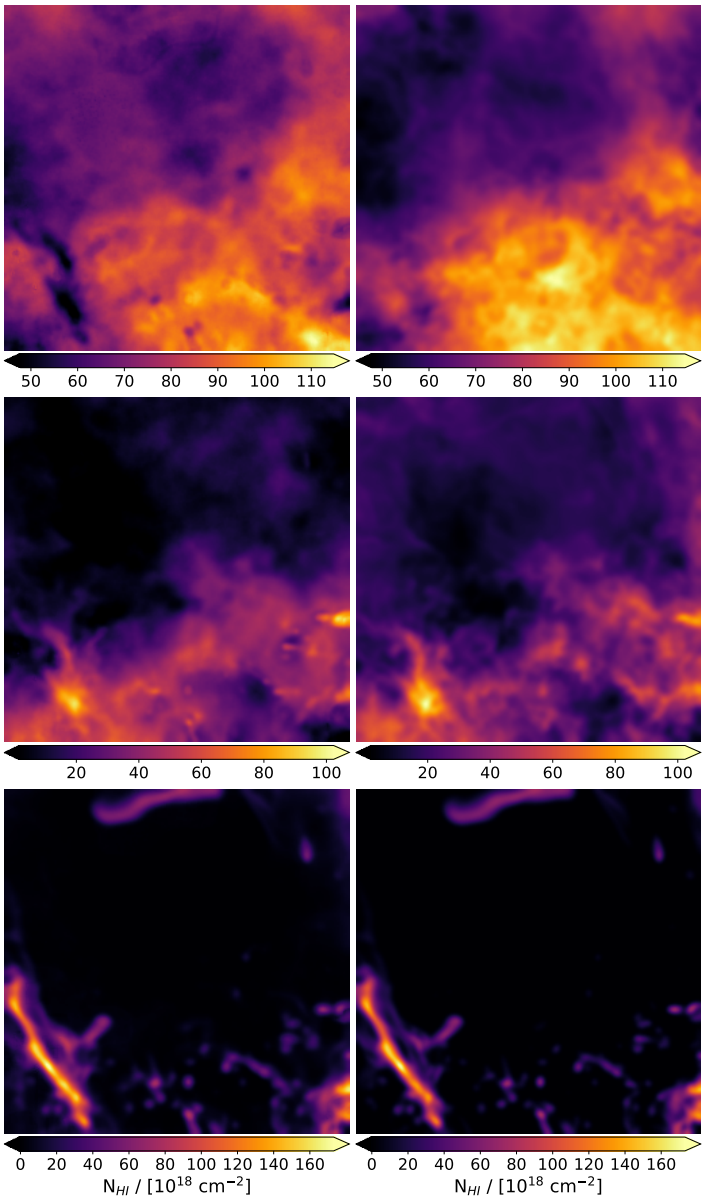

Fig. 4.11.: Left: Integrated column density maps of the three-phase model extracted by ROHSA. Right: Integrated column density maps of the three-phase model inferred directly from the simulation using the canonical values $T_{k\,\mathrm{lim,CNM/LNM}}$ = 500 and $T_{k\,\mathrm{lim,LNM/WNM}}$ = 5000 K. The phases WNM, LNM, and CNM are presented from top to bottom.

The eight velocity fields and velocity dispersion fields are presented in Figs. 4.9 and 4.10, respectively. At some location of the fields, when there is no need for a Gaussian to describe the signal over several pixels, the amplitude goes to zero. The corresponding velocity and velocity dispersion fields then have no reason to fluctuate. It turns out that where a_n goes to zero, $\boldsymbol{\mu}_n$ and $\boldsymbol{\sigma}_n$ are flat. This explains the apparent variation of spatial resolution as seen for example in Fig. 4.9 (bottom right). We notice that the first component G_1 (top left) and the second component G_2 (top right), encoding the WNM and the LNM, respectively, are defined everywhere, meaning that $\boldsymbol{\mu}_1$ and $\boldsymbol{\sigma}_1$ also have fluctuations everywhere. The implications of this are discussed in Sect. 4.4.

Mapping the three-phase neutral ISM In order to compare the result of the decomposition with the reality given by the numerical simulations, we grouped the eight components into three fields corresponding to the WNM, the LNM, and the CNM. The comparison with the numerical simulations requires that we identify ranges in temperature that demarcate these three phases. As with most numerical simulations that include the classical heating and cooling processes of the ISM (Wolfire et al., 1995a), the simulation of Saury et al. (2014) we use here shows a continuum of temperature, with no clear separation and with a significant fraction of the gas present at temperatures corresponding to the thermally unstable regime (see their Figs. 14 and 15). To facilitate the comparison with previous studies, we decided to use the canonical values $T_{k\,\mathrm{lim,CNM/LNM}} = 500\,\mathrm{K}$ and $T_{k\,\mathrm{lim,LNM/WNM}} = 5000\,\mathrm{K}$ (Heiles and Troland, 2003a) to separate the simulation in three components. The integrated column density maps associated to each phase are computed following the methodology described in Sect. 4.2.2.

The comparison between the integrated column density maps recovered with ROHSA and those inferred directly from the simulation is presented Fig. 4.11. The intensity and the morphology of each phase is well recovered. It is nevertheless possible to see some leakages between the phases, in particular between WNM and LNM. This is due partly to the poorly defined temperature thresholds used to separate the phases. It is also due to small confusions during the Gaussian decomposition where the intensity, the dispersion velocity, and velocity centroid of each component in the PPV space are close to each other. In other words, for similar central velocities, the scales of fluctuations on the velocity axis characterizing each component are too close to one another (see Figs. 4.6 and 4.7). One way to evaluate the quality of the reconstruction is to compare the statistical properties of the cloud and inter-cloud components. Three different fields are used: the integrated column density field of the cloud medium (CNM), the integrated column density field of the inter-cloud medium (LNM+WNM), and, because it is fully sampled in the plan-of-sky, the centroid velocity field of the inter-cloud medium. Figure 4.12 presents the integrated column density field and the centroid velocity field, computed using Eq. (4.21), of the inter-cloud medium obtained combining the LNM and the WNM inferred with ROHSA and those obtained directly from the simulation.

In order to compare the estimates from ROHSA to the ones obtained from the simulation, we compute the spatial power spectrum (SPS) of each image. The SPSs of the integrated column density of the cloud and inter-cloud medium are presented Fig. 4.13 and the SPS of the centroid velocity field of the inter-cloud medium is presented in Fig. 4.14. In each case, the statistics recovered by ROHSA are consistent with the numerical simulation over all scales. The shape of these power spectra is interesting in itself; the inter-cloud medium is featureless with an almost constant power law, as the cloud phase is more structured, with a break at about 20 pixels, showing a typical scale linked to the condensation process. Interestingly, ROHSA is able to capture all these features very well.

4.3 Application on high-latitude HI gas

After validating the identification of the HI phases on numerical simulations, in this section we present the application of ROHSA on a 21 cm observation of a region with high Galactic latitude.

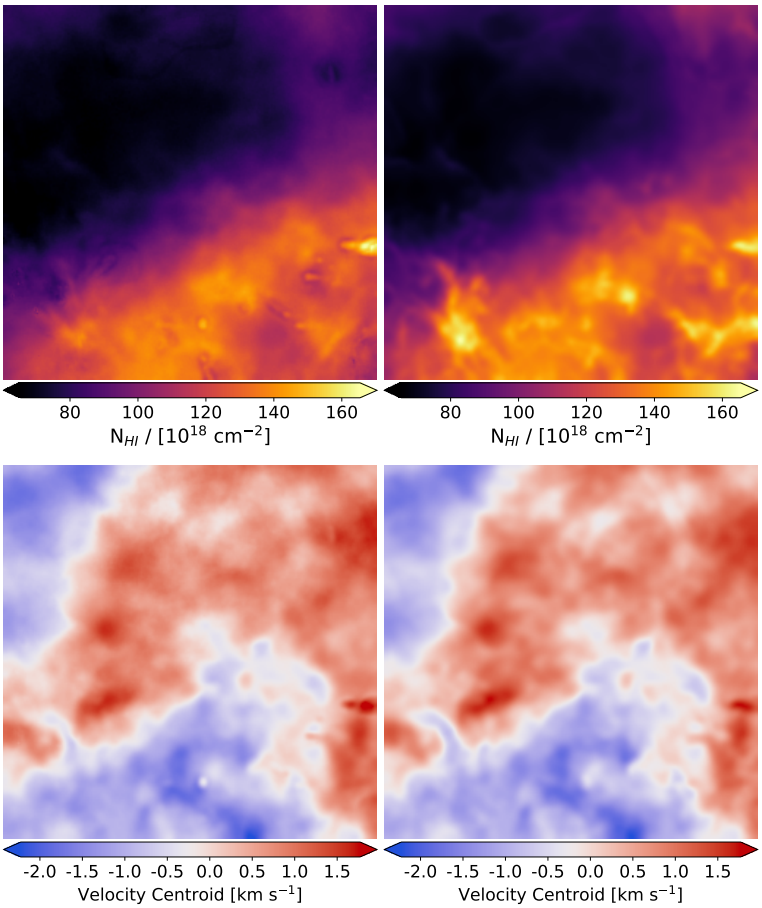

Fig. 4.12.: Synthetic observation of the integrated column density field (top) and the centroid velocity field (bottom) associated to the inter-cloud medium (WNM+LNM). Left: Inferred with ROHSA; Right: inferred directly from the simulation using all cells with $T_{klim,LNM/WNM}$ > 500 K. For statistical comparison, the spatial power spectra of each one are shown in Figs. 4.13 and 4.14.

4.3.1 North ecliptic pole

To avoid the complication of low-latitude observations, where the 21 cm emission is significantly affected by velocity crowding and self-absorption, we chose to apply ROHSA to one of the high Galactic latitude fields of the GHIGLS[1] survey (Martin et al., 2015). We chose the North ecliptic pole (NEP) field, a 12°$\times$ 12°region centered on $l = 96°.40$, $b = 30°.03$ observed with the Green Bank Telescope, providing a 9'.55 spatial resolution. The HI spectra have an effective velocity resolution of 0.807 km s^{-1} and cover -200 < v [km s^{-1}] < 50. The integrated column density map computed using Eq. (4.20) is shown in Fig. 4.15 and a mosaic of representative emission spectra is shown in Fig. 4.16.

As Fig. 4.16 shows, high-latitude spectra of HI are more complex that the synthetic observations computed from the numerical simulations of Saury et al. (2014). This is caused by a combination of the longer line of sight in the observation (about 200 pc at $b = 30°$ compared to the 40 pc box of the simulation) and to the presence of nonlocal velocity components. The 21 cm emission in NEP indeed

[1] http://www.cita.utoronto.ca/GHIGLS/

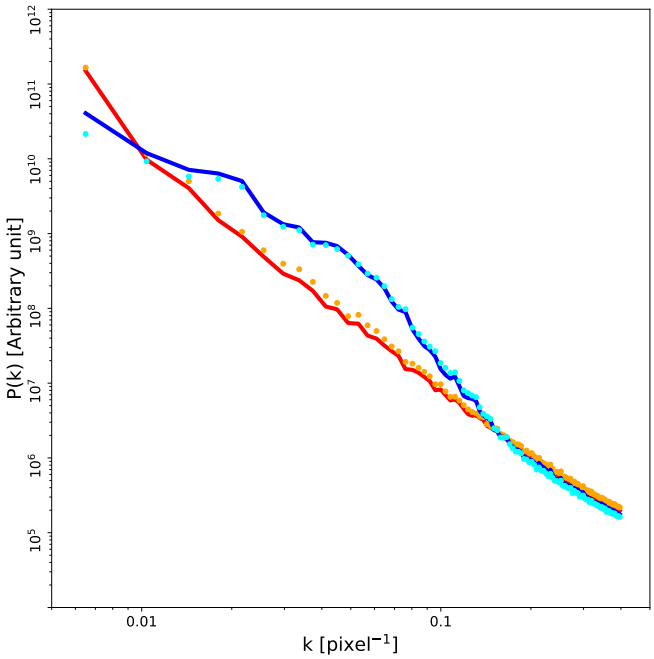

Fig. 4.13.: Spatial power spectrum of the column density. The inter-cloud medium (WNM+LNM) is represented by the orange dotted line (simulation) and the red line (ROHSA). The CNM is shown as a cyan dotted line (simulation) and blue line (ROHSA).

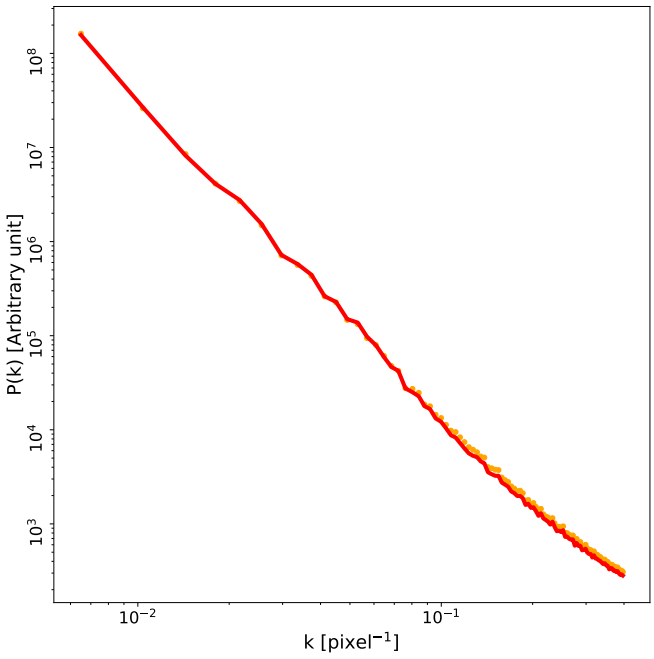

Fig. 4.14.: Spatial power spectrum of the centroid velocity field for the inter-cloud medium (WNM+LNM). The orange dotted line indicates the inter-cloud medium inferred directly from the simulation using all cells with $T_{klim,LNM/WNM}$ > 500 K (bottom-right panel of Fig. 4.12). The red line shows the inter-cloud medium inferred with ROHSA (bottom-left panel of Fig. 4.12).

exhibits significant emission in the intermediate velocity cloud (IVC) and high velocity cloud (HVC)

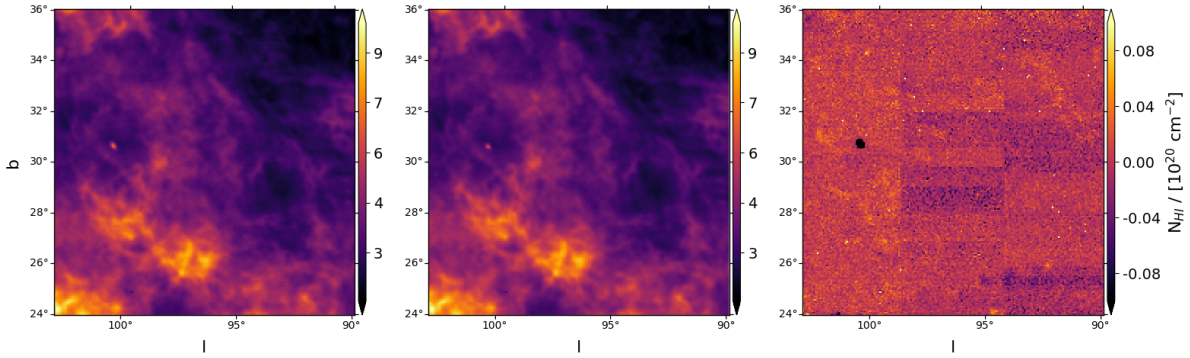

Fig. 4.15.: Left: Integrated column density $N_{\rm HI}$ of the NEP field which is part of the GHIGLS survey. $N_{\rm HI}$ was computed in the optically thin approximation (see Eq. 4.20). Middle: Integrated column density $\tilde{N}_{\rm HI}$ of NEP inferred with ROHSA. Right: Residual $\tilde{N}_{\rm HI}$-$N_{\rm HI}$ between the integrated column density field inferred with ROHSA and the original integrated column density field computed with the data.

ranges. In this paper we do not consider the velocity channels with HVC emission; we focus on the phase separation of the local velocity cloud (LVC) and IVC components.

The LVC range between $-20\,\mathrm{km\,s^{-1}}$ and $+20\,\mathrm{km\,s^{-1}}$ shows relatively smooth emission profiles, with a narrow peak around $-3\,\mathrm{km\,s^{-1}}$ on top of a broader feature (see Fig. 4.16). The latter is rather smooth but when inspected in detail it shows faint spectral structures on all scales along the velocity axis. The sensitivity of the GHIGLS data is such that these fluctuations of the emission profiles are not due to noise. In fact, they can be followed from one spectrum to the next quite easily. These fluctuations of the emission spectra at scales of a few kilometres per second reveal the presence of CNM and LNM features on a range of velocities.

This field was selected because of its representative 21 cm emission for Galactic latitudes of $b \sim 30°$. The emission features are not particularly complex, nor are they especially simple. In addition, a first Gaussian decomposition of NEP 21 cm data was performed by Martin et al. (2015) which provides an interesting point of comparison. Unlike ROHSA, Martin et al. (2015) used a method similar to the one described by Haud (2000) that considers only the term $\|L(v_z, \boldsymbol{r}, \boldsymbol{\theta}(\boldsymbol{r}))\|_2^2$ in the parameter optimization. We highlight some qualitative comparisons in the following sections.

4.3.2 Results

In order to decompose the 21 cm emission of the NEP field, we used ROHSA with $N = 12$ Gaussian components and each hyper-parameter has been set to 1000. As for the previous case, these values have been chosen empirically following the same methodology as described in Sect. 4.2.3, allowing us to converge toward a noise-dominated residual with a minimum number of Gaussian components. We note that the hyper-parameter values are not the same as for the first application presented in Sect. 4.1. The complexity of the underlying signal structure and its signal-to-noise ratio are the main causes of these differences. However, a detailed understanding of the behavior of these hyper-parameters would require testing different values over a large number of observations. Such exploration is currently complicated by computation limitations. A GPU version of the code is under development to overcome this main limitation.

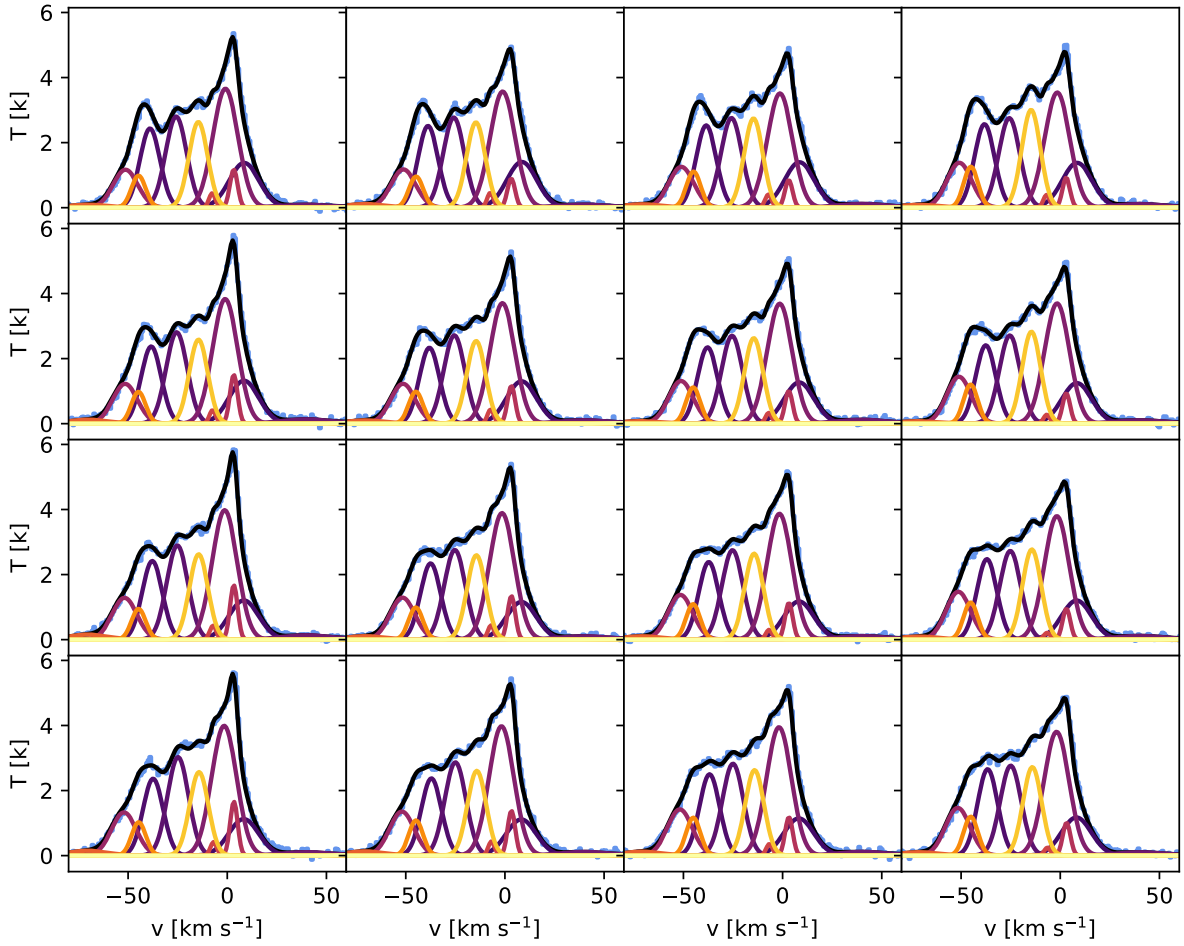

Fig. 4.16.: Example of the Gaussian decomposition obtained by ROHSA (colored line) for a random 4x4 mosaic of NEP. The original signal is shown by the blue histogram and the total brightness temperature encoded by ROHSA is shown in black. The other lines detail the components of the Gaussian model. The spatial coherence of the solution can be seen over the mosaic with a smooth variation of the amplitude, central velocity, and velocity dispersion of each Gaussian component.

The combination of 12 Gaussian components produces a solution that recovers 99% of the total emission with spatially coherent components. The total integrated column density encoded by ROHSA and the residual between our model and the data are shown in Fig. 4.15 (middle and right panels).

Global properties of the Gaussian sample Like for the application on the synthetic observations, the Gaussian parameters recovered for the NEP field have a strong spatial coherence; ROHSA converges towards a solution with smooth variations of the Gaussian parameters across the field. It turns out that ROHSA converges toward a multiphase model with Gaussian components of various widths, very similar to the application to numerical simulations presented in Sect. 4.2.3 but more complex due to the presence of an IVC component in the data.

To have a global view of the thermal state of the gas as a function of velocity, it is useful to look at the two-dimensional dispersion-velocity diagram $\boldsymbol{\sigma} - v$ weighted by the fraction of total emission of each Gaussian $\sqrt{2\pi}\boldsymbol{a}_n\boldsymbol{\sigma}_n / \sum_{\boldsymbol{r}} N_{HI}(\boldsymbol{r})$ shown in Fig. 4.17. This diagram shows isolated complexes of

	G_1	G_2	G_3	G_4	G_5	G_6	G_7	G_8	G_9	G_{10}	G_{11}	G_{12}
$\langle \boldsymbol{\mu}_n \rangle$ [km s^{-1}]	-74.1	-53.9	-44.7	-35.0	-22.9	-12.6	-4.8	-1.3	0.2	10.9	40.8	75.9
$\langle \boldsymbol{\sigma}_n \rangle$ [km s^{-1}]	9.7	6.2	3.5	5.1	5.3	4.7	1.6	6.3	1.9	7.5	12.5	9.3

Tab. 4.2.: Mean velocity $\langle \boldsymbol{\mu}_n \rangle$ and mean velocity dispersion $\langle \boldsymbol{\sigma}_n \rangle$ of the 12 Gaussian components G_n inferred by `ROHSA` in NEP.

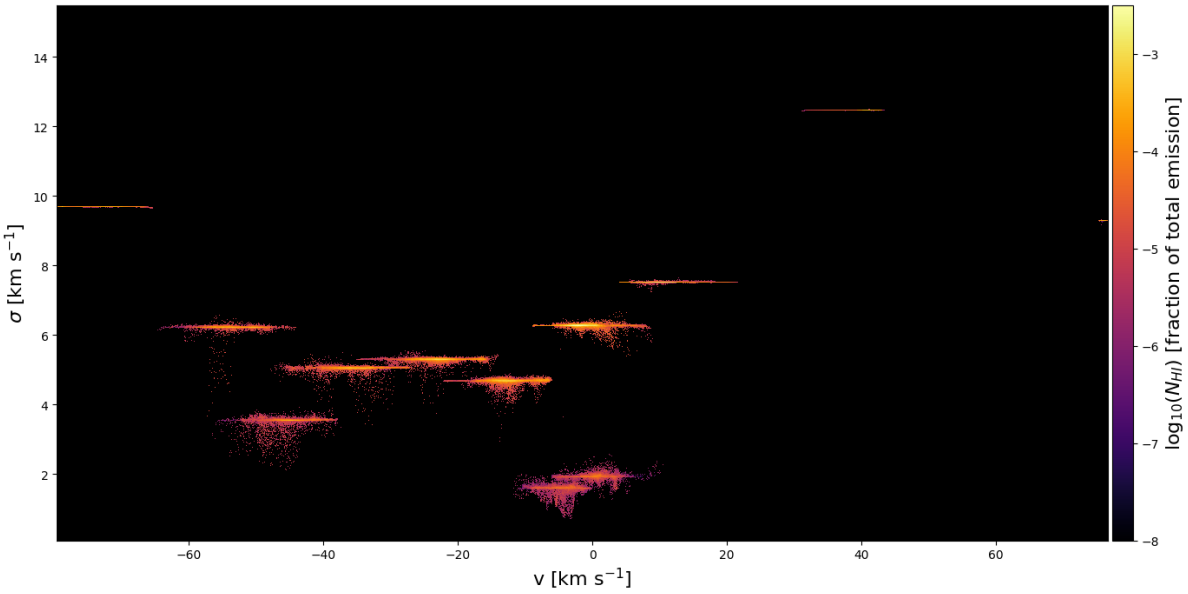

Fig. 4.17.: Two-dimensional probability distribution function σ-v weighted by the fraction of total emission of each Gaussian $\sqrt{2\pi}\boldsymbol{a}_n\boldsymbol{\sigma}_n / \sum_{\boldsymbol{r}} N_{HI}(\boldsymbol{r})$ of NEP. The NEP is mainly composed of negative intermediate velocity components.

Gaussian components in the $\boldsymbol{\sigma} - v$ space. This is a direct result of the way the parameter optimization is done in ROHSA, with a regularization term that favors the minimum variance of $\boldsymbol{\sigma}$. Figure 4.17 highlights the fact that the 21 cm emission in NEP is mainly composed of negative-velocity components. A clear trend is visible in the velocity range $-60 < v < 0\,\mathrm{km\,s^{-1}}$ with $\boldsymbol{\sigma}$ decreasing from 10 to 1 $\mathrm{km\,s^{-1}}$ going from negative to positive velocities. This likely reflects the radiative condensation of warm intermediate velocity clouds into the local velocity component of the neutral ISM.

At this point it is interesting to compare the results of ROHSA with the Gaussian decomposition of the same data performed by Martin et al. (2015). The $\boldsymbol{\sigma} - v$ diagram of Martin et al. (2015) (see their Fig. 7) shows a continuous distribution with arches that bridge together the LVC and IVC gas, an effect that is not observed in our results. Similarly to what we have done here, Martin et al. (2015) used numerical simulations to evaluate the performances of their Gaussian decomposition algorithm. Their tests revealed that such arches in the $\boldsymbol{\sigma} - v$ diagram are unphysical; they are the result of LVC and IVC gas components that overlap in velocity.

It is important to point out that both solutions provide as good a representation of the same dataset. The significant difference between the two solutions highlights the challenge of extracting a physically meaningful representation of the data. We recall that Martin et al. (2015) used an algorithm similar to the ones used by Haud (2000); Miville-Deschênes et al. (2017); Kalberla and Haud (2018) where the spatial coherence of the solution is not enforced through regularization terms in the cost function. In these previous studies spatial coherence is attempted by providing spatially coherent initial guesses. Each spectrum is then fitted independently and no spatial coherence in the solution is enforced. In practice, this method is rather effective for relatively sparse emission data like CO (Miville-Deschênes et al., 2017a), but in the case of the more confused 21 cm data it produces parameter maps that are more affected by small-scale noise due to the degeneracy of the solution.

A Gaussian decomposition algorithm that fits each spectrum individually is easily fooled by components that overlap in velocity. In this specific case, such an algorithm would find a solution with a smaller number of components but with larger values of $\boldsymbol{\sigma}$. The main innovation in ROHSA is that it is able to cluster different phases even if they are close in velocity. The four energy terms added to the cost function $J(\boldsymbol{\theta}(\boldsymbol{r}))$ allow ROHSA to find a spatially coherent solution while avoiding the mix of components due to the high confusion present in the emission.

A cloud/inter-cloud medium vision of the North ecliptic pole Integrated column density maps, centroid velocity fields, and dispersion velocity fields obtained with ROHSA are presented in Figs. 4.18, 4.19, and 4.20, respectively. Mean velocities $\langle \boldsymbol{\mu}_n \rangle$ and mean velocity dispersions $\langle \boldsymbol{\sigma}_n \rangle$ of the 12 Gaussian components G$_n$ are presented in Table 4.2. In this section we focus on building a coherent cloud/inter-cloud medium vision considering the local component of the emission identified previously. Two of the four components of the local gas, G_7 and G_9, are associated with the CNM with $\langle \boldsymbol{\sigma}_7 \rangle$ = 1.6 km s^{-1} and $\langle \boldsymbol{\sigma}_9 \rangle$ = 1.9 km s^{-1}. The other components are used to build the inter-cloud medium. Integrated column density fields and centroid velocity fields of the cloud medium and inter-cloud medium are presented in Fig. 4.21.

As noted by Martin et al. (2015) in their two-phase decomposition of the local component, filamentary structures are observed in the narrow component. The associated velocity dispersion fields (see Fig. 4.20, component G_7 and G_9) show coherent fluctuating values over a large part of the field. The core of these filamentary structures appears narrower than the envelope with velocity dispersion reaching about 0.87 km s^{-1} (the spectral resolution) in their centers.

The broader component has an integrated column density field with no particular structure like filaments (see Fig. 4.21, top-right). Like for the numerical simulation, the sum of the broad components is likely to represent a phase that fills a large fraction of the volume, as would an inter-cloud medium. One interesting aspect of the ROHSA decomposition is that it then allows to extract the velocity field of this volume-filling component (Fig. 4.21, bottom-right), enabling the characterization of the turbulent cascade in a mixture of lukewarm phase and warm phase.

4.4 Discussion

Historically, a large number of studies used a Gaussian basis to model 21 cm data. Different algorithms have been developed; all of them are fitting each spectrum individually, with or without information from the neighboring solutions to initialize the fit. To further constrain the degeneracy of the fit, solutions with the smallest number of Gaussian components have often been favored (e.g., Lindner et al., 2015). Because of velocity blending, the solution with the smallest number of components is not necessarily the best one. In some cases, narrow features overlap in velocity, making it impossible to separate them if the environment is not considered. Usually, this confusion breaks apart a few beams away and more components can be recovered. The fundamental idea behind ROHSA is that we are trying to extract diffuse components that have column density, centroid velocity, and velocity dispersion with smooth spatial variations. The optimization scheme has been designed with that concept at its core. In order to achieve this, ROHSA fits the whole data cube at once.

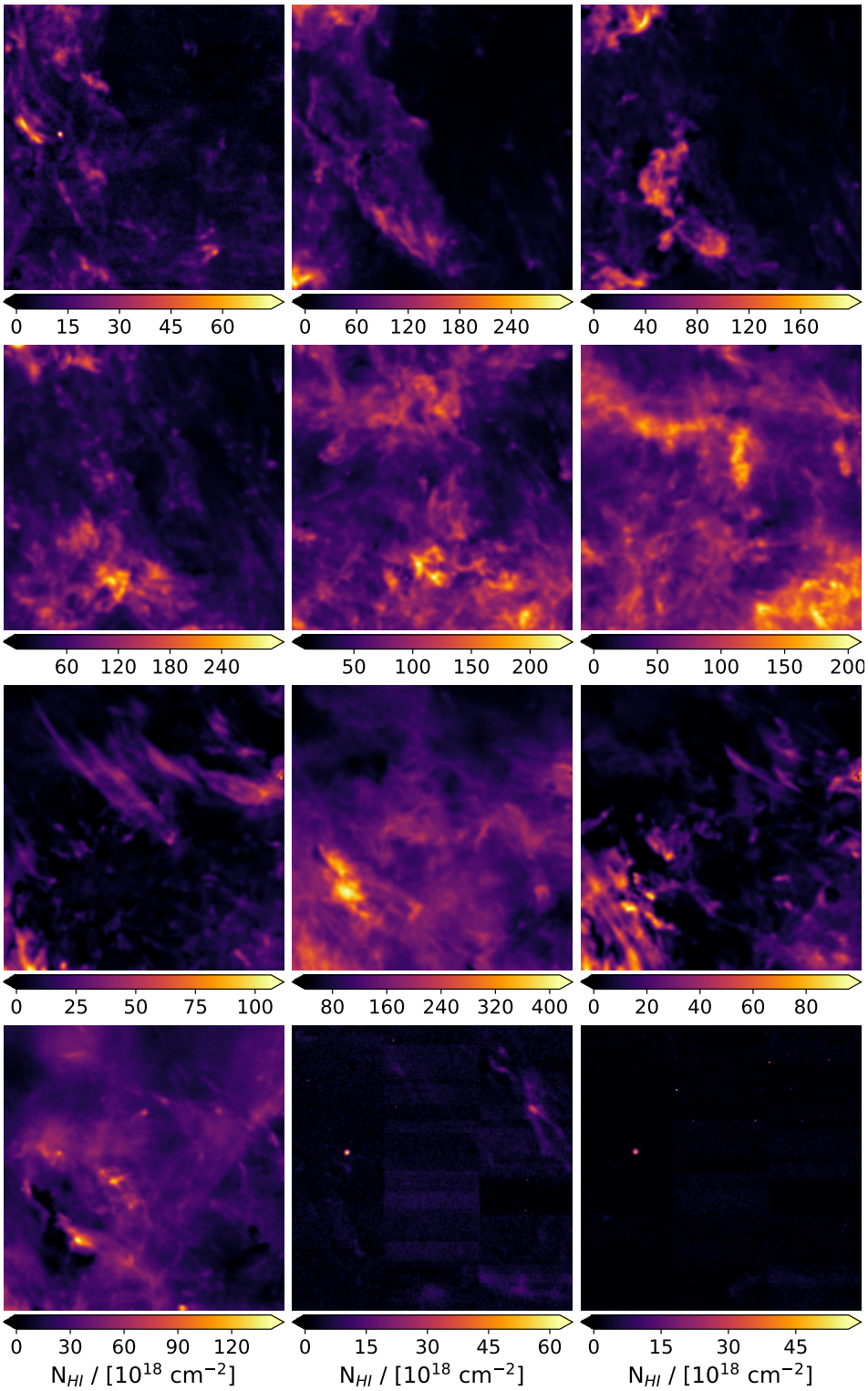

Fig. 4.18.: Integrated column density maps (left: G_1, G_4, G_7, G_{10}; middle: G_2, G_5, G_8, G_{11}; right: G_3, G_6, G_9, G_{12}) obtained by `ROHSA` applied on NEP. Mean velocity $\langle \boldsymbol{\mu}_n \rangle$ and mean velocity dispersion $\langle \boldsymbol{\sigma}_n \rangle$ are presented in Table 4.2.

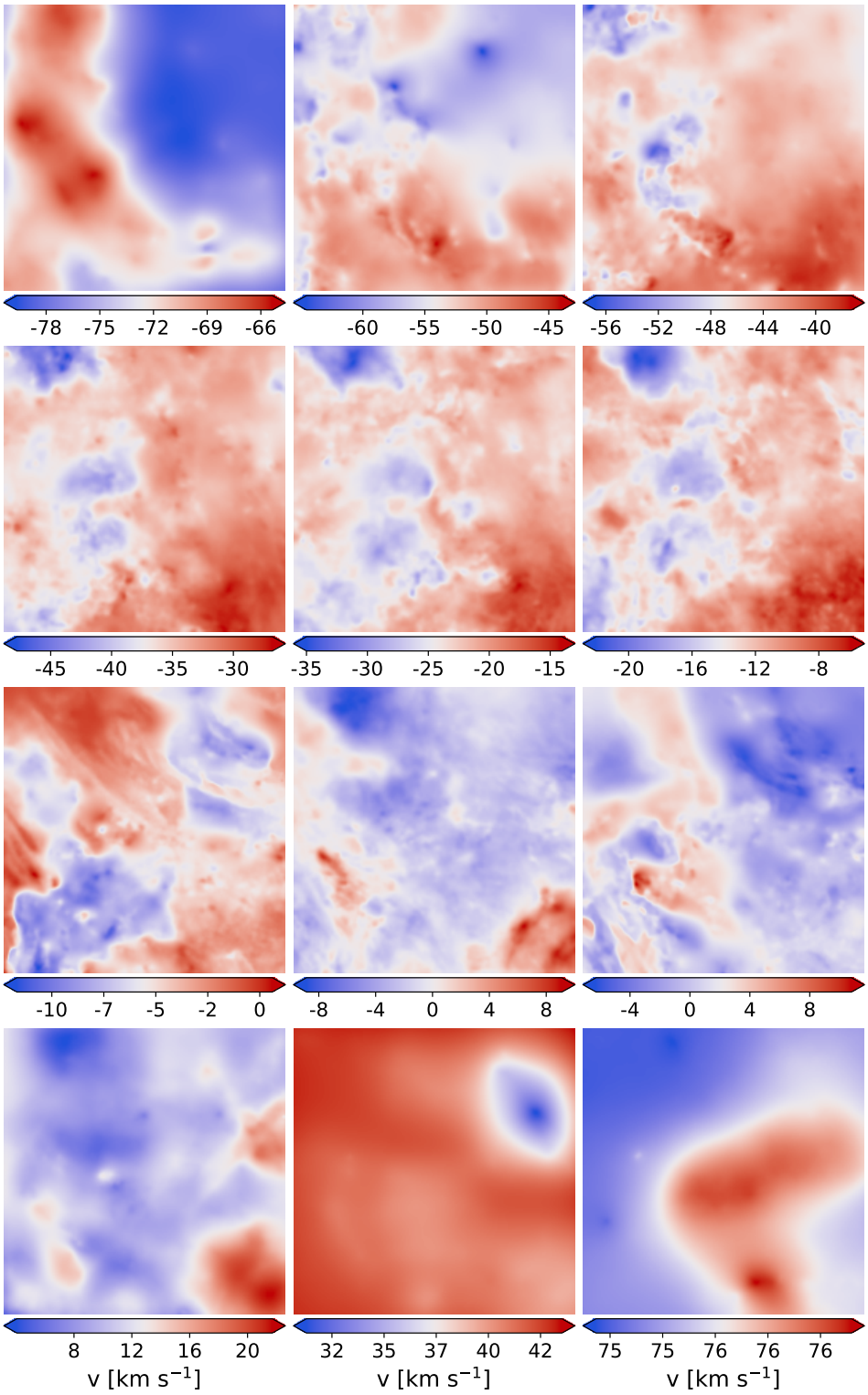

Fig. 4.19.: Centroid velocity fields $\boldsymbol{\mu}$ (left: μ_1, μ_4, μ_7, μ_{10}; middle: μ_2, μ_5, μ_8, μ_{11}; right: μ_3, μ_6, μ_9, μ_{12}) obtained by ROHSA applied on NEP.

The application of ROHSA on both synthetic observations from numerical simulations and observational data converges naturally toward a multiphase model of the neutral ISM. The ability of ROHSA to extract

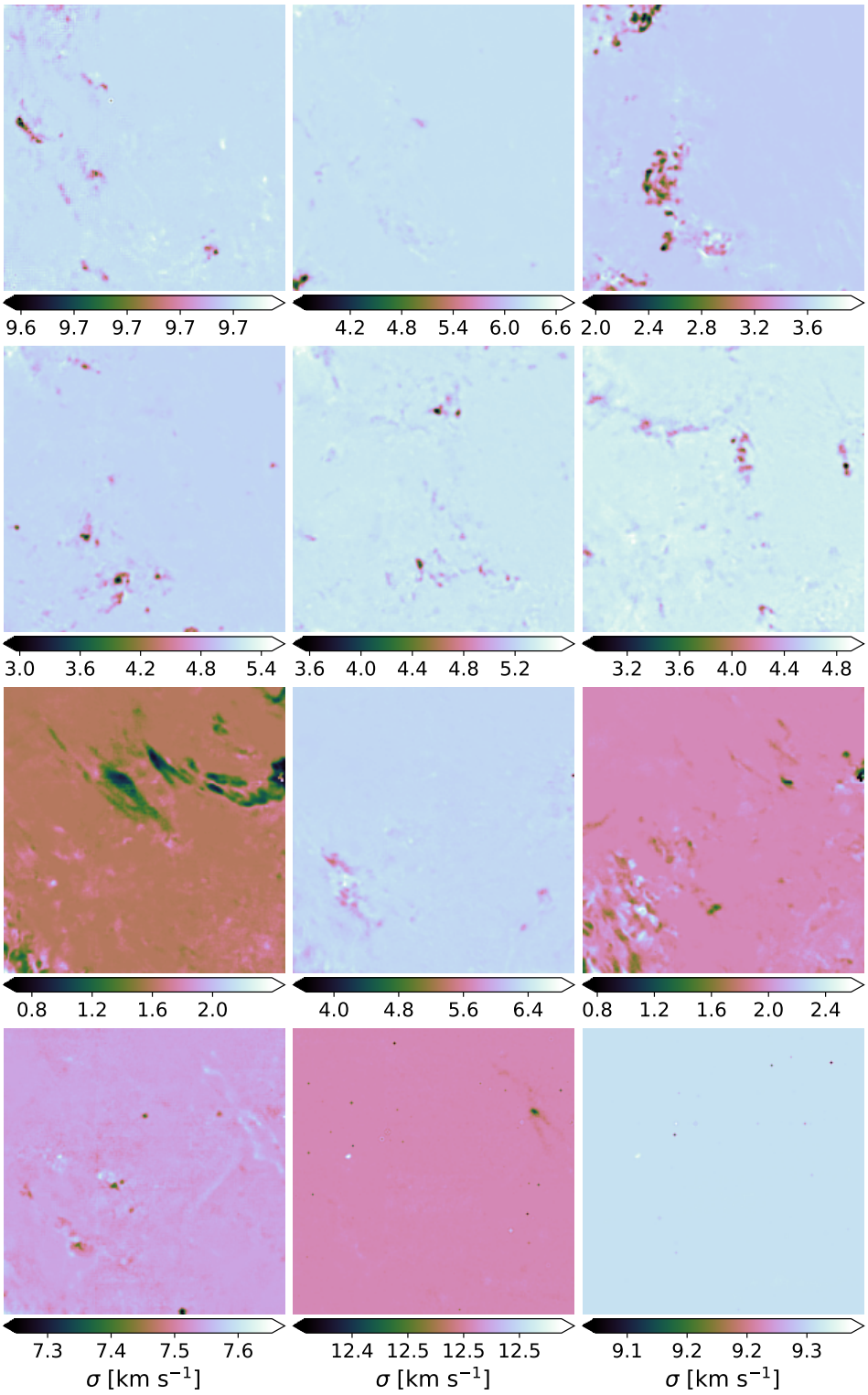

Fig. 4.20.: Velocity dispersion maps $\boldsymbol{\sigma}$ (left: σ_1, σ_4, σ_7, σ_{10}; middle: σ_2, σ_5, σ_8, σ_{11}; right: σ_3, σ_6, σ_9, σ_{12}) obtained by ROHSA applied on NEP.

the multiphase nature of the neutral ISM opens a totally new perspective on the study of the nature of the condensation process acting in the ISM. It is clear from a numerical point of view that the formation

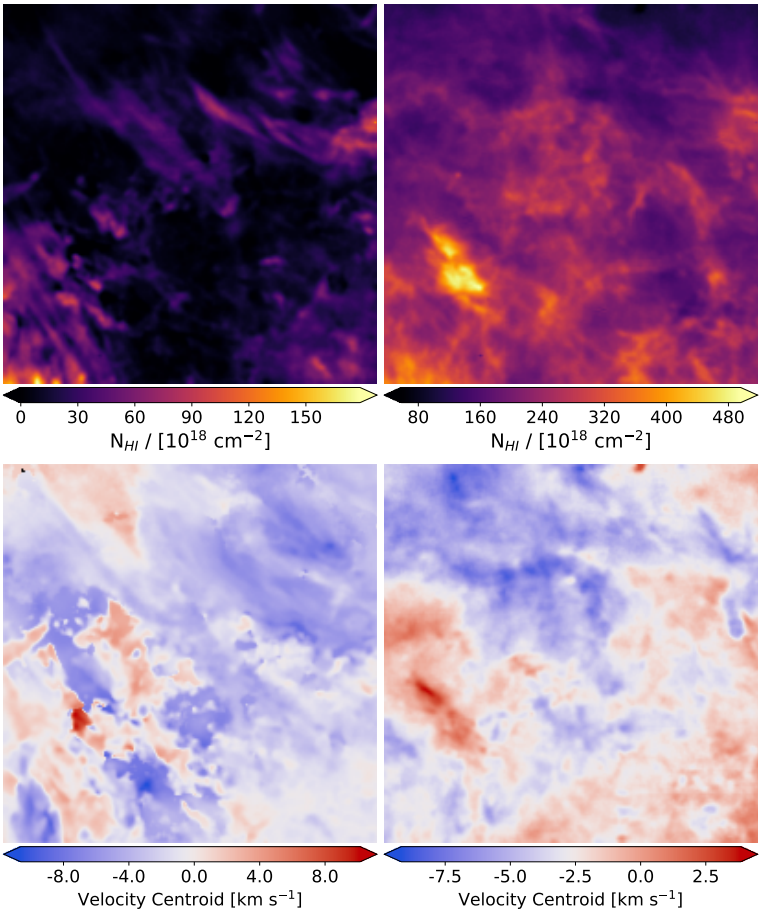

Fig. 4.21.: Left : CNM; Right : inter-cloud medium (WNM+LNM) in NEP inferred with ROHSA. The top and bottom panels show the column density and centroid velocity fields, respectively.

of cold clouds is the result of the condensation of the warm and diffuse gas through the thermal instability coupled with turbulence. From an observational point of view, spatial correlations between the different phases can now be made in order to more precisely quantify how the CNM emerges from this condensation process. This separation also opens the possibility to describe the properties of the very specific multiphase turbulence of the HI. ROHSA appears to be efficient at clustering different structures in PPV space, even when there is a high level of confusion. In particular, the separation of the LVC and IVC is known to be particularly challenging as the CNM and WNM of both components overlap significantly in velocity (Martin et al., 2015). As shown in Fig. 4.17, ROHSA significantly limits the "Arch effect" typical of this confusion (see Sect. 4.3). Globally, the performance in ROHSA on regions of high Galactic latitude opens a large range of possibilities regarding the study of infalling neutral clouds from the galactic halo.

We would also like to point out that no a priori information about the number of phases present in the neutral ISM is provided to ROHSA. The algorithm rests only on the hypothesis of the existence of components with similar line width through the energy term $\lambda'_{\boldsymbol{\sigma}} \|\boldsymbol{\sigma}_n - m_n\|_2^2$. In that respect, ROHSA is perfectly adapted to decomposing hyper-spectral observations of any type, not only 21 cm emission.

At this time the main limitations of ROHSA are computational. First, as the whole PPV cube is fitted at once, the use of ROHSA is limited to cubes that can fit in memory. Second, the current computation time of ROHSA is not negligible (e.g., about two hours on a single CPU for a $256 \times 256 \times 100$ PPV cube with 8 Gaussians). This limits the possibility to make a deep exploration of the hyper-parameters λ_i. In particular it would be interesting to explore various weights of the hyper-parameters for the deduced quantities (a, μ and σ). It is expected that the amplitude of the spatial variations of these quantities are not the same. For instance, in a multi-phase medium like the HI, the density field (represented by a) might vary more strongly on smaller scales than the velocity field. This might require different values of λ_a compared to $\lambda_{\boldsymbol{\mu}}$, $\lambda_{\boldsymbol{\sigma}}$ and $\lambda'_{\boldsymbol{\sigma}}$. A GPU version of the code is under development that would allow such an exploration.

4.5 Summary

Here we present a new Gaussian decomposition algorithm named ROHSA. Energy terms have been added to the classical cost function to take into account the spatial coherence of the emission and the multiphase nature of the gas simultaneously. In order to identify a solution with spatially smooth parameters, the fit is performed on the whole hyper-spectral cube at once.

The performance of ROHSA has been evaluated using a synthetic 21 cm observation computed from a numerical simulation of thermally bi-stable turbulence. It was then tested on a 21 cm observation of a field of high Galactic latitude observed with the GBT. The main conclusions are as follows.

1. ROHSA is able to naturally highlight the physics of any multiphase medium without a priori information regarding the number of phases.
2. Evaluation on numerical simulation of thermally bi-stable turbulence shows that the sum of Gaussian components is a good approximation to model the multiphase nature of the neutral ISM.
3. The multiphase model inferred with ROHSA provides a spatially coherent vision of the integrated column density map, the centroid velocity field, and the velocity dispersion field of each component.
4. The power spectra of the integrated column density and centroid velocity fields are well recovered with ROHSA. Statistical properties of turbulence in the multiphase neutral ISM now become accessible.
5. The decomposition of a high-latitude HI gas observation shows the wide range of applications enabled with ROHSA, for instance to study the radiative condensation of the WNM and the nature of the ISM at the disk-halo interface.

North Ecliptic Pole : A new window on the multiphase neutral ISM

5

> *He remembers those vanished years. As though looking through a dusty window pane, the past is something he could see, but not touch. And everything he sees is blurred and indistinct.*
>
> **— In the Mood for Love (2000)**
> Wong Kar-wai

Contents

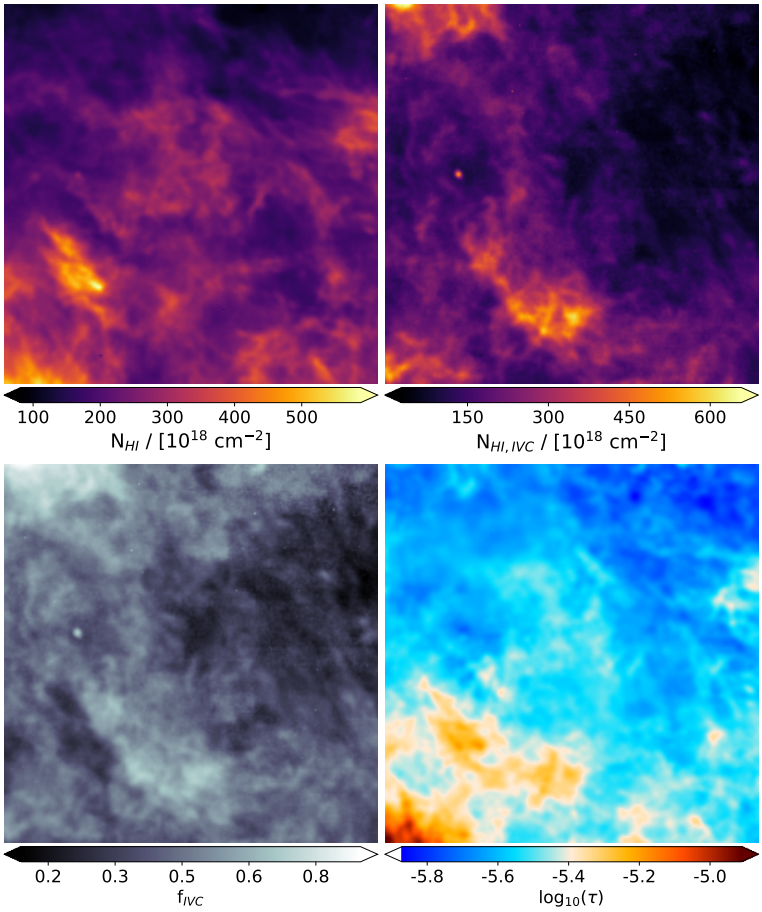

Fig. 5.1.: Top left: Integrated column density field N_{HI} of the local gas in NEP. Top right: Integrated column density field $N_{HI,IVC}$ of IVCs. Bottom left: IVC mass fraction f_{IVC} map. Bottom right: Dust optical depth map from *PLANCK*.

In this chapter, we use the decomposition obtained in Chapt. 4 to study the properties of the neutral gas observed in NEP. A three-component separation (WNM, LNM and CNM) is used. In Sect. 5.1, we analyze the properties of the column density fields of each phase as well as their respective mass fraction maps. In Sect. 5.2, we analyze the average fluid topology observed along the line-of-sight using a 3D dust extinction map. Two methods to disentangle thermal and turbulent velocity dispersions from the observed velocity dispersion of the WNM are presented in Sect. 5.3. The volume filling factor of the WNM is discussed in Sect. 5.4. The thermal properties, the statistical properties of the turbulent cascade acting in the fluid, and the condensation mode of thermal instability in the WNM of NEP are analyzed and discussed in Sect. 5.5. Discussion and summary are presented in Sects. 5.6 and 5.7.

5.1 North ecliptic pole

5.1.1 General description

The Gaussian components extracted from NEP with ROHSA in previous Chapt. 4 are grouped here in two categories to facilitate their analysis. The first group is composed of the IVCs present in the field. As Fig. 4.17 of Chapt. 4 shows, a multiphase structure is clearly seen in this component. However, since it is not the main goal of this study to quantify the phase transition occurring in IVCs, we deliberately group them into a single component. The second group of Gaussians represents the local velocity component (LVC) of the emission. Its multiphase structure will be analyzed in detail in the following Sect. 5.1.2. Figure 5.1 (top left and top right) shows the integrated column density maps of the LVC and IVCs in NEP obtained from the ROHSA decomposition. The mass fraction map of IVCs is shown in Fig. 5.1 (bottom left). Many structures appear at all scales with significant variations of the integrated column density over the field, from ~ 1 to 6×10^{20} cm^{-2}. Interestingly the average and variations of the column density are very similar for the LVC and IVC components of NEP. These variations are directly reflected in the f_{IVC} map where the mass fraction in IVCs has a median around $\sim$0.39.

The presence of dust in LVCs and IVCs has been investigated by Planck Collaboration et al. (2011) by looking at the correlation between the 21 cm column density and *Planck* 857, 545 and 353 GHz and IRAS 100 and 60 μm tracing the far-infrared and sub-millimeter emission of dust. It is clear from this study that dust is detected in both components (see. I_{857} vs. N_{HI} scatter plots in Fig. 14 of Planck Collaboration et al. (2011) for the correlation with IVCs). To illustrate this, we show in Fig. 5.1 (bottom right) the dust optical depth map inferred from *PLANCK*. The presence of dust in IVCs appears visually in this map, especially on the bottom left quadrant where a mixture of LVC and IVCs is clearly visible.

5.1.2 Integrated density fields of local gas

For the purpose of the analysis, we shall refine the multiphase view of the LVC component observed in NEP. Instead of computing a cloud/inter-cloud model as done in Chap. 4, we choose to separate the fluid into three components: WNM, LNM and CNM. This three phase model is clearly seen in the $\sigma - v$ diagram presented in Fig. 4.17. Gaussian G_8 and G_{10} are added to obtain the WNM, Gaussian G_6 forms the LNM and Gaussian G_7 and G_9 belong to the CNM. Each component is used with the objective of providing a global vision of this neutral medium that we are studying here, but we decide to focus mainly on describing the properties of the fluid in which the LNM and CNM structures are immersed: the WNM. Characterization of the other two phases will be addressed in a further work.

We start this section by a qualitative description of the multiphase decomposition obtained in NEP. Integrated column density fields of each phases are presented in Fig. 5.2 (top panels). Column density maps of the WNM and LNM show strong anti-correlations in some regions. Three main regions have been identified and annotated in Fig. 5.2 (top left) by letters A, B and C. At position A, the under-density in the WNM seems to correspond to an elongated filament of thermally unstable gas seen in the LNM column density map. Regions B and C also show similar behaviours. On the other hand, the column density map of the CNM, composed of clumpy structures and elongated filaments, does not appear to be reflected in any other phase. Interestingly, region C shows a concentration of CNM whose spatial extension seems to be smaller than its LNM counterpart. This region highlights the possible phase transition occurring along these lines-of-sight.

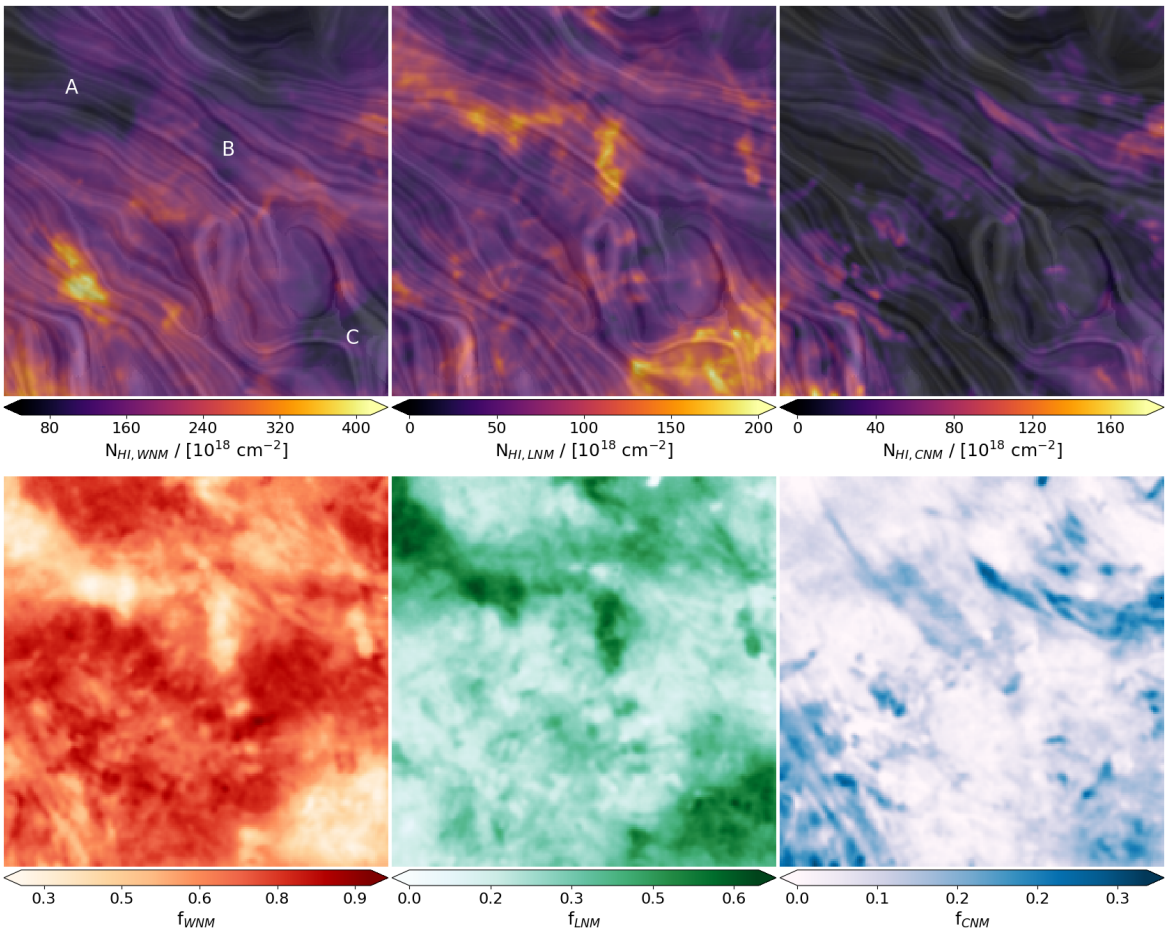

Fig. 5.2.: Top: Integrated column density $N_{HI,WNM}$, $N_{HI,LNM}$ and $N_{HI,CNM}$ fields of the three phase model. Bottom: f_{WNM}, f_{LNM} and f_{CNM} mass fraction maps. The orientation of the magnetic field on the plane of the sky measured by *Planck* is overlaid using the line integral convolution representation. Letters A, B and C indicated three anti-correlated regions of WNM and LNM discussed in the text.

We characterized the statistics of these three integrated column density fields (WNM, LNM and CNM) using one-point probability distribution functions (PDF). Figure 5.3 shows the dN/dlog(N_{HI}) diagram of the CNM (blue), LNM (green) and WNM (red). Each phase shows a complex distribution that we fit with a log-normal (solid lines) to obtain first order estimates. Centers of these log-normal distributions, $N_{HI,fit}$, are given in Table 5.1, showing a factor 10 between the WNM and the CNM and a factor 2.5 between the WNM and and LNM (so a factor 4 between the LNM and the CNM). It is important to specify that these relative mass fractions are representative of the fluid only in NEP and that because they depend drastically on the density and topology of the environment, we should expect considerable variations over the entire sky. To compare the NEP properties to variations of column densities of each phase observed across the sky, Fig. 5.3 also shows the PDFs of the three phase model inferred from the 21-Sponge survey (Murray et al., 2018b) based on a joint analysis of emission and absorption spectra over the sky, including high and low latitude observations. For each phase of this survey, the ranges of N_{HI} of NEP is included in the broader 21-Sponge distribution. We note that (Murray et al., 2018b) reports values of N_{HI} that are significantly larger than the maximum values in NEP. A possible explanation for this trend towards high column density might be related to large variations of path

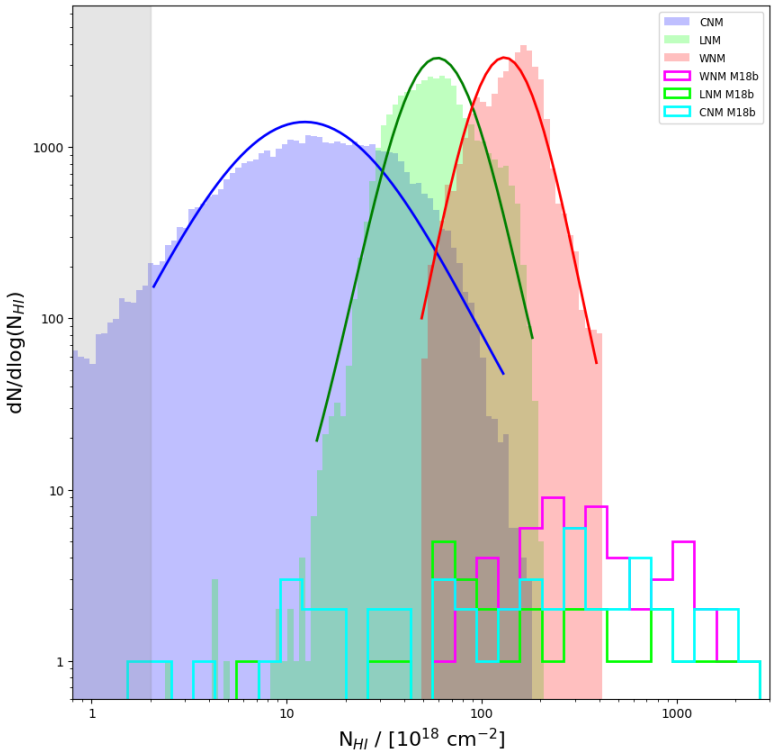

Fig. 5.3.: dN/dlog(N_{HI}) diagram of the CNM (blue), LNM (green) and WNM (red). Solid lines are log-normal fits of the distributions. The grey part shows the values that are not considered to fit the model. Integrated column densities inferred from the 21-Sponge survey (Murray et al., 2018b) are added for the WNM (magenta), the LNM (lime) and the CNM (cyan).

	$\tilde{N}_{HI}$ (10^{18} cm^{-2})	$N_{HI,fit}$ (10^{18} cm^{-2})	$\tilde{f}$	σ_f
WNM	146.5	130.0	0.642	0.13
LNM	56.9	59.0	0.28	0.11
CNM	13.5	12.2	0.077	0.06

Tab. 5.1.: Averaged physical properties of the integrated column density field and dispersion velocity field in NEP. From the left to the right: Median integrated column density $\tilde{N}_{HI}$, center of a the log-normal distribution shown in Fig. 5.3 $N_{HI,fit}$, mean mass fraction $\tilde{f}$, and standard deviation of the mass fraction.

length in the 21-Sponge survey that includes lines-of-sight randomly distributed over the sky (see Fig 1. from Murray et al. (2018)). As a first approximation, considering the geometry of the disk, the lower the latitude the longer the path length observed should be. To verify this simple hypothesis, we took for each phase the column densities from 21-Sponge exceeding NEP PDFs. Then we calculate the fraction of these values that have a latitude lower than the lowest latitude available in NEP, i.e. |b| < 24°. For the WNM, LNM and CNM, these fractions are respectively: 89 %, 69 %, and 68 %, showing that high column densities from 21-Sponge are indeed generally associated with observations of lower latitudes. This shows that 21-Sponge spans a much larger range of conditions than what is seen in NEP, and that the comparison should not be over-interpreted. In conclusion, 21-Sponge covers a wider variety of environments (especially with higher column densities) while NEP covers a low column density medium with more statistics.

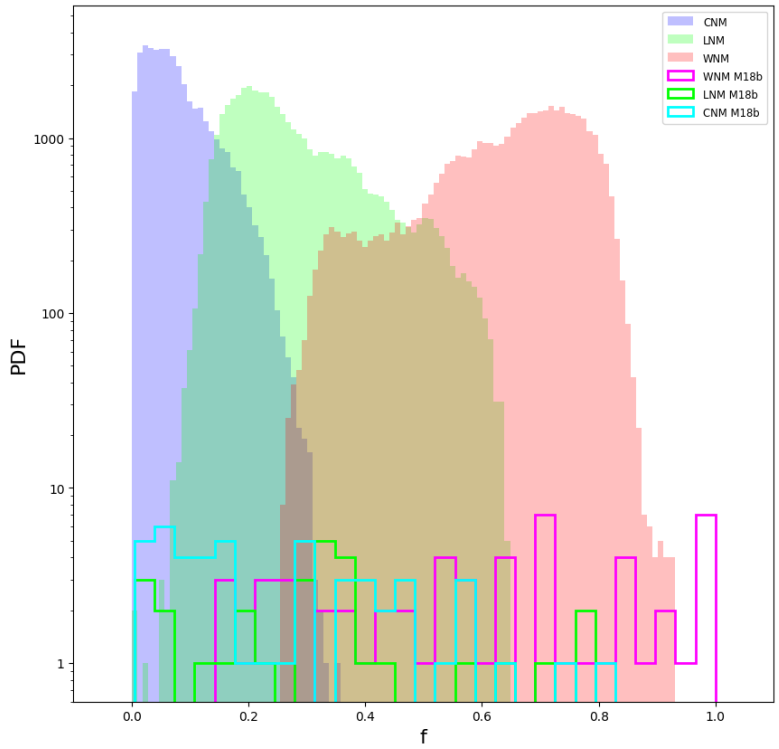

Fig. 5.4.: Probability distribution function of the mass fraction of the WNM (red), LNM (green) and CNM (blue) in NEP. Mass fraction inferred from the 21-Sponge survey (Murray et al., 2018b) are added for the WNM (magenta), the LNM (lime) and the CNM (cyan).

5.1.3 Mass fractions of local gas

Mass fraction maps f_i=$N_{H,i}/N_{H,tot}$ of each phase are presented in Fig. 5.2 (bottom panels). Anti-correlated regions A, B and C discussed in previous Sect. 5.1.2 appear clearly in these maps. In the mass fraction map of the WNM, these regions are associated to low mass fraction ($\sim$0.4) while in the mass fraction map of the LNM, regions A, B and C show high mass fraction ($\sim$0.6). For example, the elongated filament of thermally instable gas (region A) shows a LNM mass fraction higher that 0.5 while its counterpart in the WNM shows a WNM mass fraction lower than 0.4. In other words, it means that about half of the mass that lies along the line-of-sight is in a thermally unstable state. Therefore, in regions A, B and C, there appears to be a link between the apparent footprint of unstable gas in the WNM column density map and their LNM mass fraction. Interpretation of this qualitative description will be discussed in Sect. 5.4.

We statistically quantify the three mass fraction maps (WNM, LNM and CNM) using one-point PDFs. Figure 5.4 shows mass fraction PDFs of each phase whose medians and standard deviations are given in Table 5.1. On average in NEP, 64 % of the mass is in the WNM, 28 % in the LNM and only 8 % is in the CNM. However, as Table 5.1 shows, the standard deviation of these map is relatively high. This reflects the important variation seen in Fig 5.2 (bottom panels) and Fig. 5.4. For the sake of comparison, we over-plot in Fig. 5.4 the corresponding PDFs from the 21-Sponge survey. It is interesting to note that the CNM mass fraction does not exceed 0.35 in NEP while it reaches more than 0.8 in 21-Sponge. We follow the same procedure as before to investigate this difference. For the CNM, we take the mass

fraction from 21-Sponge exceeding the NEP mass fraction PDF. We then calculate the fraction of these values that have a latitude lower than the lowest latitude available in NEP, i.e. |b| < 24°. We find a fraction of 61 %, showing that a latitude effect is likely to be responsible for this discrepancy between NEP and 21-Sponge at high CNM mass fractions. This difference cannot be understood, as before, considering a plane parallel model with two different scale heights for the CNM and the WNM. In this model, the CNM fraction does not vary with latitude. However, when considering the presence of a bubble of a size comparable to the height scale of the CNM, the CNM fraction decreases with latitude due to the large CNM lake within this bubble.

5.2 Spatial distribution of the gas along the line of sight

In this section, we study the spatial distribution of the gas along the line-of-sight. We start by analyzing the emission from the Very Local Interstellar Medium (VLISM). Then we analyze the distribution of the remaining matter along the line-of-sight using 3D tomography techniques. In particular, the goal of this section is to determine the typical length scales of the observed HI analyzed in this work. Access to this information is of primary interest since it allows to determine the local volume density of the fluid which is one of the fundamental thermodynamic properties we are trying to access.

5.2.1 Emission from the Local Interstellar Cloud (LIC)

The emission of neutral hydrogen in the 100 square degree field centered on the North Ecliptic Pole results from the superposition of different environments along the line-of-sight. The first coherent fluid element encountered in the VLISM is the Local Interstellar Cloud (LIC) named by McClintock et al. (1978), one of the 15 warm clouds surrounding the Sun within 15 pc (Redfield and Linsky, 2000). The LIC is a "compact" cloud (term opposed to "filamentary" cloud such as the local Leo cold cloud (Peek et al., 2011b)) whose temperature has been estimated to be 7000±1000 K with a neutral hydrogen density of 0.1 cm^{-3} and a hydrogen ionization fraction $X(H) = n_p/(n_{HI} + n_p)$ of 0.52±0.18. Its dimensions vary between 4.7 pc and 6.8 pc. The Sun is located inside the LIC, not far from the edge of the Galactic (G) cloud. Figure 5.5 shows an artist view of this environment. Based on absorption-line transitions in the UV from the Hubble Space Telescope (HST) and CaII optical measurements, Redfield and Linsky (2008) found for the LIC a heliocentric velocity V_0 = 23.84±0.90 km.s^{-1} flowing toward the Galactic coordinates l_0=187.0°±3.4° and b_0=-13.5°±3.3 °. The G cloud follows almost the same stream with a heliocentric velocity V_0 = 29.6±1.1 km.s^{-1} flowing towards l_0=184.5°±1.9° and b_0=-20.6°±3.6 °. Redfield and Linsky (2008) provide the following equation to project the velocity V_0 of any cloud into a radial velocity V_r

$$V_r = V_0 \left[\cos b \cos b_0 \cos(l_0 - l) + \sin b_0 \sin b\right]. \tag{5.1}$$

where l and b are new galactic coordinates where V_r is observed. Using Eq. 5.1, it follows that the LIC projected radial velocity (in the Local Standard of Rest) in direction of NEP varies between -2.5 < $V_{r,lsr}$ [km.s^{-1}] < 0. At the center of the field (l∼ 96° and b∼ 30°) the distance to the edge of the LIC is 0.755 pc[1], corresponding to a column density of 2.3297 × 10^{17} cm^{-2} assuming a constant density of 0.1

[1]This value has been computing using the LIC Model Column Density Calculator available on the following web-page : http://sredfield.web.wesleyan.edu

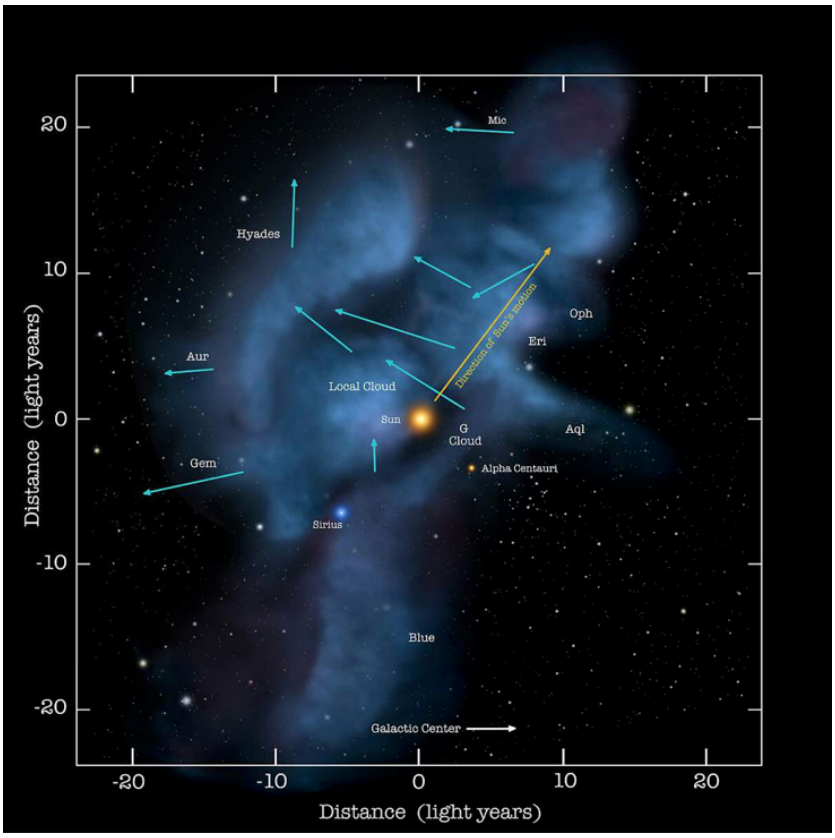

Fig. 5.5.: The solar journey through space is carrying us through a cluster of very low density interstellar clouds. Right now the Sun is inside of a cloud that is so tenuous that the interstellar gas detected by IBEX is as sparse as a handful of air stretched over a column that is hundreds of light years long. These clouds are identified by their motions. Credit: NASA/Goddard/Adler/U. Chicago/Wesleyan

cm^{-3}. We will see in following section that the column density PDF of the local WNM in NEP peaks around 1.46 $\times$ 10^{20} cm^{-2}. The LIC in direction of NEP represents $\sim$ 0.15 % of the emission of the local WNM. It is therefore a fair approximation to neglect this component for the rest of our analysis.

5.2.2 Beyond the Local Interstellar Cloud

One may wonder what is the distribution of matter after the LIC, and if it is possible to link this to the emission of the 21 cm line in NEP. For almost two decades, significant efforts have been made to map the interstellar medium in 3D using tomography techniques (Vergely et al., 2010; Vergely et al., 2010; Lallement et al., 1995; Lallement et al., 2003; Lallement et al., 2018; Lallement et al., 2019; Green et al., 2014; Green et al., 2018; Rezaei Kh. et al., 2017). Using interstellar Lyα absorption line toward 454 stars (Diplas and Savage, 1994b; Diplas and Savage, 1994a) and a regularized Bayesian inversion method, Vergely et al. (2001) mapped out a 3D density distribution of the neutral hydrogen within 250 pc of the Sun. Figure 5.6 shows the cross-section of the 3D density distribution of HI in the Galactic plane (viewed from above). Note that the smoothing length used by the inversion method is 60 pc, which is considerably higher than the VLISM described previously. The clouds of the VLISM are therefore not visible at this scale. More precisely, this smoothing length is a result of the small number of stars available in Diplas and Savage (1994), which is relatively low with respect to the volume

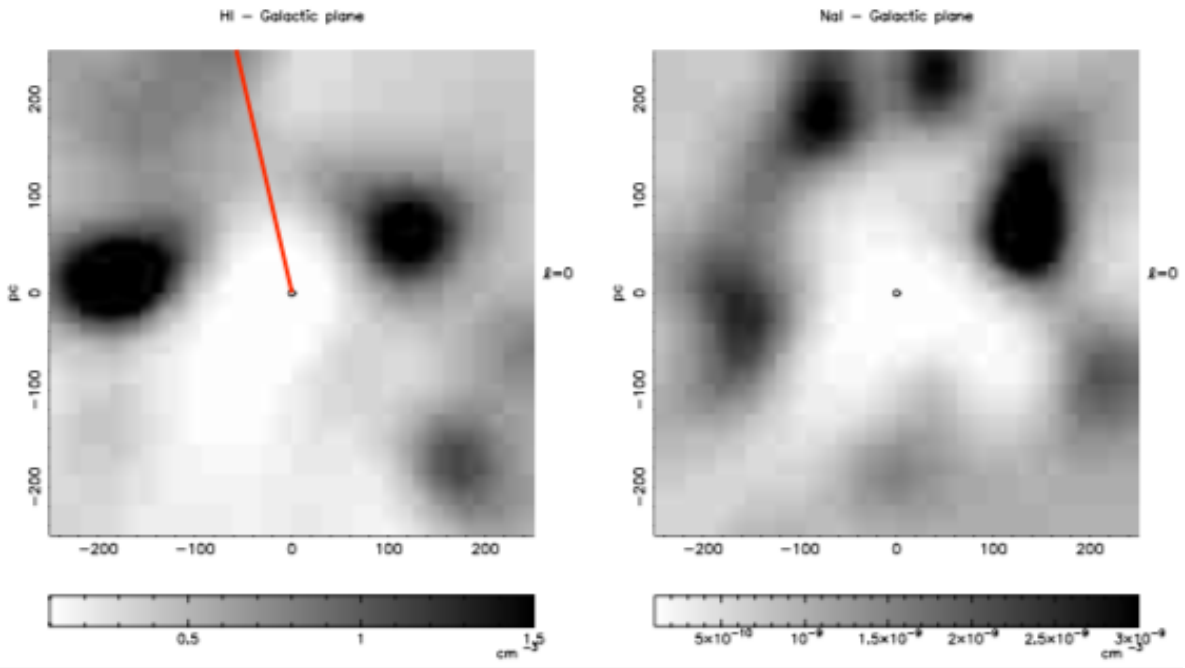

Fig. 5.6.: Fig 6. from Vergely et al. (2001)) : Comparison between cross sections of HI and NaI clouds in the Galactic plane (viewed from above). The smoothing length is ζ = 60 pc. The Sun is in the center of each cross section. The red line over-plotted on the left panel shows approximately the longitudinal direction of NEP.

considered. Nevertheless, this gives us a first idea of how the HI is distributed in the direction of NEP. A large cavity (the Local Bubble) is observed around the Sun with a density of about 0.1 cm^{-3}. This cavity seems to extend over 200 pc. Beyond that, as Fig. 5.6 (left) shows no clouds with significant HI density are observed in the direction of NEP.

No direct 3D mapping of the neutral hydrogen has been performed beyond 250 pc. However, it is possible to approach it using a 3D dust extinction map and the so-called N_H/E(B-V) relationship (Liszt, 2013). Using the same formalism as Vergely et al. (2001), Lallement et al. (2019) used Gaia DR2 photometric data combined with 2MASS to derive extinction measurements toward stars in a 6×6×0.8 kpc^3 volume around the Sun. We use this product to compute the mean dust extinction profile in the direction of NEP as shown in Fig. 5.7 (top). The presence of a large cavity, the Local Bubble appears clearly in this profile. From 150 to 250 pc, we observe a smooth increase of the dust extinction per parsec, similarly to the N_{HI} distribution in Fig. 5.6. This makes it difficult to estimate a clear frontier for the Local Bubble. Beyond this first wall, the dust extinction per parsec remains rather constant for ∼130 pc and then starts to decrease smoothly, as before, on a hundred parsec scale. From this Av.pc^{-1} profile, we infer the density

$$n_H(l) = \frac{\text{Av.pc}^{-1}(l)}{3.1} \times \frac{N_H}{E(B-V)} \tag{5.2}$$

The N_H/E(B-V) relationship shows a certain dispersion when different fields are considered to perform the regression (Liszt, 2013). To visualize a realistic range of possibilities, we present in Fig. 5.7 (bottom) the $n_H(l)$ density profile deduced from dust extinction, considering a N_H/E(B-V) ratio between 6-10×10^{21} cm^{-2}.mag^{-1}. For the sake of comparison, we over-plot the density profile from Dickey and

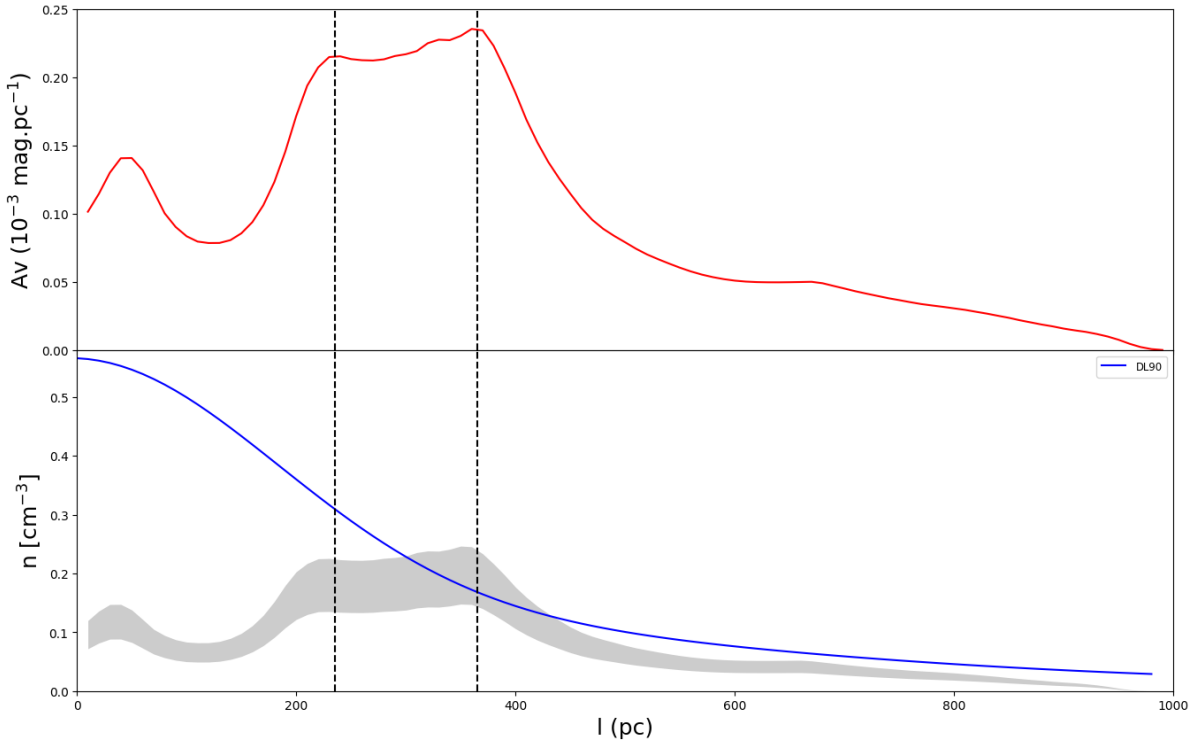

Fig. 5.7.: Top: Mean extinction profile Av/pc in NEP based on the 3D extinction dust map performed by Lallement et al. (2019). Bottom: Mean HI density profile in NEP for an N_H/E(B-V) ratio between 6-10$\times 10^{21}$ (gray), and total HI local density profile from Dickey and Lockman (1990) (blue).

Lockman (1990). The DL90 model and the model computed from the dust extinction curve appear to be roughly consistent in the range l ∼200-400 pc where most of the local HI mass is. This agreement is reassuring but one should not expect a perfect match; the DL90 model being a Galactic model[2], it does not take into account the particular conditions present in the solar neighbourhood, i.e. the Local Bubble.

A good way to validate the approach we have just presented above is to predict and compare the mean total $\tilde{N}^{Dust}_{H,TOT}$ column density computed from the mean dust extinction curve described previously and $\tilde{N}^{21cm}_{H,TOT}$ inferred from the 21 cm line. Integrating the density profile inferred from the dust extinction, we find that the value should be around $\tilde{N}^{Dust}_{H,TOT}$ = 2.43$\times 10^{20}$ cm^{-2}. Using a ratio N_H/E(B-V)=8$\times 10^{21}$ cm^{-2}.mag^{-1} (mean value of the range considered before), the mean total integrated column density of the local gas inferred from the 21 cm line is $\tilde{N}^{21cm}_{H,TOT}$=2.25$\times 10^{20}$ cm^{-2}. The two values are in very good agreement with a relative difference of 7.4 %. Note that considering the lower and upper value of N_H/E(B-V) (6-10$\times 10^{21}$ cm^{-2}.mag^{-1}), the relative difference is about ±30 %.

One can then wonder why the mean column density $\tilde{N}^{Dust}_{H,TOT}$ previously deduced from the extinction curve on about 1000 pc along the line-of-sight and the mean column density $\tilde{N}^{21cm}_{HI,TOT}$ of local HI gas are in such good agreement. $\tilde{N}^{Dust}_{H,TOT}$ traces the total amount of hydrogen atoms along the line-of-sight (HI, HII and H_2). In NEP, we have seen in previous Sect. 5.1.1 that dust is observed in the LVC and IVCs. Its presence suggests that IVCs are likely to be located beyond 1 kpc in NEP. A significant

[2]The density profile of DL90 was obtained using tangent point measurements. Its reflects the average $n_{HI}(z)$ in the inner Galaxy.

fraction of the volume along the line-of-sight is likely to be occupied by ionized gas (the WIM). The correspondence between $\tilde{N}_{H,TOT}^{Dust}$ and $\tilde{N}_{HI,TOT}^{21cm}$ therefore suggests that the WIM could be deficient in dust or that the column density of ionized gas N_{HII} is low in the direction of NEP. Distinction between these two possibilities remains impossible to date in view of the non-detection of dust in the WIM.

Following the previous Sect. 5.2, it is now possible to estimate the physical sizes L_x (longitude), L_y (latitude) and L_z (depth) of the studied field in the region of NEP. Using the size of the plateau delimited by two vertical lines in Fig. 5.7, we approximate the typical depth of the fluid along the line-of-sight L_z ∼130 pc. The 12°×12° region on the plane-of-sky translate into L_x=L_y ∼63 pc at l=300 pc (halfway down L_z).

5.3 Disentangling thermal and turbulent velocity dispersions in the WNM

Each of the spatially coherent phases discussed so far contains information on the thermal and turbulent properties of gas. These two contributions to the line shape are mixed together in a single observable which is the velocity dispersion of the velocity field component along the line-of-sight. We model these two contributions by a quadratic sum of thermal and turbulent broadening:

$$\sigma_{obs,w}^2 = \sigma_{th,w}^2 + \sigma_{v_{z,w}}^2. \tag{5.3}$$

This observational mixture makes their separation impossible when considering each line-of-sight independently. To overcome this difficulty, we investigate two independent methods to disentangle thermal and turbulent velocity dispersions from Eq. 5.3. The first method uses the velocity information contained in the CNM extracted from NEP as tracer particles to estimate the turbulent velocity dispersion $\sigma_{v_{z,w}}$ of the WNM. The second method aims to use directly the centroid velocity field of the WNM $v_{c,w}$. For each method, we make the assumption that the statistical properties of $v_{z,w}$ are isotropic. These two different models will be respectively denoted (1) and (2).

5.3.1 Use of CNM structures as tracer particles

For this first method, we assume that the velocity dispersions $\sigma_{v_{z,c}}$ of dense CNM structures observed in NEP are representative of the turbulent velocity field $\sigma_{v_{z,w}}^{(1)}$ of the WNM. In this picture, the volume of each dense CNM structure is very small compared to the volume in which they evolve. By analogy to fluid mechanics experiments conducted in Earth laboratory, these CNM structures are seen as coloured tracer particles added to the fluid (WNM) to highlight the statistical properties of these turbulent motions. Furthermore, we consider as a first approximation that the majority of the CNM observed in NEP is homogeneously distributed in the observed typical volume $\mathcal{V}_{\mathcal{NEP}}$=$L_x \times L_y \times L_z$. This hypothesis is probably not true in reality, especially since we analyze in this study a fluid, part of which forms the wall of the Local Bubble. Under such conditions, it is likely that CNM structures are unevenly distributed and maybe more located along the wall as what has been observed in HI shells (e.g., McClure-Griffiths et al., 2003b). Since the Sun is located inside the Local Bubble, this would mean that these structures

sample a volume smaller than $\mathcal{V}_{\mathcal{NEP}}$, with a typical depth lower than L_z. Consequently, it is likely that $\sigma_{v_{z,c}}$ underestimates the turbulent velocity dispersion of the WNM on a scale L_z. Therefore, we will consider the inferred value as a lower limit of $\sigma^{(1)}_{v_{z,w}}(L_z)$.

To compute the velocity dispersion of CNM structures, we use the whole Gaussian sample obtained with ROHSA in previous Chapt. 4. We remind the reader that each Gaussian i has three parameters, namely its amplitude a_i, its projected velocity along the line-of-sight μ_i and its velocity dispersion σ_{v_i}. The velocity dispersion of CNM structures $\sigma_{v_{z,c}}$ is defined as the square of the weighted variance of the velocity parameters of the Gaussian sample.

$$\sigma_{v_{z,c}} = \sqrt{\frac{\sum_{i=0}^{N} w_i \left(\mu_i - \overline{\mu}^*\right)^2}{\sum_{i=0}^{N} w_i}} \tag{5.4}$$

where

$$\overline{\mu}^* = \frac{\sum_{i=0}^{N} w_i \mu_i}{\sum_{i=0}^{N} w_i} \tag{5.5}$$

and,

$$w_i = a_i \sigma_i. \tag{5.6}$$

We find a velocity dispersion $\sigma_{v_{z,c}}$=3.44 km.s^{-1}. We infer from the hypothesis discussed above that $\sigma^{(1)}_{v_{z,w}}(L_z) = \sigma_{v_{z,c}}$.

5.3.2 Use of the centroid velocity field of the WNM

In this second method, we use the velocity information contained directly in the emission lines of the WNM. For this purpose, it is necessary to discuss first the nature of the observed centroid velocity field. Indeed, the projected velocity field $\langle v_{z,w} \rangle_z$ is not directly accessible with observations. Instead, we have access to the first moment map of the hyper-spectral cube called the velocity centroid and noted $v_{c,w}$. Its expression, presented in Eq. 4.21 with observable quantities, can also be written in the optically thin limit using the underlying 3D velocity and density fields

$$v_{c,w} = \frac{\int_0^{L_z} \rho(\mathbf{r}, z) v_{z,w}(\mathbf{r}, z) \mathrm{d}z}{\int_0^{L_z} \rho(\mathbf{r}, z) \mathrm{d}z} \tag{5.7}$$

where L_z is the depth of the observed medium. Therefore, Eq. 5.7 is a density weighted projection of the 3D velocity field $v_{z,w}$ along the line-of-sight. The link between the statistics of $v_{c,w}$ and $\langle v_{z,w} \rangle_z$ is not trivial and has been actively studied in the early 21th century (Ossenkopf et al., 2006; Esquivel et al., 2007; Miville-Deschênes et al., 2003b; Levrier, 2004). Following Ossenkopf et al. (2006), we write the density and velocity field as

$$\rho(\mathbf{r}, z) = \rho_0 + \delta\rho, \tag{5.8}$$

$$v_{z,w}(\mathbf{r}, z) = v_{z,w0} + \delta v_{z,w}, \tag{5.9}$$

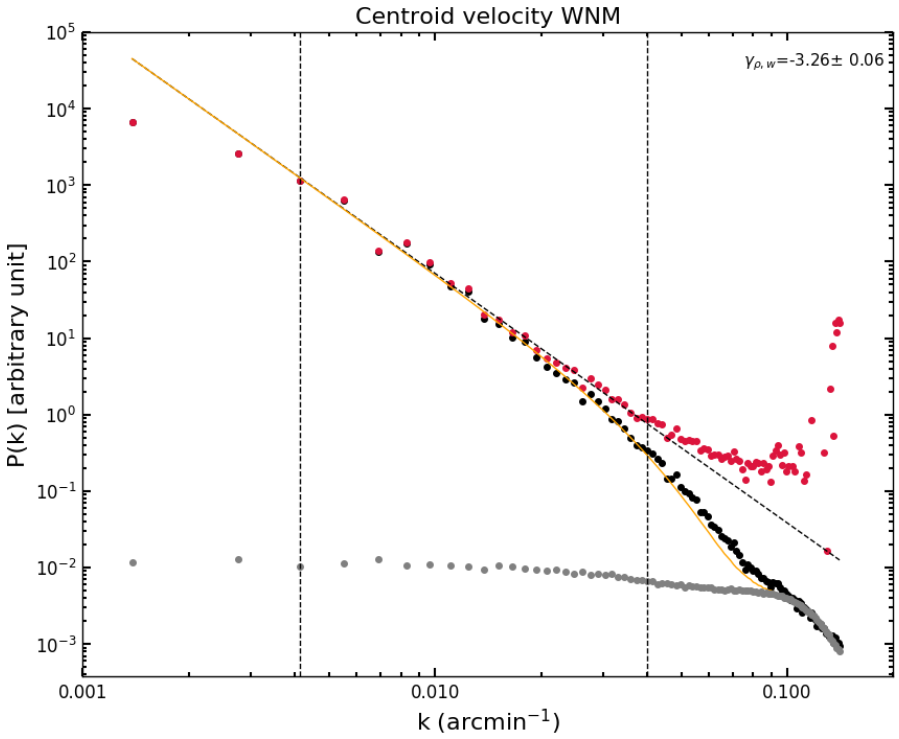

Fig. 5.8.: Spatial power spectrum model of the centroid velocity field of the WNM in NEP. $\left\langle P_{v_{z,w}} \right\rangle (k)$ is given by the black dots. Grey points represent the noise component $N(k)$. Red points show the corrected power spectrum ($P(k) - N(k)/B(k)$). The dotted line shows the fit of the corrected power spectrum between the two vertical dashed line, and the orange line shows the result of the global modeling of Eq. A.1. The power spectrum index is $\gamma_{v_{z,w}}$ = -3.26±0.06.

where ρ_0 and $v_{z,w0}$ denote averages of the density and velocity fields, and $\delta\rho$ and $\delta v_{z,w}$ their fluctuations across the fluid. Combining Eqs. 5.9 and 5.7, the velocity centroid becomes

$$v_{c,w} = \frac{\int_0^{L_z} (\rho_0 + \delta\rho)\,(v_{z,w0} + \delta v_{z,w})\,\mathrm{d}z}{\int_0^{L_z} (\rho_0 + \delta\rho)\,\mathrm{d}z}. \tag{5.10}$$

Equation 5.10 shows that the velocity centroid involves a complex combination of density and velocity fluctuations. However, as shown respectively analytically and numerically by Levrier (2004) and Miville-Deschênes et al. (2003), the centroid velocity statistics behave as the 3D velocity field when density fluctuations are small compared to the mean density of the fluid ($\delta\rho/\rho_0 \lesssim 1$). Although this criterion is theoretically well established, it is not trivial to have access to it from observations.

In a multiphase medium like the neutral ISM, these strong density contrasts are mainly caused by unstable gas and CNM structures. By nature these structures arise from the condensation of WNM via thermal instability and are consequently associated to dense regions. Thanks to the phase separation obtained with `ROHSA`, we have minimized the mentioned effect on the WNM centroid velocity statistics (see Appendix 6 for a power spectrum analysis of the column density field and centroid velocity field of the WNM). The second origin of strong density contrast in a turbulent fluid is related to the strength of turbulent motions. For an isothermal fluid, it has been shown that discontinuities of weak shocks generated by supersonic turbulence globally increase the density contrast of the whole fluid (Kim and

Ryu, 2005). As we will see in following Sect. 5.4, the considerations regarding the volume filling factor of the fluid has an impact on the statistics of projected fields. These considerations are not trivial and beyond the scope of this work. A short analysis using fractional Brownian motion fields is presented in Appendix A. This shows in particular that the power spectrum index of both density and velocity projected field are flattened by a partial filling of the 3D volume. As Fig. 5.8 shows, the power spectrum index of the centroid velocity field of the WNM is $\gamma_{v_{z,w}}$= -3.29±0.04, flatter than the Kolmogorov "-11/3" value. A similar effect is seen for the column density (see Appendix 6). Considering the partial volume filling factor of the WNM, the power spectrum slopes observed for the centroid and column density are compatible with a subsonic/sonic turbulence. Consequently, the strength of turbulence acting in the WNM of NEP is not likely to be important enough to induce strong density fluctuations and rule out the criterion $\delta\rho/\rho_0 \lesssim 1$. Therefore, we think it is a fair approximation to write $\langle v_{z,w} \rangle_z \sim v_{c,w}$.

A method for reconstructing the variance of a 3D physical field from 2D observation has been developped by Brunt et al. (2010) assuming only statistical isotropy of the underlying 3D physical field. The statistics of projected variance from 3D to 2D was then applied to a CO observation of the Taurus molecular cloud (Brunt et al., 2010a) to study the relative strength of solenoidal to compressive modes of the turbulent driving via the variance-Mach number relationship. While this method is generally applied to density fields, the work of Brunt et al. (2010) is general enough to be applied on any kind of field, including velocity fields. Using the same formalism, we adapt this method to the centroid velocity field of the WNM to infer the velocity dispersion of the 3D velocity field $\sigma_{v_{z,w}}$ from the velocity dispersion of its projection along the line-of-sight $\sigma_{\langle v_{z,w} \rangle_z}$. Using Parseval's Theorem, it was shown by Brunt et al. (2010) that $\sigma_{\langle v_{z,w} \rangle_z}$ and $\sigma^{(2)}_{v_{z,w}}$ are linked by the ratio

$$\sqrt{R} = \frac{\sigma_{\langle v_{z,w} \rangle_z}}{\sigma^{(2)}_{v_{z,w}}} = \sqrt{\frac{\left(\sum_{k_x=-L_x/2+1}^{L_x/2} \sum_{k_y=-L_y/2+1}^{L_y/2} P^{3D}_{v_{z,w}}(k) \right) - P^{3D}_{v_{z,w}}(0)}{\left(\sum_{k_x=-L_x/2+1}^{L_x/2} \sum_{k_y=-L_y/2+1}^{L_y/2} \sum_{k_z=-L_z/2+1}^{L_z/2} P^{3D}_{v_{z,w}}(k) \right) - P^{3D}_{v_{z,w}}(0)}} \tag{5.11}$$

where $P^{3D}_{v_{z,w}}(k)$ is the azimuthally-averaged power spectrum of $v_{z,w}$. For a given field of size $L_x \times L_y$, two parameters control the ratio R: 1) The slope of $P^{3D}_{v_{z,w}}(k)$, and 2) the depth of the cube L_z over which velocity fluctuations are averaged. We consider for this model $P^{3D}_{v_{z,w}}(k) \propto k^{-11/3}$, representative of a subsonic/sonic turbulence. We find R=0.093, leading to a turbulent velocity dispersion $\sigma^{(2)}_{v_{z,w}}(L_z)$=6.78 km.s^{-1}.

It turns out that velocity dispersion $\sigma^{(1)}_{v_{z,w}}(L_z)$ and $\sigma^{(2)}_{v_{z,w}}(L_z)$ differ by a factor ∼2. It is useful to compare the corresponding mean kinetic temperatures obtained using Eq. 5.3. Considering the mean observed velocity dispersion $\sigma_{obs,w}$=8.02 km.s^{-1} of the WNM, the mean kinetic temperatures associated are respectively $T^{(1)}_{k,w}$=6372 K, and $T^{(2)}_{k,w}$=2234 K. While the first value seems to be coherent with the kinetic temperature of the WNM, the second one falls clearly into the unstable regime (Wolfire et al., 1995a; Wolfire et al., 2003).

To understand the impact of the two parameters controlling model (2) (the slope of $P^{3D}_{v_{z,w}}(k)$ and the typical length scale $L_z$on the result of $\sigma^{(2)}_{v_{z,w}}(L_z)$), let us try to set one of these two parameters in turn in order to obtain the plausible value of method (1). When fixing L_z, the hypothetical value of $\gamma_{v,z}$ required to obtain $\sigma^{(1)}_{v_{z,w}}(L_z)$ is clearly incompatible with a subsonic/sonic turbulent fluid. On the other

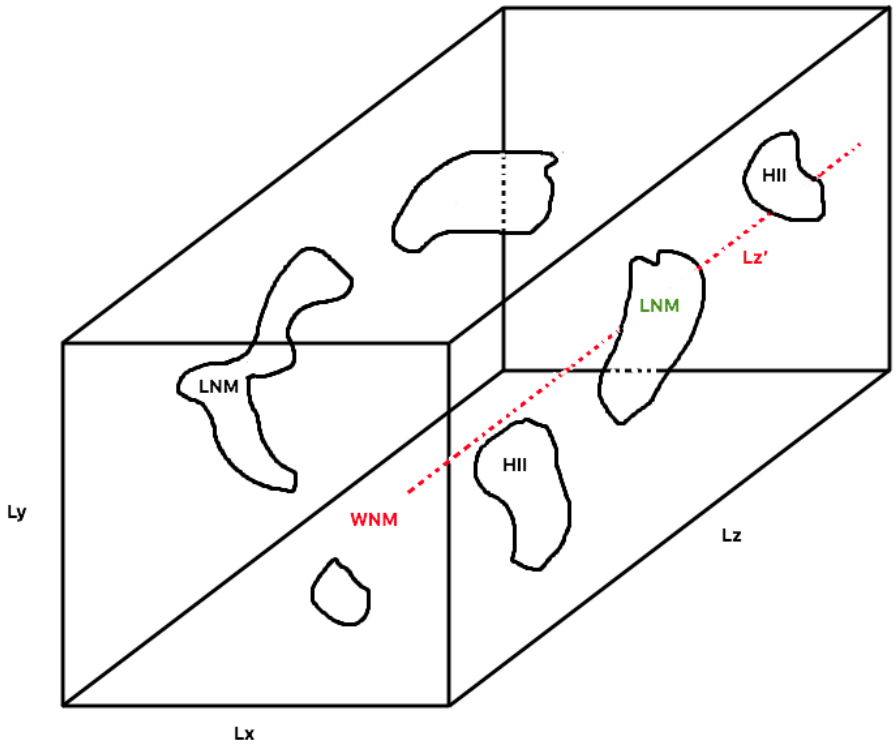

Fig. 5.9.: Sketch of the modelling of the length scales observed in NEP. Random LNM regions and ionized regions of the DIG are drawn and labeled to illustrate the difference between the total length scale L_z along the line-of-sight and the effective length scale L'_z of the WNM represented by the red dashed line that shows the typical path occupied by the WNM along a random line-of-sight.

hand, when fixing the slope of $P^{3D}_{v_{z,w}}(k)$, the length scale required to obtain $\sigma^{(1)}_{v_{z,w}}(L_z)$ corresponds to 56 pc. One way to solve this discrepancy is to consider that the WNM does not occupy the totality of the volume $\mathcal{V}_{\mathcal{NEP}}$. This allow us to introduce an effective length scale L'_z=$f_{v,w} \times L_z$, where $f_{v,w}$ is the average volume filling factor of the WNM. We can now infer what would be the volume filling factor of the WNM to reconcile model (1) and (2). We find $f^{(1)}_{v,w}$=0.43[3]. One can now wonder what sets the volume filling factor of the WNM.

5.4 Volume filling factors

In this section, we explore the possible volume filling factor values of the WNM in NEP. In Sect. 5.4.1, we return to the anti-correlation of regions A, B, and C discussed in Sect. 5.1. A numerical simulation of bi-stable turbulence is used for a first comparison in an idealized framework where the HI occupies the entire observed volume. The possible impact of ionized gas is discussed in Sect. 5.4.2.

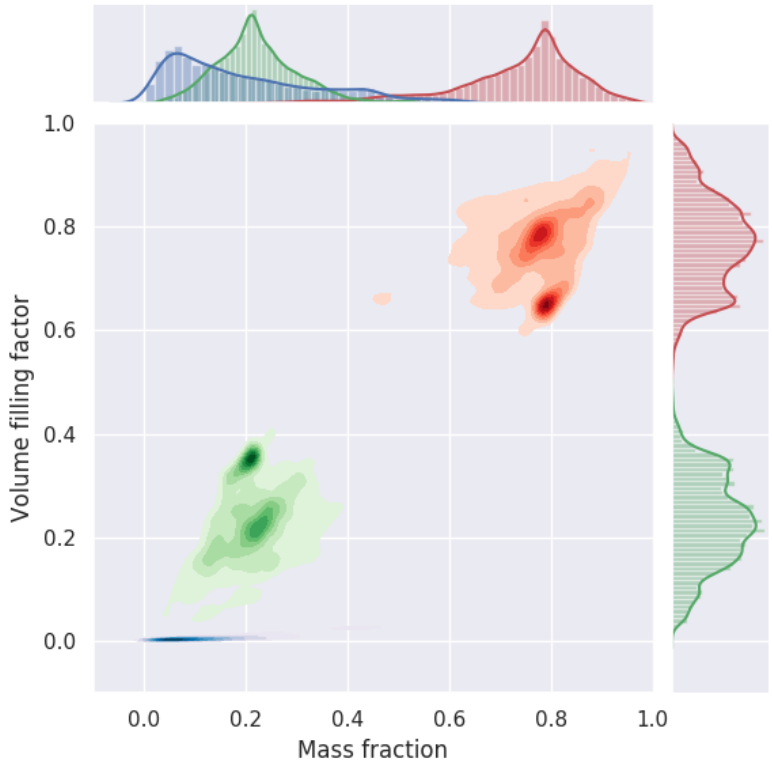

Fig. 5.10.: Two dimensional probability distribution function of the volume filling factor as function of the mass fraction for the WNM (red), LNM (green) and CNM (blue) along each line of light of a $256 \times 256 \times 1024$ pixels region with moderate CNM fraction (same region as in Marchal et al. (2019) of the numerical simulation of thermally bi-stable turbulence performed by Saury et al. (2014).

5.4.1 Filling factor of the multiphase HI

Let us start by considering the volume filling factor of each phase of the multiphase HI, in the case where the neutral gas occupies the totality of the volume $\mathcal{V}_{\mathcal{NEP}}$ (no contribution from ionized gas). In this case, one can wonder what are the volume filling factors of each phase. Our current view of the volume difference occupied by cold CNM structures immersed in diffuse WNM comes from a rather simple reasoning. At the first order, we have determined in Sect. 5.1.2 that there is a factor of 10 between the column densities of the WNM and the CNM in NEP. Considering a typical factor of 100 between densities, and if CNM structures sample $\mathcal{V}_{\mathcal{NEP}}$, this means that the volume ratio is in the order of 1000. We follow the same reasoning between the LNM and the WNM. Considering that there is a factor of 2.5 between the column densities of the WNM and the LNM in NEP, and a typical factor 5 between densities, it results that the volume ratio is in the order of 10. While it seams reasonable to neglect the volume occupied by the CNM, the volume occupied by the LNM seems to be important. These approximate estimates are based on typical densities and must obviously be taken with caution. This important volume occupied by unstable gas can be understood from a more theoretical point of view by looking at the cooling scale associated to the condensation mode of the thermal instability. As derived in Chapt. 3, when the gas experiences compression, this cooling scale noted λ_{cool}, corresponds to the scale at which the gas is non-linearly unstable. For example, Hennebelle and Pérault (1999)

[3]Note that we labelled this volume filling factor by (1) since it is obtained by fixing $\sigma^{(1)}_{v_{z,w}}(L_z)$.

estimated λ_{cool} ∼15 pc. Regarding the typical length scale L_z estimated using the dust extinction map along the line-of-sight, it seems clear that the volume occupied by the unstable gas must be important.

These previous rough estimates allow us to revisit the interpretation of the anti-correlated regions A, B and C discussed in Sect. 5.1, corresponding to a footprint of the LNM in the WNM. If a gas cloud, located at a certain distance along the line of sight and whatever its density, occupies only a very small part of the space along this axis, it will only marginally affect the total column density of the gas surrounding it. Therefore, no clear spatial variations in the column density of the surrounding fluid will be observed on the plane of the sky. If, on the other hand, this cloud occupies a significant portion of the space along the line of sight, this should cause a clear decrease in the total column density of the medium in which it is immersed. This behaviour in the integrated column density fields of the LNM and the WNM is likely to be due to a signature of an important volume filling factor of the LNM and that its value is not very small compared to the volume filling factor of the WNM. On the other hand, since no clear anti-correlation is seen between the LNM and the CNM (top right), the volume filling factor of the CNM should be considerably smaller than the volume filling factor of the LNM : $f_{v,CNM}/f_{v,LNM} \ll 1$. Nevertheless, it is complicated to determine more precise numbers considering the complex unknown geometry of this multi-phase fluid along the line of sight. A sketch of the modelling of the length scales observed in NEP considering that unstable gas structures occupy an important part of the volume is shown in Fig. 5.9.

As stated in Sect. 5.1, regions A, B and C are clearly associated with high LNM mass fraction regions. In order to go further and investigate this relation between volume filling factor and mass fraction, we use the same region as in Chapt. 4 of the numerical simulation of thermally bi-stable turbulence performed by Saury et al. (2014) as a first element of comparison. For each line-of-sight, we computed the mass fraction and the volume filling factor of each phase. Fig. 5.10 shows the two dimensional probability distribution function of these two quantities for the WNM (red), LNM (green) and CNM (blue) and their PDFs. The PDFs of the mass fraction of the three-phase model in NEP (Fig. 5.4) and those from this numerical simulation (top of Fig. 5.10) show remarkable similarities. It turns out that mass fractions and volume filling factors are extremely correlated. These two quantities are indeed linked by the density of the gas which is itself correlated to the phase to which it belongs. The volume occupied by the CNM in the simulation is very low. On the other hand, the volume filling factor of the LNM and WNM are respectively around $f_{v,l} \sim 0.3$ and $f_{v,w} \sim 0.7$. These numbers must obviously be taken with caution since they come from a highly idealized simulation. Furthermore, it is important to note that the numerical simulation of Saury et al. (2014) represents one realization of the thermally bi-stable HI fluid. The mass fraction in each phase depends on the initial conditions and on the properties of the turbulent forcing. It appears that the choice made in Saury et al. (2014) reproduces rather well the mass fractions observed in NEP. From the similarities of the PDFs and the strong correlation between mass fraction and volume filling factor, we conclude that the volume filling factor of the WNM in NEP is likely to be of the order of $f_{v,w}$=$\tilde{f}_w$ ∼0.65 (see also Table 5.1).

This rough estimate is however higher than $f^{(1)}_{v,w}$=0.43. Despite the considerable uncertainty associated to this parameter, a possible explanation of this difference could be the presence of ionized gas clouds constituting the diffuse ionized gas (DIG).

5.4.2 Impact from diffuse ionized gas

The coarse estimate of $f_{v,w}$ estimated in previous Sect. 5.4.1 has been determined in the idealized context where the totality of the gas is neutral. However, as summarize by Gaensler et al. (2008), the presence of the diffuse WIM (DIG) is known since a few decades from several techniques: "pulsar dispersion measures (DMs), free-free absorption of low-frequency Galactic synchrotron emission, interstellar scattering of compact radio sources, and faint Hα and Hβ emission". Using a joint analysis of pulsar DMs and diffuse Hα emission, Gaensler et al. (2008) have determined a scale-height of 1830^{+120}_{-250} pc for the DIG. It is important to note for this study that this phase is likely to be made of discrete structures instead of an homogeneous and continuous medium (Reynolds, 1977; Berkhuijsen et al., 2006; Gaensler et al., 2008). In particular, the volume of the diffuse WIM occupied by these structures has been introduced to solve the discrepancy between DMs and emission measurement (EM) from Hα emission. DMs have a linear dependency on the free electron density while EMs are functions of the square of the electron density (Gaensler et al., 2008). Estimates of the mid-plane volume filling factor of the WIM from the literature have been summarized in Table 2 from Gaensler et al. (2008). This shows a typical value of $f_{v,DIG}$ ~10 %, increasing with the distance above the Galactic plane. These models are, as models of the multiphase HI by Dickey and Lockman (1990) and Kalberla et al. (2007), Galactic models. Since these values are likely to vary locally we restrict ourselves by considering that a 10 % contribution of localized ionized clouds are likely to reduce the volume filling factor of the WNM compared to the idealized case of pure neutral gas.

We use the $f_{v,w}$=0.65 as an upper limit to define our realistic range of volume filling factor. The corresponding L'_z=$f_{v,w} \times L_z$ ~85 pc. Using $f^{(1)}_{v,w}$=0.43, the volume filling factor range used in the following is 0.43 < $f_{v,w}$ < 0.65 and the corresponding turbulent velocity dispersion range is 3.44 < $\sigma_{v_{z,w}}(L_z)$ (km.s^{-1}) < 4.58

5.5 Thermodynamics and turbulence of the WNM

In this section we analyze the statistical properties of the turbulent WNM in NEP. The thermodynamic properties of the WNM in NEP are presented in Sect. 5.5.1. In Sect. 5.5.2, we analyze the statistical properties of the turbulence cascade acting in the fluid. In particular, we discuss the scaling laws of the turbulent sonic Mach number and the possible mechanisms of energy dissipation in the fluid. Finally, in Sect. 5.5.3, the properties inferred in Sects. 5.5.1 and 5.5.2 are combined to discuss the condensation criterion of the thermal instability arising in the WNM. It will allow us to understand the bi-stable nature of the neutral interstellar medium and the formation of LNM and CNM structures. All quantities inferred in this section are reported in Table 5.2.

5.5.1 Thermodynamic properties

In this section, we determine the mean thermodynamic properties of the fluid in NEP: the pressure $\overline{P}_w/k_B$, the density $\overline{n}_w$ and the temperature $\overline{T}_{k,w}$. These values are derived from the turbulent velocity

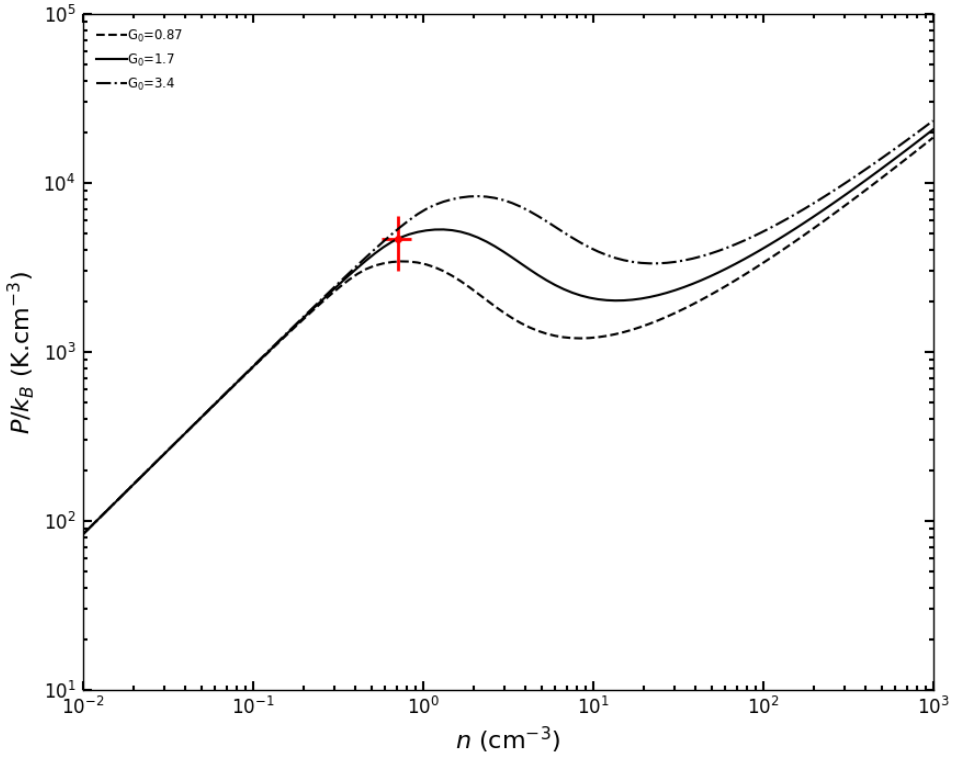

Fig. 5.11.: P-n diagram: Range of pressure and density are shown by the red cross. The standard model (N_c=1.e19) of Wolfire et al. (2003) is over-plotted for three different values of Draine ISRF in the range 0.87 < G_0 < 3.4.

dispersion range 3.44 < $\sigma_{v_{z,w}}(L_z)$ (km.s^{-1}) < 4.58, and volume filling factor range 0.43 < $f_{v,w}$ < 0.65 derived in previous Sect. 5.4.

Using Eq. 5.3, we compute the corresponding mean thermal velocity dispersion range 6.59 < $\sigma_{th,w}$ (km.s^{-1}) < 7.25. The kinetic temperature of the WNM is then

$$\overline{T}_{k,w} = \frac{\overline{\sigma}^2_{th,w}\, m_H}{k_B} \tag{5.12}$$

where m_H is the hydrogen atom mass and k_B the Boltzmann constant. We find 5264 < $T_{k,w}$ (K) < 6372.

Using the effective line-of-sight path lengths L'_z, we compute the density of the WNM along each line-of-sight given by

$$\overline{n}_w = \frac{\overline{N}_{HI,w}}{L'_z}. \tag{5.13}$$

We find 0.57 < $\overline{n}_w$ (cm^{-3}) < 0.86. The thermal pressure is simply given by the product between the density and the temperature

$$\overline{P}_w/k_B = \overline{n}_w\, \overline{T}_{k,w}. \tag{5.14}$$

We find 3000 < $\overline{P}_w/k$ (K cm^{-3}) < 5489.

Figure 5.11 shows the $P-n$ diagram with the pressure and density range inferred in this work by the red cross. For the sake of comparison, the standard model (N_c=1.e19) of Wolfire et al. (2003) is over-plotted for three different values of Draine ISRF in the range 0.87 < G_0 < 3.4. These variations are motivated by two factors: 1) variations due to the distribution of stars which can locally increase or decrease G_0, and 2) variations due to the density field topology. The latter induces a natural shielding of the radiation field, causing a decrease proportional to the column density of the gas. Considering this realistic range of G_0, Fig. 5.11 shows that the values of pressure and density in the WNM of NEP seem to be compatible with a thermal equilibrium state. Note that the model of Wolfire et al. (2003) includes other secondary parameters such has the abundance of PAH playing an important role in the photoelectric heating, and major coolants like OI and CII. All the curves here are computed using standard values in the solar neighbourhood.

5.5.2 Properties of the turbulent cascade

In this section, we combine the previous estimations of $\overline{T}_{k,w}$, $\overline{n}_w$, and $\overline{P}_w/k_B$ to $\sigma_{v_{z,w}}(L_z)$, to infer the statistical properties of turbulence of the WNM in NEP. For this purpose, we calculate the $\sigma_v - l$ relation and turbulent sonic Mach number $\mathcal{M}_{s,w}$ scaling laws. These are then used to estimate the Reynolds number Re_l, the kinematic viscosity η the dissipation time τ_D, the dissipation scale ν, and the energy transfer rate ϵ. The values we obtained for these parameters are summarized in Table 5.2.

Turbulent sonic Mach number In this section, we discuss the scaling law of the turbulent sonic Mach number $\mathcal{M}_{s,w}(l)$ of the WNM in NEP defined as

$$\mathcal{M}_{s,w}(l) = \frac{\sqrt{3}\,\sigma_{v_{z,w}}(l)}{C_{s,w}} \tag{5.15}$$

where the adiabatic sound speed is

$$C_{s,w} = \sqrt{\frac{\gamma k_B \overline{T}_{k,w}}{\mu m_H}}, \tag{5.16}$$

with μ=1.4 the molecular weight for fully atomic hydrogen and $\gamma = 5/3$ the adiabatic index of monoatomic gas. In this study, the largest scale available is the depth of the fluid along the line-of-sight. This scale, previously noted L_z, has been estimated around ∼130 pc and the corresponding turbulent velocity dispersion between 3.44 < $\sigma_{v_{z,w}}(L_z)$ (km.s^{-1}) < 4.58. Using Eq. 5.15 we compute the corresponding turbulent sonic Mach numbers. As Table. 5.2 shows, 0.75 < $\mathcal{M}_{s,w}(L_z)$ < 1.1. These values show that the WNM in NEP is in a subsonic/transonic regime on a scale of L_z ∼130 pc.

As derived in Chapt. 2, an important property of $\sigma_{v_{z,w}}(l)$ is that it follows a scaling law dictated by the nature of the turbulent cascade and controlled via the parameter q. This relation, called the $\sigma_v - l$ relation, can be written here as

$$\sigma_{v_{z,w}}(l) = \sigma_{v_{z,w}}(1)\, l_{pc}^{q} \tag{5.17}$$

where $\sigma_{v_{z,w}}(1)$ is the velocity dispersion of the turbulent velocity field along the line-of-sight at a scale of 1 pc, and l_{pc} is the scale in pc. The application of this law to the WNM in NEP is an important point and requires some justification. Equation 5.17 is valid if the turbulence is in a regime where an inertial range $l_0 \ll l \ll \eta$ with a constant energy transfer rate exists. The existence of an inertial range in NEP

Quantity	Symbol	Value	Units
Thermodynamic			
Volume filling factor	$f_{v,w}$	0.43-0.65	
Largest scale observed	l=L_z	$\sim$130	pc
Mean pressure	$\overline{P}_w$/k$_B$	5489-3000	K.cm^{-3}
Mean density	$\overline{n}_w$	0.86-0.57	cm^{-3}
Mean kinetic temperature	$\overline{T}_{k,w}$	6372-5264	K
Turbulent cascade			
$\sigma_v - l$ scaling exponent	q	1/3	
Observed velocity dispersion at l	$\sigma_{obs,w}$	8.02	km.s^{-1}
Turbulent velocity dispersion at l	$\sigma_{v_{z,w}}$	3.44-4.58	km.s^{-1}
Thermal velocity dispersion	$\sigma_{th,w}$	6.59-7.25	km.s^{-1}
Turbulent sonic Mach number at l	$\mathcal{M}_{s,w}(l)$	0.75-1.1	
Velocity dispersion at l=1 pc	$\sigma_{v_{z,w}}(1)$	0.68-0.90	km.s^{-1}
Turbulent sonic Mach number at 1 pc	$\mathcal{M}_{s,w}(1)$	0.14-0.22	
Sonic scale	λ_s	304-97	pc
Mean free path	λ	3.76-5.69$\times$10^{-4}	pc
Kinematic molecular viscosity	ν	4.89-6.71$\times$10^{20}	cm^2.s^{-1}
Knudsen number	K_n	2.89-4.38$\times$10^{-6}	
Reynolds number	Re_l	3.26-3.16$\times$10^5	
Dissipation scale	η	9.53-9.75$\times$10^{-3}	pc
Dissipation time	t_η	56-43	kyr
Energy transfer rate	ϵ	0.81-1.92$\times$10^{-4}	L$_\odot$M$_\odot^{-1}$
Ambipolar diffusion scale	l_{AD}	0.029-0.036	pc
Thermal instability			
Dynamical time	t_{dyn}	37.6-13.2	Myr
Cooling time	t_{cool}	2.10-2.35	Myr
Cooling length	λ_{cool}	17.23-17.25	pc
Condensation criterion	$\mathcal{I}$	0.057-0.178	
Field length	λ_F	0.090-0.109	pc

Tab. 5.2.: Summary of parameters extracted from the 21 cm local emission of the WNM in NEP. Quantities are divided in three: thermodynamic properties, properties of the turbulence cascade, and thermal instability criteria.

is made clear by the spatial power spectrum of the centroid velocity field presented previously. However, the largest spatial scale available in projection on the sky ($\sim$63 pc) is considerably lower than the scale L_z along the line of sight where turbulent velocity fluctuations $\sigma_{v_{z,w}}(L_z)$ are measured. Therefore, one may wonder to what extent the $\sigma_v - l$ relation observed in projection on the sky is applicable to the whole WNM in NEP. Does this scaling law extend to L_z ? As noted by Wolfire et al. (2003), it is likely that the outer scale of turbulence is greater that the disk thickness. As stated in the previous Sect. 5.1.3, the FWHM of the vertical distribution of the WNM has been estimated $\sim$ 530 pc (Dickey and Lockman, 1990). As Fig. 5.7 shows, the fluid reaches $\sim$400 pc, which at l=30° corresponds to a scale height of about 200 pc. Regarding the significant difference between the two and assuming that the outer scale of turbulence is greater than the disk thickness, we estimate that it is fair to extrapolate the $\sigma_v - l$ relation up to L_z.

The value of the exponent q is an important point to discuss here. As derived in Chapt. 2 we shall expect q=1/3 for incompressible turbulence, while for highly compressible turbulence (Burger turbulence) we

expect q=0.5 (Vogel, 2011). The more the turbulent sonic Mach number, the higher the compressibility. The transition between the two regimes is theoretically expected to occur around $\mathcal{M}_{s,w}(\lambda_s)$=1, where λ_s is defined as the sonic scale. So far, only one numerical simulation of compressible hydrodynamic turbulence has been able to resolve this transition using a resolution of 10.048^3 cells (Bastian et al., 2018). In particular, this simulation shows that the transition region around the sonic scale is about a factor 3 in l, and that the evolution between the two regimes is smooth. Based on this study, and since we concluded previously that the regime observed at about ∼130 pc is subsonic/transonic, it is likely that the scaling law characterizing the turbulent cascade varies between q=1/3 and q=0.5. However, since we are interested in extrapolating the scaling law on smaller scales, we shall use the value of q=1/3. Combining Eqs. 5.15 and 5.17, it follows

$$\mathcal{M}_{s,w} = \mathcal{M}_{s,w}(1)\, l_{pc}^{1/3}. \tag{5.18}$$

For $\mathcal{M}_{s,w}(\lambda_s)$=1, the sonic scale can be written as

$$\lambda_s = \mathcal{M}_{s,w}(1)^{-3} \tag{5.19}$$

Using Eq. 5.19, we computed the sonic scale λ_s of the WNM in NEP for 3.44 < $\sigma_{v_{z,w}}(L_z)$ (km.s^{-1}) < 4.58. We found 97 < λ_s (pc) < 304. It is interesting to note that the lower scale inferred here is not resolved by the power spectrum of the centroid velocity field presented Fig. 5.8. The values of q discussed previously would respectively translate into $P(k) \propto k^{-11/3}$ and $P(k) \propto k^{-4}$. We therefore expect to observed the value of "-11/3" on scale lower than λ_s. The value $\gamma_{v_{z,w}}$= -3.29±0.04, close to a Kolmogorov's "11/3" law, is in line with this picture of the turbulent cascade in the WNM having a sonic scale higher than the maximum scale available on the plane of sky in NEP, i.e ∼63 pc. A better sampling of high spatial scales could confirm a break in the scaling law of the projected velocity field and allow a parallel and complementary determination of the sonic scale in the WNM of NEP.

How does energy dissipate in the WNM of NEP ? In this section, we discuss the possible mechanisms of energy dissipation along the turbulent cascade. Figure 5.8 seems to indicate that the turbulent cascade is still present on a parsec scale (vertical dashed line in Fig. 5.8 at 300 pc). Below, no information is available in the data of this study. A higher spatial resolution would be required to continue this analysis at a smaller scale. However, knowing the thermodynamic properties of the gas, it is possible to extrapolate the properties of the turbulent cascade using two mechanisms: 1) the kinematic molecular diffusion, and 2) the ambipolar diffusion.

The kinematic molecular diffusion arises on a scale where the viscous forces become dominant. The viscosity of neutral fluid can be written as

$$\nu = \frac{1}{3}\lambda v_{th} \tag{5.20}$$

where we assume a mean free path λ=1/σn_w with σ=1×10^{-15} cm^2 for the hydrogen cross-section (Lequeux, 2012), and a thermal velocity v_{th}=$\sqrt{8/\pi}C_{s,w}$. We find 3.76×10^{-4} < λ (pc) < 5.69×10^{-4}. In the WNM of NEP, we find 4.89×10^{20} < ν (cm^2.s^{-1}) < 6.71×10^{20}. We can now derive the properties of the turbulent cascade down to the dissipation scale assuming a constant energy transfer rate ϵ. For

an isothermal gas, the Reynolds number and the sonic Mach number are directly linked through the Knudsen number Kn

$$Re_l = \sqrt{\frac{\pi}{2}} \frac{\mathcal{M}_{s,w}(l)}{Kn}. \tag{5.21}$$

where $Kn = \lambda/l$. At scale L_z in the WNM of NEP, we find $3.16\times10^5 < Re_l < 3.26\times10^5$ (see also Table 5.2 for the corresponding Knudsen numbers). The Reynolds number allows us to determine the dissipation scale, which as derived in Chapt. 2, can be written as

$$\eta = lRe^{-3/4}. \tag{5.22}$$

Using Eq. 5.22, we find $9.53\times10^{-3} < \eta$ (pc) $< 9.75\times10^{-3}$ which appears to be an order of magnitude higher than the mean free path of hydrogen atoms constituting the fluid. The dissipation time t_η is obtained using the viscosity and the dissipation scale and can be written as

$$t_\eta = \frac{\eta^2}{\nu}. \tag{5.23}$$

As Table 5.2 shows, we find $43 < t_\eta$ (kyr) < 56. Finally, combining the dissipation scale and the dissipation time, one can infer the energy transfer rate ϵ

$$\epsilon = \frac{\eta^2}{t_\eta^3}. \tag{5.24}$$

We find $0.88\times10^{-4} < \epsilon$ ($L_\odot M_\odot^{-1}$) $< 1.92\times10^{-4}$. It is interesting to compare this value with the energy transfer rate ϵ_{CNM} estimated in the CNM derived in Hennebelle and Falgarone (2012). They found $\epsilon_{CNM} \sim 10^{-3}$ which appears to be comparable to the value derived in the WNM of NEP. As noted by these authors, ϵ_{CNM} is considerably lower than the energy transferred to the ISM via UV and visible radiation from stars. It is therefore also the case for the WNM in NEP.

We now consider the case where ambipolar diffusion due to ion-neutral friction is the dominant mechanism of energy dissipation. Following Miville-Deschênes et al. (2017), the ambipolar diffusion typical scale is

$$l_{AD} = \sqrt{\frac{\pi}{\mu m_H}} \frac{B}{2X \langle\sigma v\rangle n_w^{3/2}} \tag{5.25}$$

where X=n_e/(n_e+n_w) is the ionization ratio with an electron density n_e=0.0213 cm^{-3} (Berkhuijsen et al., 2006), $\langle\sigma v\rangle$=2×10^{-9} cm^3 s^{-1} is the collision rate between ions and neutral assumed to be the Langevin rate, and B=6μG is the typical value of the magnetic field strength in the WIM/WNM of the solar neighborhood (Beck, 2001). As Table 5.2 shows, we find $0.029 < l_{AD}$ (pc) < 0.036. These values are typically a factor 3-4 higher than the dissipation scale inferred from the molecular viscosity. Given the possible variations of ionization fraction or magnetic field strength, these two scales could be comparable. Therefore, it seems difficult to conclude which mechanism dominates the turbulent energy dissipation in the WNM of NEP. More precise determinations of parameters of Eq. 5.25 would be necessary to improve this result.

5.5.3 Thermal condensation of the WNM in NEP

In this section, we present a qualitative description of the dynamical conditions under which a perturbation leading to a phase transition may or may not be inhibited. As stated in Chapt. 3, when the gas experiences a perturbation, i.e. it undergoes a compression, a condensation is possible if the cooling time of the fluid element is shorter than its dynamical time. Otherwise, the energy lost by radiation is small when compared to the increase of internal energy and the process can be considered as an adiabatic process (no transfer of heat between the system, i.e. the fluid element, and the surrounding medium). The system can therefore return to its initial state. The natural scale at which we define the dynamical time, noted t_{dyn}, is the sonic scale. It is indeed the scale where perturbations begin to become important in the fluid. At this scale, the information travels at sound speed $C_{s,w}$ and t_{dyn} can be written as

$$t_{dyn} = \frac{\lambda_s}{C_{s,w}}. \tag{5.26}$$

As Table 5.2 shows, we find 13.2 < t_{dyn} (Myr) < 37.6 in the WNM of NEP. Following Eq. 3.32, the cooling time t_{cool} can be written as

$$t_{cool} = \frac{k_B \overline{T}_{k,w}}{(\gamma - 1) n_w \Lambda(\overline{T}_{k,w})} \tag{5.27}$$

where $\Lambda(T_{k,w})$ is the cooling function based on the standard model from Wolfire et al. (2003) shown in Fig. 5.11. Note that we only consider here a standard ISRF G_0=1.7. We find 2.10 < t_{cool} (Myr) < 2.35, which is considerably lower than the dynamical time. We define the condensation criterion $\mathcal{I}$ such as the ratio between t_{cool} and t_{dyn}:

$$\mathcal{I} = \frac{t_{cool}}{t_{dyn}} < 1 \tag{5.28}$$

For each volume filling factor considered, $\mathcal{I}$ is satisfied in the WNM of NEP. This result shows that when a parcel of fluid undergoes a compression, the condensation mode of the thermal instability can grow freely and lead to the formation of CNM structures. An alternative and equivalent way to define this condensation criterion is to compare directly the dynamical scale (here the sonic scale) to the cooling length. The cooling length can be also seen as the scale at which the WNM is non-linearly unstable (Audit and Hennebelle, 2005)

$$\lambda_{cool,w} = C_{s,w}\, t_{cool,w}. \tag{5.29}$$

In the WNM of NEP, we find 17.23 < λ_{cool} (pc) < 17.25 < λ_s. In other words, we find that at a scale of about 17 pc, the fluid is non-linearly unstable and can undergo a condensation. Finally, since condensations of fluid parcels are possible in the WNM of NEP, it is interesting to calculate the Field length. The Field length (Field, 1965), also called the conduction length is the length at which the radiative heating and cooling processes become comparable to thermal diffusion and is defined as

$$\lambda_F = \sqrt{\frac{\kappa(\overline{T}_{k,w})\, \overline{T}_{k,w}}{n_w^2\, \Lambda(\overline{T}_{k,w})}} \tag{5.30}$$

where κ=2.5$\times$10$^3\overline{T}_{k,w}^{1/2}$ erg cm^{-1}K^{-1}s^{-1} is the thermal conductivity for hydrogen atoms (Parker, 1953). It is also the typical size of the front between the WNM and the CNM. We find 0.090 < λ_F (pc) < 0.109 in the WNM of NEP.

5.6 Discussion

Our current knowledge of the thermodynamical state of the neutral ISM comes from the joint analysis of emission-absorption spectra toward radio-sources. Statistical properties of turbulence in the CNM have been studies using this technique but the properties of the turbulent cascade acting in the WNM has remained elusive due to: 1) the difficulty of extracting its signal from hyper-spectral observation of the 21 line in emission, and 2) the difficulty of disentangling thermal and turbulent velocity dispersions from the observed velocity dispersion of the emission line. In this study, we have demonstrated that the use of ROHSA to perform a multiphase separation of the fluid, and the determination of typical length scales using 3D dust extinction mapping allow the determination of both the thermal and turbulent properties of the WNM.

Statistical analysis of integrated column density field and mass fraction of each phase have revealed important variations over a relatively small part of the sky, covering $12^\circ \times 12^\circ$ at high Galactic latitude. In particular, the studied region centred on the north ecliptic pole shows a very low CNM mass fraction (<0.1). The comparison with the results of the 21-Sponge survey has shown that NEP covers a lower range of column density but with more statistics. The multiphase decomposition of lower latitude observations would allow us to probe regions with higher column densities.

We would like to point out that the use of a 3D dust extinction map is an important ingredient of this work. Having access to the physical scale length observed, along the line-of-sight and on the plane of sky, is key to understand the thermal and turbulent properties of the neutral ISM using 21 cm hyper-spectral data. In this study, a mean dust extinction profile has been used to quantify the topology of the fluid over a 12° $\times$ 12° region. The use of the information contained in these 3D dust extinction maps will be an important element in the future to progress in understanding the properties of the neutral ISM over larger regions of the sky.

The extraction of CNM structures from the rest of the fluid has allowed us to use it as tracer particles to probe the turbulent velocity dispersion of the WNM over scales of $\sim$130 pc. To our knowledge, it is the first time that this technique is used. The use of the centroid velocity field of the WNM to disentangling thermal and turbulent velocity dispersion components have highlighted the importance of the volume filling factor of the WNM when analyzing the statistics of projected quantities such as the column density field and centroid velocity field. In particular, we have shown that the unstable gas observed in NEP is likely to occupy an important fraction of the volume, reducing the volume filling factor of the WNM. The impact of coherent structures of diffuse ionized gas has been also briefly discussed.

The thermal properties of the WNM extracted from NEP are in good agreement with theoretical predictions based on heating and cooling processes acting in the neutral ISM. The observed fluid seems to be in thermal equilibrium. The statistical properties of the turbulent cascade acting in the WNM show that under 97 < λ_s (pc) < 304 the turbulence is subsonic. Extrapolating these properties to smaller scales, we find that the typical velocity dispersion at a scale of 1 pc is in the range 0.68 < $\sigma_{v,w}(1)$ (km.s^{-1}) < 0.90. This range is remarkably close to the velocity dispersion obtained in molecular clouds (Hennebelle and Falgarone, 2012; Miville-Deschênes et al., 2017b). It is also the case for the observed energy transfer rate 0.88 $\times 10^{-4}$ < ϵ ($L_\odot M_\odot^{-1}$) < 1.92 $\times 10^{-4}$ in the WNM. These similarities

suggests that properties of the turbulent cascade in molecular clouds have a possible connection with the energy injected on very large scales, in the WNM.

Thermal and turbulent properties have allowed us to study the dynamical and static scales involved in the condensation mode of the thermal instability. The relatively low strength of turbulence observed in the WNM of NEP coupled to the thermal state of the gas shows that thermal instabilities can grow freely to form cold dense structures observed in the CNM. In particular we have confirmed theoretical prediction of the typical length scale where the warm gas is non-linearly unstable (Hennebelle and Pérault, 1999). In addition we provide, to our knowledge, the first determination of the Field length $0.090 < \lambda_F \text{ (pc)} < 0.109$, also coherent with theoretical predictions.

5.7 Summary

Here we present a new study of the multiphase neutral ISM based on the analysis of 21 cm emission observations of a high latitude field centred on the north ecliptic pole. ROHSA have been used to model a coherent view of the local WNM, LNM and CNM phases. Statistical analysis of integrated density fields and mass fraction maps have been performed. Typical length scales of the WNM have been determined using 3D dust extinction map. Two independent methods have been used to disentangle the mean thermal and turbulent velocity dispersion components from the mean observed velocity dispersion in the WNM. Based on an apparent discrepancy between the two methods, we introduced and discussed the volume filling factor of the WNM. Using previous considerations, a realistic range of turbulent velocity dispersion and volume filling factor were defined in order to study the thermal and turbulent properties of the WNM in NEP. The main conclusions are as follows.

1. Mass fraction maps of the three-phase view of NEP shows that considerable variations are observed over 12°$\times$ 12° patch of the sky.
2. Determination of typical length scales of the observed fluid have allowed us to disentangle thermal and turbulent velocity dispersions in the WNM of NEP.
3. Temperature and pressure of the WNM in NEP are respectively in ranges $5264 < T_{k,w} \text{ (K)} < 6372$, and $3000 < \overline{P}_w/k \text{ (K cm}^{-3}) < 5489$.
4. The sonic scale of the WNM in NEP is $97 < \lambda_s \text{ (pc)} < 304$.
5. The condensation criterion $0.057 < \mathcal{I} < 0.178$ of the thermal instability if significantly lower than 1 (i.e., the cooling time t_{cool} is significantly lower than the dynamical time t_{dyn}), showing that instabilities associated with compression on scales higher than $17.23 < \lambda_{cool} \text{ (pc)} < 17.25 < \lambda_s$ in the WNM can grow freely to form CNM structures.
6. The Field length (typical size of the front between the WNM and the CNM) is $0.090 < \lambda_F \text{ (pc)} < 0.109$.
7. The energy transfer rate of the turbulent cascade is $0.88 \times 10^{-4} < \epsilon \text{ (L}_\odot\text{M}_\odot^{-1}) < 1.92 \times 10^{-4}$. This is comparable to values observed in molecular clouds.

6 Conclusion and perspectives

Conclusion The study of the neutral interstellar medium within our galaxy is incredibly rich in terms of the quality of the observations available, namely their spatial and spectral resolution. This in particular allowed to reveal the richness of the environments that constitute the neutral ISM, illustrating the complexity of the dynamical character of this open system that is the Milky Way. One of the main challenges mentioned in Chapt 3 to understand this complexity seems to be related to understanding the thermal condensation of the WNM. Whether it is located along a shell wall, in HVCs of the Galactic corona, or in the diffuse inter-cloud medium of the Galaxy, everything seems to indicate that this gas is able to form dense and cold structures. In addition, as stated in Chapt. 2, the ubiquitous nature of turbulence in the ISM seems to be an important parameter of this condensation process. The understanding of the formation of this condensed cold gas is key to understanding the life cycle of galaxies since it is at the origin of the HI-H2 transition which is the first process of molecular cloud formation. The analysis of hyper-spectral observations as part of the study of the neutral interstellar medium, and more generally for interstellar gas, is a major challenge. In this thesis, we present an original work whose goal is to provide new techniques and insights about the multiphase structure of the neutral ISM in galaxies.

In Chapt. 4, we developed a new Gaussian decomposition algorithm named `ROHSA`. `ROHSA` uses a regularized non-linear least-square criterion to take into account simultaneously the spatial coherence of the emission and the multiphase nature of the gas. The evaluation of `ROHSA` on synthetic 21 cm observations shows that it is able to recover the multiphase nature of the HI. For each phase, the power spectra of the column density and centroid velocity are well recovered. More generally, this test reveals that a Gaussian decomposition of HI emission is able to recover physically meaningful information about the underlying three-dimensional fields (density, velocity, and temperature). The application on a real 21 cm observation of a field at high Galactic latitude produces a picture of the multiphase HI, with isolated, filamentary, and narrow ($\sigma \sim 1-2\,\mathrm{km\,s^{-1}}$) structures, and broader ($\sigma \sim 4-10\,\mathrm{km\,s^{-1}}$), diffuse, and space-filling components. The test-case field used here contains significant intermediate-velocity clouds that were well mapped out by the algorithm. As `ROHSA` is designed to extract spatially coherent components, it performs well at filtering out the noise. `ROHSA` makes no assumption about the nature of the sources, except that each one has a similar line width. The tests we made show that `ROHSA` is well suited to decompose complex 21 cm line emission of regions at high Galactic latitude, but its design is general enough that it could be applied to any hyper-spectral data type for which a Gaussian model is relevant.

In Chapt. 5, we demonstrated the ability to extract the thermal and turbulent properties of the warm diffuse phase of the neutral ISM from a joint analysis of 21 cm hyper-spectral data and 3D dust extinction mapping in the vicinity of the Sun. In particular, the multiphase decomposition of the 21 cm line using `ROHSA` allowed us to analyze the properties of the turbulent velocity field of the WNM using two independent methods. The first method consists of using cold structures of CNM, occupying a very

small volume of the fluid, as tracer particles. The second one directly uses the centroid velocity field of the WNM. These two methods, seemingly incompatible, are reconciled when considering the volume filling factor of the WNM (< 1, due to a significant fraction of the LNM and ionized gas) for the statistical study of projected quantities. This work shows that thermal properties are in agreement with previous studies based on emission-absorption measurement toward radio sources. Statistical properties of the turbulent cascade acting in the WNM are for the first time highlighted from an observational point of view and are in agreement with theoretical predictions. Static and dynamical scales related to the condensation mode of the thermal instabilities show that thermal and turbulent properties are compatible with a two phase description of the gas where cold dense CNM structures are originated from the thermal condensation of the warm diffuse phase, the WNM.

Perspectives The methodology presented here is only based on the emission line of the neutral hydrogen. We believe that, with the emission-absorption measurement technique, it provides a complementary approach for the study of the neutral gas. Since both methods are based on a Gaussian model, an interesting perspective to combine these two approaches would be to consider the development of a new code where all the information (fully sampled emission data and absorption measurements on discrete lines of sight) would be taken into account together in the cost function of this optimization problem.

ROHSA has demonstrated that it is possible to push the limits of a Gaussian description of hyper-spectral data. However, freeing oneself from this Gaussian aspect is a very conceivable option. Several works are in progress to experiment with this (e.g., Claire Murray talk during the GAIA Ψ^2 program, 2018). In particular, methods using deep neural networks open up a wide range of possibilities for the exploration of source separation algorithms in hyper-spectral observations.

The methodology presented in Chapt. 5 to study the thermal and turbulent properties of WNM must be reproduced in other directions of the sky, tracing similar or different environments. This should provide us with a new perspective on the variations of the properties of this phase and the associated physical phenomena. An interesting question would be to study the properties of the multiphase HI in the chimney of the Local Bubble instead of pointing toward its wall. One could expect considerable variations in such environments.

The ability to perform multiphase separations of the 21 cm line will allow to study with unprecedented detail the condensation of diffuse warm gas in a wide variety of environments such as those described in Chapt. 3. Among them, the use of ROHSA to build new catalogues of IVCs and HVCs with a description of the multiphase state of the fluid constituting each structure is now possible. As discussed in Chapt. 3, the determination of the thermal state of the gas accreted from the Galactic corona, providing gas supply to our Galaxy, is of primary interest for the understanding of star formation in the Milky Way.

In terms of data analysis, the work initiated here is of primary interest for the preparation of next generation telescopes. In particular, the construction of the Square Kilometer Array (SKA) presents a major technological challenge. The amount of data generated by this radio telescope will exceed anything we are currently able to store. Real-time data analysis and compression is therefore of major interest. ROHSA is a perfect example of a software precursor since it allows both the compression of data in Gaussian form and a first fundamental step in their analysis, the spatially coherent multiphase

separation. In order to go further and really provide an efficient tool for SKA, a GPU implementation of ROHSA is required. Fortunately, this work is under development.

Finally, as stated in Chapt. 4, ROHSA is general enough to be applied to any kind of hyper-spectral observations. Consequently, we would like to point out that this work (Chapt. 4) should open a wide range of possibilities for other subjects and communities. For example, ROHSA has already proved its worth in the study of carbonaceous nano-grains features in the protoplanetary disks observed in the near infrared range. In particular, it allows to produce emission maps of different dust features (Boutéraon et al. 2019 in prep.).

Spatial power spectrum analysis

A

A.1 Spatial power spectrum of the column density field

To understand the behaviour of the spatial power spectrum of the projected density of the WNM in NEP, we discuss in this section the power spectra of the total emission (hereafter TOT), the CNM, the LNM and the WNM, respectively shown in Figs. A.1, A.2, A.3 and A.4. To estimate the $P(k)$, we follow the same methodology as Martin et al. (2015) and Miville-Deschênes et al. (2016). Each power spectrum $P(k)$ is the azimuthal average of the modulus of the Fourier transform of the corresponding field, and is modelled as

$$P(k) = B(k) \times P_0 k^{\gamma} + N(k) \tag{A.1}$$

where, P_0 is the amplitude of the power spectrum, γ is the scaling exponent, $B(k)$ is the beam of the instrument assuming a 2D Gaussian of FWHM = 9.24', and $N(k)$ is the noise estimated by taking the

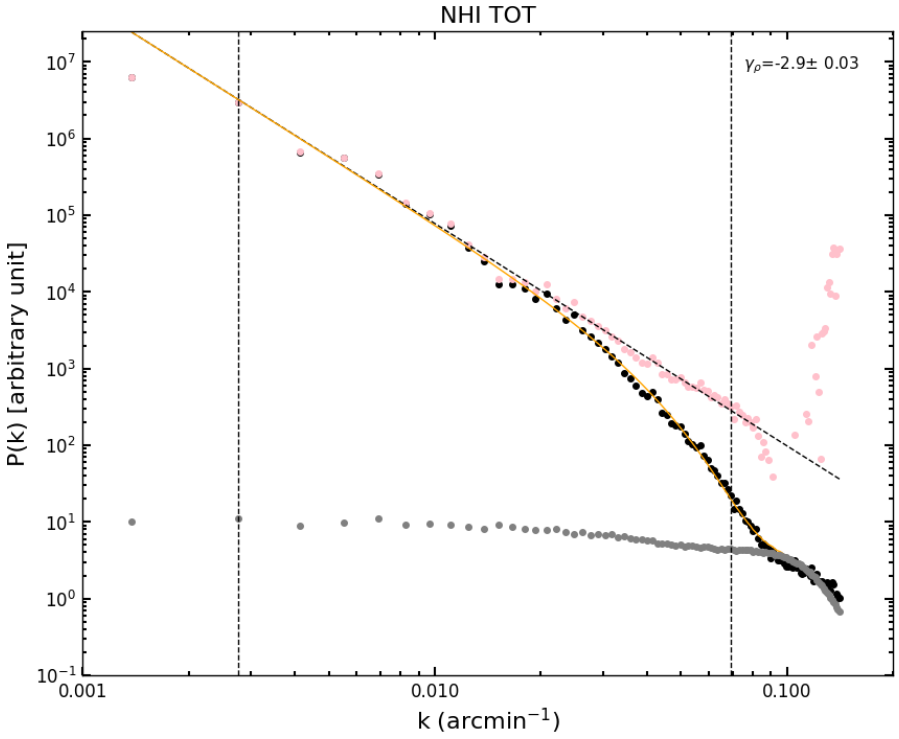

Fig. A.1.: Spatial power spectrum model of the integrated column density field of the total local emission in NEP. $\langle P_{N_{HI}} \rangle (k)$ is given by the black dots. Grey points represent the noise component $N(k)$. Pink points show the corrected power spectrum ($P(k) - N(k)/B(k)$). The dotted line shows the fit of the corrected power spectrum between the two vertical dashed line, and the orange line shows the result of the global modeling of Eq. A.1. The power spectrum index is γ_ρ = -2.90±0.03.

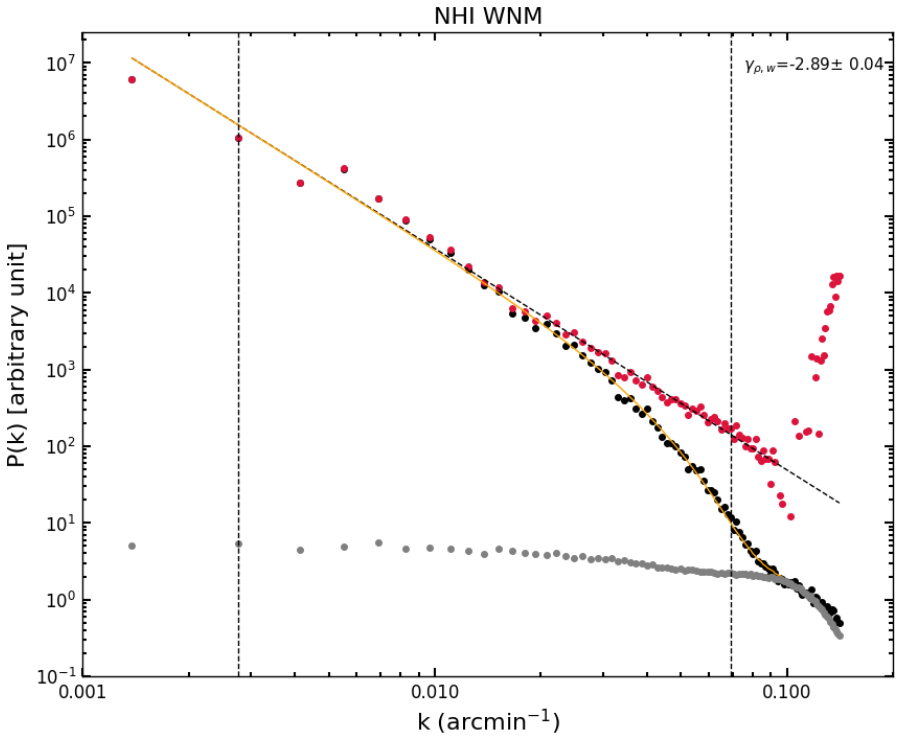

Fig. A.2.: Spatial power spectrum model of the integrated column density field of the WNM in NEP. $\left\langle P_{N_{HI,w}} \right\rangle (k)$ is given by the black dots. Grey points represent the noise component $N(k)$. Red points show the corrected power spectrum ($P(k) - N(k)/B(k)$). The dotted line shows the fit of the corrected power spectrum between the two vertical dashed line, and the orange line shows the result of the global modeling of Eq. A.1. The power spectrum index is γ_{ρ_w} = -2.89±0.04.

power spectrum of empty channels of the PPV cube. Finally, edges of the image are apodized using a cosine function to avoid effect due to the replication done by the Fourier transform algorithm.

The spatial power spectrum of the TOT is well fitted by a power spectral index γ_ρ=-2.90±0.03. Note that Martin et al. (2015) performed the same analysis using the total emission of the local gas in NEP defined between -20.5 < v_z (km.s^{-1}) < 47.9. Here we use all components extracted with ROHSA whose centroid velocities are between -20 < v_z (km.s^{-1}) < 20. Despite this difference, we find a power spectrum index in agreement within errors with Martin et al. (2015) who found γ_ρ^{M15}=-2.86±0.04. We find a power spectrum index $\gamma_{\rho,w}$=-2.89±0.04 in the WNM slightly steeper that Martin et al. (2015) who found $\gamma_{\rho,w}^{M15}$=-2.70±0.1. Note however, that the WNM presented in Martin et al. (2015) is a combination of our WNM and LNM. In the LNM, we find $\gamma_{\rho,l}$=-2.84±0.03, which is close to $\gamma_{\rho,w}$. Finally, we find a power spectrum index $\gamma_{\rho,c}$=-2.48±0.04 in the CNM. This value is not in agreement with Martin et al. (2015) who found $\gamma_{\rho,c}^{M15}$=-1.90±0.1. We think that this difference is likely to be due to additional noise introduced in their Gaussian decomposition (see Chapt. 4 for more details about the decomposition perform by Martin et al. (2015)) and visible on small scales of their power spectrum (see Fig. 9 Martin et al. (2015)). Introduction of noise on small scales is likely to induce a flattening of the power spectrum.

Despite this difference, we conclude that the tendency is the same as what was found by Martin et al. (2015), with $\gamma_{\rho,w} \sim \gamma_{\rho,l} > \gamma_{\rho,c}$, and argue that this behaviour reflects the condensation of WNM in the

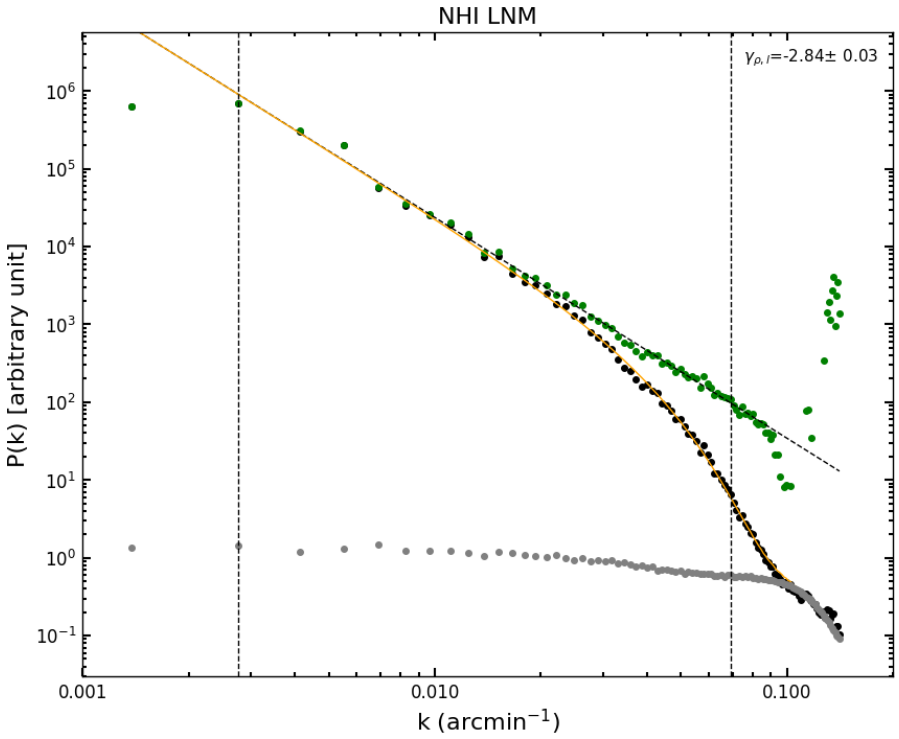

Fig. A.3.: Spatial power spectrum model of the integrated column density field of the LNM in NEP. $\left\langle P_{N_{HI,l}} \right\rangle (k)$ is given by the black dots. Grey points represent the noise component $N(k)$. Green point show the corrected power spectrum ($P(k) - N(k)/B(k)$). The dotted line shows the fit of the corrected power spectrum between the two vertical dashed line, and the orange line shows the result of the global modeling of Eq. A.1. The power spectrum index is γ_{ρ_l} = -2.84±0.03.

neutral gas of NEP. Indeed, the denser the phase, the flatter the power spectrum. In other words, cold gas has more power on small scale than lukewarm and warm gas. This picture is coherent with the vision of a bi-stable fluid shaped by the thermal instability since the volume occupied by the CNM in this scenario is a small fraction of the space. This is also in agreement with the discussion presented in Sect. 5.1.3 where we concluded that the correlation between the mass fraction and the volume filling factor of the gas also implies that the CNM occupies a small fraction of the volume.

Since the WNM is likely to occupy a large fraction of the space and has been dissociated from low temperature gas with large density contrasts, it opens the possibility to compare $\gamma_{\rho,w}$ with predictions from numerical simulations of isothermal and compressible turbulence. For example, Kim and Ryu (2005) investigated the behaviour of the velocity and density power spectrum of numerical simulations of isothermal, compressible turbulence and found that both spectra follow the Kolmogorov's "5/3" law if the turbulent fluid is subsonic/sonic. On the other hand, when increasing the strength of turbulence (by increasing the turbulent sonic Mach number), they found that the power spectrum index of the density field decrees due to presence of discontinuities of weak shocks. Following this comparison, $\gamma_{\rho,w}$=-2.89±0.04 would correspond to a supersonic turbulence, characterized by $\mathcal{M}_s$ ∼3-5. At first glance, this value seems incompatible with the commonly accepted idea of subsonic/sonic turbulence in the WNM. One can have an idea of the turbulence strength in the WNM by considering a typical temperature $\overline{T}_k$ = 7000 K (i.e $\overline{\sigma}_{th,w}$ = 7.6 km.s^{-1}) and the mean velocity dispersion $\overline{\sigma}_{obs}$ = 8 km.s^{-1} along the line-of-sight in NEP. Modeling $\overline{\sigma}_{obs}$ by a quadratic sum of a thermal and a turbulent velocity

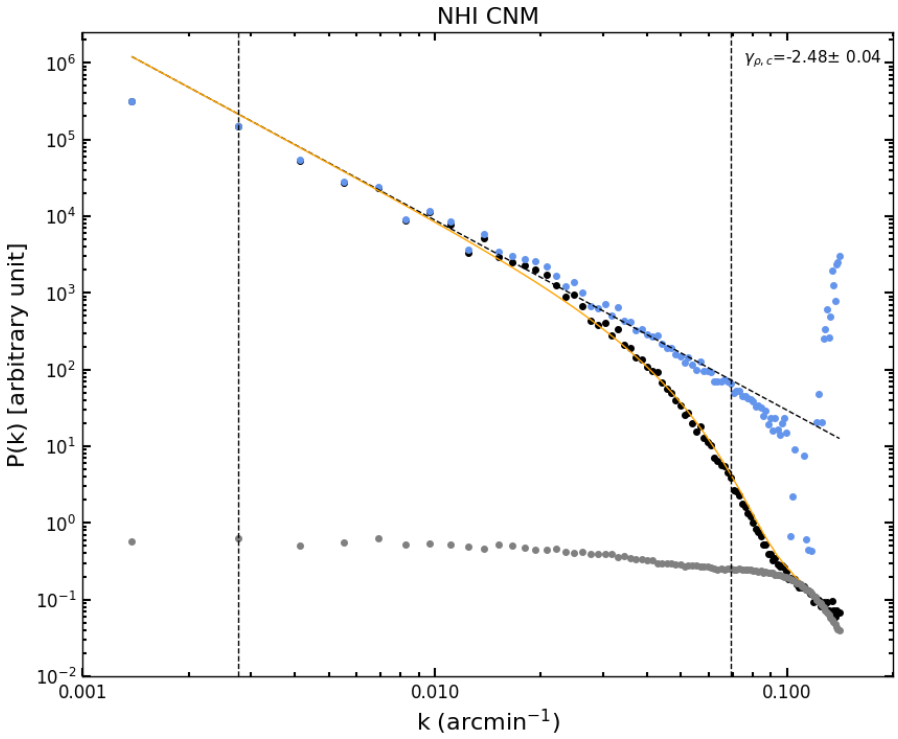

Fig. A.4.: Spatial power spectrum model of the integrated column density field of the CNM in NEP. $\left\langle P_{N_{HI,c}} \right\rangle (k)$ is given by the black dots. Grey points represent the noise component $N(k)$. Blue point show the corrected power spectrum $(P(k) - N(k)/B(k))$. The dotted line shows the fit of the corrected power spectrum between the two vertical dashed line, and the orange line shows the result of the global modeling of Eq. A.1. The power spectrum index is γ_{ρ_c} = -2.48±0.04.

dispersion, the corresponding turbulent sonic Mach number is $\overline{\mathcal{M}}_{s,w}$ = 0.67. Note however that the Mach number computed here corresponds to the depth of the fluid along the line-of-sight (see also the following Sect. 5.5.2), which is higher than the scales probed by the power spectrum, corresponding to the scales projected on the sky (∼12°, and ∼63 pc halfway down the 130 pc depth along the line-of-sight). Consequently, $\overline{\mathcal{M}}_{s,w}$ on scales probed by the power spectrum should be somehow lower than this value. What can then be the causes of this flattening of the power spectrum ? A possible answer to that question is the footprint caused by the LNM in the WNM column density map. We believe that it is likely to introduce power on a range of scales and to change the value of the power spectrum index. A numerical experiment showing the impact of the volume filling factor of the LNM in the power spectrum analysis of the projected column density of the WNM is addressed in following Sect. A.2.

A.2 Impact of volume filling factor on the statistics of projected quantities

The interpretation of power law slopes of projected quantities, like the column density and the centroid velocity, has been the subject of several theoretical and numerical studies in the past 20 years (e.g., Miville-Deschênes et al., 2003b). The general consensus is that the power spectrum of column density, estimated from optically thin lines, is a reliable proxy for the power spectrum of the 3D density field. As

mentioned earlier, the centroid velocity is a reliable proxy for the velocity field only in the limit of small 3D density contrasts.

All the previous studies devoted to the understanding of the link between the statistical properties of projected and 3D fields are based on the assumption that the fluid that projects on the sky fills the 3D volume completely. In reality this is rarely satisfied. For instance, the properties of molecular clouds are often analyzed using line tracers like ^{12}CO or ^{13}CO that depend strongly on the local gas volume density. This provides information only about the densest part of the fluid in 3D.

One could think that HI is less affected by this density effect and that the 21 cm emission would be a more reliable tracer of the whole 3D volume. This is most probably the case for the whole 21 cm emission but then the difficulty lies in the estimate of the statistical properties of a 3D multi-phase fluid with density contrasts of the order of 100-1000.

The separation of the thermal phases from the 21 cm emission data with *ROHSA* allows the extraction of the low density WNM, opening the possibility to study interstellar turbulence by comparing its multi-scale statistics of density and velocity to the ones of controlled numerical experiments of isothermal turbulence. In this context, one interesting question is to what extent the fact that WNM does not occupy the full volume on the line of sight affects the relationship between the statistical properties of the 3D fields (density and velocity) and the projected quantities (column density and centroid velocity). To our knowledge, this has never been explored specifically.

The evaluation of the effect of a partial filling of a fluid on the projected quantities is clearly beyond the scope of this thesis. In fact it is a rather ill-defined problem as one needs to define the statistics of the physical fields (density, velocity) as well as the 3D shape of the volume occupied by the fluid. That shape of that mask is likely to be defined by a density threshold in the case of CO emission or CNM structures. For the more diffuse inter-cloud HI medium (LNM and WNM), the shape of the volume is probably related to the temperature field, linked to heating and cooling processes. So it could be partly related to the density field but also to the radiation field intensity field. A proper study of this effect should be done with dedicated numerical simulations of the multi-phase ISM. In order to explore the main trends of the expected effects, we present a short study based only on fractional Brownian motion fields.

A.2.1 Density field

Let's first look at the effect on the column density. To do so we have constructed 3D density fields $n_H(r)$ over a grid of $128 \times 128 \times 256$ pixels. We have chosen to produce 3D cubes with a depth (L_z) twice the size in $[x, y]$ to mimic an observation like NEP. The statistics of $n_H(r)$ are assumed to follow a log-normal distribution, with $\delta(n_H)/ < n_H >= 1$, and a 3D power spectrum slope of $\gamma_n = -11/3$, reminiscent of what is seen for compressible, sub or trans-sonic turbulent flows.

With such low value of $\delta(n)/ < n >$, the power spectrum of the column density $N_H = \sum_z n_H \, dz$ integrated over the full volume has the same slope as the 3D density field : $\gamma_N = \gamma_n$. The question is what is the power spectrum slope of N_H if a fraction of the volume is removed from n_H. We have

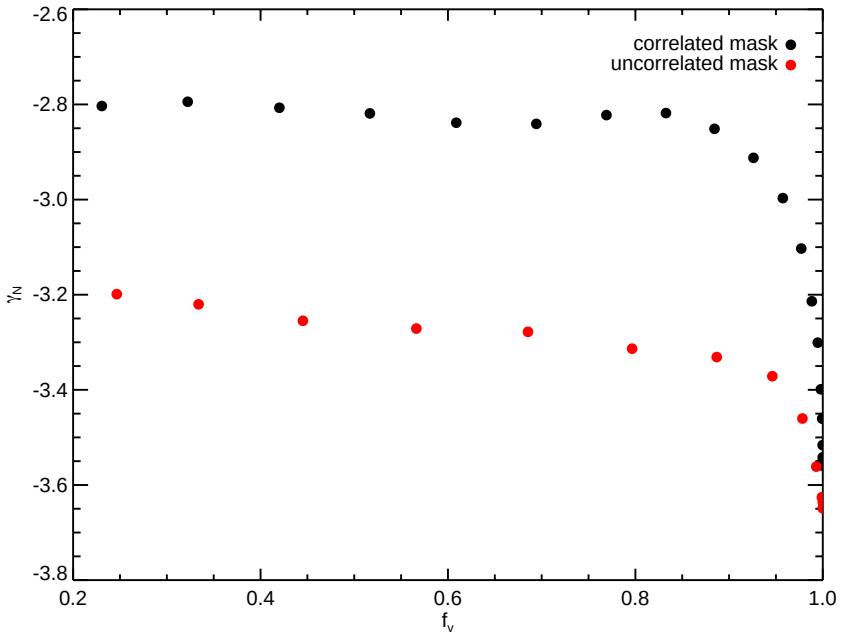

Fig. A.5.: Power spectrum slope of the column density resulting from the projection of 3D density fields with partial 3D sampling.

explored two possibilities: 1) a threshold in density and 2) a mask independent of density. In the first case we have gradually put to zero the density values above a given threshold. As the threshold is lowered, the volume filling factor of the gas gets smaller.

In the second case, $n_H(r)$ is put to zero in region based on a second independent field $m(r)$. At this point it is difficult to evaluate what should be the statistics of $m(r)$. We decided to use a positive, low contrast ($\sigma(m)/ < m >$ = 1/5) Gaussian field with a power spectrum slope of -11/3. Like for the first case, region of n_H are put to zero but here we use the criteria on m, where $m > m_0$. As m_0 is lowered, larger and larger region of n_H are put to zero, lowering the volume filling factor.

Figure A.5 shows the power spectrum slope of γ_N recovered in both cases, as a function of the volume filling factor f_v. The black and red points corresponds to case 1) and 2) respectively. As expected, when the fluid occupies to full volume ($f_v = 1$), we recover the result $\gamma_N = \gamma_n$. The main result we obtained is that, as the volume filling factor is lowered, the power spectrum slope increases (the $P(k)$ is flatter). Interestingly it seems that γ_N reaches an almost constant value for $f_v < 0.8$, both that value depends on the way the 3D mask is built.

The main result here is the fact that a volume filling factor lower than unity introduces a systematic bias in the determination of the 3D density slope from the column density. A value of $f_v < 1$ systematically flattens the power spectrum. The power spectrum slope γ_N obtained from observations provides an upper limit of the true value of γ_n. The effect is important. According to our little experiment it could be as much as $\gamma_n = \gamma_N - 1$. This has important consequences on the use of the column density power spectrum slope to constrain the properties of turbulence, the Mach number in particular (Kim and Ryu, 2005).

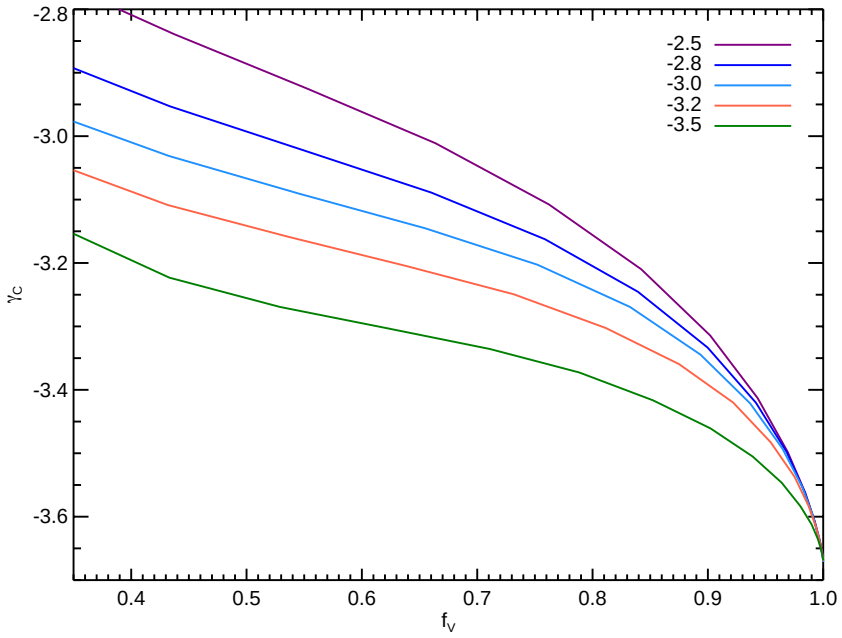

Fig. A.6.: Power spectrum slope of the centroid velocity field as a function of the volume filling factor of the fluid. The masked regions are defined using a gradual threshold on a log-normal density field with a power spectrum slope γ_n. The different curves show the result for a range of γ_n.

A.2.2 Velocity field

We developed a similar experiment for the velocity field. We built uncorrelated 3D density and velocity cubes, $n(r)$ and $v_z(r)$, using the same method as previously. The velocity field has a Kolmogorov slope ($\gamma_v = -11/3$). The masking is done on n, by removing pixels in 3D where the density if above a given threshold $n > n(0)$. Then the centroid velocity field C is estimated by calculating the average velocity on each line of sight, using only the unmasked pixels. Like for the column density field case, the partial filling of the 3D volume introduces a bias in the projected field. Whatever the statistical properties of the masking field, the power spectrum slope of the centroid velocity is flatter than the true 3D value. We note thought that the effect is less dramatic than for the column density field.

Interestingly, the slope of the centroid velocity of the WNM (see Fig. 5.8) is $\gamma_C = -3.29$ which is flatter than the expected -11/3 value. Nevertheless we note that the effect of a partial volume filling factor of the WNM could easily explain that difference. Therefore from the power spectrum of the centroid velocity itself it is impossible to conclude on the nature of the turbulence, especially on its Mach number. Nevertheless we note that our results are compatible with $\gamma_v = -11/3$, the expected value for sub and trans-sonic turbulence.

B

Publication in Astronomy & Astrophysics

B.1 ROHSA : Regularized Optimization for Hyper-Spectral Analysis - Application to phase separation of 21 cm data

A&A 626, A101 (2019)
https://doi.org/10.1051/0004-6361/201935335

Astronomy & Astrophysics

ROHSA: Regularized Optimization for Hyper-Spectral Analysis*

Application to phase separation of 21 cm data

Antoine Marchal[1,2], Marc-Antoine Miville-Deschênes[1], François Orieux[2,3], Nicolas Gac[3], Charles Soussen[3], Marie-Jeanne Lesot[4], Adrien Revault d'Allonnes[4], and Quentin Salomé[5]

[1] AIM, CEA, CNRS, Université Paris-Saclay, Université Paris Diderot, Sorbonne Paris Cité, 91191 Gif-sur-Yvette, France
[2] Institut d'Astrophysique Spatiale, CNRS UMR 8617, Université Paris-Sud 11, Batiment 121, 91405 Orsay, France
e-mail: antoine.marchal@ias.u-psud.fr
[3] Laboratoire des Signaux et Systèmes (CNRS, CentraleSupélec, University of Paris-Sud), Université Paris-Saclay, 91192 Gif-sur-Yvette, France
[4] LIP6, Université Pierre et Marie Curie-Paris 6, UMR7606, 4 Place Jussieu Paris cedex 05, 75252 Paris, France
[5] Instituto de Radioastronomía y Astrofísica, Universidad Nacional Autónoma de México, 58089 Morelia, Mexico

Received 21 February 2019 / Accepted 29 April 2019

ABSTRACT

Context. Extracting the multiphase structure of the neutral interstellar medium is key to understanding star formation in galaxies. The radiative condensation of the diffuse warm neutral medium producing a thermally unstable lukewarm medium and a dense cold medium is closely related to the initial step leading the atomic-to-molecular (HI-to-H_2) transition and the formation of molecular clouds. Up to now, the mapping of these phases out of 21 cm emission hyper-spectral cubes has remained elusive mostly due to the velocity blending of individual cold structures present on a given line of sight. As a result, most of the current knowledge about the HI phases rests on a small number of absorption measurements on lines of sight crossing radio sources.
Aims. The goal of this work is to develop a new algorithm to perform separation of diffuse sources in hyper-spectral data. Specifically the algorithm was designed in order to address the velocity blending problem by taking advantage of the spatial coherence of the individual sources. The main scientific driver of this effort was to extract the multiphase structure of the HI from 21 cm line emission only, providing a means to map each phase separately, but the algorithm developed here should be generic enough to extract diffuse structures in any hyper-spectral cube.
Methods. We developed a new Gaussian decomposition algorithm named ROHSA based on a multi-resolution process from coarse to fine grid. ROHSA uses a regularized nonlinear least-square criterion to take into account the spatial coherence of the emission and the multiphase nature of the gas simultaneously. In order to obtain a solution with spatially smooth parameters, the optimization is performed on the whole data cube at once. The performances of ROHSA were tested on a synthetic observation computed from numerical simulations of thermally bi-stable turbulence. We apply ROHSA to a 21 cm observation of a region of high Galactic latitude from the GHIGLS survey and present our findings.
Results. The evaluation of ROHSA on synthetic 21 cm observations shows that it is able to recover the multiphase nature of the HI. For each phase, the power spectra of the column density and centroid velocity are well recovered. More generally, this test reveals that a Gaussian decomposition of HI emission is able to recover physically meaningful information about the underlying three-dimensional fields (density, velocity, and temperature). The application on a real 21 cm observation of a field of high Galactic latitude produces a picture of the multiphase HI, with isolated, filamentary, and narrow ($\sigma \sim 1$–$2\,\mathrm{km\,s^{-1}}$) structures, and broader ($\sigma \sim 4$–$10\,\mathrm{km\,s^{-1}}$), diffuse, and space-filling components. The test-case field used here contains significant intermediate-velocity clouds that were well mapped out by the algorithm. As ROHSA is designed to extract spatially coherent components, it performs well at projecting out the noise.
Conclusions. In this paper we introduce ROHSA, a new algorithm that performs a separation of diffuse sources in hyper-spectral data on the basis of a Gaussian decomposition. The algorithm makes no assumption about the nature of the sources, except that each one has a similar line width. The tests we made shows that ROHSA is well suited to decomposing complex 21 cm line emission of regions of high Galactic latitude, but its design is general enough that it could be applied to any hyper-spectral data type for which a Gaussian model is relevant.

Key words. ISM: clouds – ISM: kinematics and dynamics – ISM: structure – methods: data analysis – methods: numerical – methods: observational

1. Introduction

Star formation in galaxies is strongly linked to the physical processes that govern the evolution of the interstellar medium (ISM). Stars form by gravitational collapse of dense ($n > 10^4\,\mathrm{cm^{-3}}$) and cold ($T \sim 10\,\mathrm{K}$) structures in molecular clouds but the process that leads to the formation of these overdensities is still unclear. One key element seems to be related to the efficiency of the formation of cold clouds of neutral hydrogen (HI; Ostriker et al. 2010).

The current vision of the HI comes from an important legacy. Early observations of the 21 cm line showed a significant difference between emission and absorption spectra. On lines of sight crossing radio-sources, the HI appears in absorption with

* ROHSA is available in free access via the following web page: https://github.com/antoinemarchal/ROHSA

very narrow features (a few km s^{-1}). In emission the 21 cm line contains these narrow features on top of much boarder spectral structures (10–20 km s^{-1}). Clark (1965) was the first to suggest that this might be the signature of a cloud-intercloud medium in pressure equilibrium. Very rapidly Field (1965) and Field et al. (1969) introduced the concept of thermal instability and laid out the theoretical ground of a "two phase" HI model showing that, at the pressure of the ISM, the heating and cooling processes naturally lead to two thermally stable states: a dense cold neutral medium (CNM – $T \sim 50$ K, $n \sim 50$ cm^{-3}) immersed in a diffuse warm neutral medium (WNM – $T \sim 8000$ K, $n \sim 0.3$ cm^{-3}). This vision was later complemented by Wolfire et al. (1995, 2003) considering updated heating (dominated by the photoelectric effect on small dust grains) and cooling (dominated by CII: 158 μm, OI: 63 μm, Lα and electron recombinations onto positive charged grains) processes of the ISM.

This description of the diffuse neutral gas complemented a parallel hypothesis that emerged in the 1950s (e.g., von Weizsäcker 1951; von Hoerner 1951; Chandrasekhar & Münch 1952) and considered the ISM as a multi-scale turbulent medium. In this case, the density and velocity structures are the result of a highly dynamical and out-of-equilibrium medium. In order to reconcile the "static/two-phase" and the "turbulent" hypotheses, several studies have aimed at understanding the production of the CNM in a turbulent and thermally unstable flow using numerical simulations (e.g., Hennebelle & Pérault 1999; Koyama & Inutsuka 2002; Audit & Hennebelle 2005; Hennebelle et al. 2008; Saury et al. 2014). In general, these numerical studies show that the WNM has the properties of a trans-sonic turbulent flow, while the CNM shows a much more contrasted density structure, in accordance with the cloud-intercloud picture. In addition, such studies indicate the presence of a significant fraction of the mass being in the thermally unstable regime (i.e., with a temperature mid-way between the CNM and WNM stable states). For instance, Saury et al. (2014) showed that 30% of the HI is in the thermally unstable regime. Interestingly, these latter authors also show that this lukewarm neutral medium (LNM) is spatially located around the cold structures, pointing at the transitional nature of this thermal state.

From an observational standpoint, studies combining 21 cm absorption and emission data have clearly revealed the presence of HI at intermediate/unstable temperatures, typically between 500 and 5000 K (e.g., Heiles & Troland 2003a; Kanekar et al. 2003; Roy et al. 2013a,b; Murray et al. 2015, 2018a). Based on a coherent modeling of emission and absorption spectra, Heiles & Troland (2003b), Murray et al. (2015, 2018a) estimated that about 30% of the HI is in the cold CNM phase, 20% in the thermally unstable regime, and 50% in the WNM. Nevertheless the fraction of the HI in each phase remains uncertain and large variations are observed: the fraction of the mass in the CNM ranges from ~1% to more than 50% (Murray et al. 2018a).

The nature of these variations and how they relate to the dynamical conditions of the gas remains largely unexplored from the observational point of view. One main hurdle in getting access to this information is the fact that our knowledge of the multiphase nature of the HI relies on 21 cm absorption measurements that are limited to lines of sight crossing radio sources. By nature, this way of observing prevents us from mapping the HI phases. To go further, and really compare with numerical simulations that are currently under-constrained by observation, it is mandatory to map the column density structure of each phase and study the spatial variations of their centroid velocity and velocity dispersion. This calls for methods that can extract the information of each HI phase from fully sampled 21 cm emission data only. Huge efforts have been made to map the 21 cm emission of the Galactic HI (recent examples are Taylor et al. 2003; Kalberla et al. 2005; Stil et al. 2006; McClure-Griffiths et al. 2009; Winkel et al. 2016; Peek et al. 2018) and a large amount of data is now available. The information about the multiphase and multi-scale nature of the HI contained in these large hyperspectral data cubes has remained elusive due to the difficulty in separating the emission from the different phases on each line of sight. In this paper we propose a new method to map out the contribution of each phase to the 21 cm emission. The method is based on a decomposition of the 21 cm emission line with Gaussian profiles and constraints that favors spatially coherent parameters.

The paper is organized as follows. In Sect. 2, we describe the methodology used to develop our Gaussian decomposition algorithm. An evaluation of numerical simulation is presented in Sect. 3. In Sect. 4 we present an application to observations. The discussion and summary are presented Sects. 5 and 6.

2. Methodology

2.1. Gaussian decomposition of the 21 cm emission

Very early on after its detection, the 21 cm line was observed to be well described by a sum of a small number of Gaussian components. This was found to be true for the least confused absorption spectra (Muller 1957, 1959; Clark 1965) but also for emission spectra observed away from the Galactic plane (Heeschen 1955). Very few spectra at high Galactic latitudes do not comply with that rule, whatever the angular resolution of the data. Recently, Kalberla & Haud (2018) showed that more than 60% of the spectra over the whole sky can be described by the sum of seven Gaussian components or less. In the two decades after the detection of the 21 cm line, many studies used the Gaussian decomposition to infer physical parameters from the data (Matthews 1957; Davis 1957; Muller 1957, 1959; Dieter 1964, 1965; Lindblad 1966; Takakubo & van Woerden 1966; Mebold 1972). The fact that a small number of Gaussian components is needed to describe the signal was seen as a convenient way to describe the emission profiles with a small set of parameters (Takakubo & van Woerden 1966). It is also a very strong element in favor of the Gaussian function as a significant descriptor of the underlying physics.

Takakubo (1967) showed that the width of the 21 cm emission line could be grouped in three components ($\sigma \leq 3$ km s^{-1}; $3 < \sigma < 7$ km s^{-1}; $\sigma \geq 7$ km s^{-1}), a result confirmed later on (Mebold 1972; Haud & Kalberla 2007; Kalberla & Haud 2018). Takakubo (1967) also showed that the narrow 21 cm features are well correlated with Ca+ K line absorption measurements. These latter authors concluded that the narrow component, also seen in 21 cm absorption spectra, is likely to be isolated cold clouds (CNM) in the Solar neighborhood. They also showed that the spatial distribution of the centroid velocity, velocity width, and column density of the large feature is compatible with a warm (WNM) and diffuse disk that follows Galactic rotation. The second group of Gaussians, with a width (σ) of between 3 and 7 km s^{-1}, is generally attributed to gas in the thermally unstable range, but a fraction of them could be caused by blending of narrow features.

The exact mass fraction of gas in each phase (CNM, LNM, and WNM) is still a matter of debate. In addition, because this knowledge is based on absorption measurements, there is very little information about the structure of these phases on the sky. Being able to separate the different phases on each line of sight

would allow us to study the structure and kinematics of the cold phase and its relationship with the more diffuse gas. In theory, one could expect that Gaussian decomposition of the emission spectra could provide such mapping.

2.2. Limitation of the Gaussian model

There are many pitfalls in the description of the 21 cm emission spectra as a sum of Gaussian components: velocity blending, ambiguities of the number of components, nonGaussian profiles, noise peaks, plurality of solutions. Another important limitation is the effect of optical depth of the 21 cm line that modifies the shape of the line. More generally, the main opposition to Gaussian decomposition of emission spectra is that any spectrum can be decomposed that way provided that enough Gaussians are used. If that is the case, how can one be sure that the Gaussian representation provides some real physical information about the emitting gas? For instance, two spatially disconnected cold structures present on the same line of sight could appear at the same projected velocity. In this case their respective emission profiles would be confused. This velocity blending affects both the emission and absorption spectra; it is present in the data, and more so at lower Galactic latitudes where the length of the line of sight is larger and the number of HI structures increases.

This line of reasoning led Dickey & Lockman (1990) to advise against using Gaussian decomposition to analyze 21 cm spectra. Later on, it continued to be used (Verschuur & Schmelz 1989; Verschuur & Magnani 1994; Poppel et al. 1994; Haud 2000; Verschuur 2004; Begum et al. 2010; Martin et al. 2015; Kalberla & Haud 2018) but overall there was a loss of interest, except for the analysis of absorption spectra. Indeed by comparing nearby absorption and emission spectra one can recover the effect of optical depth on the 21 cm emission. In addition, absorption measurements are only sensitive to cold gas, limiting the velocity blending problem. For these reasons, the Gaussian decomposition continued to be used in this context (Dickey et al. 2003; Kanekar et al. 2003), and especially after the seminal work of Heiles & Troland (2003b) who developed a dedicated formalism which has been used in several other studies since (e.g. Stanimirović & Heiles 2005; Begum et al. 2010; Stanimirović et al. 2014; Lee et al. 2015; Murray et al. 2014, 2015, 2018b). Indeed, key information about the nature of the HI came from the joint Gaussian decomposition of emission and absorption spectra.

2.3. Development of a new approach

Following what has been done for the comparison of emission and absorption spectra where the Gaussian decomposition is considered valid, we would like to argue that a similar decomposition could be envisaged for emission data only, at least at high Galactic latitudes where the effect of optical depth of the 21 cm line has been shown to be negligible (Murray et al. 2018b).

The fact that physical information could be obtained using a Gaussian decomposition of absorption data reveals the fact that thermal broadening has a significant effect in shaping the line profile, or in other words, that the dynamics of each HI phase is typical of sub- or trans-sonic turbulence. When the amplitude of turbulent and thermal motions are commensurate, the line appears smooth and can be represented by a small number of Gaussian components (Miville-Deschênes et al. 2003). If the HI at high Galactic latitude is indeed represented by a two-phase medium with small, cold, and trans-sonic structures immersed in a relatively low-Mach-number and warm diffuse phase, the Gaussian representation could bear significant physical information.

The perspective of mapping the phases of the HI is so important that we ventured to explore new ways of decomposing the emission spectra that could be applicable to the high Galactic sky. The main difficulty is the effect of velocity blending for cold structures. As mentioned by Takakubo & van Woerden (1966), there will always be cases where a given spectrum can be fitted with a smaller number of components than its neighbors, if two or more components have similar central velocity and velocity dispersion. One way to avoid this confusion is to look for solutions that have a spatial continuity, or that have a slow spatial variation. Poppel et al. (1994), Haud (2000), Martin et al. (2015) and Miville-Deschênes et al. (2017b) have implemented Gaussian decomposition methods that use some information about their neighbors in order to favor spatially coherent solutions. Formally nevertheless, these algorithms do not force solutions to be spatially coherent; they simply provide initial guesses to the fit of a single spectrum based on the most likely solutions found in some surrounding area. The optimization is not bound to this initial guess and it can always converge to another solution that would break the spatial smoothness of the parameter space.

The novelty of the algorithm we present here is that it is the first one that imposes the spatial coherence in the determination of the parameters. In order to do that, all the spectra of the emission cube are fitted at the same time. To make sure that the recovered parameters are spatially smooth, specific regularization terms are added to the cost function with non-negativity constraints on the amplitude. This algorithm, called `ROHSA`, is described below.

2.4. `ROHSA`

`ROHSA` performs a regression analysis using a regularized nonlinear least-square criterion. We formulate in this section the Gaussian model used as well as the energy terms added to the cost function to take into account the spatial coherence of the emission and the multiphase nature of the gas simultaneously. The quasi-Newton algorithm, L-BFGS-B, used to perform the optimization is then briefly described. Finally, we formulate the algorithm performed by `ROHSA` based on a multi-resolution process from coarse to fine grid.

2.4.1. Model

The data are the measured brightness temperature $T_{\rm B}(v_z, \boldsymbol{r})$ at a given projected velocity v_z across sky coordinates $\boldsymbol{r}$. The proposed model $\tilde{T}_{\rm B}(v_z, \boldsymbol{\theta}(\boldsymbol{r}))$ is a sum of N Gaussian $G(v_z, \boldsymbol{\theta}_n(\boldsymbol{r}))$

$$\tilde{T}_{\rm B}(v_z, \boldsymbol{\theta}(\boldsymbol{r})) = \sum_{n=1}^{N} G(v_z, \boldsymbol{\theta}_n(\boldsymbol{r})), \tag{1}$$

with $\boldsymbol{\theta}(\boldsymbol{r}) = (\boldsymbol{\theta}_1(\boldsymbol{r}), \dots, \boldsymbol{\theta}_n(\boldsymbol{r}))$ and where

$$G(v_z, \boldsymbol{\theta}_n(\boldsymbol{r})) = \boldsymbol{a}_n(\boldsymbol{r}) \exp\left(-\frac{(v_z - \boldsymbol{\mu}_n(\boldsymbol{r}))^2}{2\boldsymbol{\sigma}_n(\boldsymbol{r})^2}\right) \tag{2}$$

is parametrized by $\boldsymbol{\theta}_n = (\boldsymbol{a}_n, \boldsymbol{\mu}_n, \boldsymbol{\sigma}_n)$ with $\boldsymbol{a}_n \geq \boldsymbol{0}$ being the amplitude, $\boldsymbol{\mu}_n$ the position, and $\boldsymbol{\sigma}_n$ the standard deviation 2D maps of the nth Gaussian profile across the plan of sky. The residual is

$$L(v_z, \boldsymbol{\theta}(\boldsymbol{r})) = \tilde{T}_{\rm B}(v_z, \boldsymbol{\theta}(\boldsymbol{r})) - T_{\rm B}(v_z, \boldsymbol{r}). \tag{3}$$

The estimated parameters $\hat{\boldsymbol{\theta}}$ are defined as the minimizer of a cost function that includes the sum of the squares of the residual,

$$Q(\boldsymbol{\theta}) = \frac{1}{2}\left\|L(v_z,\boldsymbol{\theta})\right\|^2_{\boldsymbol{\Sigma}} = \frac{1}{2}\sum_{v_z,\boldsymbol{r}}\left(\frac{L(v_z,\boldsymbol{\theta}(\boldsymbol{r}))}{\boldsymbol{\Sigma}(\boldsymbol{r})}\right)^2, \tag{4}$$

where Σ is the standard deviation 2D map of the noise assumed without spatial correlation. In practice this term is estimated using a sequence of empty velocity channels of $T_{\rm B}(v_z,\boldsymbol{r})$.

For each of the N Gaussians, we want to obtain a spatially coherent solution, meaning that for each parameter, the values have to be close for neighboring lines of sight. This can be done by penalizing the small-scale spatial fluctuations of each parameter, measured by the energy at high spatial frequencies. The considered high-pass filter is the second-order differences, that is the Laplacian filtering, defined by the 2D convolution kernel,

$$d = \begin{bmatrix} 0 & -1 & 0 \\ -1 & 4 & -1 \\ 0 & -1 & 0 \end{bmatrix}. \tag{5}$$

The following regularization term, itself containing energy terms, is added to the cost function given in Eq. (4),

$$R(\boldsymbol{\theta}) = \frac{1}{2}\sum_{n=1}^{N}\lambda_{\boldsymbol{a}}\|\boldsymbol{D}\boldsymbol{a}_n\|_2^2 + \lambda_{\boldsymbol{\mu}}\|\boldsymbol{D}\boldsymbol{\mu}_n\|_2^2 + \lambda_{\sigma}\|\boldsymbol{D}\boldsymbol{\sigma}_n\|_2^2, \tag{6}$$

where $\boldsymbol{D}$ is a matrix performing the 2D convolution using the kernel d and $\lambda_{\boldsymbol{a}}$, $\lambda_{\boldsymbol{\mu}}$, and λ_{σ} are hyper-parameters than tune the balance between the different terms.

These terms ensure a positive spatial correlation of the model parameters for neighboring pixels. However, each term is free to have large variation across the field at larger scale. Since $\boldsymbol{\sigma}_n$ contains information about the gas thermodynamics, we design an additional term in the cost function to group Gaussians with similar σ_n. This is implemented in order to favor any solution that would produce components ascribable to each of the phases (WNM, LNM or CNM). In order to do that we add another term, $\lambda'_{\sigma}\|\boldsymbol{\sigma}_n - m_n\|_2^2$, which constrains $\boldsymbol{\sigma}_n$ to be close to an unknown scalar value m_n. The full regularization term is then

$$\begin{aligned} R(\boldsymbol{\theta},\boldsymbol{m}) = \frac{1}{2}\sum_{n=1}^{N}&\lambda_{\boldsymbol{a}}\|\boldsymbol{D}\boldsymbol{a}_n\|_2^2 + \lambda_{\boldsymbol{\mu}}\|\boldsymbol{D}\boldsymbol{\mu}_n\|_2^2 + \lambda_{\sigma}\|\boldsymbol{D}\boldsymbol{\sigma}_n\|_2^2 \\ &+ \lambda'_{\sigma}\|\boldsymbol{\sigma}_n - m_n\|_2^2, \end{aligned} \tag{7}$$

with $\boldsymbol{m} = (m_1,\ldots,m_N)$ and $\boldsymbol{a}_n \geq 0, \forall\, n \in [1,\ldots,N]$. The last two terms in Eq. (7), representative of a joined constraint imposed on σ_n, allow us to interpret a posteriori and simultaneously the morphology and the thermodynamical state of each component extracted from the data. The full cost function is then

$$J(\boldsymbol{\theta},\boldsymbol{m}) = Q(\boldsymbol{\theta}) + R(\boldsymbol{\theta},\boldsymbol{m}). \tag{8}$$

2.4.2. Optimization algorithm

Unlike $Q(\boldsymbol{\theta})$, each energy term proposed in Eq. (6) involves linear dependences on the parameter $\boldsymbol{\theta}$. The cost function in Eq. (8) is therefore a regularized nonlinear least-square criterion. The minimizer,

$$[\hat{\boldsymbol{\theta}},\hat{\boldsymbol{m}}] = \underset{\boldsymbol{\theta},\boldsymbol{m}}{\operatorname{argmin}}\, J(\boldsymbol{\theta},\boldsymbol{m}),\ \text{wrt. } \boldsymbol{a}_n \geq 0,\ \forall\, n \in [1,\ldots,N], \tag{9}$$

Algorithm 1 ROHSA based on a multi-resolution process from coarse to fine grid where $\langle T_{\rm B}\rangle_i$ is the averaged data at i scale.

Require: $T_{\rm B}(v_z,\boldsymbol{r})$, $\boldsymbol{\theta}^{(0)}$, $\boldsymbol{m}^{(0)} = \boldsymbol{0}$, N, $\lambda_{\boldsymbol{a}}$, $\lambda_{\boldsymbol{\mu}}$, λ_{σ}, λ'_{σ}
1: **for** $i = 1$ to I **do**
2: $\left[\boldsymbol{\theta}^{(i)},\boldsymbol{m}^{(i)}\right] \leftarrow \underset{\boldsymbol{\theta},\boldsymbol{m}}{\operatorname{argmin}}\, J\left(\boldsymbol{\theta}^{(i-1)};\boldsymbol{m}^{(i-1)},\langle T_{\rm B}\rangle_i\right)$.
3: **end for**
return $\boldsymbol{\theta}^{(I)}$, $\boldsymbol{m}^{(I)}$

has no closed form expression and is not directly tractable because of the complexity of the model $\tilde{T}_{\rm B}$ and the size of the unknown and data. The proposed solution relies instead on an iterative optimization algorithm that uses the gradient

$$\nabla J(\boldsymbol{\theta},\boldsymbol{m}) = \begin{bmatrix}\nabla L(\boldsymbol{\theta}) \times L(\boldsymbol{\theta}) \\ \boldsymbol{0}\end{bmatrix} + \begin{bmatrix}\nabla_{\boldsymbol{\theta}} R(\boldsymbol{\theta},\boldsymbol{m}) \\ \nabla_{\boldsymbol{m}} R(\boldsymbol{\theta},\boldsymbol{m})\end{bmatrix}, \tag{10}$$

which is tractable since it involves the residual, the Jacobian of the residual $\nabla L(\boldsymbol{\theta})$, and 2D convolutions with the kernel d for $\boldsymbol{D}$ and $\boldsymbol{D}^t$. The gradient $\nabla R^t(\boldsymbol{\theta},\boldsymbol{m}) = [\nabla_{\boldsymbol{\theta}} R^t(\boldsymbol{\theta},\boldsymbol{m}), \nabla_{\boldsymbol{m}} R^t(\boldsymbol{\theta},\boldsymbol{m})]$ and $\nabla J(\boldsymbol{\theta})$ are detailed in Appendix A.

For the optimization, RHOSA relies on L-BFGS-B (for Limited-memory Broyden-Fletcher-Goldfarb-Shanno with Bounds), a quasi-Newton iterative algorithm described by Zhu et al. (1997) which allows for the positivity constraints of the amplitudes to be taken into account. In this algorithm, after an initialization $\boldsymbol{\theta}_{(0)}$, the solution is approached iteratively by

$$\boldsymbol{\theta}_{(k+1)} = \boldsymbol{\theta}_{(k)} - \alpha_{(k)}\boldsymbol{H}^{-1}_{(k)}\nabla J\left(\boldsymbol{\theta}_{(k)},\boldsymbol{m}_{(k)}\right), \tag{11}$$

where $\boldsymbol{H}^{-1}\nabla J\,(\boldsymbol{\theta},\boldsymbol{m})$ is approximated with the L-BFGS formula. The iterations are repeated until one of the two following criteria is met: (1) the total number of evaluations of $J(\boldsymbol{\theta},\boldsymbol{m})$ and $\nabla J(\boldsymbol{\theta},\boldsymbol{m})$ exceeds a maximum number of iterations defined by the user; (2) the projected gradient is sufficiently small (i.e., $|\text{proj}\ \nabla J(\boldsymbol{\theta},\boldsymbol{m})|/(1+|J(\boldsymbol{\theta},\boldsymbol{m})|) < 10^{-10}$).

Due to its nonlinearity, the least-square criterion $J(\boldsymbol{\theta},\boldsymbol{m})$ described in Eq. (8) is likely to include local minimizers. Therefore, the L-BFGS-B algorithm used by ROHSA is also likely to converge toward one of these local minima, making the solution highly dependent on the initialization $\boldsymbol{\theta}^{(I)}_{(0)}$. In order to overcome this difficulty, we based the design of ROHSA on an iterative multi-resolution process from coarse to fine grid (described in the following section) to automatically choose $\boldsymbol{\theta}^{(I)}_{(0)}$ and to converge towards a satisfactory local minimum.

2.4.3. ROHSA algorithm

ROHSA is based on an iterative algorithm using a multi-resolution process from coarse to fine grid presented in Algorithm 1. The number of iterations I depends on the size of the fine grid S and is defined by the relation $2^I = S$. For example, a grid of size $S^2 = 256^2$ requires $I = 8$ iterations. Each iteration is made of three steps.

1. Data are averaged at scale i as

$$\langle T_{\rm B}\rangle_i = \frac{1}{K_i}\sum_{k\in\mathcal{V}_i} T_{\rm B}(v_z,\boldsymbol{r}_k), \tag{12}$$

where $\mathcal{V}_i$ defines the neighborhood at scale i, as described in Fig. 1, and K_i is the number of positions in that neighborhood. For $i = 1$, all the spatial information is compressed into a single spectrum: $\langle T_{\rm B}\rangle_1 = \langle T_{\rm B}(v_z,\boldsymbol{r})\rangle$.

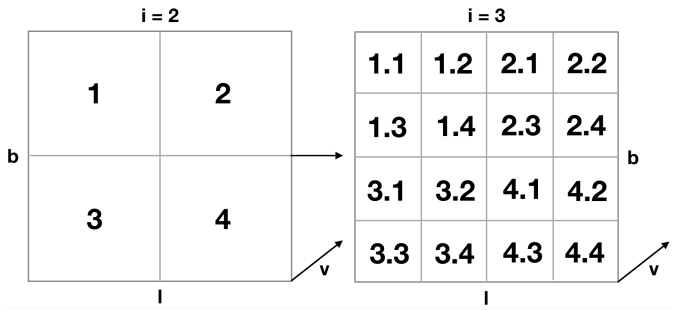

Fig. 1. Graphic visualization of neighborhoods $\mathcal{V}_2$ and $\mathcal{V}_3$ used to obtain the spatially averaged data versions $\langle T_\mathrm{B}\rangle_2$ and $\langle T_\mathrm{B}\rangle_3$.

2. The parameters $\boldsymbol{\theta}^{(i)}$ and $\boldsymbol{m}^{(i)}$ are estimated on that spatially averaged data version $\langle T_\mathrm{B}\rangle_i$ by minimizing the cost function given in Eq. (8).
The minimization (line 2 of Algorithm 1) is made using L-BFGS, described in the previous section. We note that for scale $i = 1$, there is no spatial information $\langle T_\mathrm{B}\rangle_1$ and the result does not depend on the regularization.
3. Parameters $\boldsymbol{\theta}^{(i)}$ are spatially interpolated at nearest neighborhood to serve as initialization for the next scale $i + 1$.

The free hyper-parameters λ_A, λ_μ, λ_σ, λ'_σ remain constant during the iterations.

3. Evaluation on numerical simulation

To evaluate the performance of ROHSA, we applied it to synthetic 21 cm observations computed from a numerical simulation of thermally bi-stable turbulence flow. This allowed us to directly compare the solution given by ROHSA to the properties of the gas present in the simulation. That direct comparison with numerical reality is an essential test to evaluate the performances of a source-separation algorithm like ROHSA.

3.1. Numerical simulation

To test ROHSA we used the hydrodynamical simulation of thermally bi-stable turbulence performed by Saury et al. (2014). We used their 1024N01 simulation (1024^3 pixels and a physical size of the box of 40 pc) characterized by (1) an initial density $n_0 = 0.1\,\mathrm{cm}^{-3}$, (2) a large-scale velocity $v_\mathrm{S} = 12.5\,\mathrm{km\,s}^{-1}$ and (3) a spectral weight $\zeta = 0.2$. The initial density corresponds to the typical density of the WNM before condensation, the large-scale velocity represents the amplitude given to the field that generates large-scale turbulent motions in the box, and finally the spectral weight controls the modes of the turbulent mixing (here a majority of compressible modes). The Mach number of this simulation has been evaluated to be around $\mathcal{M} = 0.85$ for $T > 200$ K.

In order to explore the performances of ROHSA we use only a subset of this simulation. We concentrate our analysis on a region of $256 \times 256 \times 1024$ pixels with a moderate CNM fraction in order to limit the effect of HI self-absorption (see Sect. 3.2.3).

3.2. 21 cm line synthetic observations

The synthetic 21 cm observations were computed using the formalism described by Miville-Deschênes & Martin (2007).

3.2.1. Distribution of velocity fluctuations

In the 3D spatial space, the neutral hydrogen can be described by three 3D fields: the temperature $T(\mathbf{x})$, the density $\rho(\mathbf{x})$, and the z-component of the turbulent velocity field $v_z(\mathbf{x})$. Here the 3D spatial positions are denoted by the vector $\mathbf{x}$ while the 2D vector expressing the line-of-sight is denoted by $\boldsymbol{r}$. The z-axis is taken along the line of sight.

Information about the velocity field is inevitably lost because of the projection along z-axis. This makes this description of HI a nonexhaustive one. For each position $\mathbf{x}$, we assume that the velocity dispersion of a given cell is dominated by thermal motions. This is a fair approximation as the turbulent velocity dispersion at the cell size (0.04 pc) is $\sigma_\mathrm{turb} \sim 0.3\,\mathrm{km\,s}^{-1}$, which is smaller than the thermal broadening everywhere in the simulation: the smallest thermal broadening for the coldest gas found in the simulation ($T = 20$ K) is $\sigma_\mathrm{therm} = 0.4\,\mathrm{km}^{-1}$. The distribution function of the z-component of the velocity $v_z(\mathbf{x})$ of a given cell is then given by $\phi_{v_z}(\mathbf{x})$, a Maxwellian shifted by $v_z(\mathbf{x})$,

$$\phi_{v_z}(\mathbf{x})\mathrm{d}v'_z = \frac{1}{\sqrt{2\pi}\Delta(\mathbf{x})} \times \exp\left(-\frac{(v'_z - v_z(\mathbf{x}))^2}{2\Delta^2(\mathbf{x})}\right)\mathrm{d}v'_z, \tag{13}$$

where $\Delta(\mathbf{x}) = \sqrt{k_\mathrm{B}T(\mathbf{x})/m_\mathrm{H}}$, which is the thermal broadening of the 21 cm line, m_H is the hydrogen atom mass, and k_B the Boltzmann constant.

3.2.2. Brightness temperature: general case

The general case for the computation of the 21 cm brightness temperature $T_\mathrm{B}(v_z, \boldsymbol{r})$ is based on the following radiative transfer equation.

$$T_\mathrm{B}(v_z, \boldsymbol{r}) = \sum_z T(\boldsymbol{r}, z)\left[1 - e^{-\tau(v_z,\boldsymbol{r},z)}\right] e^{-\sum_{z'<z}\tau(v_z,\boldsymbol{r},z')}, \tag{14}$$

where $\tau(v_z, \boldsymbol{r}, z)$ is the optical depth of the 21 cm line defined as

$$\tau(v_z, \boldsymbol{r}, z) = \frac{1}{C}\frac{\rho(\boldsymbol{r}, z)\,\phi_{v_z}(\boldsymbol{r}, z)}{T(\boldsymbol{r}, z)}\,\mathrm{d}z, \tag{15}$$

and $C = 1.82243 \times 10^{18}\,\mathrm{cm}^{-2}\,(\mathrm{K\ km\ s}^{-1})^{-1}$. In this representation, a gas cell at position z' absorbs emission from the cell located behind it along the line of sight, i.e., at $z > z'$.

3.2.3. Optically thin limit

In the optically thin limit, in cases where the self-absorption is negligible (i.e., $\tau(v_z, r, z) \ll 1$ everywhere), the 21 cm brightness temperature is proportional to the density ρ:

$$T_\mathrm{B}^\mathrm{thin}(v_z, \boldsymbol{r})\,\mathrm{d}v'_z = B(\boldsymbol{r}) \otimes \frac{1}{C}\int_0^H \mathrm{d}z\,\rho(\boldsymbol{r}, z)\,\phi_{v_z}(\boldsymbol{r}, z)\,\mathrm{d}v'_z, \tag{16}$$

where H is the depth of the cloud and $\otimes$ the spatial convolution. Here we consider the case that includes spatial smoothing by a telescope beam $B(\boldsymbol{r})$.

The integrated column density $N_\mathrm{HI}^\mathrm{thin}(\boldsymbol{r})$ and the centroid velocity $\langle v_z(\boldsymbol{r})\rangle$ of the 21 cm line can be obtained directly by integrating $T_\mathrm{B}^\mathrm{thin}(v_z, \boldsymbol{r})$ along the velocity axis:

$$N_\mathrm{HI}^\mathrm{thin}(\boldsymbol{r}) = C\int_{-\infty}^{+\infty} T_\mathrm{B}(v_z, \boldsymbol{r})\,\mathrm{d}v_z, \tag{17}$$

and

$$\langle v_z(\boldsymbol{r})\rangle = \frac{\int_{-\infty}^{+\infty} v_z\,T_\mathrm{B}(v_z, \boldsymbol{r})\,\mathrm{d}v_z}{\int_{-\infty}^{+\infty} T_\mathrm{B}(v_z, \boldsymbol{r})\mathrm{d}v_z}. \tag{18}$$

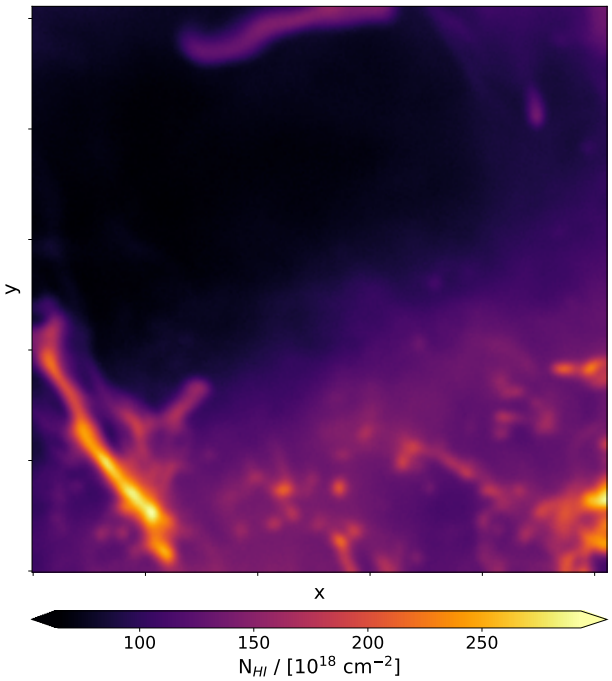

Fig. 2. Integrated column density $N_{\rm HI}$ (optically thin approximation) of the 21 cm synthetic observation computed from the thermally bi-stable numerical simulation of Saury et al. (2014).

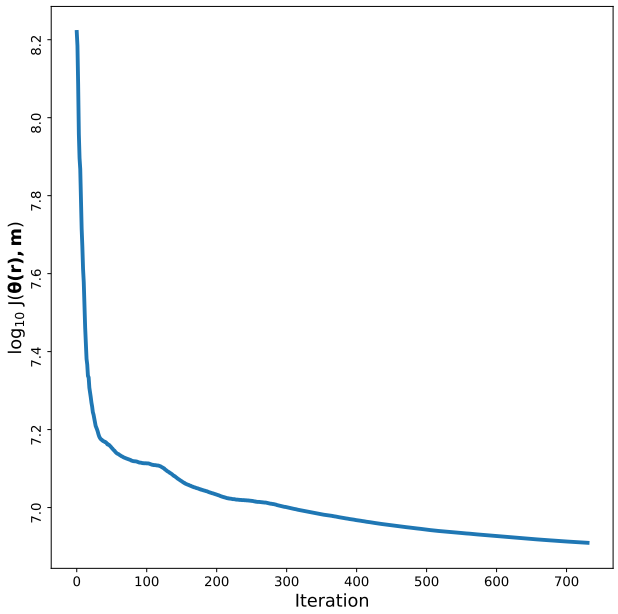

Fig. 3. Evolution of the cost function $J(\boldsymbol{\theta}(\boldsymbol{r}), \boldsymbol{m})$ as a function of the number of iterations performed by ROHSA on the synthetic observation computed in Sect. 3.2.

3.2.4. Synthetic observation

We computed the synthetic position-position-velocity (PPV) data cube in the general case using Eq. (14). Each spectrum has an effective velocity resolution of 0.8 km s^{-1} and covers $-40 < v_z < 40$ km s^{-1}. We considered the beam $B(\boldsymbol{r})$ of the instrument by convolving the synthetic PPV cube with a Gaussian kernel characterized by standard deviations of two pixels along the spatial axis. We then added a homogeneous Gaussian noise of 0.05 K to each spectrum.

In order to mimic observation, integrated column density maps shown in the rest of the paper are computed using the optically thin limit presented in Eq. (17). The integrated column density map of the synthetic PPV cube is shown in Fig. 2.

3.3. Results

ROHSA was then applied to decompose the synthetic observation computed in Sect. 3.2. In this section we discuss the choice of the free parameters of ROHSA, the global properties of the Gaussian sample, and the properties of individual components identified by the decomposition. Subsequently, the mapping of a three-phase coherent model is presented with direct comparisons to the phases extracted directly from the simulation.

3.3.1. Choosing the free parameters of ROHSA

ROHSA has six free parameters : the number of Gaussian components N, four hyper-parameters λ_i and, the maximum number of iterations of the LBFGS algorithm.

The most important parameter is N. This has to be sufficiently high to ensure a complete encoding of the signal, that is, to ensure that the residual is dominated by noise. As we discuss in Sect. 3.3.3, a given number of Gaussian components does not imply that all components are used to describe the signal along every line of sight. Components are allowed to have an amplitude of zero at any position. This is especially relevant for components encoding cold features. Since the CNM clouds occupy a small fraction of the total volume (see also Sect. 3.3.3), we expect the associated amplitude fields to have a large fraction close to zero. This is ensured by the energy term $\|\boldsymbol{\sigma}_n - m_n\|_2^2$ which minimizes the variance of the dispersion velocity of each component. Amplitudes are brought to zero if there is no need for a Gaussian to describe the signal at some location, instead of encoding another phase like the WNM for example. Avoiding phase mixing allows for overfitting to be prevented.

As with N, different values of the hyper-parameters $\lambda_{\boldsymbol{a}}$, $\lambda_{\boldsymbol{\mu}}$, $\lambda_{\boldsymbol{\sigma}}$, $\lambda'_{\boldsymbol{\sigma}}$ can be tested to obtain a satisfactory solution. If the hyper-parameters are null (i.e., no regularization) the signal could be fully encoded, but no spatial coherence will appear in the solution $\boldsymbol{\theta}^{(I)}$. On the other hand, if the hyper-parameters are too high, the solution will tend towards a solution that could be too spatially coherent, or even flat, wiping out small-scale fluctuations and providing a bad fit to the data. A spatially coherent solution that describes the data well with the smallest value of N is a good criterion to select the values of the hyper-parameters.

The last criterion set by the user is the maximum number of iterations of the LBFGS algorithm computing Eq. (11); see Sect. 2.4.2. That parameter must be large enough to ensure the convergence of the solution. The convergence of ROHSA from a numerical perspective is presented in Fig. 3, which shows the evolution of the cost function $J(\boldsymbol{\theta}(\boldsymbol{r}), \boldsymbol{m})$ for 730 iterations.

The decomposition of the synthetic observations presented in this section converges to a satisfactory solution with $N = 8$, $\lambda_{\boldsymbol{a}} = 10\,000$, $\lambda_{\boldsymbol{\mu}} = 10\,000$, $\lambda_{\boldsymbol{\sigma}} = 10\,000$, and $\lambda'_{\boldsymbol{\sigma}} = 1000$. As previously recommended, these values are empirically found to converge towards a noise-dominated residual and a signal that is encoded with a minimum number of Gaussian components. To illustrate this, Fig. 4 shows the normalized probability distribution function of the relative difference $(N_{\rm HI} - \tilde{N}_{\rm HI})/N_{\rm HI}$ between the solution $\tilde{N}_{\rm HI}$ inferred with ROHSA and the data $N_{\rm HI}$ for different values of N.

As an a posterior assessment, the skewness μ_3 of the residual is shown to quantify the quality of the encoding. As the

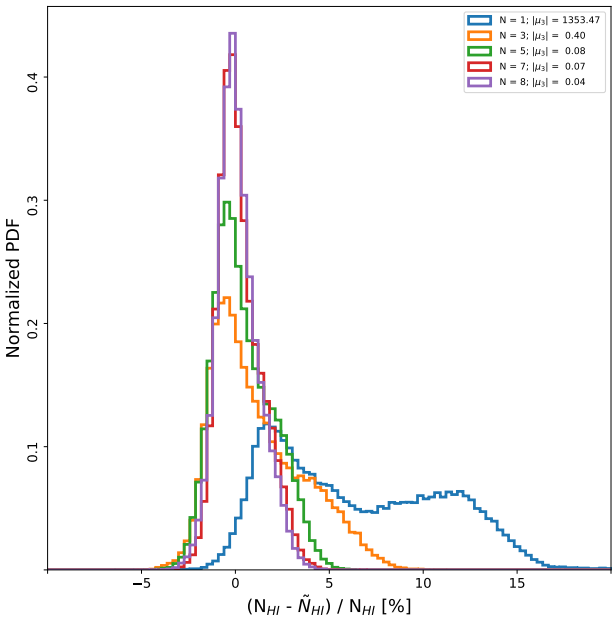

Fig. 4. Normalized probability distribution function of the relative difference $(N_{\rm HI} - \tilde{N}_{\rm HI})/N_{\rm HI}$ between the solution $\tilde{N}_{\rm HI}$ inferred with ROHSA and the data $N_{\rm HI}$ for different numbers of Gaussian components $N = [1, 3, 5, 7, 8]$. The norm of the skewness $|\mu_3|$ is shown in the legend to quantify the quality of the encoding.

emission is only positive and noise has a symmetric distribution centered on zero, the skewness of the residual can be used as a way to evaluate if the emission is well estimated or if the algorithm has over-fitted the data and included some noise in the solution. A positive skewness is usually an indication that some emission is left in the residual. If the model has not enough freedom to encode the emission fully; more components are needed or the regularization terms should be lowered. On the other hand, a negative skewness indicates that the decomposition is overfitting the data; positive noise fluctuations are included in the model leaving more negative noise fluctuations than positive ones in the residual. This is usually an indication that the regularization coefficients (λ_i) should be larger to increase the spatial smoothness of the solution. A skewness of the residual close to zero is an indication of a valid solution, one that is not distorted by the regularization and that does not overfit the signal. For the case of the synthetic observations presented here, $N = 8$ fully encodes the signal with a relatively low skewness $|\mu_3| = 0.04$.

The computation time of ROHSA depends on the maximum number of iterations, the dimension of the PPV cube, and the number of Gaussian components. For each step of the multi-resolution process from coarse to fine grid, the computation time used by ROHSA for this particular case (purple line) is presented in Appendix B with a lower number of Gaussian components for the sake of comparison. The evaluation performed here requires nearly two hours of computation time on a single CPU, which makes it difficult to explore a large range of hyper-parameters and number of Gaussian components. To overcome this difficulty, a GPU implementation of ROHSA is under development.

3.3.2. Global properties of the Gaussian sample

ROHSA recovered the total emission of the synthetic observation with a relative variation of 0.3%. An example of the Gaussian decomposition for a representative 4×4 mosaic of the simulation is shown Fig. 5. The spatial coherence of the solution can be seen over the mosaic with a smooth variation of the amplitude, the central velocity, and the velocity dispersion of each Gaussian. It is already possible to distinguish in those spectra the convergence of the decomposition toward different velocity dispersions, that is, different temperatures/phases of the gas due to the energy term $\lambda'_\sigma \|\boldsymbol{\sigma}_n - m_n\|_2^2$. To have a clear view of these different components, let us take a look at the probability distribution function $\boldsymbol{\sigma}$ weighted by the fraction of total emission of each Gaussian $\sqrt{2\pi}\boldsymbol{a}_n\boldsymbol{\sigma}_n / \sum_{\boldsymbol{r}} N_{\rm HI}(\boldsymbol{r})$ presented in Fig. 6. This diagram shows the amount of gas in a given range of velocity dispersion (i.e., indirectly a certain range of temperature). It is clear that ROHSA, in this case, converges toward a three-phase model with typical velocity dispersion close to the expected values in the CNM ($\sigma < 2\,{\rm km\,s^{-1}}$), LNM ($\sigma \sim 6\,{\rm km\,s^{-1}}$), and WNM ($\sigma \sim 8\,{\rm km\,s^{-1}}$). We see that a similar behavior is also present in the application to an observation of high Galactic latitude presented in Sect. 4. We note also that since eight Gaussian components have been used by ROHSA, some phases are encoded by several components. Association of the different components to characterize a three-phase model is presented in Sect. 3.3.4.

3.3.3. Properties of individual components

Integrated column density maps of each component obtained with ROHSA for $N = 8$ Gaussian are presented in Fig. 7. For each component G_n, the mean velocity $\langle \boldsymbol{\mu}_n \rangle$ and mean velocity dispersion $\langle \boldsymbol{\sigma}_n \rangle$ averaged over the field are presented in Table 1. The surface filling factor appears to vary considerably between the eight components. The components with low values of $\langle \boldsymbol{\sigma}_n \rangle$ are sparsely present, while the component with the largest velocity dispersion is present everywhere on the field.

We recall that the numerical simulations used here were designed to reproduce the WNM–CNM condensation process of the HI through the thermal instability. The factor 100 difference in density between the two phases, and the fact that the mass fraction in each one is about 50%, implies that the cold phase fills only a few percent of the volume (Saury et al. 2014). This translates directly in the column density maps recovered by ROHSA; the narrow components, corresponding to colder structures, fill only a fraction of the projected field of view, while the larger component is present everywhere.

The eight velocity fields and velocity dispersion fields are presented in Figs. 8 and 9, respectively. At some location of the fields, when there is no need for a Gaussian to describe the signal over several pixels, the amplitude goes to zero. The corresponding velocity and velocity dispersion fields then have no reason to fluctuate. It turns out that where a_n goes to zero, $\boldsymbol{\mu}_n$ and $\boldsymbol{\sigma}_n$ are flat. This explains the apparent variation of spatial resolution as seen for example in Fig. 8 (bottom right). We notice that the first component G_1 (top left) and the second component G_2 (top right), encoding the WNM and the LNM, respectively, are defined everywhere, meaning that $\boldsymbol{\mu}_1$ and $\boldsymbol{\sigma}_1$ also have fluctuations everywhere. The implications of this are discussed in Sect. 5.

3.3.4. Mapping the three-phase neutral ISM

In order to compare the result of the decomposition with the reality given by the numerical simulations, we grouped the eight components into three fields corresponding to the WNM, the LNM, and the CNM. The comparison with the numerical simulations requires that we identify ranges in temperature that demarcate these three phases. As with most numerical simulations that include the classical heating and cooling processes

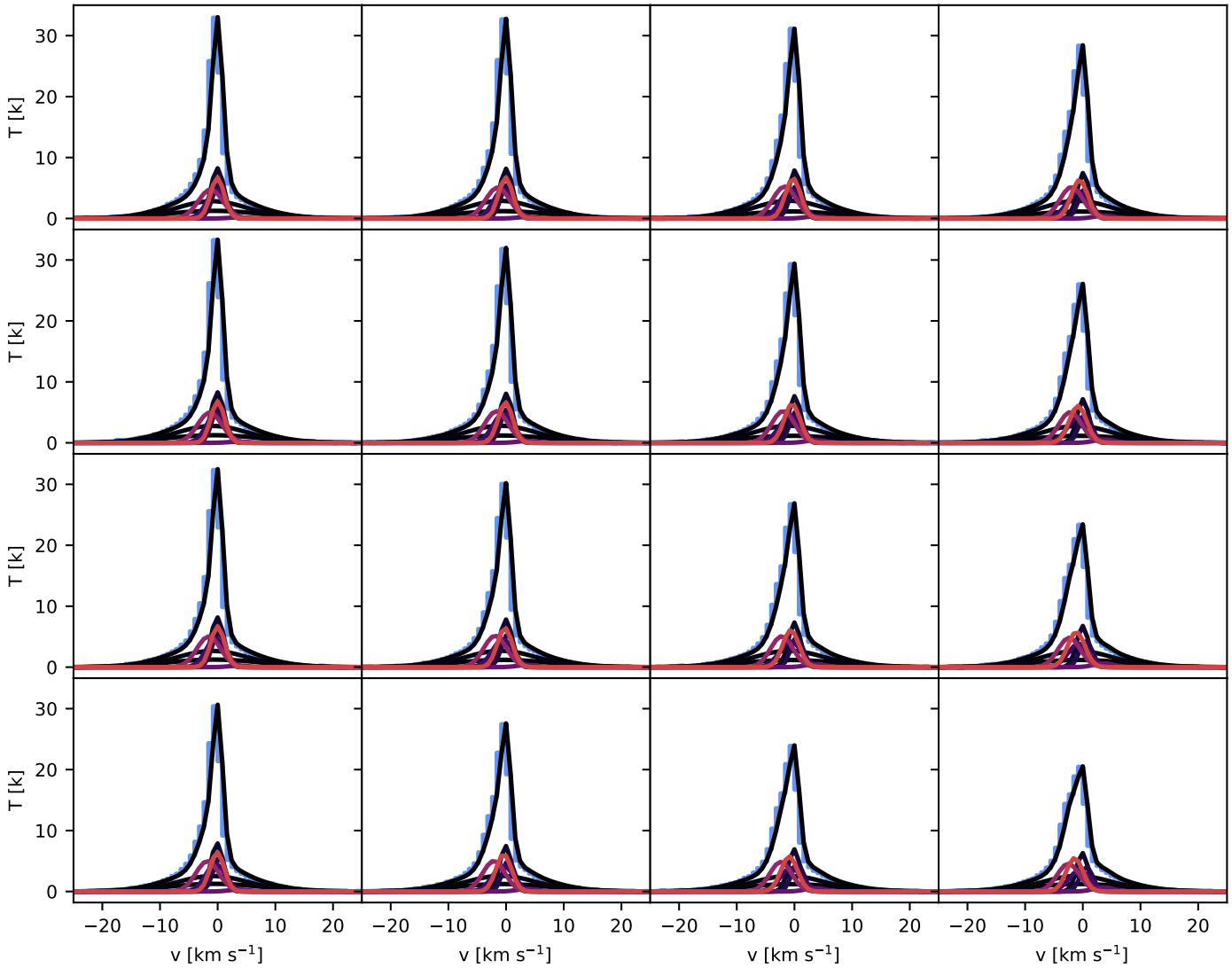

Fig. 5. Example of the Gaussian decomposition obtained by ROHSA for a random 4×4 mosaic of the synthetic observation. The original signal is shown in blue and the total brightness temperature encoded by ROHSA is shown in black. The other lines show the individual Gaussian components. The spatial coherence of the solution can be seen over the mosaic with a smooth variation of the amplitude, the central velocity and the dispersion velocity of each component.

of the ISM (Wolfire et al. 1995), the simulation of Saury et al. (2014) we use here shows a continuum of temperature, with no clear separation and with a significant fraction of the gas present at temperatures corresponding to the thermally unstable regime (see their Figs. 14 and 15). To facilitate the comparison with previous studies, we decided to use the canonical values $T_{\mathrm{k\,lim,CNM/LNM}} = 500\,\mathrm{K}$ and $T_{\mathrm{k\,lim,LNM/WNM}} = 5000\,\mathrm{K}$ (Heiles & Troland 2003b) to separate the simulation in three components. The integrated column density maps associated to each phase are computed following the methodology described in Sect. 3.2.

The comparison between the integrated column density maps recovered with ROHSA and those inferred directly from the simulation is presented Fig. 10. The intensity and the morphology of each phase is well recovered. It is nevertheless possible to see some leakages between the phases, in particular between WNM and LNM. This is due partly to the poorly defined temperature thresholds used to separate the phases. It is also due to small confusions during the Gaussian decomposition where the intensity, the dispersion velocity, and velocity centroid of each component in the PPV space are close to each other. In other words, for similar central velocities, the scales of fluctuations on the velocity axis characterizing each component are too close to one another (see Figs. 5 and 6).

One way to evaluate the quality of the reconstruction is to compare the statistical properties of the cloud and inter-cloud components. Three different fields are used: the integrated column density field of the cloud medium (CNM), the integrated column density field of the inter-cloud medium (LNM + WNM), and, because it is fully sampled in the plan of sky, the centroid velocity field of the inter-cloud medium. Figure 11 presents the integrated column density field and the centroid velocity field, computed using Eq. (18), of the inter-cloud medium obtained combining the LNM and the WNM inferred with ROHSA and those obtained directly from the simulation.

In order to compare the estimates from ROHSA to the ones obtained from the simulation, we compute the spatial power spectrum (SPS) of each image. The SPSs of the integrated column density of the cloud and inter-cloud medium are presented Fig. 12 and the SPS of the centroid velocity field of the inter-cloud medium is presented in Fig. 13. In each case, the statistics recovered by ROHSA is consistent with the numerical simulation over all scales. The shape of these power spectra is interesting in

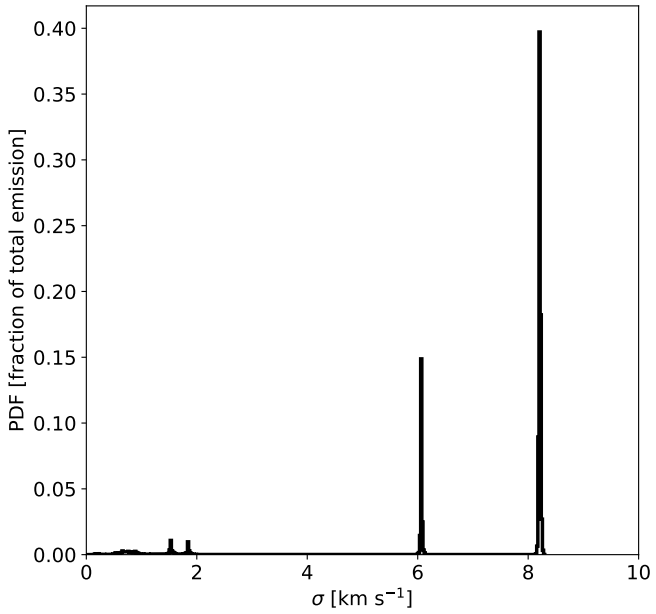

Fig. 6. Probability distribution function $\boldsymbol{\sigma}$ weighted by the fraction of total emission of each Gaussian $\sqrt{2\pi}\boldsymbol{a}_n\boldsymbol{\sigma}_n / \sum_{\boldsymbol{r}} N_{\rm HI}(\boldsymbol{r})$ of the simulated field. ROHSA converges toward three distinguishable phases associated to the WNM, LNM, and CNM.

Table 1. Mean velocity $\langle \boldsymbol{\mu}_n \rangle$ and mean velocity dispersion $\langle \boldsymbol{\sigma}_n \rangle$ of the eight Gaussian components G_n inferred by ROHSA on the 21 cm synthetic observation of the numerical simulation described in Sect. 3.2.

	G_1	G_2	G_3	G_4	G_5	G_6	G_7	G_8
$\langle \boldsymbol{\mu}_n \rangle$ (km s^{-1})	0.2	−1.7	0.5	2.3	−0.1	5.0	−3.7	−2.5
$\langle \boldsymbol{\sigma}_n \rangle$ (km s^{-1})	8.2	6.1	0.5	0.6	1.5	1.5	1.8	0.9

itself; the inter-cloud medium is featureless with an almost constant power law, as the cloud phase is more structured, with a break at about 20 pixels, showing a typical scale linked to the condensation process. Interestingly, ROHSA is able to capture all these features very well.

4. Application on high-latitude HI gas

After validating the identification of the HI phases on numerical simulations, in this section we present the application of ROHSA on a 21 cm observation of a region with high Galactic latitude.

4.1. North ecliptic pole

To avoid the complication of low-latitude observations, where the 21 cm emission is significantly affected by velocity crowding and self-absorption, we chose to apply RHOSA to one of the high Galactic latitude fields of the GHIGLS[1] survey (Martin et al. 2015). We chose the North ecliptic pole (NEP) field, a $12^\circ \times 12^\circ$ region centered on $l = 96^\circ.40$, $b = 30^\circ.03$ observed with the Green Bank Telescope, providing a $9'.55$ spatial resolution. The HI spectra have an effective velocity resolution of 0.807 km s^{-1} and cover $-200 < v$ (km s^{-1}) < 50. The integrated column density map computed using Eq. (17) is shown in Fig. 14 and a mosaic of representative emission spectra is shown in Fig. 15.

[1] http://www.cita.utoronto.ca/GHIGLS/

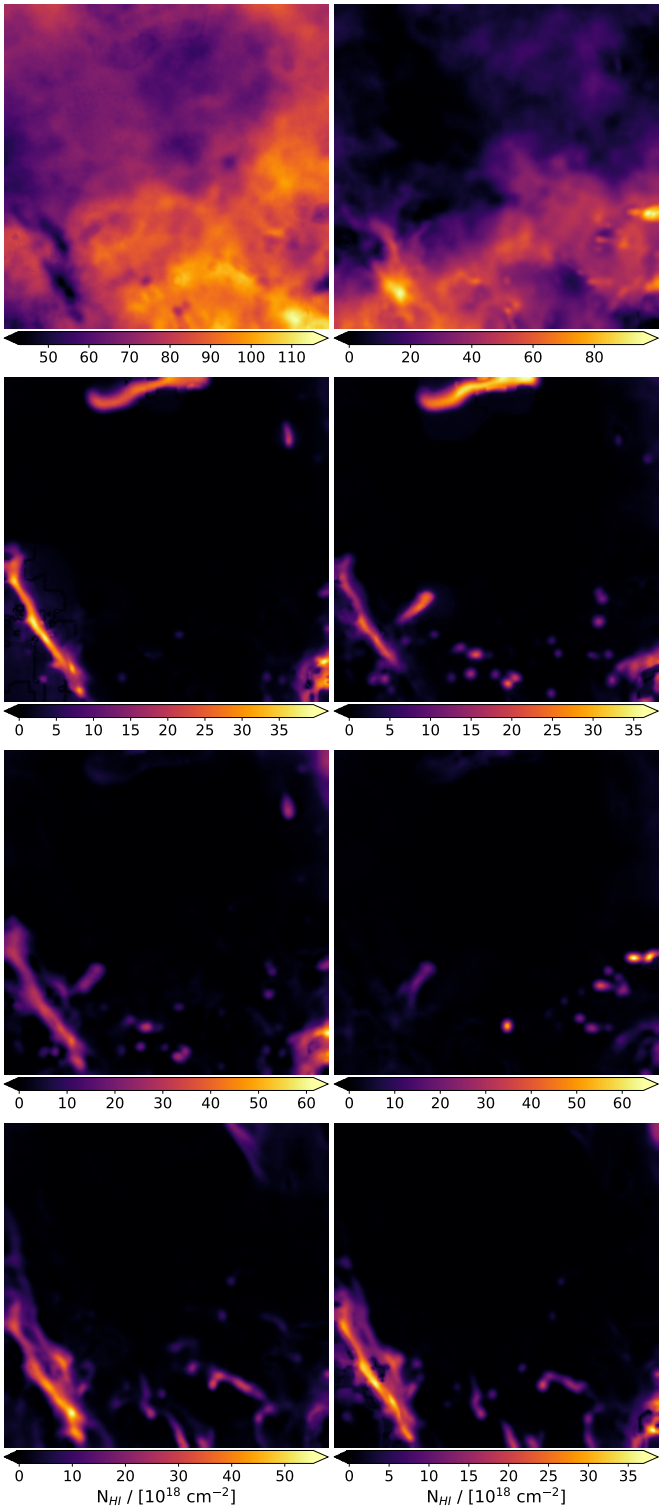

Fig. 7. Integrated column density maps (*left*: G_1, G_3, G_5, G_7); (*right*: G_2, G_4, G_6, G_8) obtained by ROHSA on the synthetic observation computed in Sect. 3.2. Mean velocity $\langle \boldsymbol{\mu}_n \rangle$ and mean velocity dispersion $\langle \boldsymbol{\sigma}_n \rangle$ are presented in Table 1. The surface filling factor varies considerably between components, depending on their $\langle \boldsymbol{\sigma}_n \rangle$ value.

As Fig. 15 shows, high-latitude spectra of HI are more complex that the synthetic observations computed from the numerical simulations of Saury et al. (2014). This is caused by a combination of the longer line of sight in the observation (about 200 pc at $b = 30^\circ$ compared to the 40 pc box of the simulation) and to the presence of nonlocal velocity components. The 21 cm

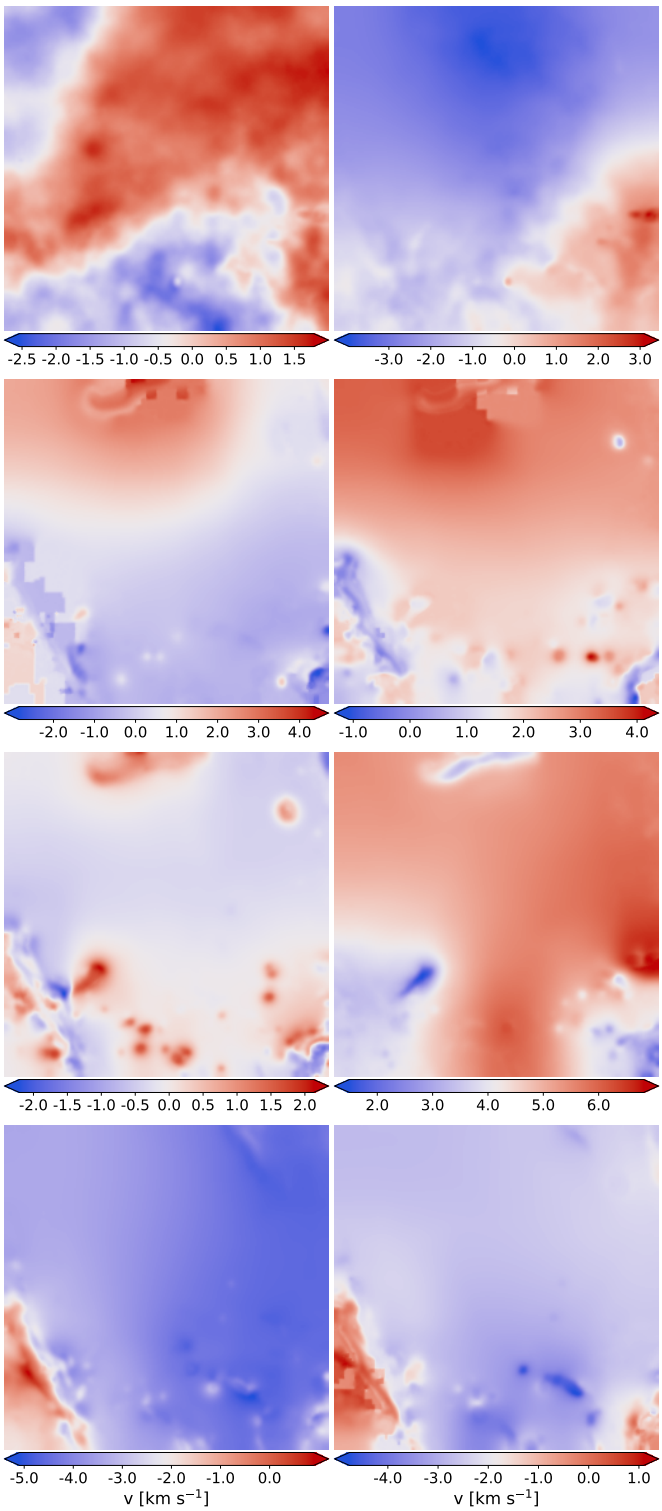

Fig. 8. Centroid velocity fields $\boldsymbol{\mu}$ (*left*: μ_1, μ_3, μ_5, μ_7); (right: μ_2, μ_4, μ_6, μ_8) obtained by ROHSA using the synthetic observation computed in Sect. 3.2.

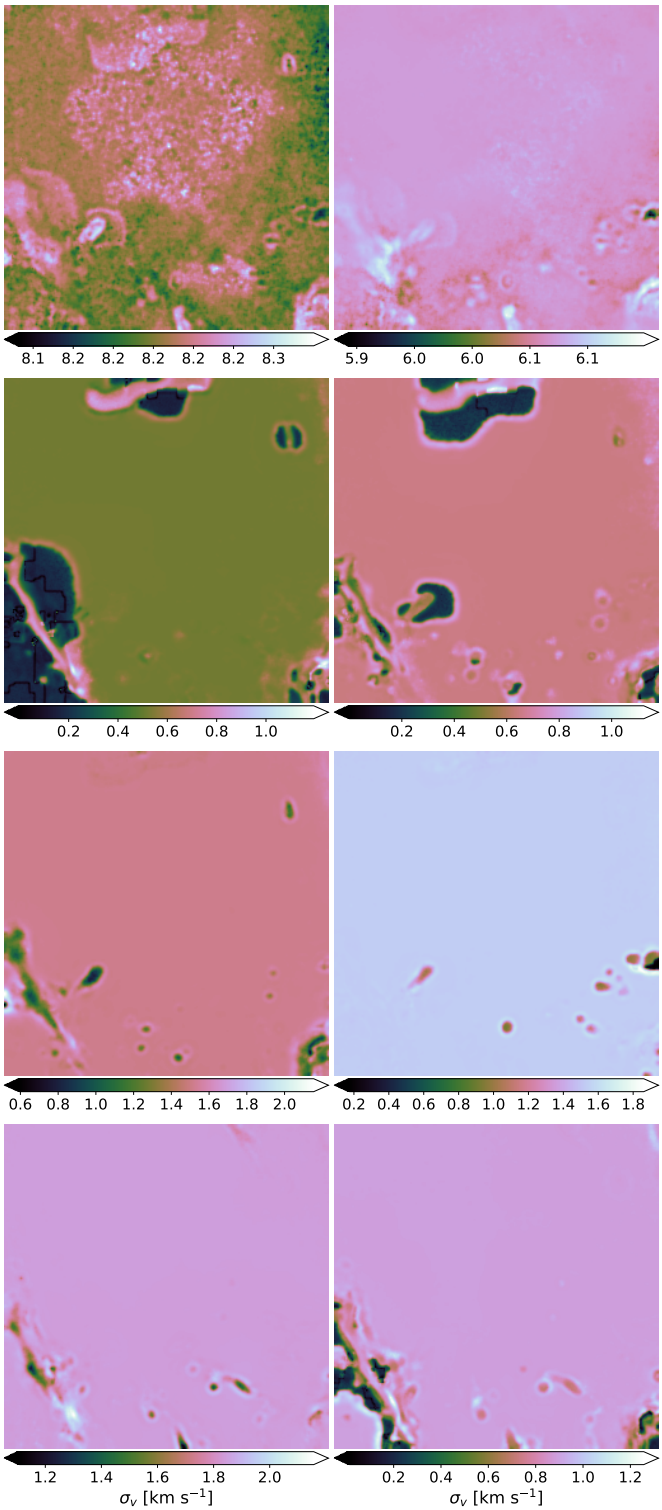

Fig. 9. Dispersion velocity fields $\boldsymbol{\sigma}$ (*left*: σ_1, σ_3, σ_5, σ_7); (*right*: σ_2, σ_4, σ_6, σ_8) obtained by ROHSA using the synthetic observation computed in Sect. 3.2.

emission in NEP indeed exhibits significant emission in the intermediate velocity cloud (IVC) and high velocity cloud (HVC) ranges. In this paper we do not consider the velocity channels with HVC emission; we focus on the phase separation of the local velocity cloud (LVC) and IVC components.

The LVC range between -20 and $+20\,\mathrm{km\,s^{-1}}$ shows relatively smooth emission profiles, with a narrow peak around $-3\,\mathrm{km\,s^{-1}}$ on top of a broader feature (see Fig. 15). The latter is rather smooth but when inspected in detail it shows faint spectral structures on all scales along the velocity axis. The sensitivity of the GHIGLS data is such that these fluctuations of the emission profiles are not due to noise. In fact, they can be followed from one spectrum to the next quite easily. These fluctuations of the emission spectra at scales of a few kilometres per second reveal the presence of CNM and LNM features on a range of velocities.

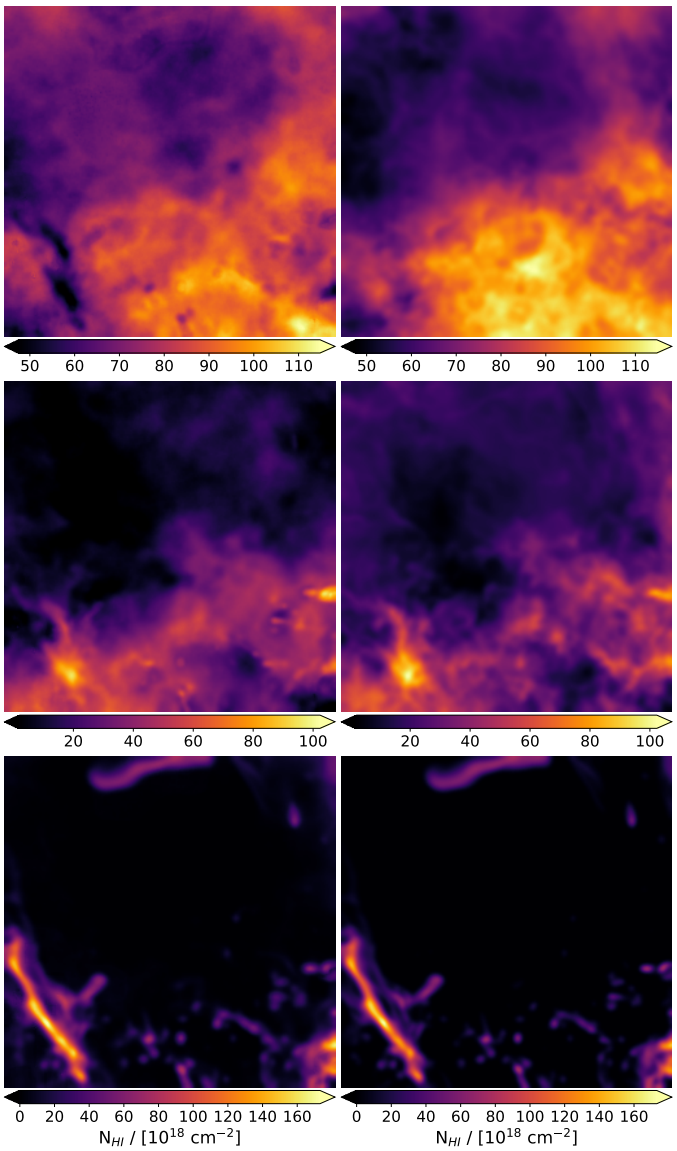

Fig. 10. *Left*: integrated column density maps of the three-phase model extracted by ROHSA. *Right*: integrated column density maps of the three-phase model inferred directly from the simulation using the canonical values $T_{\mathrm{k\,lim,CNM/LNM}} = 500$ and $T_{\mathrm{k\,lim,LNM/WNM}} = 5000$ K. The phases WNM, LNM, and CNM are presented from top to bottom.

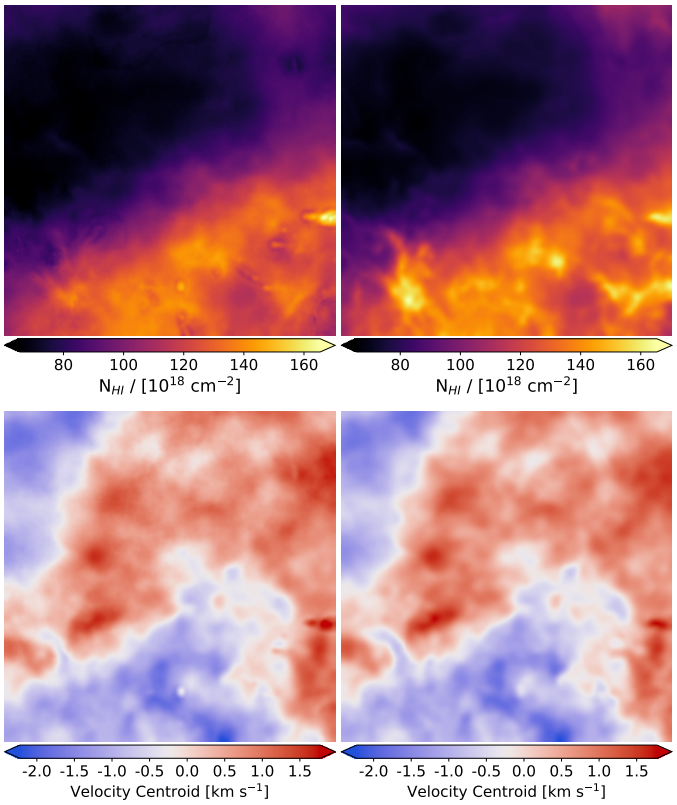

Fig. 11. Synthetic observation of the integrated column density field (*top*) and the centroid velocity field (*bottom*) associated to the inter-cloud medium (WNM + LNM). *Left*: inferred with ROHSA. *Right*: inferred directly from the simulation using all cells with $T_{\mathrm{k\,lim,LNM/WNM}}$ >500 K. For statistical comparison, the spatial power spectra of each one are shown in Figs. 12 and 13.

This field was selected because of its representative 21 cm emission for Galactic latitudes of $b \sim 30°$. The emission features are not particularly complex, nor are they especially simple. In addition, a first Gaussian decomposition of NEP 21 cm data was performed by Martin et al. (2015) which provides an interesting point of comparison. Unlike ROHSA, Martin et al. (2015) used a method similar to the one described by Haud (2000) that considers only the term $||L(v_z, \boldsymbol{r}, \boldsymbol{\theta}(\boldsymbol{r}))||_2^2$ in the parameter optimization. We highlight some qualitative comparisons in the following sections.

4.2. Results

In order to decompose the 21 cm emission of the NEP field, we used ROHSA with $N = 12$ Gaussian components and each hyper-parameter has been set to 1000. As for the previous case, these values have been chosen empirically following the same methodology as described in Sect. 3.3.1, allowing us to converge

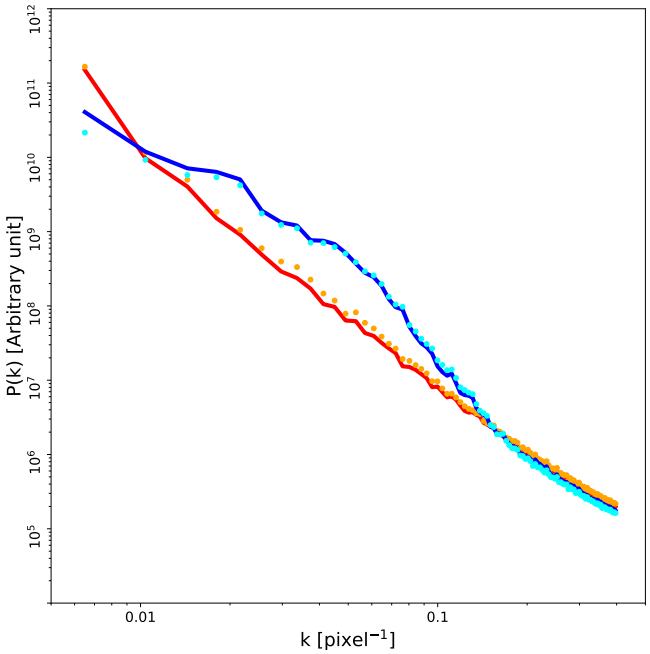

Fig. 12. Spatial power spectrum of the column density. The inter-cloud medium (WNM + LNM) is represented by the orange dotted line (simulation) and the red line (ROHSA). The CNM is shown as a cyan dotted line (simulation) and blue line (ROHSA).

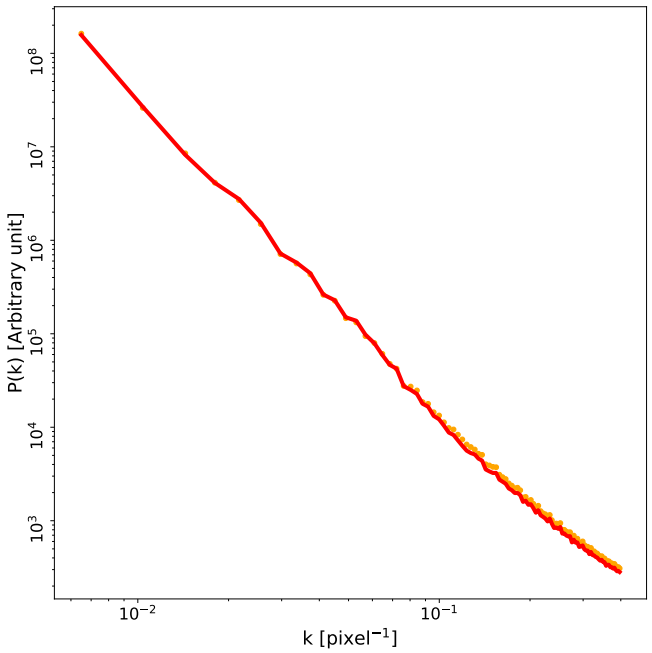

Fig. 13. Spatial power spectrum of the centroid velocity field for the inter-cloud medium (WNM + LNM). The orange dotted line indicates the inter-cloud medium inferred directly from the simulation using all cells with $T_{\mathrm{k\,lim,LNM/WNM}} > 500$ K (bottom-right panel of Fig. 11). The red line shows the inter-cloud medium inferred with ROHSA (bottom-left panel of Fig. 11).

toward a noise-dominated residual with a minimum number of Gaussian components. We note that the hyper-parameter values are not the same as for the first application presented in Sect. 2. The complexity of the underlying signal structure and its signal-to-noise ratio (S/N) are the main causes of these differences. However, a detailed understanding of the behavior of these hyper-parameters would require testing different values over a large number of observations. Such exploration is currently complicated by computations limitations. A GPU version of the code is under development to overcome this main limitation.

The combination of 12 Gaussian components produces a solution that recovers 99% of the total emission with spatially coherent components. The total integrated column density encoded by ROHSA and the residual between our model and the data are shown in Fig. 14 (middle and right panels).

4.2.1. Global properties of the Gaussian sample

Like for the application on the synthetic observations, the Gaussian parameters recovered for the NEP field have a strong spatial coherence; ROHSA converges towards a solution with smooth variations of the Gaussian parameters across the field. It turns out that ROHSA converges toward a multiphase model with Gaussian components of various widths, very similar to the application to numerical simulations presented in Sect. 3.3 but more complex due to the presence of an IVC component in the data.

To have a global view of the thermal state of the gas as a function of velocity, it is useful to look at the two-dimensional dispersion-velocity diagram $\boldsymbol{\sigma} - v$ weighted by the fraction of total emission of each Gaussian $\sqrt{2\pi}\boldsymbol{a}_n\boldsymbol{\sigma}_n / \sum_{\boldsymbol{r}} N_{\mathrm{HI}}(\boldsymbol{r})$ shown in Fig. 16. This diagram shows isolated complexes of Gaussian components in the $\boldsymbol{\sigma} - v$ space. This is a direct result of the way the parameter optimization is done in ROHSA, with a regularization term that favors the minimum variance of $\boldsymbol{\sigma}$. Figure 16 highlights the fact that the 21 cm emission in NEP is mainly composed of negative-velocity components. A clear trend is visible in the velocity range $-60 < v < 0\,\mathrm{km\,s^{-1}}$ with $\boldsymbol{\sigma}$ decreasing from 10 to $1\,\mathrm{km\,s^{-1}}$ going from negative to positive velocities. This likely reflects the radiative condensation of warm intermediate velocity clouds into the local velocity component of the neutral ISM.

At this point it is interesting to compare the results of ROHSA with the Gaussian decomposition of the same data performed by Martin et al. (2015). The $\boldsymbol{\sigma} - v$ diagram of Martin et al. (2015, see their Fig. 7) shows a continuous distribution with arches that bridge together the LVC and IVC gas, an effect that is not observed in our results. Similarly to what we have done here, Martin et al. (2015) used numerical simulations to evaluate the performances of their Gaussian decomposition algorithm. Their tests revealed that such arches in the $\boldsymbol{\sigma} - v$ diagram are unphysical; they are the result of LVC and IVC gas components that overlap in velocity.

It is important to point out that both solutions provide as good a representation of the same dataset. The significant difference between the two solutions highlights the challenge of extracting a physically meaningful representation of the data. We recall that Martin et al. (2015) used an algorithm similar to the ones used by Haud (2000); Miville-Deschênes et al. (2017a); Kalberla & Haud (2018) where the spatial coherence of the solution is not enforced through regularization terms in the cost function. In these previous studies spatial coherence is attempted by providing spatially coherent initial guesses. Each spectrum is then fitted independently and no spatial coherence in the solution is enforced. In practice, this method is rather effective for relatively sparse emission data like CO (Miville-Deschênes et al. 2017a), but in the case of the more confused 21 cm data it produces parameter maps that are more affected by small-scale noise due to the degeneracy of the solution.

A Gaussian decomposition algorithm that fits each spectrum individually is easily fooled by components that overlap in velocity. In this specific case, such an algorithm would find a solution with a smaller number of components but with larger values of $\boldsymbol{\sigma}$. The main innovation in ROHSA is that it is able to cluster different phases even if they are close in velocity. The four energy terms added to the cost function $J(\boldsymbol{\theta}(\boldsymbol{r}))$ allow ROHSA to find a spatially coherent solution while avoiding the mix of components due to the high confusion present in the emission.

4.2.2. A cloud/inter-cloud medium vision of the North ecliptic pole

Integrated column density maps, centroid velocity fields, and dispersion velocity fields obtained with ROHSA are presented in Figs. 17–19, respectively. Mean velocities $\langle\boldsymbol{\mu}_n\rangle$ and mean velocity dispersions $\langle\boldsymbol{\sigma}_n\rangle$ of the 12 Gaussian components G_n are presented in Table 2. In this section we focus on building a coherent cloud/inter-cloud medium vision considering the local component of the emission identified previously. Two of the four components of the local gas, G_7 and G_9, are associated with the CNM with $\langle\boldsymbol{\sigma}_7\rangle = 1.6$ km s^{-1} and $\langle\boldsymbol{\sigma}_9\rangle = 1.9$ km s^{-1}. The other components are used to build the inter-cloud medium. Integrated column density fields and centroid velocity fields of the cloud medium and inter-cloud medium are presented in Fig. 20.

As noted by Martin et al. (2015) in their two-phase decomposition of the local component, filamentary structures are observed in the narrow component. The associated velocity

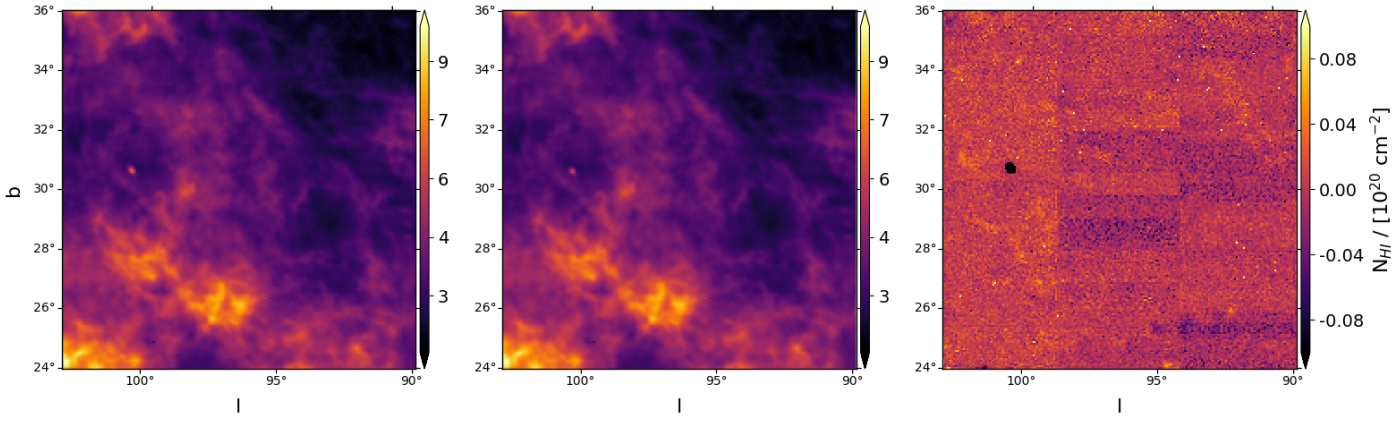

Fig. 14. *Left*: integrated column density $N_{\rm HI}$ of the NEP field which is part of the GHIGLS survey. $N_{\rm HI}$ was computed in the optically thin approximation (see Eq. (17)). *Middle*: integrated column density $\tilde{N}_{\rm HI}$ of NEP inferred with ROHSA. *Right*: residual $\tilde{N}_{\rm HI}$–$N_{\rm HI}$ between the integrated column density field inferred with ROHSA and the original integrated column density field computed with the data.

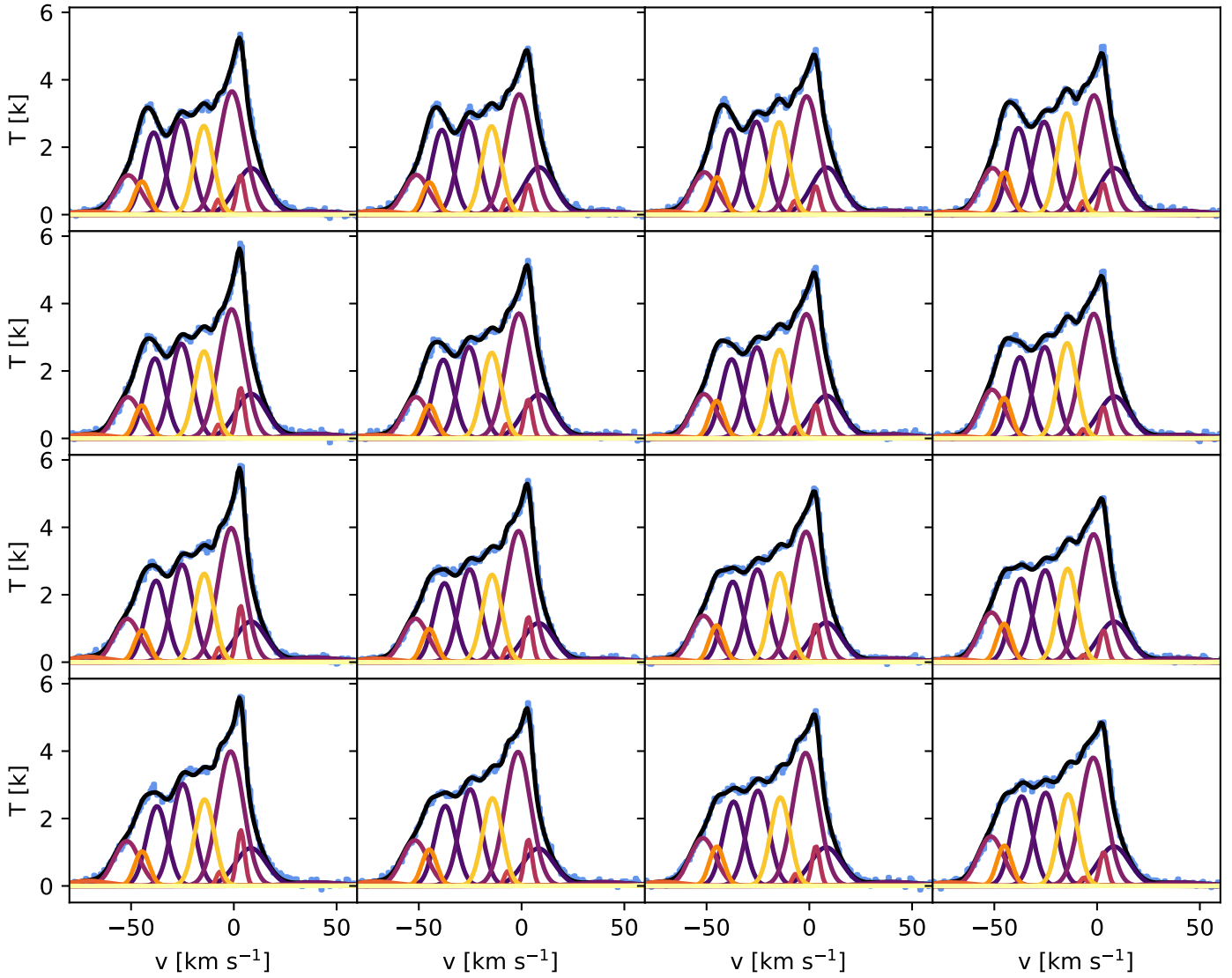

Fig. 15. Example of the Gaussian decomposition obtained by ROHSA (colored line) for a random 4×4 mosaic of NEP. The original signal is show by the blue histogram and the total brightness temperature encoded by ROHSA is shown in black. The other lines detail the components of the Gaussian model. The spatial coherence of the solution can be seen over the mosaic with a smooth variation of the amplitude, central velocity, and velocity dispersion of each Gaussian component.

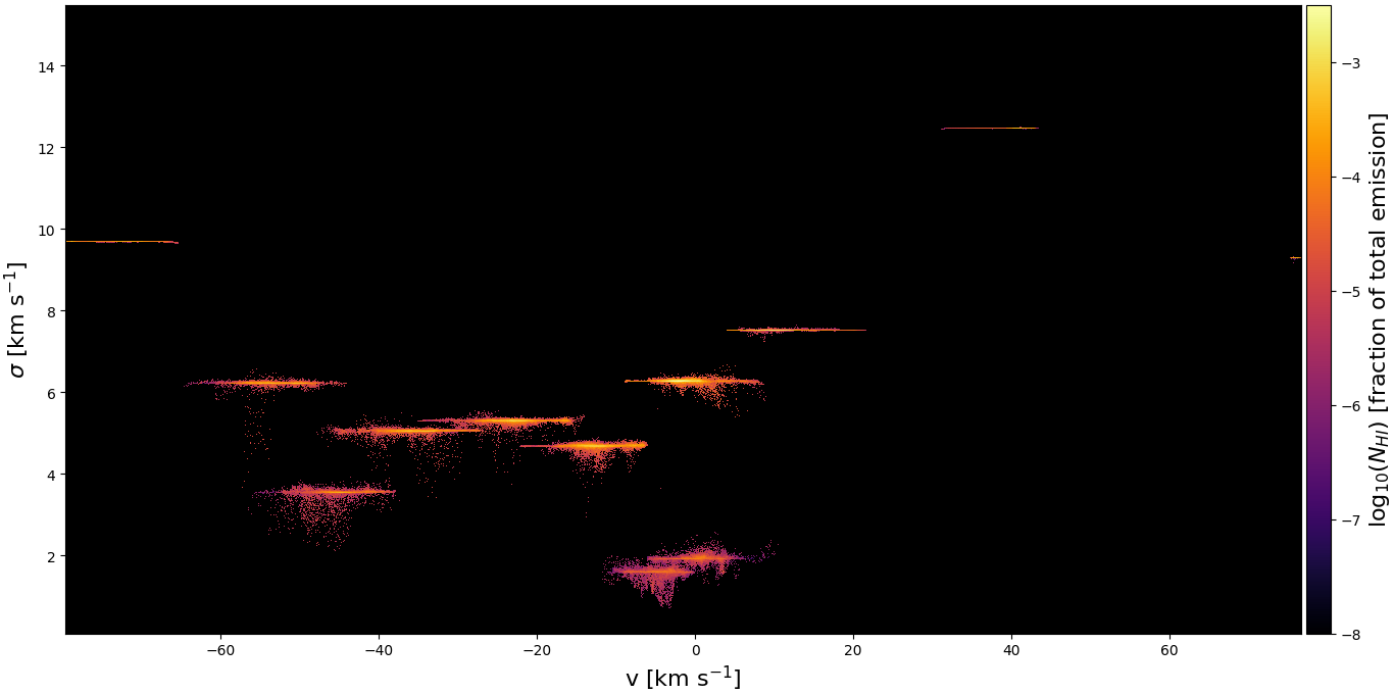

Fig. 16. Two-dimensional probability distribution function σ-v weighted by the fraction of total emission of each Gaussian $\sqrt{2\pi}\boldsymbol{a}_n\boldsymbol{\sigma}_n / \sum_{\boldsymbol{r}} N_{\rm HI}(\boldsymbol{r})$ of NEP. The NEP is mainly composed of negative intermediate velocity components.

Table 2. Mean velocity $\langle\boldsymbol{\mu}_n\rangle$ and mean velocity dispersion $\langle\boldsymbol{\sigma}_n\rangle$ of the 12 Gaussian components G_n inferred by ROHSA in NEP.

	G_1	G_2	G_3	G_4	G_5	G_6	G_7	G_8	G_9	G_{10}	G_{11}	G_{12}
$\langle\boldsymbol{\mu}_n\rangle$ (km s^{-1})	−74.1	−53.9	−44.7	−35.0	−22.9	−12.6	−4.8	−1.3	0.2	10.9	40.8	75.9
$\langle\boldsymbol{\sigma}_n\rangle$ (km s^{-1})	9.7	6.2	3.5	5.1	5.3	4.7	1.6	6.3	1.9	7.5	12.5	9.3

dispersion fields (see Fig. 19, component G_7 and G_9) coherent fluctuating values over a large part of the field. The core of these filamentary structures appears narrower than the envelop with velocity dispersion reaching about 0.87 km s^{-1} (the spectral resolution) in their centers.

The broader component has an integrated column density field with no particular structure like filaments (see Fig. 20, top-right). Like for the numerical simulation, the sum of the broad components is likely to represent a phase that fills a large fraction of the volume, as would an inter-cloud medium. One interesting aspect of the ROHSA decomposition is that it then allows to extract the velocity field of this volume-filling component (Fig. 20, bottom-right), enabling the characterization of the turbulent cascade in a mixture of lukewarm phase and warm phase.

5. Discussion

Historically, a large number of studies used a Gaussian basis to model 21 cm data. Different algorithms have been developed; all of them are fitting each spectrum individually, with or without information from the neighboring solutions to initialize the fit. To further constrain the degeneracy of the fit, solutions with the smallest number of Gaussian components have often been favored (e.g., Lindner et al. 2015). Because of velocity blending, the solution with the smallest number of components is not necessarily the best one. In some cases, narrow features overlap in velocity, making it impossible to separate them if the environment is not considered. Usually, this confusion breaks apart a few beams away and more components can be recovered. The fundamental idea behind ROHSA is that we are trying to extract diffuse components that have column density, centroid velocity, and velocity dispersion with smooth spatial variations. The optimization scheme has been designed with that concept at its core. In order to achieve this, ROHSA fits the whole data cube at once.

The application of ROHSA on both synthetic observations from numerical simulations and observational data converges naturally toward a multiphase model of the neutral ISM. The ability of ROHSA to extract the multiphase nature of the neutral ISM opens a totally new perspective on the study of the nature of the condensation process acting in the ISM. It is clear from a numerical point of view that the formation of cold clouds is the result of the condensation of the warm and diffuse gas through the thermal instability coupled with turbulence. From an observational point of view, spatial correlations between the different phases can now be made in order to more precisely quantify how the CNM emerges from this condensation process. This separation also opens the possibility to describe the properties of the very specific multiphase turbulence of the HI. ROHSA appears to be efficient at clustering different structures in PPV space, even when there is a high level of confusion. In particular, the separation of the LVC and IVC is known to be particularly challenging as the CNM and WNM of both components overlap significantly in velocity (Martin et al. 2015). As shown in Fig. 16, ROHSA significantly limits the "Arch effect" typical of this confusion (see Sect. 4). Globally, the performance in ROHSA on regions of high

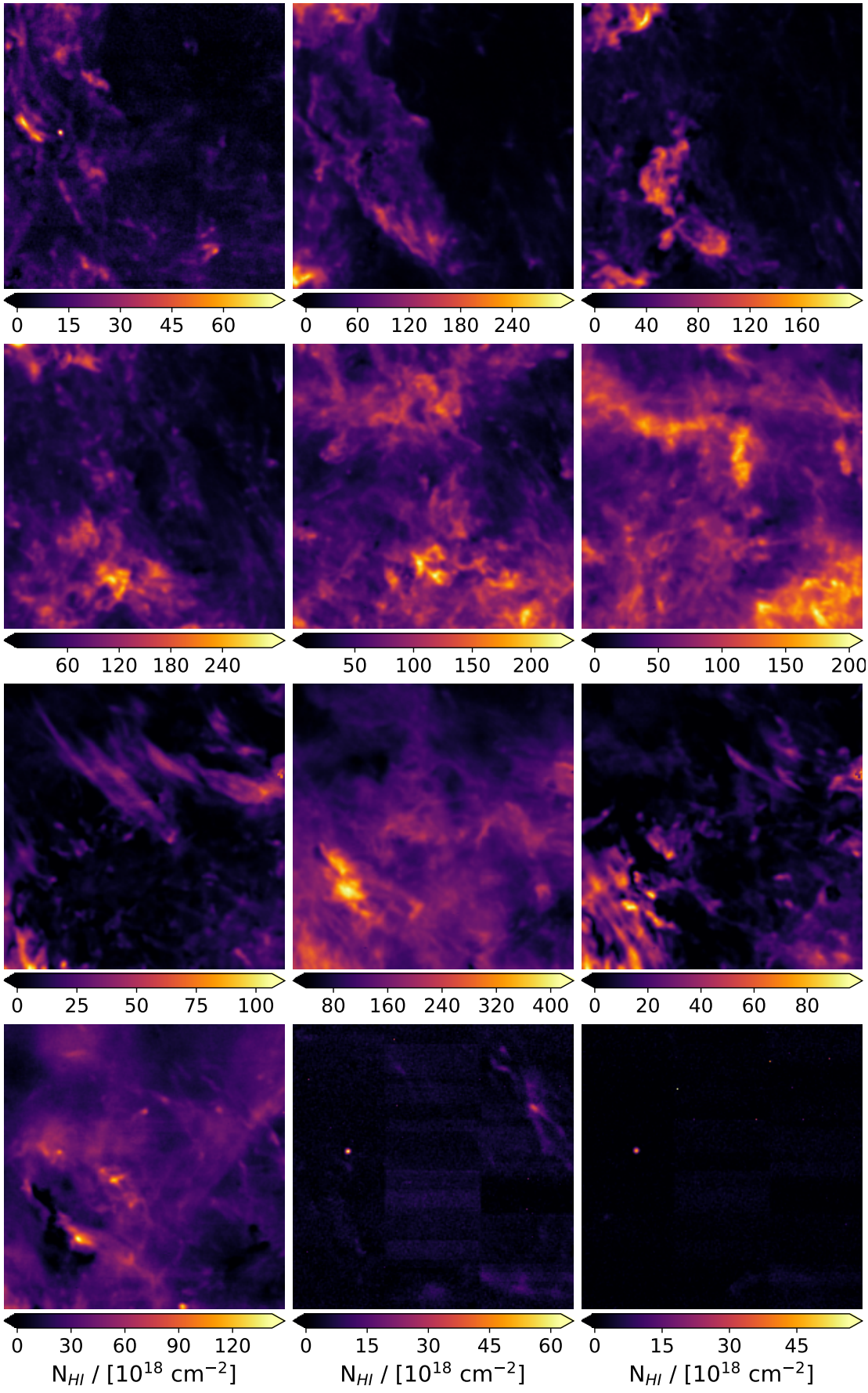

Fig. 17. Integrated column density maps (*left*: G_1, G_4, G_7, G_{10}; *middle*: G_2, G_5, G_8, G_{11}; *right*: G_3, G_6, G_9, G_{12}) obtained by ROHSA applied on NEP. Mean velocity $\langle \boldsymbol{\mu}_n \rangle$ and mean velocity dispersion $\langle \boldsymbol{\sigma}_n \rangle$ are presented in Table 2.

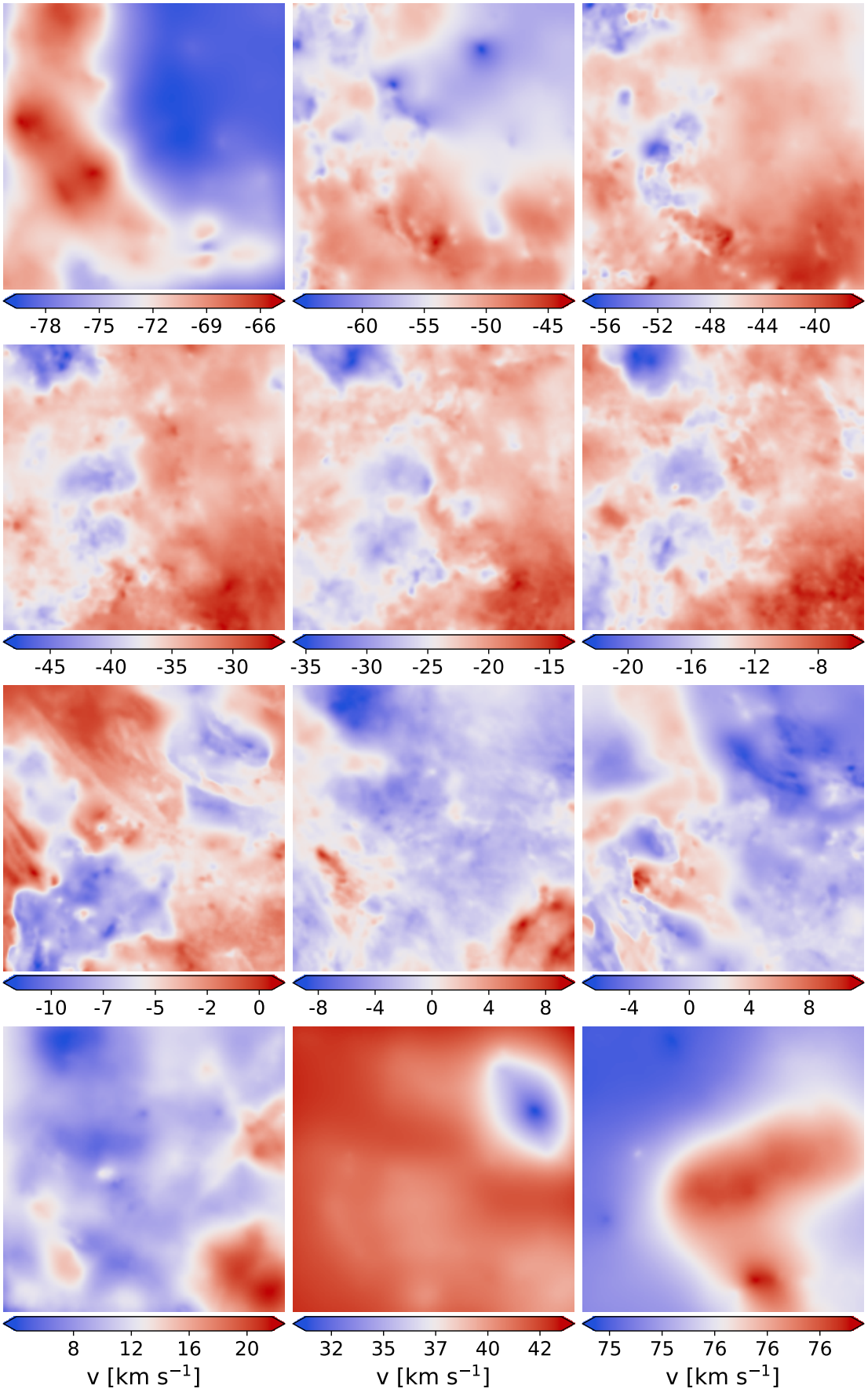

Fig. 18. Centroid velocity fields $\boldsymbol{\mu}$ (*left*: $\mu_1, \mu_4, \mu_7, \mu_{10}$; *middle*: $\mu_2, \mu_5, \mu_8, \mu_{11}$; *right*: $\mu_3, \mu_6, \mu_9, \mu_{12}$) obtained by ROHSA applied on NEP.

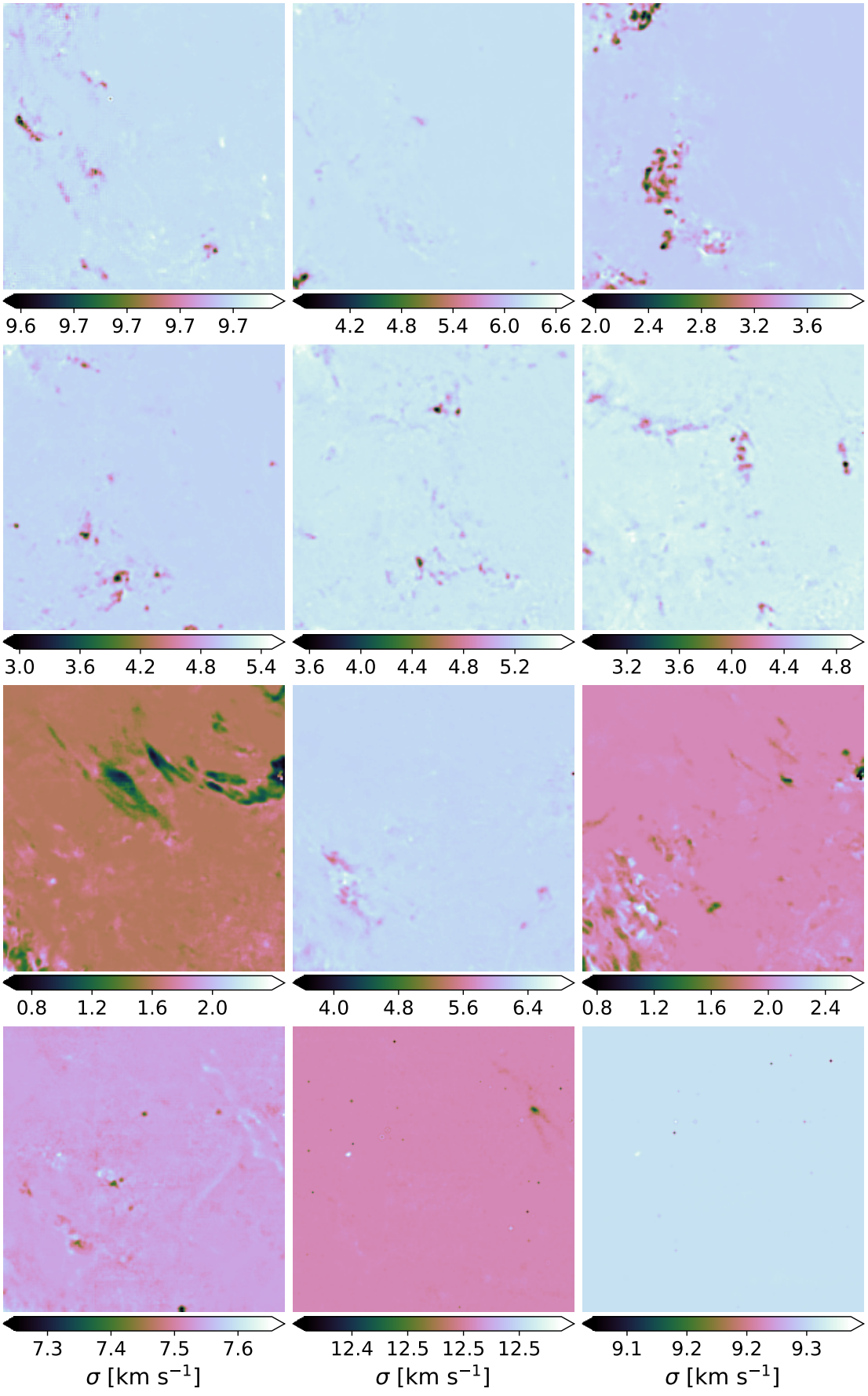

Fig. 19. Velocity dispersion maps $\boldsymbol{\sigma}$ (*left*: σ_1, σ_4, σ_7, σ_{10}; *middle*: σ_2, σ_5, σ_8, σ_{11}; *right*: σ_3, σ_6, σ_9, σ_{12}) obtained by `ROHSA` applied on NEP.

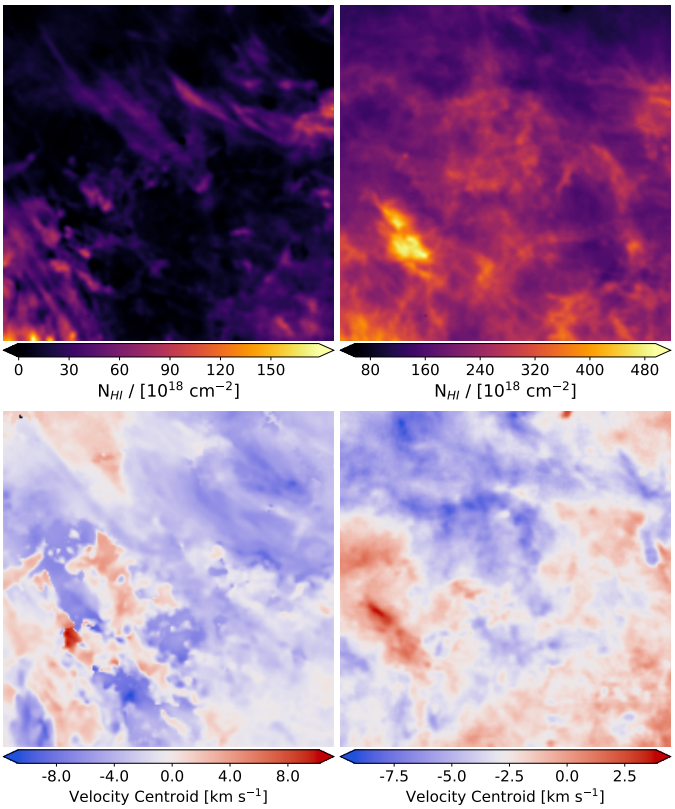

Fig. 20. *Left*: CNM. *Right*: inter-cloud medium (WNM+LNM) in NEP inferred with ROHSA. *Top and bottom*: column density and centroid velocity fields, respectively.

Galactic latitude opens a large range of possibilities regarding the study of infalling neutral clouds from the galactic halo.

We would also like to point out that no a priori information about the number of phases present in the neutral ISM is provided to ROHSA. The algorithm rests only on the hypothesis of the existence of components with similar line width through the energy term $\lambda'_\sigma \|\boldsymbol{\sigma}_n - m_n\|_2^2$. In that respect, ROHSA is perfectly adapted to decomposing hyper-spectral observations of any type, not only 21 cm emission.

At this time the main limitations of ROHSA are computational. First, as the whole PPV cube is fitted at once, the use of ROHSA is limited to cubes that can fit in memory. Second, the current computation time of ROHSA is not negligible (e.g., about two hours on a single CPU for a $256 \times 256 \times 100$ PPV cube with 8 Gaussians). This limits the possibility to make a deep exploration of the hyper-parameters λ_i. In particular it would be interesting to explore various weights of the hyper-parameters for the deduced quantities (a, μ and σ). It is expected that the amplitude of the spatial variations of these quantities are not the same. For instance, in a multi-phase medium like the HI, the density field (represented by a) might vary more strongly on smaller scales than the velocity field. This might require different values of λ_a compared to λ_μ, λ_σ and λ'_σ. A GPU version of the code is under development that would allow such an exploration.

6. Summary

Here we present a new Gaussian decomposition algorithm named ROHSA. Energy terms have been added to the classical cost function to take into account the spatial coherence of the emission and the multiphase nature of the gas simultaneously. In order to identify a solution with spatially smooth parameters, the fit is performed on the whole hyper-spectral cube at once.

The performance of ROHSA has been evaluated using a synthetic 21 cm observation computed from a numerical simulation of thermally bi-stable turbulence. It was then tested on a 21 cm observation of a field of high Galactic latitude observed with the GBT. The main conclusions are as follows.

1. ROHSA is able to naturally highlight the physics of any multiphase medium without a priori information regarding the number of phases.
2. Evaluation on numerical simulation of thermally bi-stable turbulence shows that the sum of Gaussian components is a good approximation to model the multiphase nature of the neutral ISM.
3. The multiphase model inferred with ROHSA provides a spatially coherent vision of the integrated column density map, the centroid velocity field, and the velocity dispersion field of each component.
4. The power spectra of the integrated column density and centroid velocity fields are well recovered with ROHSA. Statistical properties of turbulence in the multiphase neutral ISM now become accessible.
5. The decomposition of a high-latitude HI gas observation shows the wide range of applications enabled with ROHSA, for instance to study the radiative condensation of the WNM and the nature of the ISM at the disk-halo interface.

Acknowledgements. Part of this work was supported by Hyperstars, a project funded by the MASTODONS initiative of the CNRS mission for interdisciplinarity and by the Programme National "Physique et Chimie du Milieu Interstellaire" (PCMI) of CNRS/INSU with INC/INP co-funded by CEA and CNES. This work took part under the program Milky-Way-*Gaia* of the PSI2 project funded by the IDEX Paris-Saclay, ANR-11-IDEX-0003-02. We gratefully acknowledge Lucie Riu for enlightening conversations. We thank the anonymous referee whose comments and suggestions have improved this manuscript.

References

Audit, E., & Hennebelle, P. 2005, A&A, 433, 1
Begum, A., Stanimirovic, S., Goss, W. M., et al. 2010, ApJ, 725, 1779
Chandrasekhar, S., & Münch, G. 1952, ApJ, 115, 103
Clark, B. G. 1965, ApJ, 142, 1398
Davis, R. J. 1957, ApJ, 125, 391
Dickey, J. M., & Lockman, F. J. 1990, ARA&A, 28, 215
Dickey, J. M., McClure-Griffiths, N. M., Gaensler, B. M., & Green, A. J. 2003, ApJ, 585, 801
Dieter, N. H. 1964, AJ, 69, 288
Dieter, N. H. 1965, AJ, 70, 552
Field, G. B. 1965, ApJ, 142, 531
Field, G. B., Goldsmith, D. W., & Habing, H. J. 1969, ApJ, 155, L149
Haud, U. 2000, A&A, 364, 83
Haud, U., & Kalberla, P. M. W. 2007, A&A, 466, 555
Heeschen, D. S. 1955, ApJ, 121, 569
Heiles, C., & Troland, T. H. 2003a, ApJS, 145, 329
Heiles, C., & Troland, T. H. 2003b, ApJ, 586, 1067
Hennebelle, P., & Pérault, M. 1999, A&A, 351, 309
Hennebelle, P., Banerjee, R., Vázquez-Semadeni, E., Klessen, R. S., & Audit, E. 2008, A&A, 486, L43
Kalberla, P. M. W., & Haud, U. 2018, A&A, 619, A58
Kalberla, P. M. W., Burton, W. B., Hartmann, D., et al. 2005, A&A, 440, 775
Kanekar, N., Subrahmanyan, R., Chengalur, J. N., & Safouris, V. 2003, MNRAS, 346, L57
Koyama, H., & Inutsuka, S.-i. 2002, ApJ, 564, L97
Lee, M.-Y., Stanimirovic, S., Murray, C. E., Heiles, C., & Miller, J. 2015, ApJ, 809, 56
Lindblad, P. O. 1966, BAN Suppl., 1, 177
Lindner, R. R., Vera-Ciro, C., Murray, C. E., et al. 2015, AJ, 149, 138
Martin, P. G., Blagrave, K. P. M., Lockman, F. J., et al. 2015, ApJ, 809, 153
Matthews, T. A. 1957, AJ, 62, 25
McClure-Griffiths, N. M., Pisano, D. J., Calabretta, M. R., et al. 2009, ApJS, 181, 398

Mebold, U. 1972, A&A, 19, 13
Miville-Deschênes, M.-A., & Martin, P. G. 2007, A&A, 469, 189
Miville-Deschênes, M.-A., Levrier, F., & Falgarone, E. 2003, ApJ, 593, 831
Miville-Deschênes, M.-A., Murray, N., & Lee, E. J. 2017a, ApJ, 834, 57
Miville-Deschênes, M.-A., Salomé, Q., Martin, P. G., et al. 2017b, A&A, 599, A109
Muller, C. A. 1957, ApJ, 125, 830
Muller, C. A. 1959, IAU Symp., 9, 360
Murray, C. E., Lindner, R. R., Stanimirovic, S., et al. 2014, ApJ, 781, L41
Murray, C. E., Stanimirović, S., Goss, W. M., et al. 2015, ApJ, 804, 89
Murray, C. E., Stanimirović, S., Goss, W. M., et al. 2018a, ApJS, 238, 14
Murray, C. E., Peek, J. E. G., Lee, M.-Y., & Stanimirović, S. 2018b, ApJ, 862, 131
Ostriker, E. C., McKee, C. F., & Leroy, A. K. 2010, ApJ, 721, 975
Peek, J. E. G., Babler, B. L., Zheng, Y., et al. 2018, ApJS, 234, 2
Poppel, W. G. L., Marronetti, P., & Benaglia, P. 1994, A&A, 287, 601
Roy, N., Kanekar, N., Braun, R., & Chengalur, J. N. 2013a, MNRAS, 436, 2352
Roy, N., Kanekar, N., & Chengalur, J. N. 2013b, MNRAS, 436, 2366
Saury, E., Miville-Deschênes, M.-A., Hennebelle, P., Audit, E., & Schmidt, W. 2014, A&A, 567, A16
Stanimirović, S., & Heiles, C. 2005, ApJ, 631, 371
Stanimirović, S., Murray, C. E., Lee, M.-Y., Heiles, C., & Miller, J. 2014, ApJ, 793, 132
Stil, J. M., Taylor, A. R., Dickey, J. M., et al. 2006, AJ, 132, 1158
Takakubo, K. 1967, BAN, 19, 125
Takakubo, K., & van Woerden, H. 1966, BAN, 18, 488
Taylor, A. R., Gibson, S. J., Peracaula, M., et al. 2003, AJ, 125, 3145
Verschuur, G. L. 2004, AJ, 127, 394
Verschuur, G. L., & Schmelz, J. T. 1989, AJ, 98, 267
Verschuur, G. L., & Magnani, L. 1994, AJ, 107, 287
von Hoerner, S. 1951, Zeitschrift fur Astrophysik, 30, 17
von Weizsäcker, C. F. 1951, ApJ, 114, 165
Winkel, B., Kerp, J., Flöer, L., et al. 2016, A&A, 585, A41
Wolfire, M. G., Hollenbach, D., McKee, C. F., Tielens, A. G. G. M., & Bakes, E. L. O. 1995, ApJ, 443, 152
Wolfire, M. G., McKee, C. F., Hollenbach, D., & Tielens, A. G. G. M. 2003, ApJ, 587, 278
Zhu, C., Byrd, R. H., Lu, P., & Nocedal, J. 1997, ACM Trans. Math. Softw., 23, 550

Appendix A: Optimization algorithm

Terms used to compute the gradient $\nabla J(\boldsymbol{\theta}, \boldsymbol{m})$ of the cost function $J(\boldsymbol{\theta}, \boldsymbol{m})$ are detailed in this appendix. Incorporated are the Jacobian of the residual $\nabla L(\boldsymbol{\theta})$ and the gradients of the regularization term $\nabla R^t(\boldsymbol{\theta}, \boldsymbol{m}) = [\nabla_{\boldsymbol{\theta}} R^t(\boldsymbol{\theta}, \boldsymbol{m}), \nabla_{\boldsymbol{m}} R^t(\boldsymbol{\theta}, \boldsymbol{m})]$

$$\nabla L(v_z, \boldsymbol{\theta}(\boldsymbol{r})) = \begin{bmatrix} \exp\left(-\frac{(v_z-\mu_1(\boldsymbol{r}))^2}{2\sigma_1(\boldsymbol{r})^2}\right) \\ \frac{a_1(v_z-\mu_1(\boldsymbol{r}))}{\sigma_1^2} \exp\left(-\frac{(v_z-\mu_1(\boldsymbol{r}))^2}{2\sigma_1(\boldsymbol{r})^2}\right) \\ \frac{a_1(v_z-\mu_1(\boldsymbol{r}))^2}{\sigma_1^3} \exp\left(-\frac{(v_z-\mu_1(\boldsymbol{r}))^2}{2\sigma_1(\boldsymbol{r})^2}\right) \\ \vdots \\ \frac{a_N(v_z-\mu_N(\boldsymbol{r}))^2}{\sigma_N^3} \exp\left(-\frac{(v_z-\mu_N(\boldsymbol{r}))^2}{2\sigma_1(\boldsymbol{r})^2}\right) \end{bmatrix} \tag{A.1}$$

$$\nabla_{\boldsymbol{\theta}} R(\boldsymbol{\theta}, \boldsymbol{m}) = \begin{bmatrix} \lambda_a \boldsymbol{D}^t \boldsymbol{D} \boldsymbol{a}_1 \\ \lambda_\mu \boldsymbol{D}^t \boldsymbol{D} \boldsymbol{\mu}_1 \\ \lambda_\sigma \boldsymbol{D}^t \boldsymbol{D} \boldsymbol{\sigma}_1 \\ \lambda'_\sigma(\boldsymbol{\sigma}_1 - m_1) \\ \vdots \\ \lambda'_\sigma(\boldsymbol{\sigma}_N - m_N) \end{bmatrix} \tag{A.2}$$

$$\nabla_{\boldsymbol{m}} R(\boldsymbol{\theta}, \boldsymbol{m}) = \begin{bmatrix} -\sum_{\boldsymbol{r}} \lambda'_\sigma(\boldsymbol{\sigma}_1 - m_1) \\ \vdots \\ -\sum_{\boldsymbol{r}} \lambda'_\sigma(\boldsymbol{\sigma}_N - m_N) \end{bmatrix}. \tag{A.3}$$

Appendix B: Computation time

The computation time needed to perform the Gaussian decomposition of the synthetic PPV cube presented in Sect. 3 is described in Fig. B.1. The computation time depends on the number of Gaussian components N, the size of the cube (number of spectra and number of velocity channels), and the maximum number of iterations used in the optimization.

For a given N, the computation time scales linearly with the number of spectra and the number of velocity channels. Therefore, as for each step of the multi-resolution process, from coarse to fine grid, the size of the grid is multiplied by a factor of four; the computation time also increases by a factor four at each step. We note that each step has the same maximum number of iterations (here 800) that also linearly impact the computation time.

Finally, we observed that the computation time depends nonlinearly on N, as seen in Fig. B.1.

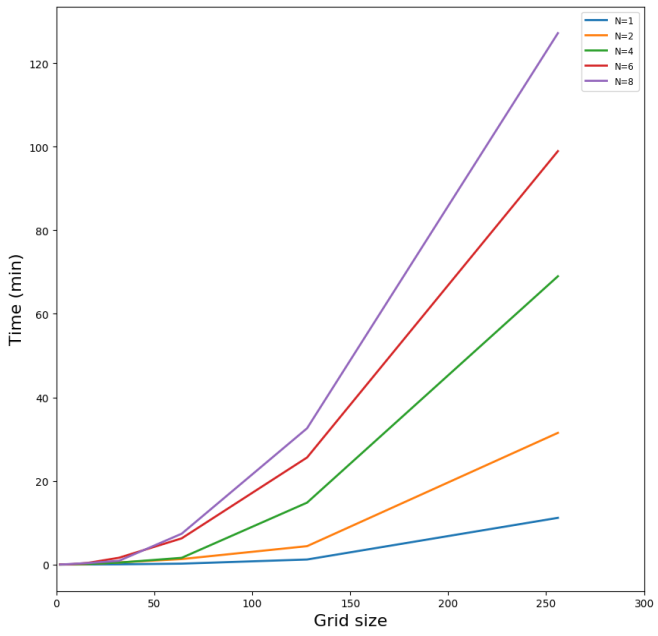

Fig. B.1. Computation time used by one CPU to perform the Gaussian decomposition of the simulated PPV cube used in Sect. 3, for $N = 1$, 2, 4, 6, and 8, as function of the size grid. The maximum number of iterations in each case has been set to 800.

Bibliography

Adams, Walter S. (1949). “Observations of Interstellar H and k, Molecular Lines, and Radial Velocities in the Spectra of 300 O and B Stars.” en. In: ApJ 109, p. 354 (cit. on p. 41).

Anderson, John (1995). Computational Fluid Dynamics. en. Google-Books-ID: dJceAQAAIAAJ. McGraw-Hill Education (cit. on pp. 6, 25).

Audit, E. and P. Hennebelle (2005). “Thermal condensation in a turbulent atomic hydrogen flow”. In: A&A 433, pp. 1–13 (cit. on pp. 2, 102).

Baker, P. L. (1973). “A Statistical Investigation of Neutral Hydrogen Line Proffles”. In: A&A 23, p. 81 (cit. on p. 44).

Bakes, E. L. O. and A. G. G. M. Tielens (1994). “The Photoelectric Heating Mechanism for Very Small Graphitic Grains and Polycyclic Aromatic Hydrocarbons”. en. In: ApJ 427, p. 822 (cit. on p. 31).

Bastian, Peter, Dieter Kranzlmüller, H Brüchle, and M Brehm (2018). High performance computing in science. en. OCLC: 1090779874 (cit. on p. 100).

Beck, Rainer (2001). “Galactic and Extragalactic Magnetic Fields”. en. In: Space Sci. Rev. 99, p. 243 (cit. on pp. 39, 101).

Begelman, Mitchell C. and Christopher F. McKee (1990). “Global effects of thermal conduction on two-phase media”. In: ApJ 358, pp. 375–391 (cit. on p. 29).

Begum, Ayesha, Snezana Stanimirovic, W. M. Goss, et al. (2010). “The Thermally Unstable Warm Neutral Medium: Key for Modeling the Interstellar Medium”. In: ApJ 725. bibtex: begum2010a, pp. 1779–1785 (cit. on p. 49).

Benjamin, Robert A., Kim A. Venn, Daniel D. Hiltgen, and Christopher Sneden (1996). “The Distance to an X-Ray Shadowing Molecular Cloud in Ursa Major”. en. In: ApJ 464, p. 836 (cit. on p. 43).

Berkhuijsen, E. M., D. Mitra, and P. Mueller (2006). “Filling factors and scale heights of the DIG in the Milky Way”. In: Astronomische Nachrichten 327.1. arXiv: astro-ph/0511172, pp. 82–96 (cit. on pp. 96, 101).

Blagrave, K., P. G. Martin, G. Joncas, et al. (2017). “DHIGLS: DRAO H I Intermediate Galactic Latitude Survey”. In: ApJ 834, p. 126 (cit. on p. 36).

Boldyrev, Stanislav (2002). “Kolmogorov-Burgers Model for Star-forming Turbulence”. In: ApJ 569, pp. 841–845 (cit. on p. 15).

Brunt, C. M., C. Federrath, and D. J. Price (2010a). “A method for reconstructing the variance of a 3D physical field from 2D observations: application to turbulence in the interstellar medium”. In: MNRAS 403, pp. 1507–1515 (cit. on p. 92).

Brunt, Christopher M., Christoph Federrath, and Daniel J. Price (2010b). “A method for reconstructing the PDF of a 3D turbulent density field from 2D observations”. In: MNRAS 405, pp. L56–L60 (cit. on p. 92).

Brüns, C., J. Kerp, and A. Pagels (2001). “Deep H {I} observations of the compact high-velocity cloud {HVC 125+41-207}”. In: A&A 370, pp. L26–L30 (cit. on p. 43).

Chandrasekhar, S. and G. Münch (1952). “The Theory of the Fluctuations in Brightness of the Milky way. V.” In: ApJ 115, p. 103 (cit. on p. 2).

Clark, B. G. (1965). “An Interferometer Investigation of the 21-CENTIMETER Hydrogen-Line Absorption.” In: ApJ 142, p. 1398 (cit. on pp. 2, 24, 48).

Clark, S. E., J. E. G. Peek, and M. E. Putman (2014). “Magnetically Aligned H I Fibers and the Rolling Hough Transform”. In: ApJ 789, p. 82 (cit. on p. 36).

Clark, S.E., J. Colin Hill, J.E.G. Peek, M.E. Putman, and B.L. Babler (2015). “Neutral Hydrogen Structures Trace Dust Polarization Angle: Implications for Cosmic Microwave Background Foregrounds”. en. In: Phys. Rev. Lett. 115.24 (cit. on p. 36).

Crovisier, J. and J. M. Dickey (1983). “The spatial power spectrum of galactic neutral hydrogen from observations of the 21-cm emission line”. In: A&A 122, pp. 282–296 (cit. on pp. 44, 45).

Davidson, P. (2015). Turbulence: An Introduction for Scientists and Engineers. Oxford University Press (cit. on pp. 6, 7, 10).

Davis, Robert J. (1957). “21-CENTIMETER Observations Near Galactic Longitude 120°.” In: ApJ 125, p. 391 (cit. on p. 48).

Dawson, J. R., N. M. McClure-Griffiths, John M. Dickey, and Y. Fukui (2011). “Molecular Clouds in Supershells: A Case Study of Three Objects in the Walls of GSH 287+04-17 and GSH 277+00+36”. en. In: ApJ 741.2, p. 85 (cit. on p. 39).

Dawson, J. R., E. Ntormousi, Y. Fukui, T. Hayakawa, and K. Fierlinger (2015). “A Young Giant Molecular Cloud Formed at the Interface of Two Colliding Supershells: Observations Meet Simulations”. en. In: ApJ 799.1, p. 64 (cit. on p. 39).

Dickey, John M. and Felix J. Lockman (1990). “H I in the Galaxy”. In: ARA&A 28, pp. 215–261 (cit. on pp. 37, 38, 49, 87, 88, 96, 99).

Dickey, John M., N. M. McClure-Griffiths, Sneźana Stanimirović, B. M. Gaensler, and A. J. Green (2001). “Southern Galactic Plane Survey Measurements of the Spatial Power Spectrum of Interstellar H I in the Inner Galaxy”. In: ApJ 561, pp. 264–271 (cit. on pp. 44, 45).

Dickey, John M., N. M. McClure-Griffiths, B. M. Gaensler, and A. J. Green (2003). “Fitting Together the H I Absorption and Emission in the Southern Galactic Plane Survey”. In: ApJ 585, pp. 801–822 (cit. on pp. 34, 35, 49).

Dieter, Nannielou H. (1964). “Neutral hydrogen near the north galactic pole”. In: AJ 69, p. 288 (cit. on p. 48).

– (1965). “Neutral hydrogen near the galactic poles”. In: AJ 70, p. 552 (cit. on p. 48).

Diplas, Athanassios and Blair D. Savage (1994a). “An IUE survey of interstellar H I LY alpha absorption. 1: Column densities”. In: ApJS 93, pp. 211–228 (cit. on p. 86).

– (1994b). “An IUE survey of interstellar H I LY alpha absorption. 2: Interpretations”. In: ApJ 427, pp. 274–287 (cit. on p. 86).

Elmegreen, Bruce G. and John Scalo (2004). “Interstellar Turbulence I: Observations and Processes”. In: ARA&A 42, pp. 211–273 (cit. on pp. 19, 20, 44).

Elmegreen, Bruce G., Sungeun Kim, and Lister Staveley-Smith (2001). “A Fractal Analysis of the H I Emission from the Large Magellanic Cloud”. en. In: ApJ 548.2, p. 749 (cit. on p. 19).

Esquivel, A., A. Lazarian, S. Horibe, et al. (2007). “Statistics of velocity centroids: effects of density-velocity correlations and non-Gaussianity”. In: MNRAS 381, pp. 1733–1744 (cit. on p. 90).

Esquivel, Alejandro and A. Lazarian (2005). “Velocity Centroids as Tracers of the Turbulent Velocity Statistics”. In: ApJ 631, pp. 320–350 (cit. on p. 22).

Field, G. B., D. W. Goldsmith, and H. J. Habing (1969). “Cosmic-Ray Heating of the Interstellar Gas”. In: ApJLetters 155, p. L149 (cit. on pp. 2, 25, 34, 44).

Field, George B. (1965). “Thermal Instability.” In: ApJ 142, p. 531 (cit. on pp. 2, 24, 25, 27–29, 44, 102).

Gaensler, B. M., G. J. Madsen, S. Chatterjee, and S. A. Mao (2008). “The Vertical Structure of Warm Ionised Gas in the Milky Way”. In: Publications of the Astronomical Society of Australia 25.4. arXiv: 0808.2550, pp. 184–200 (cit. on p. 96).

Gazol, Adriana and Jongsoo Kim (2010). “Density Power Spectrum in Turbulent Thermally Bistable Flows”. In: ApJ 723, pp. 482–491 (cit. on p. 21).

Goldman, I. (2000). “Interpretation of the Spatial Power Spectra of Neutral Hydrogen in the Galaxy and in the Small Magellanic Cloud”. In: ApJ 541, pp. 701–706 (cit. on p. 44).

Green, Gregory M., Edward F. Schlafly, Douglas Finkbeiner, et al. (2018). “Galactic Reddening in 3D from Stellar Photometry - An Improved Map”. In: ArXiv e-prints 1801, arXiv:1801.03555 (cit. on p. 86).

Green, Gregory Maurice, Edward F. Schlafly, Douglas P. Finkbeiner, et al. (2014). “Measuring Distances and Reddenings for a Billion Stars: Towards A 3D Dust Map from Pan-STARRS 1”. In: ApJ 783.2. arXiv: 1401.1508, p. 114 (cit. on p. 86).

Haud, U. (2000). “Gaussian decomposition of the Leiden/Dwingeloo survey. I. Decomposition algorithm”. In: A&A 364, pp. 83–101 (cit. on pp. 49, 50, 69, 72).

Haud, U. and P. M. W. Kalberla (2007). “Gaussian decomposition of H I surveys. III. Local H I”. In: A&A 466. bibtex: haud2007, pp. 555–564 (cit. on p. 48).

Hayes, M. A. and H. Nussbaumer (1984). “The C II infrared and ultraviolet lines”. en. In: A&A 134.1, p. 193 (cit. on p. 32).

Heeschen, David S. (1955). “Some Features of Interstellar Hydrogen in the Section of the Galactic Center.” In: ApJ 121, p. 569 (cit. on p. 48).

Heiles, C. and E. B. Jenkins (1976). “An almost complete survey of 21-cm line radiation for”. en. In: A&A 46.3, p. 333 (cit. on p. 35).

Heiles, Carl and T. H. Troland (2003a). “The Millennium Arecibo 21 Centimeter Absorption-Line Survey. I. Techniques and Gaussian Fits”. In: ApJS 145, pp. 329–354 (cit. on pp. 2, 34, 49, 66).

– (2003b). “The Millennium Arecibo 21 Centimeter Absorption-Line Survey. II. Properties of the Warm and Cold Neutral Media”. In: ApJ 586, pp. 1067–1093 (cit. on pp. 2, 34).

– (2005). “The Millennium Arecibo 21 Centimeter Absorption-Line Survey. IV. Statistics of Magnetic Field, Column Density, and Turbulence”. In: ApJ 624, pp. 773–793 (cit. on p. 35).

Heiles, Carl, Di Li, Naomi McClure-Griffiths, Lei Qian, and Shu Liu (2019). “The Interstellar Medium: The Key Component in Galactic Evolution and Modern Cosmology”. In: Research in A&A 19.2. arXiv: 1904.01237, p. 017 (cit. on p. 35).

Heitsch, F., B. Bartell, S. E. Clark, et al. (2016). “Three-dimensional orientation of compact high velocity clouds”. en. In: MNRAS 462.1, p. L46 (cit. on p. 43).

Hennebelle, P. and M. Pérault (1999). “Dynamical condensation in a thermally bistable flow. Application to interstellar cirrus”. In: A&A 351, pp. 309–322 (cit. on pp. 2, 29, 94, 104).

Hennebelle, P., R. Banerjee, E. Vázquez-Semadeni, R. S. Klessen, and E. Audit (2008). “From the warm magnetized atomic medium to molecular clouds”. In: A&A 486, pp. L43–L46 (cit. on p. 2).

Hennebelle, Patrick and Edith Falgarone (2012). “Turbulent molecular clouds”. en. In: A&AReview 20, p. 55 (cit. on pp. 101, 103).

HI4PI Collaboration, N. Ben Bekhti, L. Flöer, et al. (2016). “HI4PI: A full-sky H I survey based on EBHIS and GASS”. In: A&A 594, A116 (cit. on p. 43).

Hoerner, S. von (1951). “Eine Methode zur Untersuchung der Turbulenz der interstellaren Materie. Mit 10 Textabbildungen”. In: Zeitschrift fur Astrophysik 30, p. 17 (cit. on pp. 2, 20).

Jenkins, Edward B. and Todd M. Tripp (2011). “The Distribution of Thermal Pressures in the Diffuse, Cold Neutral Medium of Our Galaxy. II. An Expanded Survey of Interstellar C I Fine-structure Excitations”. In: ApJ 734, p. 65 (cit. on p. 34).

Kalberla, P. M. W. and L. Dedes (2008). “Global properties of the H I distribution in the outer Milky Way. Planar and extra-planar gas”. In: A&A 487, pp. 951–963 (cit. on pp. 36, 37).

Kalberla, P. M. W. and U. Haud (2018). “Properties of cold and warm H I gas phases derived from a Gaussian decomposition of HI4PI data”. en. In: Astronomy & Astrophysics 619, A58 (cit. on pp. 48, 49, 72).

Kalberla, P. M. W., W. B. Burton, Dap Hartmann, et al. (2005). “The Leiden/Argentine/Bonn (LAB) Survey of Galactic HI. Final data release of the combined LDS and IAR surveys with improved stray-radiation corrections”. In: A&A 440, pp. 775–782 (cit. on pp. 2, 36).

Kalberla, P. M. W., L. Dedes, J. Kerp, and U. Haud (2007). “Dark matter in the Milky Way, II. the HI gas distribution as a tracer of the gravitational potential”. In: Astronomy & Astrophysics 469.2. arXiv: 0704.3925, pp. 511–527 (cit. on pp. 37, 38, 96).

Kalberla, Peter M.W. and Jürgen Kerp (2009). “The Hi Distribution of the Milky Way”. In: ARA&A 47.1, pp. 27–61 (cit. on pp. 36, 37, 43).

Kanekar, Nissim, Ravi Subrahmanyan, Jayaram N. Chengalur, and Vicky Safouris (2003). “The temperature of the warm neutral medium in the Milky Way”. In: MNRAS 346, pp. L57–L61 (cit. on pp. 2, 34, 49).

Kim, Jongsoo and Dongsu Ryu (2005). “Density Power Spectrum of Compressible Hydrodynamic Turbulent Flows”. In: ApJLetters 630, pp. L45–L48 (cit. on pp. 21, 91, 111, 114).

Koyama, Hiroshi and Shu-ichiro Inutsuka (2002). “An Origin of Supersonic Motions in Interstellar Clouds”. In: ApJLetters 564, pp. L97–L100 (cit. on p. 2).

Lallement, R., R. Ferlet, A. M. Lagrange, M. Lemoine, and A. Vidal-Madjar (1995). “Local Cloud structure from HST-GHRS”. In: A&A 304, p. 461 (cit. on p. 86).

Lallement, R., B. Y. Welsh, J. L. Vergely, F. Crifo, and D. Sfeir (2003). “3D mapping of the dense interstellar gas around the Local Bubble”. In: A&A 411, pp. 447–464 (cit. on p. 86).

Lallement, R., L. Capitanio, L. Ruiz-Dern, et al. (2018). “Three-dimensional maps of interstellar dust in the Local Arm: using Gaia, 2MASS, and APOGEE-DR14”. In: A&A 616, A132 (cit. on p. 86).

Lallement, R., C. Babusiaux, J. L. Vergely, et al. (2019). “Gaia-2MASS 3D maps of Galactic interstellar dust within 3 kpc”. In: arXiv:1902.04116 [astro-ph]. arXiv: 1902.04116 (cit. on pp. 86–88).

Larson, R. B. (1979). “Stellar kinematics and interstellar turbulence”. In: MNRAS 186, pp. 479–490 (cit. on pp. 15, 21, 44).

– (1981). “Turbulence and star formation in molecular clouds”. In: MNRAS 194, pp. 809–826 (cit. on pp. 15, 20, 21, 44).

Launay, J.-M. and E. Roueff (1977). “Fine-structure excitation of ground-state C/+/ ions by hydrogen atoms”. en. In: Journal of Physics B Atomic Molecular Physics 10, p. 879 (cit. on p. 32).

Lazarian, A. and D. Pogosyan (2000). “Velocity Modification of H I Power Spectrum”. In: ApJ 537, pp. 720–748 (cit. on pp. 44, 45).

Lee, Min-Young, Snezana Stanimirovic, Claire E. Murray, Carl Heiles, and Jesse Miller (2015). “Cold and Warm Atomic Gas around the Perseus Molecular Cloud. II. The Impact of High Optical Depth on the HI Column Density Distribution and Its Implication for the HI-to-H2 Transition”. In: ApJ 809.1. arXiv: 1504.07405, p. 56 (cit. on p. 49).

Lequeux, J. (2012). Le Milieu interstellaire. SAVOIRS ACTUELS. EDP Sciences (cit. on pp. 19, 21, 31, 100).

Lesieur, M. (1987). Turbulence in fluids. Stochastic and numerical modelling. (Cit. on pp. 16, 17).

Levrier, F. (2004). “Velocity centroids and the structure of interstellar turbulence. I. Analytical study”. en. In: A&A 421, p. 387 (cit. on pp. 90, 91).

Lindblad, P. O. (1966). “Dwingeloo Atlas of 21-cm profiles, Part III, with a representation in Gaussian components”. In: JRASCSupplement Series 1, p. 177 (cit. on p. 48).

Lindner, Robert R., Carlos Vera-Ciro, Claire E. Murray, et al. (2015). “Autonomous Gaussian Decomposition”. In: AJ 149, p. 138 (cit. on p. 73).

Liszt, H. S. (2013). “N(H I)/E(B-V)”. In: ApJ 780.1. arXiv: 1310.6616, p. 10 (cit. on p. 87).

Marchal, Antoine, Marc-Antoine Miville-Deschênes, François Orieux, et al. (2019). “ROHSA: Regularized Optimization for Hyper-Spectral Analysis. Application to phase separation of 21 cm data”. en. In: A&A 626, A101 (cit. on p. 94).

Martin, P. G., K. P. M. Blagrave, Felix J. Lockman, et al. (2015). “GHIGLS: H I Mapping at Intermediate Galactic Latitude Using the Green Bank Telescope”. In: ApJ 809, p. 153 (cit. on pp. 36, 45, 49, 50, 67, 69, 72, 73, 77, 109, 110).

Mathis, J. S., W. Rumpl, and K. H. Nordsieck (1977). “The size distribution of interstellar grains.” en. In: ApJ 217, p. 425 (cit. on p. 31).

Matthews, Thomas A. (1957). “Observations of neutral hydrogen in the 21-cm line at various latitudes near galactic longitude 100”. In: AJ 62, p. 25 (cit. on p. 48).

McClintock, W., R. C. Henry, J. L. Linsky, and H. W. Moos (1978). “Ultraviolet observations of cool stars. VII - Local interstellar hydrogen and deuterium Lyman-alpha”. In: ApJ 225, pp. 465–481 (cit. on p. 85).

McClure-Griffiths, N. M., John M. Dickey, B. M. Gaensler, and A. J. Green (2003a). “Loops, Drips, and Walls in the Galactic Chimney GSH 277+00+36”. en. In: ApJ 594.2, p. 833 (cit. on pp. 38, 39).

McClure-Griffiths, N. M., J. M. Dickey, B. M. Gaensler, and A. J. Green (2003b). “Shells, Bubbles, and Chimneys in the Southern Galactic Plane Survey”. en. In: Revista Mexicana de Astronomia y Astrofisica Conference Series 15, p. 287 (cit. on p. 89).

McClure-Griffiths, N. M., D. J. Pisano, M. R. Calabretta, et al. (2009). “Gass: The Parkes Galactic All-Sky Survey. I. Survey Description, Goals, and Initial Data Release”. In: ApJS 181, pp. 398–412 (cit. on pp. 3, 36).

Mebold, U. (1972). “On the Intercloud Hi-Gas”. In: A&A 19, p. 13 (cit. on p. 48).

Mebold, U., O. Hachenberg, and C. A. Laury-Micoulaut (1974). “A Statistical Model for the Intercloud HI-Gas. I. Theory”. In: A&A 30, p. 329 (cit. on p. 44).

Miville-Deschenes, Marc-Antoine, Gilles Joncas, and Daniel Durand (1995). “The H II Region Sharpless 170: A Multiscale Analysis of the H alpha Velocity Field”. In: ApJ 454, p. 316 (cit. on p. 20).

Miville-Deschênes, M.-A. and P. G. Martin (2007). “Physical properties of a very diffuse HI structure at high Galactic latitude”. In: A&A 469, pp. 189–199 (cit. on p. 54).

Miville-Deschênes, M.-A., G. Joncas, E. Falgarone, and F. Boulanger (2003a). “High resolution 21 cm mapping of the Ursa Major Galactic cirrus: Power spectra of the high-latitude H I gas”. In: A&A 411, pp. 109–121 (cit. on p. 45).

Miville-Deschênes, M.-A., F. Levrier, and E. Falgarone (2003b). “On the Use of Fractional Brownian Motion Simulations to Determine the Three-dimensional Statistical Properties of Interstellar Gas”. In: ApJ 593, pp. 831–847 (cit. on pp. 22, 49, 90, 91, 112).

Miville-Deschênes, M.-A., P.-A. Duc, F. Marleau, et al. (2016). “Probing interstellar turbulence in cirrus with deep optical imaging: no sign of energy dissipation at 0.01 pc scale”. In: A&A 593, A4 (cit. on p. 109).

Miville-Deschênes, M.-A., Q. Salomé, P. G. Martin, et al. (2017a). “Structure formation in a colliding flow: The Herschel view of the Draco nebula”. In: A&A 599, A109 (cit. on pp. 50, 72, 101).

Miville-Deschênes, Marc-Antoine, Norman Murray, and Eve J. Lee (2017b). “Physical Properties of Molecular Clouds for the Entire Milky Way Disk”. In: ApJ 834, p. 57 (cit. on pp. 21, 72, 103).

Moss, V. A., N. M. McClure-Griffiths, T. Murphy, et al. (2013). “High-velocity Clouds in the Galactic All Sky Survey. I. Catalog”. en. In: ApJS 209.1, p. 12 (cit. on p. 43).

Muller, C. A. (1957). “21-CM Absorption Effects in the Spectra of Two Strong Radio Sources.” In: ApJ 125, p. 830 (cit. on p. 48).

– (1959). “21-cm hydrogen-line absorption in the spectra of discrete sources”. In: vol. 9, p. 360 (cit. on p. 48).

Muller, C. A., J. H. Oort, and E. Raimond (1963). “Hydrogène neutre dans la couronne galactique?” en. In: Academie des Sciences Paris Comptes Rendus 257, p. 1661 (cit. on p. 41).

Murray, Claire E., Robert R. Lindner, Snezana Stanimirovic, et al. (2014). “Excitation Temperature of the Warm Neutral Medium as a New Probe of the Lyalpha Radiation Field”. In: ApJLetters 781. bibtex: murray2014, p. L41 (cit. on p. 49).

Murray, Claire E., Snežana Stanimirović, W. M. Goss, et al. (2015). “The 21-SPONGE HI Absorption Survey I: Techniques and Initial Results”. In: ApJ 804, p. 89 (cit. on pp. 2, 34, 49).

Murray, Claire E., J. E. G. Peek, Min-Young Lee, and Snezana Stanimirovic (2018a). “Optically thick HI does not dominate dark gas in the local ISM”. In: arXiv:1806.01300 [astro-ph]. arXiv: 1806.01300 (cit. on p. 49).

Murray, Claire E., Snežana Stanimirović, W. M. Goss, et al. (2018b). “The 21-SPONGE H i Absorption Line Survey. I. The Temperature of Galactic H i”. en. In: ApJS 238.2, p. 14 (cit. on pp. 2, 34, 35, 82–84).

Oort, J. H. and L. Spitzer Jr. (1955). “Acceleration of Interstellar Clouds by O-Type Stars.” In: ApJ 121, p. 6 (cit. on p. 44).

Ossenkopf, V., A. Esquivel, A. Lazarian, and J. Stutzki (2006). “Interstellar cloud structure: the statistics of centroid velocities”. In: A&A 452, pp. 223–236 (cit. on pp. 21, 22, 90).

Ostriker, Eve C., Christopher F. McKee, and Adam K. Leroy (2010). “Regulation of Star Formation Rates in Multiphase Galactic Disks: A Thermal/Dynamical Equilibrium Model”. In: ApJ 721, pp. 975–994 (cit. on p. 1).

Parker, Eugene N. (1953). “Instability of Thermal Fields.” en. In: ApJ 117, p. 431 (cit. on p. 102).

Peek, J. E. G., Carl Heiles, Kevin A. Douglas, et al. (2011a). “The GALFA-HI Survey: Data Release 1”. In: ApJS 194, p. 20 (cit. on p. 36).

Peek, J. E. G., Carl Heiles, Kathryn M. G. Peek, David M. Meyer, and J. T. Lauroesch (2011b). “The Local Leo Cold Cloud and New Limits on a Local Hot Bubble”. In: ApJ 735, p. 129 (cit. on p. 85).

Peek, J. E. G., Brian L. Babler, Yong Zheng, et al. (2018). “The GALFA-H I Survey Data Release 2”. In: ApJS 234, p. 2 (cit. on pp. 3, 36).

Pingel, Nickolas, Min-Young Lee, Blakesley Burkhart, and Snezana Stanimirović (2018). “The Multi-phase Turbulence Density Power Spectra in the Perseus Molecular Cloud”. In: arXiv:1802.10092 [astro-ph]. arXiv: 1802.10092 (cit. on p. 44).

Planck Collaboration, A. Abergel, P. A. R. Ade, et al. (2011). “Planck early results. XXIV. Dust in the diffuse interstellar medium and the Galactic halo”. In: A&A 536, A24, A24 (cit. on p. 81).

Poppel, W. G. L., P. Marronetti, and P. Benaglia (1994). “The warm and cold neutral phase in the local interstellar medium at absolute value of B greater than or equal to 10 deg”. In: A&A 287, pp. 601–619 (cit. on pp. 49, 50).

Putman, M. E., D. R. Saul, and E. Mets (2011). “Head-Tail Clouds: Drops to Probe the Diffuse Galactic Halo”. In: MNRAS 418.3. arXiv: 1110.0013, pp. 1575–1586 (cit. on p. 43).

Redfield, Seth and Jeffrey L. Linsky (2000). “The Three-dimensional Structure of the Warm Local Interstellar Medium. II. The Colorado Model of the Local Interstellar Cloud”. In: ApJ 534, pp. 825–837 (cit. on p. 85).

– (2008). “The Structure of the Local Interstellar Medium. IV. Dynamics, Morphology, Physical Properties, and Implications of Cloud-Cloud Interactions”. en. In: ApJ 673.1, pp. 283–314 (cit. on p. 85).

Reynolds, Osborne (1883). “An Experimental Investigation of the Circumstances Which Determine Whether the Motion of Water Shall Be Direct or Sinuous, and of the Law of Resistance in Parallel Channels”. In: Philosophical Transactions of the Royal Society of London 174, pp. 935–982 (cit. on p. 11).

Reynolds, R. J. (1977). “Pulsar dispersion measures and H-alpha emission measures - Limits on the electron density and filling factor for the ionized interstellar gas”. In: ApJ 216, pp. 433–439 (cit. on p. 96).

Rezaei Kh., S., C. A. L. Bailer-Jones, R. J. Hanson, and M. Fouesneau (2017). “Inferring the three-dimensional distribution of dust in the Galaxy with a non-parametric method . Preparing for Gaia”. In: A&A 598, A125 (cit. on p. 86).

Roy, Nirupam, Nissim Kanekar, Robert Braun, and Jayaram N. Chengalur (2013a). “The temperature of the diffuse H I in the Milky Way - I. High resolution H I-21 cm absorption studies”. In: MNRAS 436, pp. 2352–2365 (cit. on pp. 2, 34).

Roy, Nirupam, Nissim Kanekar, and Jayaram N. Chengalur (2013b). “The temperature of the diffuse H I in the Milky Way - II. Gaussian decomposition of the H I-21 cm absorption spectra”. In: MNRAS 436, pp. 2366–2385 (cit. on p. 2).

Röhser, T., J. Kerp, D. Lenz, and B. Winkel (2016a). “All-sky census of Galactic high-latitude molecular intermediate-velocity clouds”. In: A&A 596, A94 (cit. on p. 43).

Röhser, T., J. Kerp, N. Ben Bekhti, and B. Winkel (2016b). “High-resolution HI and CO observations of high-latitude intermediate-velocity clouds”. In: A&A 592, A142 (cit. on p. 43).

Saury, E., M.-A. Miville-Deschênes, P. Hennebelle, E. Audit, and W. Schmidt (2014). “The structure of the thermally bistable and turbulent atomic gas in the local interstellar medium”. In: A&A 567, A16 (cit. on pp. 2, 21, 54, 55, 63, 66, 67, 94, 95).

Saury, Eléonore (2012). “Turbulence et instabilité thermique du milieu interstellaire atomique neutre : une approche numérique”. thesis. Paris 11 (cit. on pp. 15, 28, 33).

Schlüter, A., H. Schmidt, and P. Stumpff (1953). “Zur Analyse der Bewegungsverhältnisse im interstellaren Gas. Mit 9 Textabbildungen”. en. In: Zeitschrift fur Astrophysik 33, p. 194 (cit. on p. 41).

Solomon, P. M., A. R. Rivolo, J. Barrett, and A. Yahil (1987). “Mass, luminosity, and line width relations of Galactic molecular clouds”. In: ApJ 319, pp. 730–741 (cit. on p. 21).

Spitzer Jr., Lyman (1978). “Review of Publications: Physical Processes in the Interstellar Medium”. In: JRASC 72, p. 349 (cit. on pp. 31, 33).

Stanimirović, Snežana and Carl Heiles (2005). “The Thinnest Cold H I Clouds in the Diffuse Interstellar Medium?” In: ApJ 631, pp. 371–375 (cit. on p. 49).

Stanimirović, Snežana, Claire E. Murray, Min-Young Lee, Carl Heiles, and Jesse Miller (2014). “COLD AND WARM ATOMIC GAS AROUND THE PERSEUS MOLECULAR CLOUD. I. BASIC PROPERTIES”. en. In: ApJ 793.2, p. 132 (cit. on p. 49).

Stil, J. M., A. R. Taylor, J. M. Dickey, et al. (2006). “The VLA Galactic Plane Survey”. In: AJ 132, pp. 1158–1176 (cit. on pp. 2, 36).

Takakubo, K. (1967). “Neutral hydrogen at intermediate galactic latitudes. III. Local kinematical properties derived from Gaussian 21-cm profile components; comparison with Ca+ K-line data”. In: JRASC 19, p. 125 (cit. on p. 48).

Takakubo, Keiya and Hugo van Woerden (1966). “Neutral Hydrogen at Intermediate Galactic Latitudes”. In: JRASC 18, pp. 488–533 (cit. on pp. 48, 50).

Taylor, A. R., S. J. Gibson, M. Peracaula, et al. (2003). “The Canadian Galactic Plane Survey”. In: AJ 125, pp. 3145–3164 (cit. on pp. 2, 36).

Vergely, J.-L., R. Freire Ferrero, A. Siebert, and B. Valette (2001). “NaI and HI 3-D density distribution in the solar neighbourhood”. en. In: A&A 366.3, pp. 1016–1034 (cit. on pp. 86, 87).

Vergely, J.-L., B. Valette, R. Lallement, and S. Raimond (2010). “Spatial distribution of interstellar dust in the Sun’s vicinity. Comparison with neutral sodium-bearing gas”. In: A&A 518, A31 (cit. on p. 86).

Verschuur, G. L. and J. T. Schmelz (1989). “High-resolution studies of 21 CM emission profiles”. In: AJ 98. bibtex: verschuur1989, pp. 267–278 (cit. on p. 49).

Verschuur, Gerrit L. (2004). “Interstellar Neutral Hydrogen Emission Profile Structure”. In: AJ 127. bibtex: verschuur2004, pp. 394–407 (cit. on p. 49).

Verschuur, Gerrit L. and Loris Magnani (1994). “On the nature of 21 CM emission profile structure at high galactic latitude: Implications for the warm neutral medium”. In: AJ 107. bibtex: verschuur1994, pp. 287–297 (cit. on p. 49).

Vogel, Christian (2011). “Statistical properties of compressible hydrodynamic and magnetohydrodynamic turbulence”. In: (cit. on pp. 21, 100).

Wakker, B. P. (2001). “Distances and Metallicities of High- and Intermediate-Velocity Clouds”. In: ApJS 136, pp. 463–535 (cit. on p. 43).

Wakker, B. P. and H. van Woerden (1991). “Distribution and origin of high-velocity clouds. III - Clouds, complexes and populations”. In: A&A 250, pp. 509–532 (cit. on p. 41).

Watson, William D. (1972). “Heating of Interstellar H i Clouds by Ultraviolet Photoelectron Emission from Grains”. en. In: ApJ 176, p. 103 (cit. on pp. 25, 31).

Weizsäcker, C. F. von (1951). “The Evolution of Galaxies and Stars.” In: ApJ 114, p. 165 (cit. on pp. 2, 20).

Wilson, O. C., Guido Minich, Edith Flather, and Mary F. Coffeen (1959). “Internal Kinematics of the Orion Nebula.” In: ApJS 4, p. 199 (cit. on p. 20).

Winkel, B., J. Kerp, L. Flöer, et al. (2016). “The Effelsberg-Bonn H I Survey: Milky Way gas. First data release”. In: A&A 585, A41 (cit. on pp. 3, 36).

Woerden, Hugo van, Bart Wakker, Ulrich Schwarz, and Klaas de Boer (2004). High-Velocity Clouds. en. Google-Books-ID: 9fFqHLtqan4C. Springer Science & Business Media (cit. on p. 41).

Wolfire, M. G., D. Hollenbach, C. F. McKee, A. G. G. M. Tielens, and E. L. O. Bakes (1995a). “The neutral atomic phases of the interstellar medium”. In: ApJ 443, pp. 152–168 (cit. on pp. 2, 25, 30, 32, 34, 66, 92).

Wolfire, Mark G., Christopher F. McKee, David Hollenbach, and A. G. G. M. Tielens (1995b). “The Multiphase Structure of the Galactic Halo: High-Velocity Clouds in a Hot Corona”. In: ApJ 453, p. 673 (cit. on p. 43).

– (2003). “Neutral Atomic Phases of the Interstellar Medium in the Galaxy”. In: ApJ 587, pp. 278–311 (cit. on pp. 2, 25, 30–34, 38, 92, 97–99, 102).

Wolleben, M., A. Fletcher, T. L. Landecker, et al. (2010). “Antisymmetry in the Faraday Rotation Sky Caused by a Nearby Magnetized Bubble”. en. In: ApJ 724.1, p. L48 (cit. on pp. 39, 40).

Zhu, Ciyou, Richard H. Byrd, Peihuang Lu, and Jorge Nocedal (1997). “Algorithm 778: L-BFGS-B: Fortran Subroutines for Large-scale Bound-constrained Optimization”. In: ACM Trans. Math. Softw. 23.4, pp. 550–560 (cit. on p. 52).

List of Figures

List of Tables

Colophon

This thesis was typeset with LaTeX 2$_\varepsilon$. It uses the *Clean Thesis* style developed by Ricardo Langner. The design of the *Clean Thesis* style is inspired by user guide documents from Apple Inc.

Download the *Clean Thesis* style at http://cleanthesis.der-ric.de/.

Title : On the multiphase structure of the turbulent neutral interstellar medium

Keywords : ISM: clouds, kinematics and dynamics, structure - methods: data analysis, numerical, observational

Abstract : Star formation in galaxies is strongly linked to the physical processes that govern the evolution of the interstellar medium. Stars form by gravitational collapse of dense and cold structures in molecular clouds but the process that leads to the formation of these over-densities is still unclear. One key element seems to be related to the efficiency of the formation of cold clouds of neutral hydrogen (HI) also called the Cold Neutral Medium (CNM).
Several studies have aimed at understanding the production of the CNM through the condensation of the Warm Neutral Medium (WNM) in a turbulent and thermally unstable flow using numerical simulations. In general, these studies indicate the presence of a significant fraction of the mass being in the thermally unstable regime, (i.e., with a temperature mid-way between the CNM and WNM stable states). However, the thermodynamical conditions of the gas remain largely unexplored from the observational point of view. To go further, and really compare with numerical simulation that are, for now, under-constrained by observation, it is mandatory to map the column density structure of each phase and study the spatial variations of their centroid velocity and velocity dispersion. This calls for methods that can extract the information of each HI phase from fully sampled 21 cm emission data only.
An original Gaussian decomposition algorithm, named *ROHSA*, is presented in this thesis. Based on a multi-resolution process from coarse to fine grid, and using a regularized non-linear least-square criterion to take into account simultaneously the spatial coherence of the emission and the multiphase nature of the gas, this method allows us to infer a spatially coherent vision of the three-phase neutral ISM.
A detailed analysis is then presented on a high latitude HI field centred on the North Ecliptic Pole. In particular we provide new constraints on the thermodynamical properties of the WNM, and the statistical properties of the turbulent cascade acting in the fluid. Finally, we discuss under which conditions the condensation mode of the thermal instability can grow in this medium and converge toward the cold phase of the neutral ISM, the CNM.

Titre : Etude de la structure multiphase du milieu interstellaire neutre turbulent

Mots clés : MIS: nuages, cinématique et dynamique, structure - methodes: analyse de données, observation

Résumé : La formation des étoiles dans les galaxies est intimement liée aux processus physiques qui régissent l'évolution du milieu interstellaire. Les étoiles se forment dans les nuages moléculaires par effondrement gravitationnel de structures denses et froides, mais le processus qui mène à la formation de ces surdensités est encore relativement mal compris. Un des élément clé semble être lié à l'efficacité de la formation de nuages froids d'hydrogène neutre (HI), également appelé "Cold neutral Medium" (CNM).
Plusieurs études ont visé à comprendre la production du CNM par condensation du "Warm Neutral Medium" (WNM) dans un écoulement turbulent et thermiquement instable à l'aide de simulations numériques. De façon générale, ces études indiquent la présence d'une fraction significative de la masse dans le régime instable (c'est-à-dire avec une température à mi-chemin entre les états stables CNM et WNM). Cependant, les conditions thermodynamiques du gaz restent largement inexplorées du point de vue de l'observation : pour aller plus loin, et comparer réellement avec les simulations numériques, il est nécessaire de cartographier la structure de densité des colonnes de chaque phase et d'étudier les variations spatiales de leurs champs de vitesse et de dispersion des vitesses. Par nature, cela nécessite le developpement de méthodes pouvant extraire ces informations de données entièrement échantillonnées spatialement: l'emission de la raie à 21 cm.
Un nouvel algorithme de décomposition en Gaussiènne, appelé *ROHSA*, est présenté dans cette thèse. Basée sur un processus multi-résolution, et utilisant un critère de moindres carrés non-linéaires régularisés prenant en compte simultanément la cohérence spatiale de l'émission et la nature multiphase du gaz, cette méthode nous permet d'inférer une vision spatialement cohérente des phases milieu interstellaire neutre.
Une analyse détaillée est ensuite présentée sur un champ à haute latitude centré sur le pôle nord écliptique. En particulier, nous apportons de nouvelles contraintes sur les propriétés thermodynamiques du WNM, ainsi que sur les propriétés statistiques de la cascade turbulente agissant dans le fluide. Enfin, nous discutons dans quelles conditions l'instabilité thermique peut se développer dans ce milieu et converger vers la phase froide du milieu interstellaire neutre, le CNM.

Université Paris-Saclay
Espace Technologique / Immeuble Discovery
Route de l'Orme aux Merisiers RD 128 / 91190 Saint-Aubin, France